GHENT UNIVERSITY

FACULTY OF SCIENCES

TWO-PHASE FLOW IN ROCKS:
NEW INSIGHTS FROM MULTI-SCALE PORE NETWORK MODELING AND FAST PORE SCALE VISUALIZATION

Tom Bultreys

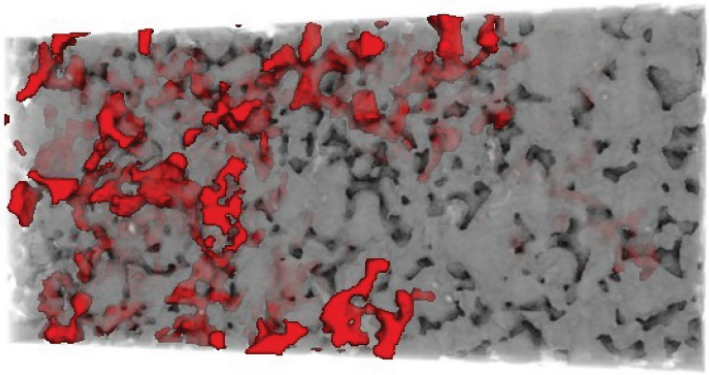

Promotors: Prof. Dr. Veerle Cnudde
Prof. Dr. Luc Van Hoorebeke

Thesis submitted in fulfillment of the requirements for the degree of
Doctor of Science: Physics and of Science: Geology

Two-phase flow in rocks: new insights from multi-scale pore network modeling and fast pore scale visualization

Tom Bultreys

November 29, 2016

Universiteit Gent
Faculteit Wetenschappen
Vakgroep Fysica en Sterrenkunde
Vakgroep Geologie

Two-phase flow in rocks: new insights from multi-scale pore network modeling and fast pore scale visualization

Promotoren:	Prof. Dr. Veerle Cnudde
	Prof. Dr. Luc Van Hoorebeke
Examencommissie:	Prof. Dr. Martin Blunt
	Prof. Dr. Amir Raoof
	Prof. Dr. Rudy Swennen
	Dr. Ir. Gemmina Di Emidio
	Dr. Ir. Matthieu Boone (secretaris)
	Prof. Dr. Luc Van Hoorebeke (promotor)
	Prof. Dr. Veerle Cnudde (promotor)
	Prof. Dr. Natalie Jachowicz (voorzitter)

Universiteit Gent

Faculteit Wetenschappen
Vakgroep Fysica en Sterrenkunde
Proeftuinstraat 86, B-9000 Gent, België
Tel.: +32-9-264.46.47

Vakgroep Geologie
Krijgslaan 281 (S8), B-9000 Gent, België
Tel.: +32-9-264.45.80

Proefschrift ter behaling van de graad van
Doctor in de Wetenschappen: Fysica
en in de Wetenschappen: Geologie
Academiejaar 2015-2016

University Press, ISBN 978-9-4619747-0-9

This work was supported by the Agency for Innovation by Science and Technology in Flanders, Belgium (IWT).

© Tom Bultreys, 2016.

Alle rechten voorbehouden. Niets uit deze uitgave mag worden vermenigvuldigd en/of openbaar gemaakt worden door middel van druk, fotokopie, microfilm, elektronisch of op welke andere wijze ook, zonder voorafgaande schriftelijke toestemming van de uitgever.

All rights reserved. No part of this publication may be reproduced in any form by print, photo print, microfilm or any other means without written permission from the author.

Dankwoord

Na de vier korte (maar heel af en toe toch ook wel eens lange) en intense jaren die een doctoraat uitmaken, komt het moment dat je al je werk samengebald ziet in één verhaal. Dit stel je niet enkel voor aan een jury van wereldwijde experts in je vak, maar ook aan je familie en je vrienden. Eigenlijk is dit een luxe, al zal geen enkele doctoraatsstudent dit beamen vooraleer zijn thesis klaar is. Het overweldigende gevoel dat hiermee gepaard gaat is dan ook dankbaarheid.

In de eerste plaats wil ik mijn promotoren Prof. Veerle Cnudde en Prof. Luc Van Hoorebeke bedanken voor de fantastische kansen om niet alleen het wetenschappelijke vak, maar ook een stukje van de wereld, te leren kennen. Dankzij jullie vertrouwen en begeleiding ben ik hier geraakt. Veerle, bedankt om mij te motiveren om mij maximaal te ontplooien op onderzoeksvlak, om mij te betrekken bij veel andere aspecten van het academische werk, en voor je constante aandacht voor het menselijke aspect van doctoreren (zo gaf je mij ooit een plastieken kamerplant te leen omdat de aanwezigheid van planten nu eenmaal opvrolijkt). Luc, bedankt voor de niet-aflatende steun en voor je oog voor fysische correctheid bij het nalezen van mijn werk.

Ook mijn collega's wil ik hier bedanken voor de vele onvergetelijke momenten in binnen- en buitenland. Jan en Wesley wens ik te bedanken voor het delen van lief en leed in ons bureau. Marijn, bedankt voor het goedbedoelde duwtje in de rug af en toe, hetgeen een grote rol speelde in het experimentele luik van dit doctoraat. Hannelore wil ik graag bedanken voor de vele bemoedigende woorden en voor discussies met wiskundige insteek. Tim en Jeroen zijn onmisbare sfeermakers geweest en bedank ik voor hun hulp bij experimenten en sample-selectie. Ook Neil, Victor, Aurélie, Delphine, Daniëlle, Maxim, Géraldine: bedankt (*thanks*)! Ook op het stralingsfysica-team (Manu, Matthieu, Thomas, Jelle, Amelie, Marjolein, Loes, Elin, Bert, Denis, Pieter) heb ik steeds kunnen rekenen.

Matthieu, Thomas, Denis, Manu en Bert, ik ben jullie bijzonder veel dank verschuldigd voor de regelmatige dépannages en voor de hulp bij het uitvoeren van de snelle scans. Matthieu: ook bedankt om secretaris van mijn examencommissie te willen zijn!

I would like to thank Prof. Martin Blunt and Ali Raeini for helping me get acquainted with their network modeling code during my stay at Imperial College London. I would also like to thank Prof. Masha Prodanovic and Ayaz Mehmani for sharing their artificial network model and the Wilcox image. Leo Ruspini and Pål-Eric Øren, thank you for hosting me in Trondheim, and for interesting discussions. Thanks to Prof. Amir Raoof for the many interesting discussions we had in Utrecht and in Ghent. I am also extremely grateful to the members of my PhD jury (Prof. Natalie Jachowicz, Prof. Rudy Swennen, Dr. Ir. Gemmina Di Emidio, Dr. Ir. Matthieu Boone, Prof. Martin Blunt and Prof. Amir Raoof), for reading my work and giving their valuable feedback.

Uiteraard ben ik niet alleen mijn dank verschuldigd aan collega's, maar ook aan familie en vrienden. In de eerste plaats mijn ouders, die mij altijd de beste kansen hebben geboden doorheen mijn hele opleiding. Hun jarenlange steun door dik en dun heeft mij hier gebracht. Ook mijn broer Jo en grootouders waren een grote steun. Mijn vrienden (Pieter, Laura, Tim, Ilse, Gaetan, Lize, Jonas en vele anderen) zorgden er voor dat ik regelmatig het werk uit mijn hoofd kon zetten om te ontspannen, en leverden zo eveneens een onmisbare bijdrage!

Finaal is er nog één persoon die haar eigen paragraafje verdient, en dat is natuurlijk Céline. Je liefde, humor en energie blijven me elke dag verbazen, en zijn een enorme steun op alle vlakken. Ik kijk er dan ook naar uit samen met jou ons avontuur tegemoet te gaan...

Tom Bultreys

English summary

Many geological applications involve the flow of multiple fluids through porous geological materials, e.g. environmental remediation of polluted ground water resources, CO_2 storage in geological reservoirs and petroleum recovery. Commonly, to model these applications, the geological materials in question are treated as continuous porous media with effective material properties. Since these properties are a manifestation of what goes on in the pores of the material, we have to study the transport processes at the pore scale to understand why and how they vary over space and time in different rocks and under different conditions. As the high cost of acquiring and testing samples in many of these applications is often a limiting factor, numerical modelling at the pore scale is becoming a key technology to gain new insights in this field. This could be crucial in reducing uncertainties in field scale projects.

The work presented in this thesis focuses on the investigation of two-phase flow in sedimentary rocks, and is an integrated numerical and experimental study. It deals primarily with two outstanding issues. First, image-based pore scale simulation methods have difficulties with representing the multiple pore scales in rocks with wide pore size distributions, due to a trade-off in the size and resolution of both modeling and imaging methods. Therefore, performing two-phase flow simulations in a number of important rock types, such as many carbonates and tight, clay-baring sandstones has remained an outstanding challenge. To tackle this problem, a new numerical model was developed to calculate capillary pressure, relative permeability and resistivity index curves during drainage and imbibition processes in such materials. The multi-scale model was based on information obtained from 3D micro-computed tomography images of the internal pore structure, complemented with information on the pores that are unresolved with this technique. In this method, pore network

models were first extracted from resolved pores in the images, by using a maximal ball network extraction algorithm. Then, pores which touched regions with unresolved porosity were connected with a special type of network element called micro-links. In the quasi-static simulations that were performed on these network models, the micro-links carried average properties of the unresolved porosity. In contrast to most previous models, the new approach to taking into account unresolved porosity therefore allowed efficient simulations on images of complex rocks, with sizes comparable to single-scale pore network models. It was able to reproduce most of the behaviour of a fully resolved pore network model, for both drainage and imbibition processes, and for different pore scale wettability distributions (water-wet, oil-wet and different mixed-wet distributions). Furthermore, simulations on images of carbonate rocks showed good agreement to experiments. A sensitivity study on carbonate rocks and tight, clay-bearing sandstones produced results that were in qualitative agreement with experiments, and allowed to analyse how the two-phase flow behaviour of these rocks is influenced by their pore scale properties.

The second issue which is treated in this thesis is related to the validation of pore scale models. Comparing predicted effective properties to experimentally measured values is useful and necessary, but is complicated by the typical difference in size between the model and the experiment. Furthermore, it does not always give a clear indication of the reasons for an observed mismatch between models and experiments. Comparing two-phase flow models to pore scale experiments in which the evolution of the fluid distributions is visualized is thus extremely useful. However, this requires to image the two-phase flow process while it is taking place in a rock, and it is necessary to do this with time resolutions on the order of tens of seconds and spatial resolutions on the order of micrometers. Previous experimental approaches used synchrotron beam lines to achieve this. In this thesis, we show that such experiments are also possible using laboratory-based micro-computed tomography scanners, which are orders of magnitude cheaper and therefore more accessible than synchrotrons. An experiment in which kerosene was pumped into a water-saturated sandstone is presented, showing that individual Haines jumps (pore filling events) could be visualized during this drainage process. Because the image quality is lower than at synchrotrons, care had to be taken to adapt the image analysis work flow to deal with high image noise levels. The work flow was designed to allow to track the fluid filling state of individual pores. The results indicate that the dynamic effects due

to viscous and inertial forces during Haines jumps do not significantly impact the evolution of the fluid distributions during drainage, which may thus be adequately described by quasi-static models.

Nederlandse samenvatting

In veel geologische toepassingen is de stroming van verschillende vloeistoffen doorheen poreuze geologische materialen belangrijk, bv. bij de sanering van vervuilde grondwaterlagen, de opslag van CO_2 in geologische reservoirs in de ondergrond en bij petroleum winning. Om dergelijke toepassingen te modelleren, worden de geologische materialen in kwestie als continue poreuze materialen met effectieve eigenschappen beschouwd. Aangezien deze effectieve eigenschappen zich manifesteren als gevolg van wat er gebeurt in de poriën van het materiaal, moeten we de transportprocessen op de porie-schaal bestuderen om te verstaan hoe en waarom zulke effectieve eigenschappen variëren doorheen de ruimte en overheen de tijd. Aangezien het bekomen en testen van stalen in veel gevallen een limiterende factor is door de hoge kostprijs die heermee gepaard gaat, zijn numerieke modellen een sleuteltechnologie aan het worden om nieuwe inzichten in deze materie te verkrijgen. Dit kan cruciaal zijn om de onzekerheid in het veld te verkleinen.

Het werk dat in deze thesis is neergeschreven is gericht op twee-fasige stroming van vloeistoffen en/of gassen in sedimentaire gesteenten, en betreft een geïntegreerde experimentele en numerieke studie. Het behandelt voornamelijk twee openstaande problemen omtrent deze problematiek. Ten eerste hebben beeld-gebaseerde numerieke modellen problemen met het omgaan met de verschillende ruimtelijke schalen die voorkomen in gesteenten met brede poriegrootte-verdelingen. Dit is het gevolg van de afweging die er moet gemaakt worden tussen resolutie en beeldgrootte, zowel in de beeldvorming als in de simulaties zelf. Daardoor is het uitvoeren van twee-fasige stromingssimulaties in een aantal belangrijke klassen van gesteenten (zoals veel carbonaatgesteenten en weinig-doorlatende zandstenen) een openstaand vraagstuk. Om dit probleem aan te pakken werd een nieuw model ontwikkeld om capillaire

drukken, relatieve permeabiliteiten en resistiviteitsindexen tijdens ontwatering (“drainage ”) en drenking (“imbibition ”) van gesteenten met een brede verdeling aan porie-groottes te berekenen. Het nieuwe model is gebaseerd op informatie die wordt onttrokken aan 3D micro-tomografische beelden van de interne poriestructuur van een steen, en wordt aangevuld met informatie over de poriën die in deze beelden niet geresolveerd zijn. In deze nieuwe methode wordt er eerst een porie-netwerk model geëxtraheerd van de geresolveerde poriën met behulp van een “maximal ball” algoritme, waarna poriën die raken aan een gebied met niet-geresolveerde porositeit verbonden worden door een nieuw soort netwerk-element. Deze netwerk-elementen dragen gemiddelde eigenschappen van de niet-geresolveerde porositeit, en de nieuwe methode laat daarom toe om efficiënte simulaties uit te voeren op beelden met vergelijkbare groottes als enkel-schalige netwerk modellen, maar dan op complexere stalen. Dit was met de meeste voorgaande methoden niet mogelijk. De voorgestelde aanpak laat toe om de belangrijkste gedragingen van een volledig geresolveerd netwerkmodel te reproduceren, zowel bij ontwatering als bij drenking, en bij verschillende verdelingen van hydrofobiciteit in de porieruimte. Verder kwamen simulaties op netwerken geëxtraheerd uit beelden van carbonaatgesteenten goed overeen met experimentele metingen. Een sensitiviteitsanalyse van het model toegepast op carbonaatgesteenten en weinig-doorlatende klei-rijke zandstenen leidde tot resultaten die in kwalitatieve overeenstemming waren met experimenten uit de literatuur, en liet toe om de link tussen het twee-fasige stromingsgedrag en de porie-kenmerken van deze complexe gesteenten te onderzoeken.

Het tweede probleem dat werd aangepakt in deze thesis heeft te maken met de validatie van modellen op de porie-schaal. De effectieve eigenschappen die deze modellen voorspellen moeten vergeleken worden met experimentele metingen hiervan, maar dit wordt bemoeilijkt door het typisch grootte-verschil tussen de modellen en experimenten. Verder geeft een dergelijke vergelijking niet altijd een duidelijke indicatie van de reden waarom het model en het experiment van elkaar afwijken. Daarom is het erg nuttig om twee-fasige vloeistofmodellen te vergelijken met experimenten waarin de evolutie van de vloeistofverdeling in 3D wordt gevisualiseerd. Daartoe moet men echter het proces visualizeren terwijl het plaatsvindt in een steen, en dit moet gebeuren met een tijdsresolutie in de orde van enkele tientallen seconden, en een spatiale resolutie in de orde van micrometers. Bij vroegere experimenten werd dit bereikt door

metingen te doen aan synchrotrons, maar in deze thesis wordt aangetoond dat dit ook mogelijk is met laboratoriumtoestellen die vele malen goedkoper en daardoor dus makkelijker beschikbaar zijn. Een experiment waarbij kerosine in een water-gesatureerde zandsteen wordt gepompt toont aan dat individuele Haines-sprongen (het vullen van individuele poriën) tijdens een ontwateringsprocess konden gevisualizeerd worden. Aangezien de beeldkwaliteit logischerwijze lager ligt dan bij synchrotrons, moest de beeldanalyse procedure aangepast worden aan het hoge beeldruis-niveau. Deze werkwijze werd zo ontworpen dat voor individuele poriën kon gevolgd worden met welke vloeistoffen ze verzadigd waren. De resultaten geven aan dat dynamische effecten ten gevolge van visceuze krachten en intertiaalkrachten tijdens Haines jumps vermoedelijk geen significante invloed hebben op de evolutie van de vloeistofverdeling tijdens ontwatering. Dit proces zou daarom adequaat kunnen beschreven worden met behulp van quasi-statische modellen, zoals het porie-netwerk model dat in deze thesis werd voorgesteld.

List of publications

Journal publications

1. **Bultreys, T.**, Van Stappen, J., De Kock, T., De Boever, W., Boone, M., Van Hoorebeke, L., and Cnudde, V. Investigating the relative permeability behavior of microporosity-rich carbonates and tight sandstones with multi-scale pore network models. *Journal of geophysical research - Solid Earth*, In Press, 2016.
2. **Bultreys, T.**, Van Hoorebeke, L., and Cnudde, V. Simulating secondary waterflooding in heterogeneous rocks with variable wettability using an image-based, multiscale pore network model. *Water Resources Research*, 52, 6833-6850, 2016.
3. **Bultreys, T.**, De Boever, W., and Cnudde, V. Imaging and image-based fluid transport modeling at the pore scale in geological materials: a practical introduction to the current state-of-the-art. *Earth-Science Reviews*, 155, 93-128, 2016.
4. **Bultreys, T.**, Boone, M., Boone, M., De Schryver, T., Masschaele, B., Van Hoorebeke, L., and Cnudde, V. Fast laboratory-based micro-computed tomography for pore-scale research: illustrative experiments and perspectives on the future. *Advances in Water Resources*, 95, 341-351, 2016.
5. **Bultreys, T.**, Boone, M., Boone, M., De Schryver, T., Masschaele, B., Van Loo, D., Van Hoorebeke, L., et al. Real-time visualization of Haines jumps in sandstone with laboratory-based microcomputed tomography. *Water Resources Research*, 51(10), 8668-8676, 2015.
6. **Bultreys, T.**, Van Hoorebeke, L., and Cnudde, V. Multi-scale, micro-computed tomography-based pore network models to simulate drainage in heterogeneous rocks. *Advances in Water Resources*, 78, 36-49, 2015.
7. Van Stappen, J., **Bultreys, T.**, Gilabert Villegas, F. A., Hillewaere, X., Garoz Gmez, D., Van Tittelboom, K., Dhaene, J., et al. The microstructure of capsule containing self-healing materials: a micro-computed tomography study. *Materials Characterization*, 119, 99-109, 2016.
8. De Boever, W., **Bultreys, T.**, Derluyn, H., Van Hoorebeke, L., and Cnudde, V. Comparison between traditional laboratory tests, permeability measurements and CT-based fluid flow modelling for cultural heritage applications. *Science of the Total Environment*, 554-555, 102-112, 2016.

9. De Boever, W., Diaz, A., Derluyn, H., De Kock, T., Van Stappen, J., Dewanckele, J., **Bultreys, T.**, et al. Characterization of composition and structure of clay minerals in sandstone with ptychographic X-ray nanotomography. *Applied Clay Science*, 118, 258-264, 2015.
10. Veselý, M., **Bultreys, T.**, Peksa, M., Lang, J., Cnudde, V., Van Hoorebeke, L., Kocirík, M., et al. Prediction and evaluation of time-dependent effective self-diffusivity of water and other effective transport properties associated with reconstructed porous solids. *Transport in Porous Media*, 110(1), 81-111, 2015.
11. Cnudde, V., De Kock, T., Boone, M., De Boever, W., **Bultreys, T.**, Van Stappen, J., Vandevoorde, D., et al. Conservation studies of cultural heritage: X-ray imaging of dynamic processes in building materials. *European Journal of Mineralogy*, 27(3), 269-278, 2015.
12. Boone, Marijn, De Kock, T., **Bultreys, T.**, De Schutter, G., Vontobel, P., Van Hoorebeke, L., and Cnudde, V. 3D mapping of water in oolithic limestone at atmospheric and vacuum saturation using X-ray micro-CT differential imaging. *Materials Characterization*, 97, 150-160, 2014.

Oral conference presentations

1. **Bultreys, T.**, Van Hoorebeke, L., and Cnudde, V. Assessing the influence of microporosity on imbibition in complex pore structures with multi-scale pore network models. *Presented at the 8th International conference on Porous Media and Annual meeting of the International Society for Porous Media*, International Society for Porous Media (Interpore), 2016.
2. **Bultreys, T.**, Van Stappen, J., Van Hoorebeke, L., and Cnudde, V. Analyzing two-phase flow in microporosity-rich rocks by integrating multiple pore scales in an image-based pore network model. *Presented at the 5th Workshop on the testing of low permeability materials*, Belgian Nuclear Research Institute (SCK $\cdot$CEN), 2016
3. **Bultreys, T.**, De Boever, W., Van Hoorebeke, L., and Cnudde, V. A multi-scale, image-based pore network modeling approach to simulate two-phase flow in heterogeneous rocks. *Presented at the 2015 International symposium of the Society of Core Analysts*, Society of Core Analysts (SCA), 2015.
4. **Bultreys, T.**, Dewanckele, J., Derluyn, H., Boone, M., De Kock, T., De Boever, W., Van Stappen, J., et al. Analysis of pore scale processes in geo-materials: perspectives on multi-scale and time-resolved 3D imaging. *Presented at the 2015 Engineering Mechanics Institute conference*, Engineering Mechanics Institute (EMI), 2015.
5. **Bultreys, T.**, Boone, M., De Schryver, T., Masschaele, B., Van Hoorebeke, L., and Cnudde, V. Investigating the influence of dynamic effects on two-phase flow at the pore scale with fast laboratory-based X-ray micro-CT. *Presented at the 7th International conference on Porous Media and Annual meeting of the International Society for Porous Media*, International Society for Porous Media (Interpore), 2015.

6. **Bultreys, T.**, De Boever, W., Van Hoorebeke, L., Mehmani, A., Prodanovic, M., and Cnudde, V. Image-based multi-scale pore network models to investigate two-phase flow in carbonate rocks. *Presented at the Shell Amsterdam Centennial conference: Rock and fluid physics: academic and industrial perspectives*, Shell, 2014.
7. **Bultreys, T.**, Raeini, A. Q., De Boever, W., Van Hoorebeke, L., and Cnudde, V. (2014). Multi-scale, image-based pore network models to simulate two-phase flow in carbonate rocks. *Presented at the 6th International conference on Porous Media*, International Society for Porous Media (Interpore), 2014.

Other selected publications

- Boone, M. A., **Bultreys, T.**, Masschaele, B., Van Loo, D., Van Hoorebeke, L., and Cnudde, V. (2016). In-situ, real time micro-CT imaging of pore scale processes, the next frontier for laboratory based micro-CT scanning. *Presented at the 30th International symposium of the Society of Core Analysts*, Society of Core Analysts (SCA).
- **Bultreys, T.**, Van Stappen, J., Van Hoorebeke, L., and Cnudde, V. (2016). Micro-CT-based modeling of the impact of microporosity on waterflooding in heterogeneously-wetted rocks. *Presented at the Gordon Research Conference on Flow and Transport in Permeable Media*, Gordon Research Conferences (GRC).
- Cnudde, V., **Bultreys, T.**, Dewanckele, J., Derluyn, H., Boone, M., De Kock, T., De Boever, W., et al. (2015). Perspectives on multi-scale and time-resolved 3D imaging of pore scale processes in geomaterials.*Presented at the 7th International conference on Porous Media and Annual meeting of the International Society for Porous Media*, International Society for Porous Media (Interpore).
- **Bultreys, T.**, De Boever, W., Van Hoorebeke, L., and Cnudde, V. (2015). Multi-scale, image-based pore network models to simulate two-phase flow in heterogeneous rocks. *Presented at the 7th International conference on Porous Media and Annual meeting of the International Society for Porous Media*, International Society for Porous Media (Interpore).
- **Bultreys, T.**, De Boever, W., Brabant, L., and Cnudde, V. (2013). Comparison of pore network models for the investigation of fluid flow properties in building stones. *Presented at the 5th International conference on Porous Media and Annual meeting of the International Society for Porous Media*, International Society for Porous Media (Interpore).

Contents

List of Figures

List of Tables

Part I

Introduction

1

Motivation and outline

Fluid flow and mass transport in geological porous media (e.g. rocks, sediments and soils) are crucial aspects of several important applications, e.g. hydrology, petroleum engineering, sub-surface storage of CO_2 and nuclear waste, geothermal energy generation and building stone performance. To reduce uncertainties related to these systems and to increase their efficiency, accurate predictions of their behaviour over time have to be made. This is typically done by running large-scale numerical models (of the order of metres to kilometres), which use constitutive equations to describe the behaviour of the geological materials in question. They therefore require the input of effective material properties such as porosity, permeability, dispersivity, etc., which are characteristic of the geological materials in which the processes take place. These materials are composed of minerals on the one hand and pores or fissures/cracks on the other hand. Properties of the pores and minerals, such as geometry, size, surface area, connectivity and distribution have a strong effect on the material's behaviour. The internal micro-structure, the chemical composition, and the macroscopic transport properties of the material are indeed strongly and directly related to each other.

The different transport processes in geological porous media can be

classified as single-component or multi-component flows (i.e. multiple chemical species may be mixed in the same fluid phase); single-phase and multi-phase flows (i.e. multiple immiscible or partially miscible fluids may be present) and non-reactive or reactive flows (i.e. fluids in the pore space may react with each other or with the solid minerals). While these processes often take place simultaneously and may be strongly coupled, this thesis focuses on the investigation of two-phase flow in geological materials, as it is crucial in most of the engineering applications mentioned earlier. Not only is it an important process, many aspects of it are still poorly understood or hard to predict, particularly in complex rock types. During two-phase flow in geological applications, one of the two fluid phases is usually water or a watery solution (e.g. brine), while the other fluid can be for example a hydrocarbon (oil or gas) in a petroleum reservoir, gaseous or supercritical CO_2 in a geological reservoir considered for carbon storage, a non-aqueous phase liquid (NAPL) in polluted soils or aquifers, air in the vadose zone of a soil, or a gas (mainly H_2, CH_4 and CO_2) produced due to degradation of nuclear waste and its packaging in underground nuclear waste repositories.

Understanding why and how the macroscopic two-phase flow properties of geological materials vary over space and time requires the examination of how the two-phase flow process proceeds at the microscale. Given the complexity and the heterogeneity of many natural porous media, such a deep understanding is crucial, as it is often impossible to acquire and test all the relevant samples at all the relevant conditions (e.g. in the case of kilometre-sized geological reservoirs). Experimental measurements of transport properties in this context are often difficult, expensive and time-consuming, making models at the scale of the material's micro-structure (typically termed "pore scale") an attractive tool to supplement direct measurements, to enhance the understanding of a material's behaviour, and therefore to interpolate and to extrapolate the relevant effective material properties. Of course, this requires detailed information on the micro-structure of the rock's pore space. Over the last few years, rapid improvement of pore scale imaging methods (notably micro-computed tomography or micro-CT, introduced in Chapter 3) has enabled three-dimensional imaging of the pore space of geological materials. These images provide input to pore scale modeling methods, to accurately simulate transport of fluid phases through the pores in digital porous media. This allows the calculation of effective properties such as capillary pressure, relative permeability and resistivity index curves, which

are introduced in Chapter 2. Although utilization of 3D rock images has proven very useful, a number of challenges have hampered their widespread application and further development.

One of the most important challenges in image-based modeling of two-phase flow in geological porous media is the common occurrence of pores on a wide range of length scales (over up to 6 orders of magnitude). This is especially the case in a number of important classes of reservoir and aquifer rock types, such as clay-bearing sandstones and certain carbonates. The importance of simulations in these types of rock is increased by the failure of most classical empirical relations such as Archie's law for electrical behaviour and the Brooks-Corey parametrization of relative permeability (chapter 2). The failure of these relations is due to the interaction of micro- and macroporosity, spurring the development of modeling methods where multiple pore scales are coupled. A wide range of pore sizes in rocks complicates simulations, because the volume of the simulation domain is mainly controlled by the largest pores, while the resolution is determined by the smallest ones. On the one hand, imaging methods have a resolution/size trade-off, meaning that an image of a representative volume to capture the largest pores will usually not resolve the smallest ones. Therefore, information from multiple images has to be integrated into one model, which is an open-standing issue. On the other hand, the sheer size of the model in terms of "simulation elements" (be it voxels, mesh elements or network elements) poses computational difficulties which are often insurmountable if one would try to solve the complete system in a standard way.

As an effort to tackle these two problems, a new multi-scale pore network model is introduced in part II of this dissertation. Previous image-based multi-scale network models either tried to include microporosity as individual network elements, which in many cases results in a prohibitively large amount of micropores, or only included the microporosity as extra terms in the saturation and conductivity of already-existing macroporous network elements. The latter is not a viable approach in materials where macro- and microporosity are predominantly coupled in series, which is the case in many tighter materials (e.g. with clay-filled macropores). The newly developed method, on the other hand, allows to incorporate high-resolution information in the simulations by treating domains with small pores in an averaged way both during the calculation of the fluid arrangement (invasion-percolation) and the flow

rate calculations. In Chapter 3, we provide a thorough literature review of the current state of the art in (image-based) pore scale modeling. Chapter 4 introduces the new multi-scale network extraction and presents drainage simulations on these networks, as well as a validation study on an artificial network and on two carbonate rocks. In Chapter 5, the model is extended to simulate imbibition under different wettability conditions. Finally, in Chapter 6 the method is used to investigate the sensitivity of different rocks on the type of microporosity they contain. Multi-scale network models were extracted from micro-CT images of carbonates and tight sandstones and were found to replicate some of the qualitative behaviour seen in experiments. The application of these models illustrates how the multi-scale pore network models developed in this work can be useful to enhance our understanding of the multi-phase flow behaviour of rocks which cannot be adequately simulated with standard pore scale models.

Another long-standing challenge has been the validation of pore scale models. While comparing predicted effective properties with the experimentally measured values is useful and necessary, it is complicated by the typical difference in the domain size between the models and the experiments. Furthermore, it does not always give a clear indication of the reasons for an observed mismatch between models and experiments. Comparing two-phase flow models to pore scale experiments in which the evolution of the fluid distributions is visualized is thus extremely useful. If one does not interrupt the fluid injection during imaging, the dynamics of the process can be investigated. This is particularly important to validate the basic assumptions in quasi-static models such as the one presented in part II of this thesis, in which the dynamical properties of the invasion are neglected. This type of validation, which poses a number of methodological difficulties, is tackled in part III of this thesis. One of the main challenges is that such experiments require image acquisition in a matter of seconds, during a well-controlled two-phase flow process. While this type of fast imaging has been performed at synchrotrons, laboratory-based micro-CT scanners typically take at least 20 minutes (and in fact often many hours) to acquire a pore space image. Since synchrotron beam time is severely restricted, there is an important need for fast imaging with laboratory-based micro-CT scanners (e.g. scanners that fit within the achievable sizes and budgets of normal university laboratories). In Chapter 7, we outline the current state of the art in this young research field, and we illustrate how it can be applied in pore scale flow research on rocks by imaging a solute transport experiment. In

Chapter 8, a drainage experiment is presented and analysed to allow a comparison with quasi-static models. Unlike previous approaches, we track the filling state of individual pores, providing validation of some of the assumptions made in the pore network models presented in part II. The experiments presented in Chapters 7 and 8 are currently the only reported sub-minute pore scale imaging experiments performed with a laboratory-based scanner in the literature, at 12 seconds for a full scan.

Each of the Chapters in parts II and III of this thesis is based on a scientific publication first-authored by the author of this work, and which was written during his Ph.D. research. At the beginning of each chapter, the corresponding publication is referenced. Finally, Part IV draws general conclusions and offers an outlook on future research.

2

Physics of flow in porous media

Even though the applications of two-phase flow in geological materials are incredibly diverse, the physics which drive it at the pore scale are often remarkably similar. In this chapter, the primary concepts used to describe these physics are introduced. To understand two-phase flow, the simpler case of single-phase flow is treated first, i.e. flow when there is only one fluid present in the pores of the material (section 2.1). The complications added by a second fluid in the pore space are treated in section 2.2. In general, fluid flow trough porous media is driven by viscous, inertial, capillary and gravitational forces. In both sections, we start with a description of these forces at the microscopic scale, and then discuss the averaged properties which are used at the continuum scale.

While this chapter is intended as a concise introduction, fluid flow in (geological) porous media is a rich study area which deserves a more detailed treatment. For this, the reader is referred to standard text books, e.g. Bear (1975); Dullien (1992); Sahimi (2011) and more recently Blunt (2016).

2.1 Single-phase flow

When there is only one fluid present in the pore space of a geological material, the main question is how easily that fluid can flow through the pores in the material. At the microscopic level, this is determined by the properties of the fluid (e.g. viscosity and density at the prevailing pressure and temperature of the system) and by the geometry and connectivity of the pore space, e.g. narrower or more tortuous flow paths result in less or more difficult flow. At this scale, the flow can be described with the Navier-Stokes equation, which follows from imposing momentum conservation on a continuous fluid (Sahimi, 2011). For incompressible fluids with constant viscosity μ this non-linear partial differential equation is (Blunt, 2016):

$$-\rho\left(\frac{\partial\vec{v}}{\partial t}+(\vec{v}\cdot\nabla)\vec{v}\right)+\mu\nabla^2\vec{v}+\rho\vec{g}-\nabla P=\vec{0} \tag{2.1}$$

where P is the pressure, $\vec{v}$ the fluid velocity, μ the fluid viscosity, ρ the (assumed constant) fluid density and $\vec{g}$ the gravitational acceleration vector. To solve this equation for both the pressure and velocity fields, an extra equation is needed, which is found from mass conservation (again assuming incompressibility):

$$\nabla\cdot\vec{v}=0 \tag{2.2}$$

Different flow regimes emerge depending on the interplay between inertial and viscous forces (represented respectively by the first and second terms in equation 2.1). The balance between these forces can be investigated by defining a dimensionless number called the Reynolds number Re:

$$Re=\frac{\rho\bar{v}L}{\mu} \tag{2.3}$$

Here, $\bar{v}$ is an average fluid velocity and L is a characteristic length relevant to the porous medium, e.g. the pore size (Meakin and Tartakovsky, 2009). In the majority of earth science applications, the flow is very slow and therefore $Re << 1$, meaning that viscous forces dominate and result in creaping, laminar flow. In the rest of this thesis, we will make the assumption that this is the case. Notable exceptions where this could be

invalid are near-wellbore flows, in which case higher Re-numbers could indicate turbulent flow (Muljadi et al., 2015). However, in the case of laminar flow the first term of equation 2.1 can be neglected, and the Navier-Stokes equation reverts to the Stokes equation (Sahimi, 2011):

$$\mu\nabla^2\vec{v} + \rho\vec{g} - \nabla P = \vec{0} \tag{2.4}$$

This is a linear differential equation which together with the mass conservation equation (2.2) can be solved for the pressure and fluid velocity everywhere in the pore space by a number of well-known methods, and its solution could therefore be perceived by someone unfamiliar with porous media as rather straightforward. However, the boundary condition imposed by the pore walls complicates this. First, there is the difficulty of finding the exact geometry of the pore walls. This can be measured with high-resolution three-dimensional imaging techniques such as micro-computed tomography (micro-CT) and focused ion beam scanning electron microscopy (FIB-SEM), but these experiments are generally not trivial. Secondly, the pore geometry is typically very complex and tortuous, posing computational challenges when solving the flow rates. Specialized numerical algorithms have been developed to deal with this, and are reviewed in Chapter 3 of this thesis.

When considering flow at a larger scale (cm, m or even km), it is not practical or feasible to attempt to solve the flow rates everywhere in the pore space. In this case, the classical approach is to consider the porous medium as a continuous material, with an averaged porosity (void volume fraction) ϕ. This is of course only valid if we consider a volume which contains many pores, and is thus "large enough" to represent a statistically meaningful average of the porous material. This idea was formalized in the concept of the "representative elementary volume" (REV), introduced by Bear (1975). Blunt (2016) provides a practical definition of the REV as the minimum volume needed to obtain an accurate computation of an average quantity. It depends both on the material and on the property in question. Through homogenization of the Stokes equation over such a volume, a linear relation between the fluid flux q and the gradient of the pressure P is found. Furthermore, the flux is inversely proportional to the fluid viscosity μ, and proportional to a constant K which depends on the material, and which we call "permeability". We therefore find Darcy's law, which was introduced on an empirical basis to describe flow through sand beds by Henry Darcy in 1856 (here stated for 1D flow):

$$q = -\frac{K}{\mu}\nabla P \tag{2.5}$$

Darcy's law is the first constitutive equation encountered in this work. The SI unit to express permeability is m^2, but in geological applications (and in this thesis) the Darcy unit (D) is often used. One Darcy is the permeability of a medium which permits a flux of 1 cm/s of a fluid with a viscosity of 1 mPa $\cdot$ s under a pressure gradient of 1 atm/cm. It equals approximately 10^{-12} m^2. The permeabilities found in geological materials vary widely, even within the same rock type. To give an idea of the orders-of-magnitude we are dealing with, the permeability of unconsolidated sand is typically on the order of 1 to 1000 D (depending on the grain size), typical conventional sedimentary reservoir rocks have permeabilities of 1 mD to 1 D, and tight materials like shales and clays have typical permeabilities on the order of nD to several μD (Bear, 1975).

Permeability can be measured experimentally by fully saturating a (cylindrical) core sample with a single fluid (usually air or water) and then bringing it into a Hassler core holder (figure 2.1). The typical sample size of so-called "core plugs"on which these measurements are performed are a diameter of 1 inch by a length of about 2 inches. A flow is then established through the sample by either imposing a constant pressure or a constant flow rate. Then, the pressure drop and/or the volumetric flow rate are measured, and since the length of the sample is known, equation 2.5 can be used to find the permeability. If the permeability is measured by gas flow, the results are usually corrected for Klinkenberg effects, caused by large mean free path lengths of gas molecules compared to the pore sizes at low gas pressures. A different kind of permeability measurement can be made using portable probe permeameters (also called "minipermeameters"). These consist out of a nozzle, which is pressed tightly to the rock, and a gas chamber (figure 2.1). The measurement is based on inducing transient gas flow through the rock and the nozzle when the pressure in the chamber is changed (e.g. by creating a vacuum or by injecting a gas). The time for the induced pressure difference to relax can then be related to the permeability of the rock. Portable probe permeameters typically have a smaller measurement volume than classical permeability experiments, and are usually not applicable to low-permeability materials. Furthermore, the results may be sensitive to non-complete saturation of the material and to surface effects (Huysmans et al., 2008). Advantages are that the method can be used to map

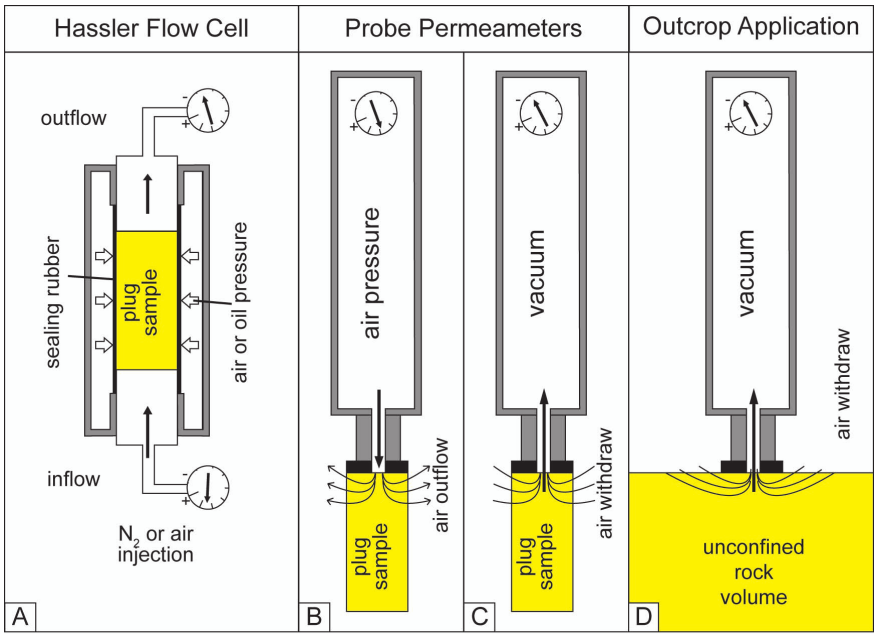

Figure 2.1: Figure A illustrates permeability measurement on a core plug in a Hassler core holder. Figures B and C illustrate the use of portable probe permeameter measurements on core plugs by applying air pressure or a vacuum, respectively. Figure D shows the application of such a permeameter on an outcrop or large rock volume. Figure from Filomena et al. (2014)

permeability on large samples (even outcrops, in-situ), and that the measurements are quick, cheap and easy.

2.2 Multi-phase flow

2.2.1 Capillary pressure

When there is more than one fluid present, we do not only have to take into account the viscous forces which occur due to friction (both internally in the fluid as due to interaction with the pore walls), but also the capillary forces. The latter occur due to intermolecular forces, which determine an energy balance for the fluid-fluid and fluid-solid interfaces in the porous medium. For example, it is usually energetically more favourable for the solid to be covered with (or "wetted by") one fluid than with the other. For the solid-

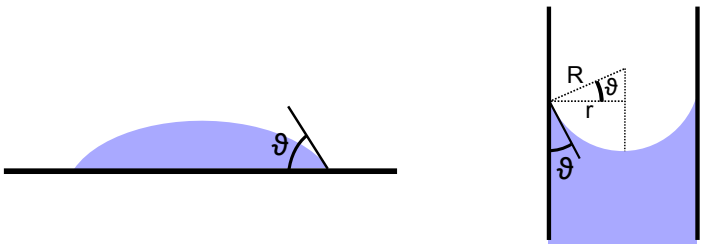

Figure 2.2: The contact angle θ of a drop on a surface or of two fluid phases in a cylindrical tube with radius r is measured through the wetting phase (in blue). In a tube, the curvature R of the interface can be related to the contact angle and the tube radius.

fluid-fluid system in question, the former fluid is called the "wetting fluid", and the latter the "non-wetting fluid". For example, the minerals which are the primary constituents of reservoir rocks (quartz, carbonate and dolomite) are typically wetted by a watery liquid when brought in contact with such a liquid on the one hand and oil, gas, CO_2, non-aqueous phase liquids or air on the other hand (Buckley et al., 2007).

Imagine a drop of liquid in contact with a solid and another liquid, presented in figure 2.2. The preference of the solid to be wetted by one of the liquids results in a curved fluid-fluid interface and determines the angle at which the interface between the two fluids intersects the solid surface. This angle is called the "contact angle" (θ), and by expressing the energy balance in terms of forces, one can find the Young-Dupré equation (Young, 1805; Dupré and Dupré, 1869):

$$\cos\theta = \frac{\sigma_{nw,s} - \sigma_{w,s}}{\sigma_{w,nw}} \tag{2.6}$$

where $\sigma_{nw,s}$ is the surface tension of the non-wetting fluid and the solid, $\sigma_{w,s}$ is the surface tension of the wetting fluid and the solid, and $\sigma_{w,nw}$ is the surface tension of the non-wetting fluid and the wetting fluid.

For similar reasons, two fluids in a tube have a curved interface as well. Since energetically, the tube wants to be filled with the wetting fluid, a pressure difference between the fluids has to exist in order for the non-wetting phase to remain in the tube and for the interface between the fluids to be in equilibrium. Writing down the energy balance leads to the Young-Laplace equation, which relates the equilibrium pressure difference

between the fluids, termed "capillary pressure"(P_c), to the principal radii of curvature of the interface (R_1 and R_2) (Young, 1805; marquis de Laplace, 1805):

$$P_c \equiv P_{nw} - P_w = \sigma \left(\frac{1}{R_1} + \frac{1}{R_2} \right) \tag{2.7}$$

For a cylindrical capillary with radius r (figure 2.2), the Young-Laplace equation reverts to:

$$P_c = \sigma \left(\frac{2 \cos \theta}{r} \right) \tag{2.8}$$

For a porous medium, the existence of capillary forces implies that work has to be performed to introduce a non-wetting fluid into the pores. This process is called drainage. Similarly, a wetting fluid can be drawn into the pores spontaneously or brought into the pores in a forced manner, during a process which is called imbibition. While the Young-Laplace equation could in theory be used to find the equilibrium capillary pressure for local points in the pore space, averaged properties are used to describe the behaviour on a larger scale and under (quasi-) dynamic circumstances. A constitutive relation between the fluid saturation (the percentage of the pore space filled with one of the two fluids) and the difference of the average pressures in the fluids is used for this purpose. This relation is called the capillary pressure curve $P_c(S_w)$. It should be noted that, although it is rather confusingly named, the macroscopic capillary pressure is not an equilibrium pressure resulting from a balance of forces, like the microscopic capillary pressure in the Young-Laplace equation is. It is rather to be regarded as an empirical relation, found (for drainage) by gradually increasing the pressure difference between the fluids in the porous medium and measuring the saturations once they have become constant. This explains why the macroscopic capillary pressure cannot be related to thermodynamic properties of the system (after all, the external fluid pressures can be varied arbitrarily) (Hassanizadeh and Gray, 1993). The capillary pressure curve is rate-dependent (Wildenschild et al., 2001), and furthermore depends on the history of the system, i.e. it is hysteretic. It is an important input factor for each grid block in a reservoir-scale simulation. It indicates how the saturation of the fluids is initially distributed with the depth in the reservoir (i.e. with the gravitational

pressure). Furthermore, it is important to describe the sealing capacity of cap rocks which lie above a reservoir or aquifer.

Capillary pressure curves for drainage (oil flooding) can be measured by bringing a sample into a similar Hassler core holder as described in figure 2.1, only now with a porous plate or membrane added on one side of the sample. This plate usually has small pores and is strongly water-wet, and therefore only allows water to flow through it (as its capillary entry pressure for non-wetting phases is very high). This allows to build up the pressure difference between a non-wetting phase (oil, air, gas, CO_2, depending on the application) and water when injecting the former into the sample from the other side than the membrane. The pressure is increased gradually and the volume of injected and displaced fluids is measured to find points on the capillary pressure curve. Since it can take a long time for the fluids to reach equilibrium, porous plate experiments are expensive and time consuming. An alternative is the use of a centrifuge to generate a pressure difference between the fluids, due to their different densities. The core is spun at a specific rotational velocity and then weighed to determine its saturation, after which the process is repeated at higher velocities and thus higher capillary pressures.

When performing multi-phase flow experiments like capillary pressure measurements, it is important to consider the wettability of the samples. When an originally water-wet mineral is brought in contact with for example crude oil and certain NAPLs, polar compounds can precipitate and render it intermediate-wet or oil-wet. This is particularly important in reservoir rocks. However, the wettability of these samples is often altered from the reservoir state during coring (e.g. by contact with drilling fluids). In an attempt to restore their original wettability, samples are usually first cleaned, then saturated with brine, and subsequently injected with crude oil which is left in the sample for several weeks at elevated pressure and temperature (“ageing”).

2.2.2 Microscopic displacement processes

Similarly to the case of single phase flow, different two-phase flow regimes exist depending on which force dominates the behaviour. To describe this, the capillary number is defined. It is a dimensionless number which expresses the balance between viscous an capillary forces:

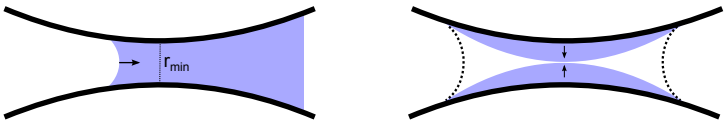

Figure 2.3: The figure on the left illustrates the occurrence of Haines jumps during drainage, when the interface passes the narrowest point at r_{min}. The figure on the right illustrates the filling of a region with wetting phase due to snap-off during imbibition, which takes place when wetting films swell and touch.

$$Ca = \frac{\mu v}{\sigma} \tag{2.9}$$

As stated before, flow rates are usually very slow in subsurface applications, resulting in low capillary numbers (of the order of 10^{-7} to 10^{-8}). Over the typical length scale of a pore, the capillary forces are typically much larger than the viscous pressure drop associated with the macroscopic flow rates. The result is that during drainage, pores are not filled in a reversible, "smooth"manner, but are rather invaded in a series of sudden pore-filling events, each of which takes place when the local capillary pressure exceeds the equilibrium capillary pressure of a local constriction in the pore space. Take for example the simplified situation in figure 2.3 (left). In an energy diagram, the location of the minimum radius of the tube is a local energy maximum. If the capillary pressure is gradually increased, the interface first slowly advances to the constriction, and then rapidly relaxes by moving to the right once the critical equilibrium capillary pressure associated with this radius has been overcome. This process is called a Haines jump, after Haines (1930). In a porous medium, multiple pores (local dilations in the pore space) may be filled during one such event, if the constrictions which separate them have larger radii than that of the constriction at the start of the Haines jump.

During imbibition, similar events may take place, only now the critical pressures are associated with local dilations. Furthermore, most media retain thin wetting films in corners and crevices after drainage (depending on the contact angle and the maximum pressure which was reached). This means that both fluids can be present in and flow through the same pore simultaneously. The presence of wetting films results in a second type of invasion process, which takes place when such films swell as the capillary

pressure decreases: if films swell enough so that the non-wetting fluid is no longer in contact with the pore wall, an unstable situation arises and the pore's centre is filled with the invading wetting phase (Lenormand and Zarcone, 1984; Mohanty et al., 1987). These are called snap-off events (figure 2.3), and they preferentially take place in small pore throats (local constrictions). Their special significance lies in the fact that they can take place anywhere in the uninvaded pore space (presuming that wetting films are connected throughout the pore network) rather than only in places neighbouring to regions which have already been invaded with wetting phase.

Many so-called quasi-static models have approximated the invasion as being purely capillary dominated (i.e. neglecting the viscous forces entirely). However, some experimental observations have been made which cast doubt on the suitability of these methods (Måloy et al., 1992; Furuberg et al., 1996; Moebius et al., 2012; Armstrong and Berg, 2013; Moebius and Or, 2014a; Armstrong et al., 2014c). During drainage, the fluid rearrangement associated with a Haines jump happens much faster than the macroscopic flow rate. Since the jumps are caused by an instability of the surface energy, the interfacial velocity during the jump is not (significantly) affected by the macroscopic flow rate, yet take place in a matter of milliseconds. However, the macroscopic flow rate does control the frequency of the jumps. Through the use of very precise pressure and acoustic measurements, researchers have found that at typical field-relevant flow rates (with capillary numbers on the order of 10^{-8}), jumps typically take place every 10 s to 20 s, spread out over the pore space (Moebius et al., 2012; Berg et al., 2013).

On the one hand, the speed with which Haines jumps proceed means that viscous and inertial forces during the event could be much larger than what is expected from the macroscopic flow rates, and could therefore influence the evolution of the fluid arrangement in the pore space. On the other hand, this also means that the invading fluid has to be redistributed from neighbouring pores for the invasion to proceed. Therefore, forces working in the surrounding pores could influence the invasion in a non-local way. The question what the importance of these dynamic effects on the effective flow properties are is investigated in part III of this thesis, yet is still not completely solved.

During drainage and imbibition, an intricate arrangement of the wetting and non-wetting phase in the pore space arises as the invading phase

moves into the pore space in a series of pore scale displacement events. Given the difficulty of simulating the evolution of the behaviour on a representative pore scale image, a theoretical line of research has investigated the properties of fluid (and in fact many other) clusters in random networks, which can be seen as model representations of the pore space. This branch of applied physics and mathematics, called "percolation theory", has discovered that much of the clusters' (statistical) behaviour is independent of the detailed structure of the network, but is in fact universal and therefore somehow natural to all random networks in the same spatial dimension. Introductions into percolation theory can be found in Sahimi (2011) and Hunt et al. (2014). While it is a fascinating, surprising field, and its application is very useful, it has to be taken into account that natural porous media are not random: their formation processes induce correlations in the pore space, which are hard to describe mathematically. Therefore, we have to (and can) go beyond percolation theory to determine the evolution of the fluid arrangement in detail. After all, this arrangement influences the capillary pressure curve and determines how easily each of the fluids flows through the part of the pore space they respectively occupy. At the macroscopic scale, the latter is expressed by relative permeability curves, which are treated in the next section.

2.2.3 Relative permeability

To describe the flow rates of both fluids during two-phase flow, the Navier-Stokes equations can be solved similarly as for single-phase flow, but to conserve energy (including interfacial energy) the interfacial pressures have to be taken into account, e.g. by including the Young-Laplace equation (equation 2.7). However, tracking the movement of the interfaces in porous materials poses severe computational difficulties when solving the equations on a grid or mesh in the pore space. Methods to approach this problem are reviewed in Chapter 3.

Like for single-phase flow, at the macroscopic scale two-phase flow is described using average properties that emerge as a consequence of the microscopic behaviour. To this end, the Darcy equation is extended to (Dullien, 1992):

$$q_i = -\frac{K_{\text{eff},i}(S_i)}{\mu_i}\nabla P_i \tag{2.10}$$

for each fluid phase i, and in which $K_{\text{eff},i}(S_i)$ is the effective permeability of phase i at fixed saturation S_i. As only a fraction S_i of the pore space is available for flow, the effective permeability is lower than the permeability K when the whole pore space is saturated with one single fluid (which in this context is referred to as the absolute permeability). To stress this dependence, the effective permeability is usually expressed as a fraction of the absolute permeability, with as saturation-dependent proportionality factor the relative permeability $K_{r,i}$ (Dullien, 1992):

$$K_{r,i}(S_i) \equiv \frac{K_{\text{eff},i}(S_i)}{K} \tag{2.11}$$

The relative permeability expresses how easily a fluid flows at a certain fixed fluid saturation, compared to how easily it flows when it occupies the whole pore space. It is usually plotted in function of the saturation (normally from $K_{r,i}(0) = 0$ to $K_{r,i}(1) = 1$). It strongly depends on how the fluids are distributed in the pore space, and since the fluid arrangement is hysteretic, so are the relative permeability curves. It should further be noted that the sum of the relative permeabilities to the two fluids at a specific saturation is usually smaller than one, due to the increased tortuosity of the flow paths of each fluid. Put simply, the presence of two fluids adds more friction, so the total amount of flow normalized to the viscosity is smaller than when there is a single fluid present.

The extended Darcy equation (equation 2.10) is the standard way of describing multi-phase flow in reservoirs, aquifers and soils, and the relative permeability curves are thus crucial input parameters to any large-scale simulation (e.g. oil recovery, CO_2 injection, NAPL intrusion or remediation after spilling in a soil). Relating the pore structure of complex rocks to relative permeability curves is thus one of the main drivers for the work presented in this thesis. Nevertheless, it is important to realize that we implicitly make some simplifications when assuming the relation in equation 2.10 by intuitively extending equation 2.5. To quote Majid Hassanizadeh (2012), one could say that "We have added bells and whistles to a simple formula to make it applicable to a much more complicated system". The primary assumptions are that the two fluids flow independently from each other and that we can ignore the impact of

fluid displacements, i.e. that the change in the fluid distributions is negligible at the typical time scale related to the flow q_i in a representative elementary volume (Blunt, 2016). However, during drainage or imbibition, fluid saturations do change, which means that $K_{\text{eff},i}$ could depend on q_i and therefore induce non-linearity in equation 2.10. Furthermore, even in cases where this would be negligible, Whitaker (1986) showed that volume averaging of the Stokes and mass conservation equations for two immiscible fluids leads to added cross-terms in equation 2.10, which represent a coupling effect between the two fluids. Intuitively, this can be understood in terms of the viscous drag exerted by the two fluids on each other, which in most cases can be neglected (Sahimi, 2011).

Relative permeability can be measured experimentally in two different ways. The most direct measurement is the steady-state method: a (brine-saturated) sample is built into a Hassler core holder, and the two fluids are injected at the same time, with a fixed ratio of flow rates. At the start of the experiment, the brine flow rate is much higher than oil flow rate. After injecting the fluids at this rate for a long time, the saturation (measured by weighing the sample or by X-ray imaging) reaches a constant value, and the pressure drop of the fluids over the sample is measured. Then, the ratio of the oil flow rate to the water flow rate is increased, and the measurement is repeated to find multiple points on the relative permeability curve of each fluid (Glover, 2001). The method is difficult, time consuming and very expensive. Alternatively, unsteady state relative permeability experiments can be performed. Here, one phase is injected and displaces the other, either in a porous plate set-up or by using a centrifuge (Kišon et al., 2015). Saturations are measured by weighing or X-ray imaging. The outflow of both fluids and the pressure drop over the sample are measured, which then allows to fit relative permeability curves by comparing the experimental data to core-scale model predictions or to analytical expressions (Ott et al., 2015). Usually, the relative permeability is parametrized by expressing it by empirical functions, which are in general used to relate relative permeability to other reservoir properties. The most well-known functions are the Brooks-Corey (Brooks and Corey, 1964) and the Van Genuchten-Mualem relations (Van Genuchten, 1980). While these classical relations are widely used, they are not always applicable to materials with complex pore spaces.

2.2.4 Electrical resistivity

In subsurface geological applications, reservoir or aquifer properties are evaluated by drilling boreholes, which can serve to extract core samples but also to perform measurements in the borehole itself, by lowering wireline tools into it. One of the oldest and most important of these measurements is (electrical) resistivity logging, pioneered by Conrad and Marcel Schlumberger (the founders of the world's currently largest oil services company Schlumberger Ltd.) in 1927. Most reservoir rock minerals are electrical insulators, while the fluids in them can either be conductive (e.g. brine) or insulators (e.g. hydrocarbons, CO_2, air). Therefore, the resistivity of a reservoir rock depends on the pore structure and on the saturation and arrangement of the fluids in the pore space. It is thus a useful indication to characterize the transport properties of the rock and to infer the fluid saturation in the reservoir (e.g. the amount of hydrocarbons in place depending on the depth in the reservoir). Of course, deducing useful information from these measurements is only possible if the rock-specific relation between the resistivity, rock properties and saturation are known. We therefore define the formation factor F as the ratio of the rock's resistivity when it is fully saturated with brine R to the brine's resistivity R_w, and the resistivity index $I(S_w)$ as the ratio of the rock's resistivity at brine saturation S_w to its resistivity at full brine saturation:

$$F \equiv \frac{R}{R_w} \tag{2.12}$$

$$I(S_w) \equiv \frac{R(S_w)}{R} \tag{2.13}$$

An important empirical relation to describe the relation between these quantities and the rock's properties is Archie's law (Archie, 1942). Here, we express it by two equations, one relevant to single-phase flow:

$$F = a\phi^{-m} \tag{2.14}$$

where ϕ is the rock's porosity and a and m are rock-dependent parameters called the tortuosity factor and the cementation exponent, respectively. When two fluid phases are present, the following relation is added:

$$I(S_w) = S_w^{-n} \tag{2.15}$$

Here, n is a rock-dependent parameter called the saturation exponent. It is usually assumed that a, m and n are constant for a specific rock type. Laboratory measurements on cored samples are usually performed to refine the values of these constants. Formation factors can be measured by bringing a cylindrical rock sample in a Hassler cell after vacuum-saturating it with brine, and measuring the electrical resistance between two electrodes brought in contact with the sample at the top and the bottom. Similarly, such measurements can be performed during drainage or imbibition experiments, where the saturation can be changed in similar ways as during capillary pressure or relative permeability measurements (e.g. by porous plate or centrifuge).

It is important to realize that Archie's law is an empirical relation, which was originally inferred for sandstones. There is no reason why it should be a good description of electrical conductivity in all rocks and over the whole saturation range, and in fact, it is not. In his original paper, Archie (1942) already stated that "it should be remembered that the equations given are not precise and represent only approximate relationships". Many rocks with more complex pore structures and wide, often multi-modal pore size distributions, e.g. many carbonate rocks (Fleury, 2002; Han et al., 2007) and clay-bearing rocks, show non-Archie behaviour. Furthermore, like relative permeability curves, resistivity index curves are hysteretic. These observations spur investigations on the pore scale, using image-based modeling methods, in order to better understand and extrapolate formation factors and resistivity index curves. The fact that rocks with multi-scale porosities often show non-Archie behaviour stresses the need for multi-scale models, like the one presented in part II of this thesis.

Part II

Multi-scale network modeling

3

State of the art: pore scale modeling

Essentially, all models are wrong, but some are useful.

– George E.P. Box

In this chapter, the literature on image-based pore scale modeling of fluid and mass transport in geological materials is reviewed. Particular attention is devoted to multi-phase flow, yet we also treat single-phase flow and solute transport, because these properties can be important to assess the representativity of more complex multi-phase flow models. Solute transport is the transport of dissolved species within a fluid phase by advection and diffusion, both of which are influenced by the pore structure. If fluids or dissolved species in them react with each other or with the minerals in the geological material, the process is called reactive transport. This kind of transport can change the internal structure of the porous medium and is often an important process in the field. Some applications of pore scale modeling in this context are briefly introduced in this Chapter.

In the following, micro-computed tomography, which is the most used imaging modality in this thesis, is first introduced (section 3.1). Then, direct pore scale modeling methods are treated, with the emphasis on

lattice-Boltzmann and classical computational fluid dynamics, as these have been the most extensively used direct models for two-phase flow simulations based on experimental 3D images (section 3.2). Finally, an overview of pore network model extraction and simulation is given (section 3.3). These models have been the most successful at simulating two-phase flow properties at the pore scale, and are thus treated in detail.

This chapter was based on a review article in Earth-Science Reviews: Bultreys et al. (2016b), *"Imaging and image-based fluid transport modeling at the pore scale in geological materials: A practical introduction to the current state-of-the-art"*. The parts included here were written by the the author of this thesis.

3.1 Pore scale imaging by micro-computed tomography

Understanding the pore scale behaviour during two-phase flow and other transport processes is a difficult problem which requires three-dimensional pore space characterization. As elaborated in Chapter 6.1, pore spaces in geological materials often have a complex microstructure, which can span the centimetre to the nanometre scale and can be very heterogeneous in nature. Therefore, their characterization requires more than experiments which measure global information like porosity and pore size distribution. Imaging techniques fill this requirement by providing local geometrical and topological information. Since pore scale transport depends on the three-dimensional structure of the pore space, it has been widely recognized that transport models should ideally be based on three-dimensional images. While stochastic and process-based algorithms to generate 3D pore structures based on 2D images exist and are under constant development (Øren and Bakke, 2003; Okabe and Blunt, 2005; Wu et al., 2006; Veselý et al., 2015; Soete, 2016), their application is challenging, especially in complex rock types. This harks back to the fact that pore structures in geological materials are not random in the mathematical sense, meaning that even in isotropic rocks complex patterns have to be reproduced to generate a representative 3D structure. In general, it is therefore preferable to use a 3D imaging technique whenever this is possible. Therefore, this chapter introduces the most commonly applied 3D pore scale imaging method in the earth-sciences:

micro-computed tomography. When high-quality pore scale images have been acquired with this technique, they can be segmented and used as input to pore scale transport simulators, introduced in sections 3.2 and 3.3.

Micro-computed tomography or micro-CT (alternatively called high-resolution X-ray tomography) is a non-destructive, three-dimensional imaging technique, based on the penetrating capabilities of X-rays. When a beam of X-ray photons (photons with energies between 100 eV and 100 keV) pass through matter, they interact with it, leading to the removal of photons from the original beam. Photons with these energies typically interact with individual electrons in the shells of atoms: they can be absorbed due to the photo-electric effect or undergo Compton scattering. The resulting attenuation of the incident beam's intensity (I_0) depends on the path followed through the different materials (and the properties of these materials) according to Lambert-Beer's law:

$$\frac{I}{I_0} = e^{-\int \mu(s) ds} \tag{3.1}$$

The linear attenuation coefficient $\mu(s)$ is of course dependent on the properties of the materials along the path, as well as on the energy of the incident photons. At the energies typically used in micro-CT on geological materials (<120 keV), the photo-electric effect is dominant. It depends linearly on the electron density, and therefore on the mass density of the material, and is strongly dependent on the atomic number of the atoms in it ($\sim Z^4$, approximately) (Boone, 2013). At higher energies, Compton scattering may become dominant.

The dependence of the X-ray absorption on the composition and geometry of an object allows to make radiographies, by placing the object in between an X-ray source and detector. These are basically shadow images and thus projections of a 3D object on a 2D plane. However, by rotating the object around an axis and acquiring radiographies from multiple angles, 3D information can be acquired. In computed tomography (CT), hundreds to thousands of images are acquired over a rotation of 180° or 360° and reconstructed into a 3D image by applying for example filtered back-projection or iterative algorithms (Kak and Slaney, 1988; Brabant et al., 2014). CT was first developed and applied in the medical sector, for diagnostical purposes. In modern medical CT, a source and a detector rotate around the patient at a very high speed, to minimize motion artefacts

(movement of the patient or object during scanning results in blurred images).

While medical CT scanners can be used to scan geological samples in order to visualize mm- and cm-scale features and fluid distributions, the resolution of these machines is too low to allow imaging at the scale of individual pores and grains in most materials. For such experiments, micro-computed tomography is used (Cnudde and Boone, 2013; Wildenschild and Sheppard, 2013). In these set-ups, the sample is usually rotated, while the X-ray source and the detector are stationary. The main components are thus an X-ray source and detector and a sample stage with a very precise rotation motor. As X-ray source a synchrotron can be used, which delivers a parallel X-ray beam of very high brilliance (Wildenschild and Sheppard, 2013). Just like in traditional photography, X-ray imaging requires enough photons to reach the detector for the images to have good signal-to-noise characteristics. Because of their high brilliance, synchrotrons are useful for extremely fast imaging (scans of a few seconds to even less then one second) when using the full beam, and have enough X-ray flux to allow passing the beam through a monochromator (based on Bragg-diffraction) for slower experiments (Boone, 2013). The latter is useful to prevent beam-hardening artefacts (see Cnudde and Boone (2013)). Magnification is obtained by converting the X-rays to visible light with a scintillator, and passing the visible light to a system of lenses before it reaches a detector. The main downside of using synchrotron beam lines as X-ray sources is their limited availability.

The alternative to synchrotron light is to use a micro-focus X-ray tube in a laboratory-based (sometimes even bench-top) set-up. These work by accelerating an electron beam to a small focal spot on a metal anode, often made out of tungsten, where the sudden deceleration of the electrons produces a conical X-ray beam (after collimation) (Boone, 2013). This results in geometrical magnification of the object on the detector. The resolution is limited by the minimal focal spot size of the X-ray tube and by the geometrical magnification which can be achieved. The latter is in turn limited by how close the object can be brought to the focal spot, and therefore by the object size. The X-ray brilliance of these sources is much smaller than that of synchrotrons, and the X-ray flux which can be achieved is limited by the size of the focal spot. Therefore, imaging times are much longer than at synchrotrons, and increase with improving resolution and with the size of the sample (due to more X-rays being

absorbed). Typically, the highest resolution achievable on regular set-ups is 0.5 μm (typically on samples of 1 mm diameter or smaller), yet can reach 50 to 100 nm on set-ups which use optical magnification (Feser et al., 2008; Gelb et al., 2009). To obtain high-quality images at resolutions of a few microns for the modeling part of this thesis, typical imaging times are between 30 and 90 minutes and samples are cylinders with a diameter of 2 to 10 mm. The issue of fast imaging with lab-based sources is treated in Chapter 7.

After image acquisition and reconstruction, different materials in the sample can be identified by performing image segmentation, provided that there is contrast between the materials. Due to the large density difference between air and mineral phases, pores larger than the image resolution can be identified. Identifying and treating porosity below the resolution is treated in chapter 4. Detailed reviews of image processing and image analysis which may precede the modeling can be found in e.g. Wildenschild and Sheppard (2013) and Maire and Withers (2014). A properly segmented micro-CT image can serve as input to the modeling methods described next.

When higher resolutions are needed than what can be achieved with micro-CT, the main alternative is focused ion beam scanning electron microscopy (FIB-SEM). FIB-SEM works by sequentially imaging a plane of the sample with SEM and milling away a thin slab with a focused ion beam, allowing to build up a 3D image. While very high resolutions with milling-spacings down to 10 nm can be obtained, the technique is sample-destructive, very time consuming, and imaged volumes are typically limited to a maximum of $(10\ \mu m)^3$ (Möbus and Inkson, 2007; Holzer and Cantoni, 2011). Another alternative is X-ray ptychography, which is based on small-angle coherent scattering on synchrotron beam lines. This technique allows very high resolution non-destructive imaging, with resolutions down to 45 nm achieved on small rock samples which contained clays (De Boever et al., 2015). However, sample sizes are limited to a few microns, the imaging is slow (on the order of 12-24h depending on the desired resolution) and beam time on these instruments is severely restricted.

3.2 Direct pore scale modeling

3.2.1 Introduction

Direct pore scale flow modeling methods attempt to solve the Navier-Stokes equations (or in some cases a simplification of it) on the complex boundary conditions provided by a 3D representation of the pore space, like a pore scale image obtained with micro-CT (section 3.1). While simulating single-phase fluid flow is fairly straightforward in principle, the complex geometries of pore spaces and fracture networks can result in practical difficulties (Meakin and Tartakovsky, 2009). Nevertheless, direct methods are currently the standard method of choice to calculate single phase flow and transport (Blunt et al., 2013). However, multi-phase flows add a number of difficulties. Since many geological multi-phase flow problems are slow, capillary dominated flows, tracking the interfaces of the fluids is paramount, as the curvature of the interfaces controls the capillary pressure (Blunt et al., 2013). This brings forth significant numerical challenges, as the fluid-fluid interfaces undergo intricate motions related to the complex boundary conditions posed by the porous medium (e.g. interfaces coalescing). Furthermore, the finite resolution of the computational grid or mesh makes it difficult to simulate small-scale processes such as wetting film flow in crevices, which is important to represent the wetting phase connectivity correctly, as well as to simulate instabilities of oil-filled pores during imbibition. The aforementioned complications add to the computationally demanding nature of direct methods, and therefore make it difficult to perform simulations on representative volumes, particularly in heterogeneous rocks. Therefore, the amount of studies performed on experimentally determined pore space geometries of real geological porous media (rather than simple model systems such as glass bead packs) is still relatively limited, compared to the large body of literature on the development of numerical algorithms to perform these simulations.

Several classes of methods can be distinguished based on the numerical scheme they employ and on the way the geometry of the pore space is treated. An overview of the most important ideas behind these methods will be presented in this chapter, along with their applications in earth science fields.

3.2.2 Lattice Boltzmann

Method

Among the most popular methods for pore-scale flow simulation is the Lattice-Boltzmann (LB) method. This class of models has evolved from lattice-gas (LG) models (cellular automatons), which are more intuitive to understand. In LG models, space is discretized by introducing a regular lattice, on which idealized gas particles can move with discretized velocities (Higuera et al., 1989; Sukop and Thorne, 2006). At each time step, these particles propagate (i.e. jump) to a neighbouring lattice point, depending on their velocity and initial position, and collide with each other, in such a way that momentum is conserved. This can be seen as a discretization of the behaviour of an ideal gas. To simulate the presence of multiple phases or components, particles can be given a label (or colour) according to the phase or component they belong to, after which the collision rules are adapted to model interactions between the different phases or components (Rothman and Zaleski, 1994). To simulate immiscible phases, particles of each phase collide such that they are directed as much as possible towards other particles with the same label, resulting in phase separation. To simulate reactive flow, particles are created or destroyed when they collide with each other or with solid walls. However, lattice-gas models suffer from noisy statistics and Galilean invariance, which can be overcome by using lattice-Boltzmann methods. Here, the moving particles on the lattice are replaced by packets of moving particles, i.e. particle velocity distributions (Meakin and Tartakovsky, 2009). Today, lattice-Boltzmann (LB) methods have almost completely replaced lattice-gas models for flow simulations in geological materials.

The LB method solves a discretized Boltzmann equation of fluid-particle distributions that move and interact on a regular lattice with very few degrees of freedom (Ramstad et al., 2010). This means that at each node on a regular lattice, a particle distribution for each possible particle velocity vector is defined. The number of these vectors is limited by only allowing particles to move to a neighbouring node in one time step. During each time step of the simulation, packets of particles are propagated according to their velocities, and the velocity populations are relaxed by a collision step (mimicking molecular collisions) (Meakin and Tartakovsky, 2009). The simplest, most popular collision rule is the single-relaxation time Bhatnagar-Gross-Krook (BGK) approximation,

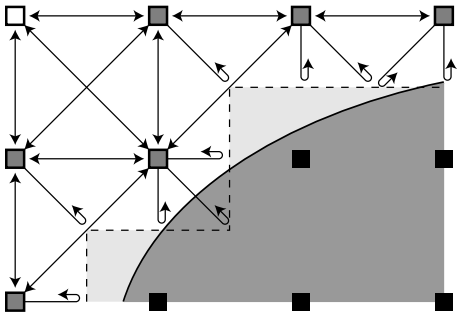

Figure 3.1: Fluid solid boundary handling in Lattice-Boltzmann methods. Solid is shown in dark gray, pore space in white. Black nodes are in the solid phase, gray nodes are in the pore space but are neighbouring solid space, and white nodes are in the pore spaces. Reprinted with permission from Llewellin (2010). At each time step, particles can be redistributed according to the arrows between the nodes.

however, correctly modeling viscosity effects requires the use of two-relaxation time models (Talon et al., 2012). It can be shown that the Navier-Stokes equations can be recovered from the lattice-Boltzmann scheme in the incompressible limit (Thijssen, 2007). Typically, the lattice is just the voxel grid of the 3D image obtained from for example a micro-CT scan. Consequently, no complicated meshing procedures have to be performed. Solid boundaries are typically handled with a simple bounce-back condition, meaning a packet of particles which hit a solid wall node at a certain time step are bounced back to the node in the pore space where they came from (see Figure 3.1, Llewellin (2010)). Sukop and Thorne (2006) provide an in-depth introduction into this numerical technique, aimed at geoscientists and engineers.

The LB method is noted for its relatively simple implementation and its suitability for parallelization (e.g. McClure et al. (2014)). Furthermore, it has a natural extensibility to represent multi-phase flow by tracking multiple types of interacting particles, each type representing a fluid phase, thereby removing the need to track interfaces explicitly (Geiger et al., 2012; Kuzmin and Mohamad, 2010; Shan and Chen, 1993). When simulating multi-phase flows, there are different methods of taking the fluid-fluid interactions into account: most notably colour gradient models (Gunstensen et al., 1991), free energy models (Swift et al., 1996) and Shan-Chen (also-called pseudo-potential) models (Shan and Chen, 1993). For detailed descriptions of how these models work, we refer to the original sources or more in-depth reviews on lattice-Boltzmann modeling

(e.g. Sukop and Thorne (2006)). One of the main disadvantages of the method is its computational inefficiency, even with a massively parallel implementation. The run time scales approximately inversely with the real flow rate, making it difficult to accurately capture capillary-controlled flow on representative images (Blunt et al., 2013). Other important limitations are that the numerical stability of the method is problematic in the situation of multiphase flows with large density and viscosity ratios, which is the case in for example water-gas systems (Meakin and Tartakovsky, 2009), and the fact that in multi-phase flows, linking the model's interaction forces to the modelled physical processes is not trivial (Ferrari and Lunati, 2013).

Applications

Single-phase flow Over the last 20 years, LB algorithms have been used extensively to study porosity-permeability relations on 3D images of rocks and sediments, obtained from stochastic or process-based reconstruction (Keehm, 2004; Wu et al., 2006), FIB-SEM images (Yoon and Dewers, 2013), and most notably micro-CT imaging (Andrä et al., 2013; Fredrich et al., 2006; Jin et al., 2004; Khan et al., 2012; Manwart et al., 2002; Shah et al., 2015). Parallel implementations allow to investigate the link between the micro-structure and the single-phase flow field in volumes of more than $(1000)^3$ voxels, allowing to achieve representative elementary volume at sufficient voxel resolution in many rock types. Most studies investigate laminar flow as this is usually the case of interest in geological problems, but LB models can also be used to study high-Reynolds number flows (Chukwudozie et al., 2012). Despite these successes, simulations in heterogeneous materials with very broad pore size distributions (e.g. many carbonates) remain challenging. To tackle this problem, so-called gray LB models are being developed (Kang et al., 2002; Li et al., 2014; Yehya et al., 2015; Zhu and Ma, 2013). In these multi-scale models, nodes which contain sub-resolution microporosity (e.g. clay or micrite) only partially bounce back the arriving fluid packets. Microporous domains in the image are therefore treated as permeable regions and contribute to the flow in the sample. While this is certainly an interesting approach, further validation is needed, and some theoretical issues have been brought forth recently (Ginzburg, 2014).

Another challenge which has recently received a lot of attention is the

simulation of flow fields in tight, often fractured materials, including shale, chalk and coal (Kelly et al., 2015). Not only do Klinkenberg effects have to be taken into account when the pore or fracture sizes are on the order of the mean free path of the fluid molecules (Chen et al., 2015), but reliably segmenting thin fractures with sufficient detail on representative samples may cause problems (Ma et al., 2010). Simulations on fracture networks with fracture openings which are only a few lattice nodes wide result in significant uncertainties on permeability (Welch et al., 2015).

Solute and reactive transport To investigate the influence of pore structure on dispersion, the transport of dilute tracers can be modelled by simulating the flow field of a carrier fluid on one lattice, and propagating each tracer on a separate lattice according to the flow field determined from the carrier fluid (Stockman, 2006). A number of such studies exist on 2D samples and single fractures (Jiménez-Hornero et al., 2005), while recent studies have also tackled 3D images extracted from micro-CT scans (Boek et al., 2014; Yang et al., 2013a). Promising LB models have also been developed to simulate reactive transport (Huber et al., 2014; Kang et al., 2010; Patel et al., 2014a,b; Sullivan et al., 2005) by adding source and sink terms to represent the chemical reactions. However, most applications of these methods have remained limited to simulations in very simplified 2D porous geometries. Very recently, such models have been applied to study the coupling between dissolution and precipitation in 3D images based on micro-CT scans of geological media (Gao et al., 2015; Jiang et al., 2014). In this context, it is interesting to couple micro-CT scans with chemical information obtained with other imaging methods like QEMSCAN, EDS or XRF (Gao et al., 2015; Landrot et al., 2012; Peters, 2009). A comprehensive review on the use of lattice-Boltzmann for pore scale reactive transport modeling can be found in Yoon et al. (2015).

Multi-phase flow The three main models (colour gradient, Shan-Chen and free energy) are compared by Yang and Boek (2013). The authors conclude that the (Oxford) free energy and colour gradient models seem appropriate to simulate the flow of binary fluids with high viscosity contrast with high numerical stability, while the Shan-Chen (pseudo-potential) model is capable of simulating high density ratio fluids (e.g. brine-gas) but provides lower numerical stability and wide interfaces for immiscible systems. Despite the computational challenges, the LB

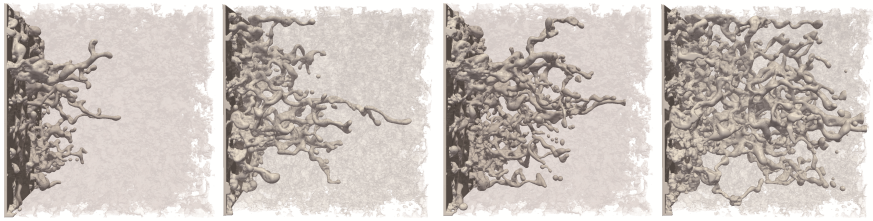

Figure 3.2: Four snapshots of the non-wetting fluid intruding in a Berea sandstone during drainage, simulated with a colour gradient lattice-Boltzmann model. Figure reprinted with permission from (Jiang et al., 2014).

method has been used for a number of studies concerning multi-phase simulations on realistic, 3D pore structures; be it usually on rather homogeneous rock types and rather small rock volumes (see Table 3.1) (Boek, 2010; De Prisco et al., 2012; Ferréol and Rothman, 1995; Harting et al., 2005; Hazlett et al., 1998; Landry et al., 2014a,b; Pan et al., 2004; Porter et al., 2009; Ramstad et al., 2010, 2012; Schaap et al., 2007; Sukop et al., 2008). As an example of the benefit of applying direct modeling, Jiang et al. (2014) show how LB can elucidate the influence of the interfacial tension on relative permeability in a sandstone: three different zones of interfacial tension values were found, each showing distinct characteristics in terms of breakthrough time, displacement patterns, equilibrium invading fluid saturation and mean flow velocity.

Some fairly mature open-source lattice-Boltzmann libraries which have been used for porous media applications are Palabos (Parmigiani et al., 2011) and Taxila (Coon et al., 2013) (see for example Figure 3.2). Lattice Boltzmann methods to simulate multi-phase, high-density-contrast flows in porous materials have been developed as well (Liu et al., 2014, 2013).

3.2.3 Traditional computational fluid dynamics

Method

A second class of methods are the traditional mesh-based computational fluid dynamics (CFD) approaches, such as finite difference, finite volume and finite element methods. These are probably the most popular methods to be used in natural porous media applications after lattice-Boltzmann. Unlike the latter, these schemes follow a top-down approach by

Table 3.1: Selection of studies presenting two-phase LB simulations on realistic 3D pore geometries

Publication	Study subject	Sample	Algorithm	Grid size
Ferréol and Rothman (1995)	Qualitative study of drain/imbibition	Fontainebleau	Color gradient	64^3
Hazlett et al. (1998)	Influence of wetting on displacement dynamics and relperm	Berea	Color gradient	128^3
Pan et al. (2004)	Hysteretic capillary pressure, REV	Digital sphere pack	Shan-Chen	512^3
Harting et al. (2005)	Fluid distributions in drainage and imbibition compared to MRI	Bentheimer	Shan-Chen	512^3
Schaap et al. (2007)	Capillary pressure compared to experiment for air-water and air-soltrol	Glass beads	Shan-Chen	405x405x100
Sukop et al. (2008)	Compare equilibrium distributions to micro-CT experiments	Sandpack	Shan-Chen	
Porter et al. (2009)	Hysteresis in capillary pressure and interfacial area	Glass beads	Shan-Chen	207x207x166
Ramstad et al. (2010)	Steady and unsteady state relative permeability, drain/imb	Bentheimer (micro-CT & process-based)	Color gradient	256^3
Boek (2010)	Rel perm, drain/imb	Bentheimer	Shan-Chen	128^3
De Prisco et al. (2012)	Rel perm, drain/imb, comparison to experiment	Middle eastern Carbonate	Phase field (two automata)	500^3
Ramstad et al. (2012)	Steady and unsteady state relative permeability, drain/imb	Bentheimer and berea	Color gradient	256^3
Landry et al. (2014a)	Interfacial areas, relperms, influence of wetting	Bead pack	Shan-Chen	100^3
Landry et al. (2014b)	Fracture-matrix fluid transfer, compared to 4D micro-CT	Fractured sintered glass	Shan-Chen	200x200x300
Mohnke et al. (2014)	Jointly simulate NMR relaxometry experiments and two-phase flow	Sandpack	Color gradient	200x200x240
Jiang et al. (2014)	Investigate influence of interfacial tension on fluid flow characteristics	Berea	Shan-Chen	320^3
Jiang and Tsuji (2015)	Impact of interfacial tension on trapped cluster size	Berea	Color gradient	400x400x400

discretizing the Stokes or Navier-Stokes equations on a (structured or unstructured) mesh (Icardi et al., 2014). The finite volume method is used most frequently, because it is naturally volume conserving. In this method, a local mass and momentum balance is written for each cell in the mesh (the control volume). These balances, which are obtained by integrating the mass and momentum balance equations (i.e. the Navier-Stokes or Stokes equations) over the control volume, are then written in terms of fluxes through the boundaries of the control volume: fluid and momentum flowing out of a cell boundary have to arrive in the neighbouring cell (Eymard et al., 2000). By also discretizing time in small time-steps, the partial differential equations which govern the fluid transport are approximated as a set of algebraic equations, which can be solved numerically (Raeini, 2013). For the working principles of finite element and finite difference methods, we refer to Thijssen (2007) and other standard works. Traditional CFD methods are numerically efficient and can simulate fluid flow with very large density and viscosity ratios (Meakin and Tartakovsky, 2009). While most geological porous media problems concern laminar flow, CFD methods can be applied to study non-Darcy flow at high flow rates as well (Muljadi et al., 2015).

Some of the difficulties encountered specifically for multiphase flow in porous and fractured media are the tracking of fluid interfaces, the implementation of a contact line/contact angle model and the increase of computational times and numerical instability for slow flow rates (Blunt et al., 2013; Meakin and Tartakovsky, 2009; Renardy and Renardy, 2002). Several strategies have been developed to deal with the problem of tracking the fluid interfaces during multi-phase flow. In the moving mesh methods, both fluids are meshed separately. Therefore, this method has the advantage of providing a sharp interface. Difficulties are the need to re-mesh often, making this method computationally inefficient, and dealing with topological changes of the interfaces (Raeini, 2013). The level-set method, on the other hand, uses an indicator function that is positive in regions occupied by one phase and negative in regions occupied by the other. The indicator function is advected with the flow. The effect of surface tension can be included as a body force (based on the curvature of the indicator function at zero), working only in the vicinity of the interface (continuous surface tension force model). The sharp interface is then replaced by a smeared out function over this region. This method handles topological changes well, but often violates mass conservation (Meakin and Tartakovsky, 2009; Prodanović and Bryant, 2006). Particle

level set methods use particles with different labels inserted on opposite sides of the interface to track it, resulting in improved mass conservation. One of the most promising interface tracking methods is the volume of fluid method (Ferrari and Lunati, 2013). Here, a fuzzy approach to the presence of multiple immiscible fluids is followed, by tracking the volume fraction of each phase in each mesh cell (i.e. some cells can formally be thought to contain a mixture of the two fluids, meaning the interface need not be sharp). The interface can then be reconstructed from the gradient of this volume fraction. The effects of surface tension are expressed in terms of a body force that acts near the cells where the gradient of the volume fraction is non-zero (Raeini, 2013).

Applications

Single-phase flow Like lattice-Boltzmann methods, classical CFD methods have been used extensively to solve single phase flow on direct, experimental 3D images of real rocks: e.g. with finite volume (Peng et al., 2014; Zhang et al., 2012) and finite element methods (Mostaghimi et al., 2013). Similarly, stochastically generated 3D pore spaces have been investigated by Hyman et al. (2012). In Veselý et al. (2015), flow and diffusion calculations on stochastically reconstructed porous geometries are compared to those on micro-CT scans of the same porous medium, illustrating both the sensitivity of the micro-CT based simulations on the image processing (filtering and segmentation), and the intrinsic difficulty of stochastically reconstructing realistic pore geometries, even in relatively homogeneous media.

A comparison of single-phase flow calculations with a finite volume and 2 finite difference schemes can be found in Siena et al. (2015). The authors note that despite significant differences in implementation and complexity between the three tested methods, consistent results were obtained. In Manwart et al. (2002), single-phase lattice-Boltzmann and finite-difference permeability simulations are compared. They note that while both methods delivered acceptable results, there were also differences, mainly caused by numerical concerns in the lattice-Boltzmann algorithm. A recent comparison between a finite volume, a lattice-Boltzmann, a smoothed-particle hydrodynamics and a pore network model was presented in Yang et al. (2015). Although all models gave broadly similar results, there were some differences believed to originate

mainly from differences in meshing and grid resolutions. It should be noted that in general, drawing broad conclusions from model inter-comparison studies is complicated due to the variable capabilities of codes, the differences between individual implementations of similar algorithms and the difficulty of obtaining ground truth data to compare results with. To obtain such ground truth data, the flow field can be measured locally in the pore space by MRI measurements (Yang et al., 2013b).

When solving single-phase flow in very heterogeneous samples with unresolved porosity features, the flexibility and generality of the classical CFD methods pays off. Two different multi-scale methods have been developed in this context (Ligaarden et al., 2010). These methods are comparable to gray lattice-Boltzmann methods in set-up, but seem to have a more firm theoretical basis. The first method is the Darcy-Stokes method, which solves Stokes flow in the larger pores and Darcy flow through regions which contain unresolved porosity and are therefore considered permeable, e.g. (Arbogast and Gomez, 2009; Scheibe et al., 2015). Coupling the Stokes and Darcy regions in the volume requires a complex treatment of the boundaries. The second approach is to solve the Stokes-Brinkman equation: the flow in both Stokes and Darcy regions is then described with this single equation with variable parameters (Krotkiewski et al., 2011; Popov et al., 2009; Yang et al., 2014), eliminating the need for complicated boundary treatment.

Work flows have also been developed to calculate single-phase flow on fractures extracted from micro-CT measurements, with or without interaction with a porous matrix around the fracture (Crandall et al., 2010; Huber et al., 2012). A finite element method specially adapted to deal with single-phase flow in coal and other tight samples with very small fractures was used by Ramandi et al. (2015). The method works with voxel-based local conductivities measured from the Euclidean distance map.

Solute and reactive transport Classical CFD methods have been used to simulate solute transport on 3D images, either by moving particles along streamlines based on the computed advective flow field (Bijeljic et al., 2013b,a; Mostaghimi et al., 2012; Pereira Nunes et al., 2015) or by solving the Navier-Stokes and advection-diffusion equations (Zaretskiy et al., 2010). Generally, particle-based methods are preferred to calculate transport of chemical species, as these methods are free of numerical

dispersion (Mehmani et al., 2015a). Such methods can be used to study for example the effect of pore space homogeneity on local velocity distributions and molecular displacement probabilities (Bijeljic et al., 2013a), showing that heterogeneous pore spaces produce non-Fickian behaviour due to a persistently immobile solute concentration long after injection. The solute transport concepts have been further adapted to simulate reactive transport (Alhashmi et al., 2015; Molins et al., 2014; Siena et al., 2014; Trebotich et al., 2014).

Multi-phase flow Only few applications of classical CFD methods to multi-phase flow on three-dimensional pore space images of geomaterials can be found in literature. Raeini et al. (2015b, 2014) performed two-phase flow simulations on segmented 3D micro-CT images of Berea sandstone (Figure 3.3) and a sand pack to investigate capillary trapping (on maximally 400^3 voxels), while Arrufat et al. (2014) showed relative permeability simulations on micro-CT images of Clashach sandstone and two carbonates (with maximally 432^3 voxels). Piller et al. (2014) presented relative permeability simulations on a synchrotron-micro-CT scan of a sandstone (200^3 voxels). All of these examples employ the volume-of-fluid method. Applications of multi-phase finite volume simulations on 2D images can be found in e.g. Ferrari and Lunati (2013); Huang et al. (2005). It should be noted that direct numerical models such as those developed and used by Cardenas (2008) and Raeini (2013) can provide highly-detailed sub-pore information, which can then be incorporated in less detailed, numerically more efficient simulations (e.g. pore network simulations).

3.2.4 Smoothed particle, semi-implicit-particle and dissipative hydrodynamics

An alternative to lattice Boltzmann and CFD methods are the Smoothed Particle Hydrodynamics (SPH) methods (Bandara et al., 2013; Berry et al., 2004; Sivanesapillai et al., 2015; Tartakovsky et al., 2009; Tartakovsky and Meakin, 2006; Tartakovsky and Panchenko, 2015). Closely related are the moving particle semi-implicit (Ovaysi et al., 2014; Ovaysi and Piri, 2011) and dissipative (Español and Warren, 2007; Pan and Tartakovsky, 2013) particle hydrodynamics. These are mesh-free Langrangian particle based methods, which share with lattice Boltzmann simulations the advantages

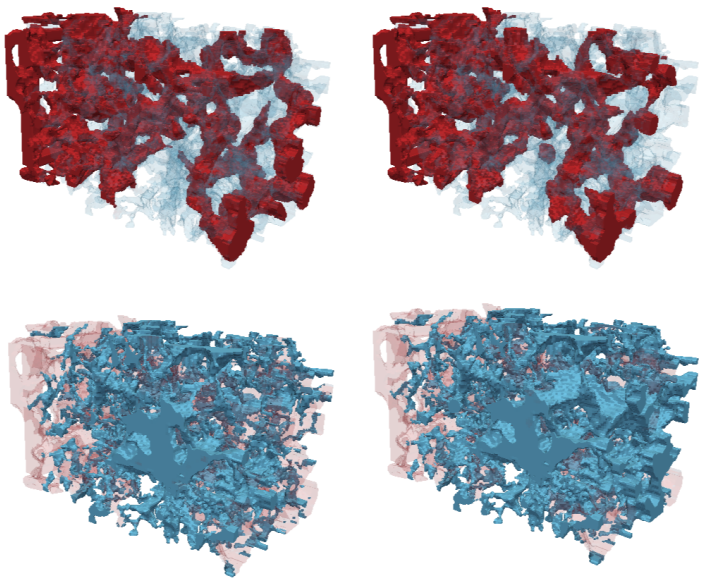

Figure 3.3: 3D rendering of the wetting phase (top, red) and the non-wetting phase (bottom, blue) at the end of primary drainage simulations on a micro-CT image of Berea sandstone, for a high capillary number (10^{-5}) on the left and lower capillary number ($2.5E^{-6}$) on the right. These simulations were performed with a finite-volume method. Figure from Raeini (2013).

of being able to deal with complex boundary conditions relatively easily, and of not requiring explicit interface tracking or contact angle models. In addition, the SPH model allows unsaturated (liquid/gas) flows with large viscosity and density ratios to be simulated (water and air with a viscosity ratio on the order of 100 and a density ratio on the order of 1000, for example). Another advantage of the SPH approach is its simple physical interpretation, since the Navier-Stokes equations are reduced to a system of ordinary differential equations with the form of Newton's Second Law of motion for each particle. This simplicity allows a variety of physical and chemical effects to be incorporated into SPH models with relatively little code-development effort through pair-wise molecular type interactions (Tartakovsky and Meakin, 2006). The method is however computationally demanding compared to other methods described here. It is thus an attractive method to study multi-phase flow in complex geometries and in the case of large interface movements, but on smaller volumes than the previously described methods (which typically run on images of 200^3 to 300^3 voxels) (Raeini, 2013).

3.2.5 Direct hydrodynamics

Since the late 2000s, researchers at Schlumberger Moscow and Shell have been jointly developing a novel direct pore-scale modeling method called direct hydrodynamics (Koroteev et al., 2013). This method is based on the density functional method for multi-phase compositional hydrodynamics (Demianov et al., 2011). It employs a diffuse description of the fluid interfaces, in combination with continuum fluid mechanics and thermodynamic principles (mass, momentum and energy balance). The method is capable of simulating a broad range of physical phenomena, including multiphase flows with phase transitions and mobile solid phase, different types of fluid-rock and fluid-fluid interactions (e.g. wettability and adsorption), and various types of fluid rheology. Thanks to the diffuse interface approach and a massively parallel GPU implementation, the method seems to be fairly efficient. Some results are shown in Figure 3.4 and Figure 3.5. A downside of this method is that to our knowledge, only one, proprietary implementation of this fairly young method exists.

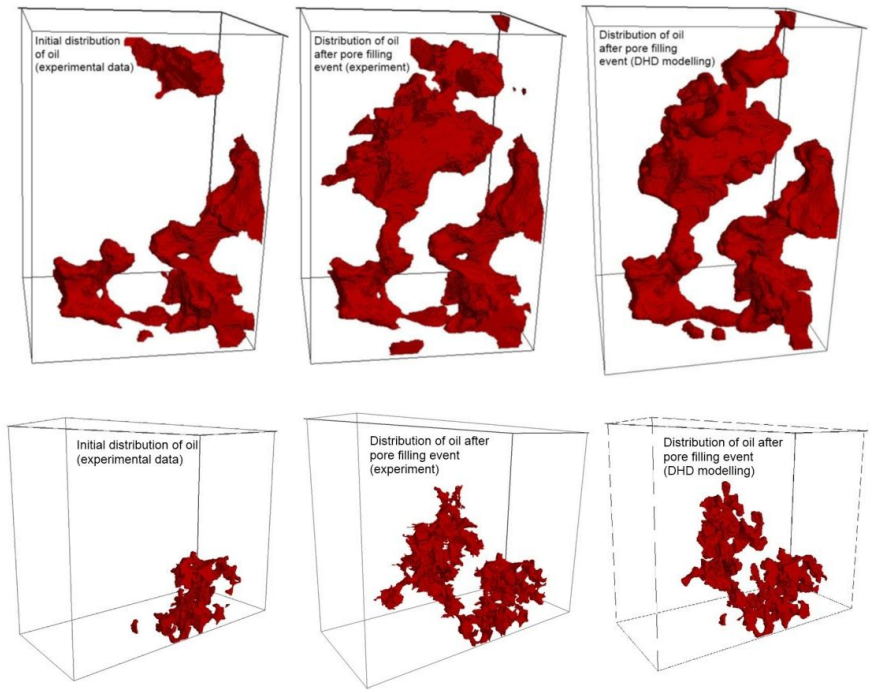

Figure 3.4: Comparison between experimental micro-CT data of pore filling during drainage in a Berea sandstone in the middle (Berg et al., 2013) and direct hydrodynamic simulations on the right. Oil is visualized in red, water and rock grains are not visualized. Numerical modeling of the pore filling event used initial oil distributions from micro-CT (on the left) as starting condition. Figure from Koroteev et al. (2013).

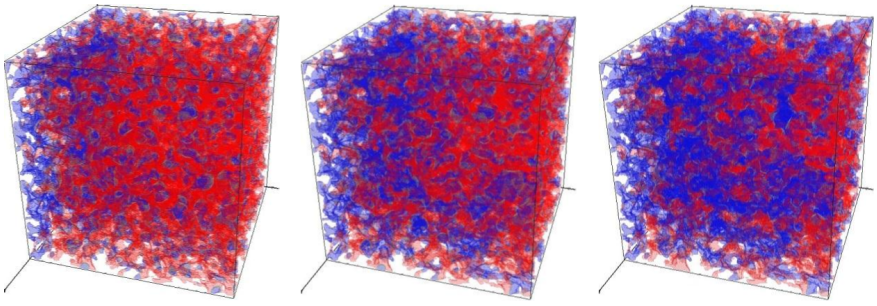

Figure 3.5: Direct hydrodynamics simulation of oil recovery by water flooding in a sandstone. Water is presented in blue, oil in red. Figure from Koroteev et al. (2013).

3.3 Pore scale modeling with pore network models

As discussed in the previous section, while advances are being made, the modeling of multi-phase transport properties directly on pore space images remains a challenging task. Specifically, the computational demands limit these simulations in most applications to small images of rather homogeneous rocks with narrow pore size distributions (typical applications are glass bead packings, sand packs and well-sorted, simple sandstones, e.g. Bentheim, Berea and Fontainebleau sandstone). In the future, direct pore scale modeling methods are expected to become more broadly applicable, but to date, pore network models (PNM) have been the most successful models for practical applications of pore scale simulations of two- and three-phase flow in the geological field (Blunt, 2001; Blunt et al., 2013). These models will be presented in this section.

3.3.1 Introduction

Pore network models represent a complex pore space by a network of pore bodies and pore throats (the narrow constrictions which link pores together) with idealized geometries (Blunt, 2001) (Figure 3.6). The first study using this idea was performed by Fatt (1956), who used a regular lattice of tubes with random radii to simulate transport through a porous medium. This model was seen to match experimental properties of porous media much better than the previously adopted bundle-of-capillary-tubes model, and has since served as a standard approach to think about transport in porous media. In later work, pore size distributions were used as constraints to regular lattices of pore bodies and throats, while some throats were removed at random to match coordination number distributions (the distribution of the amount of neighbours each pore has). However, it is very difficult to generate a lattice-based network model in such a way that the spatial correlations of, and between, the properties of the network elements (e.g. throat and pore radii, connectivity) honour reality. Furthermore, networks based on regular lattices often have difficulties with representing the topology of complex porous media adequately. Replicating the real topology is crucial (Vogel and Roth, 2001), and it has been shown that simply matching an average coordination number is insufficient to replicate realistic drainage (Arns et al., 2004) and imbibition (Mahmud et al., 2007) behaviour. In

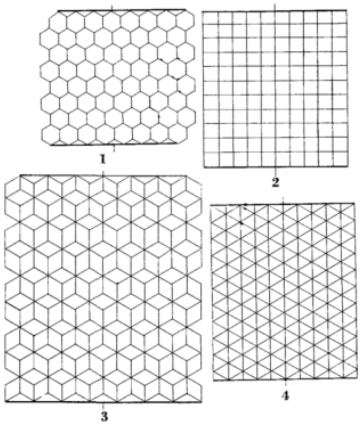

Figure 3.6: Two-dimensional, lattice-based networks originally investigated by Fatt in 1956 (figure from (Fatt, 1956)). Compare this to the contemporary 3D image-based networks in Figure 3.7.

conclusion, both the topology and the correlations greatly affect transport behaviour, meaning it is often difficult to simulate realistic rock behaviour on lattice-based network models (Sok et al., 2002). While such models may prove tremendously useful if these issues are taken into account (Jerauld and Salter, 1990; Raoof et al., 2010), image-based network models are currently gaining in popularity.

Since the 1990s, much effort has been put into extracting network models directly from 3D image-based representations of pore spaces by using image analysis techniques (Figure 3.7), in contrast to using stochastically generated lattice-based networks constrained by experimental data. In addition to circumventing the problem of characterizing all the correlations in the porous medium by basing the network on local measurements of pore space geometry, these methods typically also attempt to capture the real topology of the pore space (Lindquist et al., 1996).

The idea of extracting networks from pore space images merits the question "what is a pore"? A pore space is continuous, and therefore splitting it up into discrete network elements will require some arbitrary decisions (Hunt et al., 2014). The assumption is that a rock's pore space can be treated as if it consists out of a number of pores, separated by constrictions. One would expect this assumption to at least be valid for a granular medium, where the grains are typically convex objects, meaning the pores will be

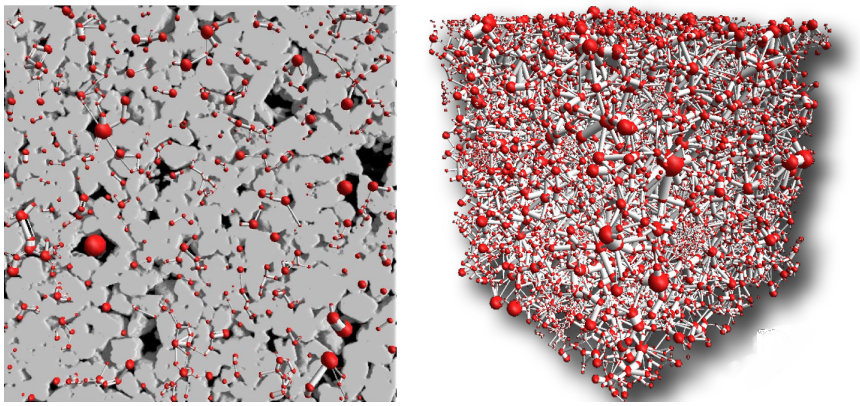

Figure 3.7: Pore network models extracted from a micro-CT scan of a Bentheim sandstone, on the left a front view of a part of a 3D network, shown on top of a rendering of the micro-CT scan it was extracted from. Note that some of the pores in the PNM are not visualized, for clarity. On the right, a full PNM is rendered separately. Networks were rendered with FEI's ECore software.

concave, yet even in this case arbitrary decisions have to be made as to where a pore ends and a constriction begins. It is therefore clear that PNM are a non-unique representation of a pore space (Arns et al., 2007), and any PNM extraction method is built on certain assumptions which might hold only for the media or the physical processes one wants to investigate with the resulting networks. This complicates comparison of different network algorithms.

Despite these theoretical objections, image-based PNMs have greatly helped to increase the understanding of geological porous media's multi-phase flow behaviour (Blunt, 2001). In addition to providing insight into the collective behaviour of a complex system of pores, which each adhere to certain well-defined (usually relatively simple) rules, pore network models have been shown to be able to actually predict constitutive relations (e.g. capillary pressure and relative permeability curves) in individual rocks (Øren et al., 1998; Valvatne and Blunt, 2004). This allows calculating transport properties (e.g. relative permeability) on small rock samples, which may be important when cored material is scarcely available. Furthermore, rock properties such as wettability can easily be varied to investigate the sensitivities involved. As a rock's wettability in reservoir conditions is often difficult to restore in lab samples, this analysis can be very useful.

In the following, we will first treat the different image-based PNM extraction algorithms in section 3.3.2; we will provide an oversight of how the resulting network models can be used to simulate transport properties in section 3.3.3, and address the influence of the PNM extraction on the simulated transport properties by reviewing comparative studies in section 3.3.4. In section 3.3.5, PNM methods specifically developed for multi-scale problems will be discussed, as an introduction to chapter 4.

3.3.2 Image based network extraction

Network extraction consists out of two parts: splitting up the pore space representation into discrete elements and subsequently measuring the geometric properties of each network element; properties that will be used in the flow modeling. Usually, these include the inscribed radius (or alternatively a hydraulic radius), the length, the volume and some sort of shape-describing parameter for each network element. Several ways of classifying PNM extraction exist, however, since the central idea is to simplify a pore space by capturing its topology and the relevant traits of its geometry, we will classify the methods into two classes: methods which split up the pore space in a topology-central way and methods which do this in a morphology-central way (Wildenschild and Sheppard, 2013). Many methods to split the pore space have been developed, often with common characteristics. We discuss the main ideas behind these methods.

Topology-central methods

One of the first image-based PNM extraction algorithms was a topology-central method developed by Brent Lindquist and co-workers (Lindquist et al., 1996; Lindquist and Venkatarangan, 1999). They used the concept of a medial axis, a representation of the pore space by a central skeleton, an approach that is still popular today (Figure 3.8). First, a medial axis extraction is performed (Saha et al., 2015), after which the branching points in the skeleton are considered to be the centres of pore bodies. Most methods use a distance-ordered homotopic thinning algorithm (DOHT) (Pudney, 1998) to find the medial axis, as this algorithm delivers homotopically equivalent skeletons which lie central in the pore space. In the original Lindquist algorithm, the throats were then found by dilating the branches of the medial axis to find the throat

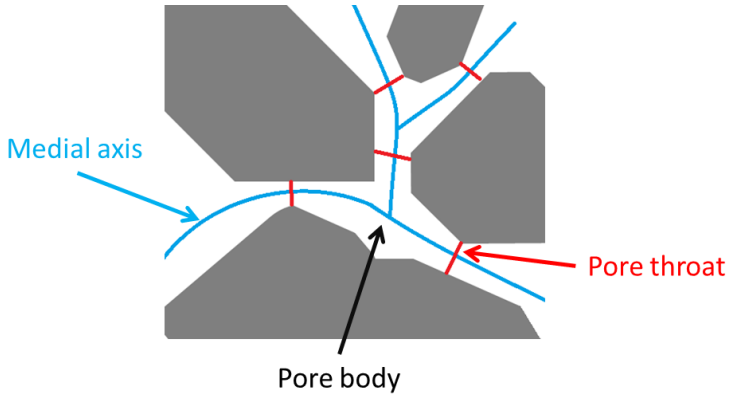

Figure 3.8: A pore space, its medial axis, and its throats identified by using a medial axis.

perimeter where the contact points of the solid space and the dilations of the medial axis form a closed loop first. Other authors follow a different approach to the throat-identification problem and to determine the parameters of individual network elements (Al-Raoush and Willson, 2005; Arns et al., 2007; Jiang et al., 2007; Youssef et al., 2007). Usually, the medial axis is used as an embedded search structure to find the throat locations in the form of the narrowest sections transversal to it (Lindquist, 2002)(see Figure 3.8), although Sheppard et al. (2006) use a watershed transform seeded by the pore centres to split up the pore space.

One of the most important problems when constructing pore network models from medial axis representations extracted from experimental pore space images, is the sensitivity of the medial axis to small defects in the pore space surface. This will lead to an over-identification of pores, as there will be spurious branches in the medial axis when image noise leads to misidentification of pore and solid voxels. Attempts to reduce these problems often propose advanced pre-and post-processing (Plougonven and Bernard, 2011; Sheppard et al., 2005) to reduce noise in the input image and to merge spurious pores a-posteriori (Figure 3.9).

It should be noted here that differences in for example the identified number of pores do not necessarily have large effects on the simulated properties, as long as the topology and the geometry (i.e. the widest and narrowest passages in the pore space) are well captured (Thompson et al., 2005). Therefore, a more fundamental problem with this type of network

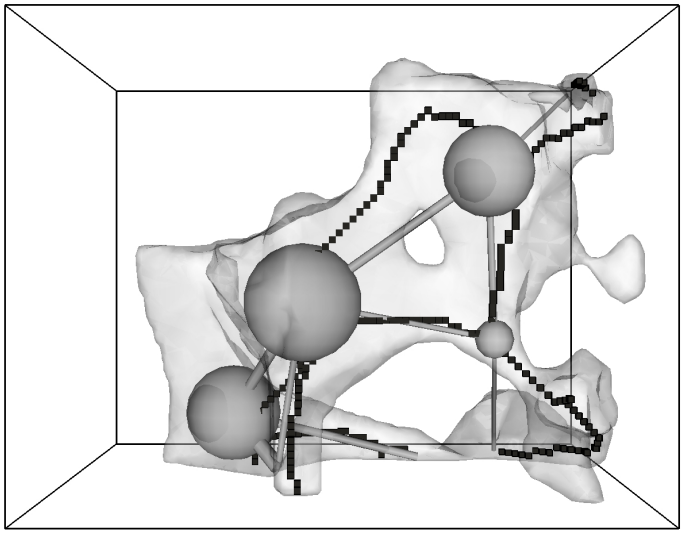

Figure 3.9: A medial axis and the pore network extracted with it, illustrating a case in which the geometry and the topology of the pore space are hard to express as a network. Figure from Sheppard et al. (2005).

extraction is that the junctions in the network, which are identified as pore bodies, do not necessarily coincide with geometrical pore bodies (i.e. points where the pore space is wider) (Arns et al., 2007). This is problematic as slow drainage and imbibition in porous media are to a large degree geometrically dominated phenomena. The advantage of using a medial axis, on the other hand, is its direct relationship to the topology of the original image.

Morphology-central methods

One of the first morphology-based pore network extraction methods was developed by Zhao et al. (1994), who used multi-orientation scanning through a digital reconstruction of a rock sample to identify constrictions. In their view, measurements on parameters like pore size and coordination number could only be reliable when the constrictions separating pores are identified first, since these actually define the individual pores (compare this to the identification of pores as branching points of a medial axis in

topological methods). However, using their approach of a discrete number of scanning orientations, some throats may be missed and some may be misidentified. Later on, other researchers like Baldwin et al. (1996) and Liang et al. (2000) improved on this approach by identifying minima in the hydraulic radius of pore space channels. Baldwin et al. (1996) used a thinning approach, while Liang et al. (2000)'s method scanned the planes perpendicular to the pore space skeleton, after which these plains defined the separate pores in the image.

A second type of morphology-based network extraction methods, which is however somewhat related to the medial axis method, is the grain-based method (Bakke and Øren, 1997). While more sophisticated methods have been developed since, this is still considered to be somewhat of a benchmark (Wildenschild and Sheppard, 2013). First, the individual solid grains in the rock are identified, after which these grains are dilated until there is no pore space left. Places where three grains touch then form a skeleton, while points where four or more grains touch are nodes in the network. The grain-identification step is heavily influenced by the rock's morphology, hence the classification of the method as morphology-central.

In this work, the authors employ a rotating vector method to scan the surfaces perpendicular to the skeleton line, in order to find the narrowest constrictions between pores (Figure 3.10) (Bakke and Øren, 1997). A similar vector scanning method is used to find the volume and the inscribed sphere radius in the pores. Furthermore, a pore shape factor is determined (see further) which describes the surface roughness of the network elements. The authors used their method on process-based reconstructions of sedimentary rocks, meaning they had all the information on individual grains in their input image. The process-based method utilizes petrographical information obtained from two-dimensional thin sections to stochastically model the results of sedimentary rock forming processes (sedimentation, compaction, and diagenesis) (Øren and Bakke, 2002). However, when one employs this method to a segmented micro-CT scan, grain identification can be a bottle neck, as noise in the image will commonly lead to oversegmentation of grains. Also, it is not clear if this grain-based method holds any validity when trying to extract networks from non-granular porous media (e.g. certain carbonate rocks like travertine). A similar grain-based method was developed by Thompson et al. (2005). It first identifies seeds for pore centre identification by triangulating the set of grain centre points. Then,

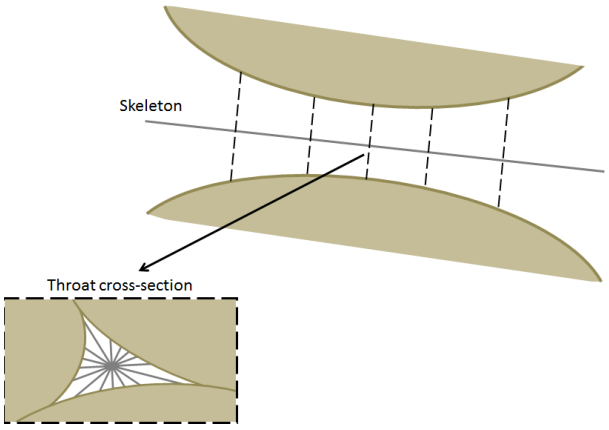

Figure 3.10: Schematic depiction of the geometrical analysis of pore throats in Bakke and Øren (1997). On the top, the skeleton line and the sections transversal to it are shown. On the bottom, the scanning vectors used to determine throat radius and volume in such a section are drawn. Figure inspired by Bakke and Øren (1997).

these seed points are used to find local maxima of the distance map by using a watershed algorithm. These local maxima define pore centres. Afterwards, all voxels in the image are assigned to pores or grains by using a restricted burn algorithm (for more details we refer to Thompson et al. (2005)). This process should be less dependent on defects in the grain identification; however, this method could use further validation.

A third very well-known morphology-based method starts from the extraction of so-called maximal balls (Silin and Patzek, 2006). These are the largest inscribed spheres centred on each voxel of the image that just touch the grain or the boundary. Then, the spheres which are fully included in other spheres are removed. The set of maximal balls describes the pore space without redundancy. The maximal balls are clustered into families according to their size and the size of the maximal balls they overlap with (Figure 3.11). Locally, the largest maximal balls (i.e. the ancestor of a family of maximal balls) identify pores. The smallest balls which belong to more than one family and therefore connect the pores identified by these families, are throats (Al-Kharusi and Blunt, 2007; Dong and Blunt, 2009). The advantage of this method is that it attempts to explicitly identify wide passages in the pore space as pores and narrow passages as throats. However, while the larger pores are identified well, the method seems to find a cascade of smaller and smaller network

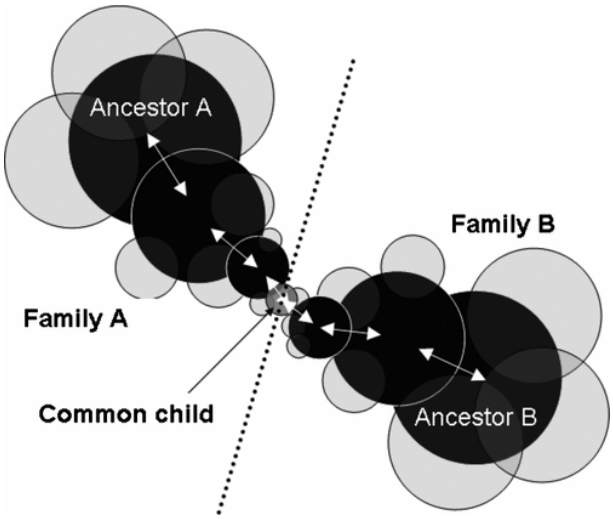

Figure 3.11: The clustering of overlapping maximal balls into families, resulting into two pores (centred on ancestors A and B) and a throat between them (at the location of the common child of the two families) (Dong and Blunt, 2009). The white arrows indicate the pore-throat chain.

elements down to the image resolution (Blunt et al., 2013).

Finally, the pore space can also be decomposed by performing a watershed algorithm on the distance map calculated from the segmented pore space image (Vincent and Soille, 1991; Brabant et al., 2011). The throats are then found as surfaces which separate the pores from each other (Rabbani et al., 2014; Wildenschild and Sheppard, 2013). Watershed algorithms have been implemented in many commercial and open source software packages, e.g. Octopus Analysis, Avizo, Fiji, ITK, etc.

Other methods

Aside from the previously discussed methods, some lesser known network extraction methods are based on genetic algorithms (Ebrahimi et al., 2013) or on single-phase flow fields calculated with computational fluid dynamics (Dong et al., 2008). To accurately represent film flow in network models (see section 3.3.3), some algorithms incorporate more complex pore and throat shapes in the geometrical characterization of network elements (Joekar-Niasar et al., 2010b; Ryazanov et al., 2009). Other

advanced geometry-determination algorithms take into account the converging/diverging nature of throats (Bauer et al., 2011), or calculate network elements' fluid conductance by running lattice Boltzmann or CFD algorithms on the sub-volumes defined by each separate network element (Sholokhova et al., 2009).

3.3.3 Transport simulations based on pore network models

Quasi-static multi-phase flow modeling

During pore network extraction, the pore space is split up into simple geometrical units (pores and throats, which from a conceptual point of view can be seen as spheres and cylinders), which locally capture features important to the process under investigation. For multi-phase flow studies, local constrictions and dilations of the pore space, as well as surface roughness, are usually captured. For slow flows (low capillary numbers), the sequence of fluid invasion in network elements during drainage and imbibition is often modelled by an invasion-percolation algorithm. For this situation, capillary forces dominate and determine which parts of the pore space can be filled with an invading fluid at a certain pressure difference imposed on the fluids. If the porous medium is wetted by the defending fluid (drainage), the constrictions limit which part of the pore space can be filled. On the other hand, if the medium is wetted by the invading fluid (imbibition), the dilations in the pore space determine which parts of the pore space can be invaded. In a cylindrical network element, Young-Laplace's law (equation 2.7) can be used to relate the radius of the inscribed sphere to the equilibrium capillary pressure (P_c), which needs to be overcome for it to be invaded.

At the beginning of the displacement process, consider one face of the network to be connected to a reservoir of the invading fluid, while the other is connected to a reservoir of the defending fluid. Invasion-percolation describes the displacement process at constant flow rate (Wilkinson and Willemsen, 1983), leading to the dynamic rule of advancing the interface at the point of least resistance: during drainage the widest network element available for invasion is filled, while during imbibition the narrowest element available is invaded (Figure 3.12).

A network element is available for invasion when it neighbours an element already filled with the invading fluid, and when the defending fluid present

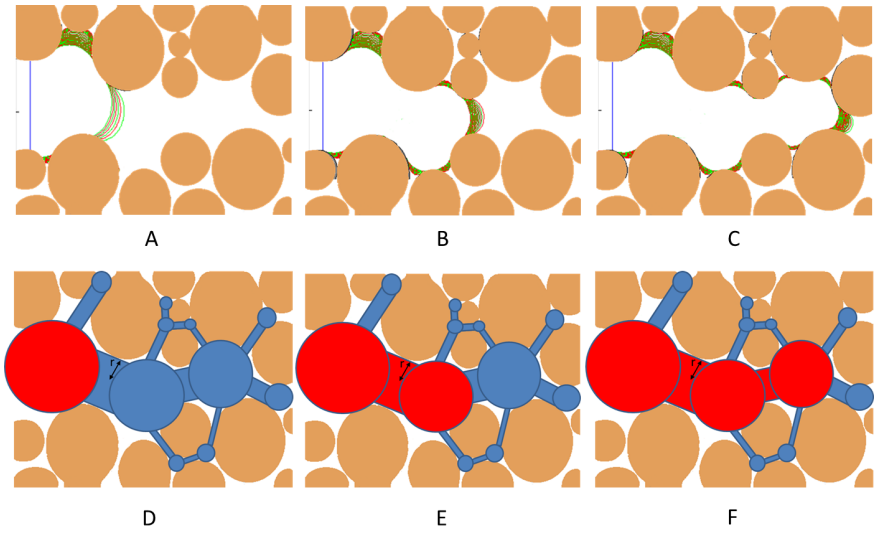

Figure 3.12: From A to C: Evolving interfaces during drainage, modelled using a level-set method (Prodanović and Bryant, 2006). From D to E: corresponding consecutive steps in a drainage process modelled with invasion percolation in a pore network model. Oil-filled network elements are shown in red, water-filled network elements in blue. The prevailing capillary pressure can be calculated at each step by applying the Young-Laplace equation to the radius of the throat invaded last. Pore space and interface images are adapted from (Prodanović, 2008).

in the element has an escape path to the outlet face. When the defending fluid in an element is not connected to the outlet face, it is considered to be trapped in that element. Advancing the interface at the point of least resistance as opposed to advancing all interfaces up to a certain threshold invasion pressure (mimicking constant pressure flow) is important when trapping is taken into account, because invasion percolation defines a unique sequence of events, which in turn determines whether or not a given portion of the defending fluid becomes trapped. Modelling the invasion as a discrete series of events is consistent with experimental observations of drainage and imbibition in porous media (Lenormand et al., 1983). The invasion percolation algorithm was pioneered by Wilkinson and Willemsen (1983).

Over the years, sophisticated invasion percolation based PNM approaches have been developed (Blunt et al., 2002; Øren et al., 1998; Patzek, 2001; Valvatne and Blunt, 2004). Many of these methods take into account the existence of water films in crevices. Usually, this is done by assigning triangular or square cross sections to the network elements, which retain wetting fluid in their corners (Figure 3.13). Often, the exact shape of the cross section is determined from the shape factor G of the part of the pore space which is represented by the element in the network:

$$G = \frac{A}{P^2} \tag{3.2}$$

with A a cross-sectional surface area and P the corresponding perimeter length of this cross-section (Patzek, 2001). The reasoning is that one does not need to include the exact pore space roughness or wall shape, but that the ratio of the cross-sectional surface areas occupied by film and by bulk fluid should be maintained in the model. This way, one can better approximate the water connectivity in the model, as well as include instabilities when swelling water films touch each other during imbibition (so-called snap-off events), an effect which has been shown important to non-wetting phase trapping (Iglauer et al., 2012; Lenormand et al., 1983). The pressure needed to overcome the capillary force in triangular and square prisms can be calculated semi-analytically (Ma et al., 1996; Mason and Morrow, 1991).

Intrinsic wettability of network elements is assigned a-priori, and is usually drawn from a user-defined range of values. Many network simulators use this value in the receding/advancing contact angle model by

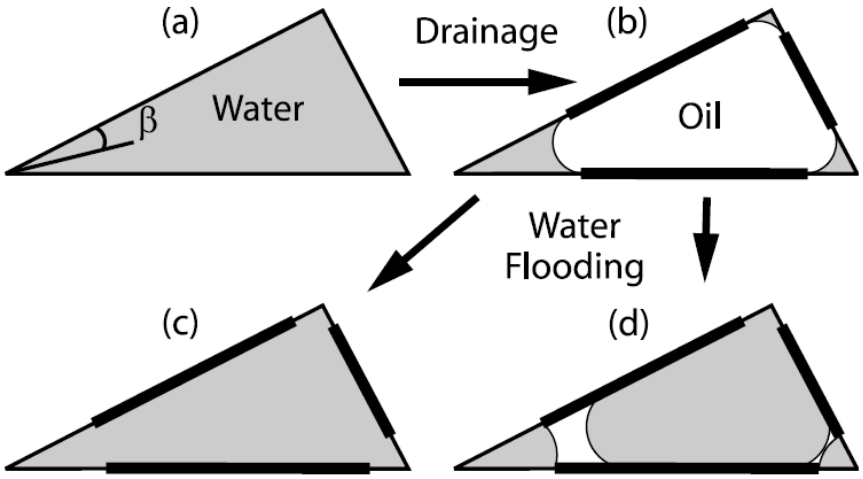

Figure 3.13: Different filling states of an initially water-wet pore with a triangular cross-section (Valvatne and Blunt, 2004), showing water films after drainage (b). After imbibition, oil films can arise if the wettability of the pore is altered by being in contact with oil (d). If this is not the case, oil films cannot exist (c). Figure from (Valvatne and Blunt, 2004).

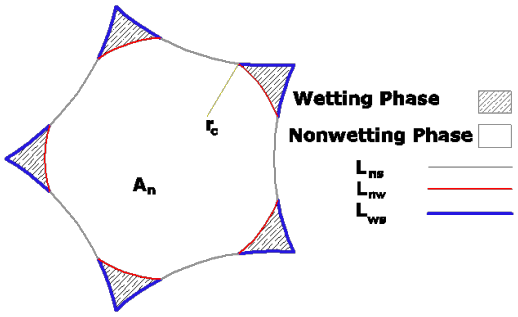

Figure 3.14: Regular hyperbolic polygonal pore cross-section used by Joekar-Niasar et al. (2010b), showing the wetting films after drainage. The curvature of the non-wetting/wetting interface is denoted by r_c. Figure reprinted with permission from Joekar-Niasar et al. (2010b)

Morrow (1975). There is currently no work flow which succeeds in assigning local wettability properties on a rigorous, experimental basis. The best approach available is usually to adapt the range of contact angles to reproduce global wettability measurements (e.g. Amott wettability). Network models are however very useful to study the dependence and sensitivity of flow parameters on that range, and on wettability modification after drainage. In many models, pores which have been in contact with oil can change their wettability from water to oil-wet, mimicking asphaltene precipitation (Figure 3.13).

More complex pore shapes than triangular and square prisms have been devised to better approximate the film flow behaviour. For example, Ryazanov et al. (2009) used n-cornered star shapes, based on shape factors and dimensionless hydraulic radii. Furthermore, in their model, corner film existence is based on a rigorous thermodynamic criterion (rather than on a geometric criterion as is usually the case). Joekar-Niasar et al. (2010b) investigate the effect of cross sectional shapes by comparing a set of regular and irregular hyperbolic polygons for the pore throats and prolate spheroids for the pore bodies (see Figure 3.14). They show that the choice of cross-sectional shapes has a significant effect on entry capillary pressure and saturation in crevices.

During the displacement process, saturations and permeabilities of both (or, in the case of three-phase flow, three (Piri and Blunt, 2005)) phases can be calculated in separate runs. To calculate the flow rates, network elements

which are completely filled with one fluid are considered to be completely closed off for flow of another fluid. Mass conservation is then imposed in every pore. If a conductivity is assigned to each pore-to-pore connection, this results in a linear system which can be solved for the pressures P_i in each pore i (Equations 3.3 and 3.4), thereby also yielding the flow rate through each pore.

$$\sum_j q_{ij} = 0, \text{ for every i} \tag{3.3}$$

$$q_{ij} = \frac{g_{ij}}{L_{ij}} (P_i - P_j) \tag{3.4}$$

with q_{ij} the flux from pore i to pore j, g_{ij} the conductivity from pore i to pore j, and L_{ij} the length of the connection from pore i to pore j.

The pore-to-pore conductivities are usually based on the inscribed sphere radius or on an equivalent hydraulic radius for the throat connecting the two pores, which can be related to its length and shape factor (Patzek, 2001). For example, for a cylindrical network element Poisseuille's law can be used. The permeability of the network can be calculated by finding the flow rates through the pores in a surface perpendicular to the flow injection. A similar calculation can yield the electrical current through the network, to calculate its electrical resistivity. This way, absolute and relative permeability curves can be calculated, as well as formation factors and resistivity index curves. These properties are relatively easily calculated (definitely when compared to the much more computationally intensive direct simulation methods), which is ultimately an effect of splitting up the pore space into simple elementary building blocks (pores and pore throats) of which the hydraulic or electric resistivity can be calculated (semi-) analytically. Note that the calculation of the fluid arrangement is decoupled from the computation of the flow rates of the separate fluids through the part of the pore space which they occupy. This comes down to neglecting the viscous pressure drop during the displacement, an assumption which is only approximately valid when capillary forces dominate over viscous forces (i.e. for low capillary numbers) (Valvatne and Blunt, 2004).

As stated in the introduction of this section, quasi-static network modeling is extremely useful to study how the wettability and pore characteristics influence the multi-phase flow behaviour in rocks. For example, Gharbi and Blunt (2012) used this approach to explain that optimal waterflood

efficiency during oil recovery in carbonates is seen in mixed-wet samples with poor connectivities. This behaviour was found to be different for sandstones, where network modeling explained why neutrally-wet conditions are optimal (Øren et al., 1998; Valvatne and Blunt, 2004). Quasi-static models can also help to investigate theoretical properties of two-phase flow behaviour, e.g. their application suggested that taking into account the specific interfacial area reduces capillary pressure hysteresis (Joekar-Niasar et al., 2010b) and showed that capillary trapping models should take the topology of the fluid phases into account (Joekar-Niasar et al., 2013).

Dynamic multi-phase flow modeling

Over the last few years, a number of models have been developed to take the previously mentioned viscous effects (e.g. viscous pressure drop) into account (Hammond and Unsal, 2012; Idowu and Blunt, 2010; Joekar-Niasar et al., 2010a; Nguyen et al., 2006). These models are usually called dynamic pore network models, and unlike static pore network models, they can be used to investigate flow rate-dependency of relative permeability curves (caused by for example displacement rate-induced inhibition of snap-off) or the remobilization of trapped fluid globules. For example, Hammond and Unsal (2012) investigated the effects of surfactant on the displacement pattern during water flooding in a dynamic network model, and found that the resulting decrease in interfacial tension reduces residual oil saturation by flushing out the large trapped oil clusters, whereas the wettability change simultaneously caused by the surfactant tends to act in the opposite direction. A comprehensive review on dynamic pore network models can be found in Joekar-Niasar and Hassanizadeh (2012).

Solute/colloid transport and reactive flow modeling

Network descriptions can also be used to simulate reactive transport in porous media. In many respects these methods can be seen as an extension on the multi-phase flow network simulations described before, where colloid or solute transport is taken into account. Similar to the multi-phase flow case, mass balance equations for all the chemical species are set up in each network element, taking into account advection, diffusion and

reaction (Raoof and Hassanizadeh, 2013). Note that this way, multi-phase, multi-component systems can be analysed. The models allow to calculate for example the mean effective reaction rate, velocity and dispersivity, as well as solute breakthrough curves. An interesting application is the simulation of dissolution or precipitation of the porous medium. After each time step, the medium's pore space is altered, changing for example porosity, permeability and specific surface area, and thereby influencing how the reaction will take place in the next time step. This way, the evolution of a porous medium can be followed through time. For example, Raoof et al. (2012) use reactive pore network modeling to explain why multiple regions with distinctly different porositities develop in cement when it is exposed to a CO_2-bearing solution, e.g. in wellbore cement during CO_2 sequestration. They show how these zones result in a decrease in average permeability of the cement in the direction parallel to the CO_2-gradient, suggesting a sealing behaviour, which was confirmed by experiments.

Reactive pore network models have been used in a variety of applications, to simulate for example dissolution of organic liquids (Held and Celia, 2001; Zhou et al., 2000), mineral precipitation and dissolution during CO_2 sequestration (Algive et al., 2012; Kang et al., 2009; Kim et al., 2011; Varloteaux et al., 2013), biomass growth (Dupin et al., 2001; Gharasoo et al., 2012; Kim and Fogler, 2000; Rosenzweig et al., 2013; Suchomel et al., 1998), solute dispersivity (Vasilyev et al., 2012), adsorption (Acharya et al., 2005; Köhne et al., 2011; Li et al., 2006; Raoof et al., 2010), particle capture and release (Ochi and Vernoux, 1999), asphalt precipitation (Sahimi et al., 2000) and deposition and dissolution in diatomite (Bhat and Kovscek, 2013).

Other applications

Further applications are drying in porous media (Freitas and Prat, 2000; Yiotis et al., 2006) and the simulation of viscous flows in granular materials where the forces exerted by the fluid on the grains (whether or not deformable) are of particular importance (Chareyre et al., 2012). PNM can also be used as static characterization tool, for example to investigate the influence of connectivity numbers or constriction ratio (the ratio of a pore's radius to one of its connecting throats' radius) (Tanino and Blunt, 2012; Vogel and Roth, 2001).

3.3.4 Comparison of network extraction methods

Given the multitude of network extraction algorithms available, it is important to compare the influence of the PNM extraction on the resulting simulations. While a number of such studies have been published (Al-Raoush et al., 2003; Dong et al., 2008; Dong and Blunt, 2009; Idowu et al., 2012, 2014; Ngom et al., 2011), the non-uniqueness of the network extraction and the possible dependence on the specifics of the investigated medium (e.g. consolidated or unconsolidated, granular or non-granular) make it difficult to predict a-priori which method is best suited to a given problem. Furthermore, comparison of the different methods is complicated by the fact that algorithms and data sets are often not publicly available to other researchers. Initiatives such as the Pore Scale Benchmark Project (porescalebenchmark.pbworks.com) or the Digital Rocks Portal (Prodanovic et al., 2015) attempt to alleviate these difficulties. In the following, some broad conclusions are drawn from the literature; however, in many cases there is no short or easy answer to the question which network extraction algorithm would be the best choice for a given problem.

Overview of comparative studies

An overview of comparative studies in the literature can be found in Table 3.2. We can discern between studies where the skeleton extraction is done using different methods, but where the geometrical characterization of pore bodies and throats is maintained (Bhattad et al., 2011; Dong et al., 2008; Idowu et al., 2012, 2014), and studies which compare completely different methods (Al-Raoush et al., 2003; Caubit et al., 2008). In other work, three methods are compared, two of which use the same skeleton, but a different geometric partitioning (Bondino et al., 2012; Idowu et al., 2013).

Wildenschild and Sheppard (2013) reported that network simulations are less sensitive to the initial pore space partitioning, and more to how the geometrical properties are assigned to each pore body and throat. This statement indeed coincides with the results from the network comparison articles: when geometrical characterization is maintained, the methods are reported to produce somewhat different absolute single-phase transport properties, but similar multi-phase properties (these properties are usually expressed relative to absolute properties, and trends were seen to be

reproduced by the different methods). Even though static network properties (e.g. number of pores) varied greatly between the methods, the spread on predicted transport results was reported to be reasonable, and a good agreement with experimental and grid simulated data was reported by Idowu et al. (2013). Some side notes are:

- The medial axis method may fail when there is a high level of noise (Dong et al., 2008; Idowu et al., 2012), as it tends to identify more isolated and dead-end pores.
- The maximal ball method seems to be good at capturing the larger pores, but is troubled by finding too many small throats which are not necessarily real hydraulic constrictions (Dong and Blunt, 2009).
- The grain-based method may give discrepancies in non-granular media (Dong et al., 2008). The networks tend to be worse at predicting electrical resistivity, as it depend more strongly on the small pores (Caubit et al., 2008; Dong et al., 2008; Dong and Blunt, 2009). The PNM methods have more problems to capture these, probably due to finite resolution of the input images.

Robustness of network extraction

A general conclusion from pore network comparison studies is that multi-phase properties are consistent, if the initial partitioning preserves the topology well (Idowu et al., 2012). This is thought to be a result of the balancing of several competing properties (Bhattad et al., 2011). For example, when a flow channel is divided into more pores, one would expect it to have a higher resistance to flow, as there are more resistors in series in that channel. However, this effect will be counterbalanced by the shorter length of each pore, resulting in a lower resistance per pore. Bhattad et al. (2011) conclude that the modeling algorithms are doing their job by counter-balancing variations in network structure by pore-geometry based modeling, therefore mitigating the non-uniqueness of PNM extraction. Caubit et al. (2008), who compare two completely different work flows performed on the same rocks, also find a relatively good match of the results. However, the difficulty in capturing the amount of microporosity and the presence of small-scale heterogeneity in the rock samples may cause differences in results, exacerbating the non-uniqueness problem of PNM methods.

Table 3.2: Overview of comparative studies on network extraction methods. The software in which the algorithms are implemented is reported between brackets.

Publication	Methods compared	Samples used for comparison
Al-Raoush et al. (2003)	– Medial axis (3DMA) – Modified Delaunay Tesselation (own)	– Computer-generated regular and random sphere packings
Dong et al. (2008)	– Medial axis: DOHT (Avizo) – Maximal ball (own) – Flow velocity-based (Lithicon) – Grain-recognition based (Lithicon)	– Computer-generated regular sphere packing – Computer-generated sandstone (process-based approach, Fontainebleau) – Micro-CTs of poorly sorted channel sandstone, vuggy replacement dolostone and Mt. Gambier limestone
Idowu et al. (2012) and Idowu et al. (2014)	– Medial axis: pore-based thinning (Fiji) – Medial axis: DOHT (Avizo) – Grain-recognition based (Lithicon)	– Micro-CT of Berea, Bentheim and Fontainebleau sandstone – Micro-CT of 4 sandstones from the Statfjord field
Bondino et al. (2012)	– Voronoi-based (origin unreported) – 2 watershed-transform based methods w/different throat lengths (origin unreported)	– Clashach sandstone
Dong and Blunt (2009)	– Maximal ball (own) – Grain-recognition based (Lithicon)	– Computer generated sphere packings and 1 computer-generated sandstone – 1 micro-CT of sandpack – 10 micro-CTs of sandstones – 2 micro-CTs of carbonates
Ngom et al. (2011)	– Medial axis (3DMA) – Delaunay tessellation (own)	– Micro-CTs of soil aggregates and soil management systems
Caubit et al. (2008)	– Medial axis (ANU) – Grain-recognition based (Lithicon)	– 6 artificial and outcrop rocks – 6 unconsolidated and consolidated reservoir rocks
Bhattad et al. (2011)	– Delauney-tesselation based (Thompson et al., 2005) – 3 different maximal-ball based (own)	– Micro-CT images of glass spheres packing, sand pack and cylinder pack
Idowu et al. (2013)	– Same as (Bondino et al., 2012)	– Same as (Bondino et al., 2012) (Clashach)

Despite these reports, using pore network models as a truly predictive tool (without the use of other experimental results as input) has shown to be difficult in a number of studies (Bondino et al., 2012; Sorbie and Skauge, 2011). The former report large variations in water and oil relative permeability when using different extraction methods on the same sandstone, including even counter-intuitive trends for some methods. Idowu et al. (2014) investigated these counter-intuitive trends, and show that they are a consequence of how volume is assigned to pore throats, providing a good example of the sensitivity of network models to the applied geometric characterization. Bondino et al. (2012) noted that applying two different networks on the same image has much larger consequences than applying the same algorithm on two different images, while using different simulators had a much milder effect than using different network extractions. They concluded that the prediction of multi-phase flow properties using digital rock physics is currently in general not possible. They state that pore network modeling, which is the most established digital rock physics technique, can produce results which are difficult to interpret due to the high number of parameters involved in the work flow, that the representation of the rock is still a weak point, and that a strict characterization of wettability is currently not possible in these methods (wettability is considered as a sort of tuning parameter, see also 4.3.1). Sorbie and Skauge (2011) also note the high number of parameters in any network modeling work flow, and state that true predictive modeling is therefore currently impossible with this approach. However, they propose a number of very useful applications of network models, including explanation, interpolation and extrapolation of experimentally observed two- and three-phase flow trends and properties. Network models are also very useful if they are anchored to some experimental data which is relatively easy to obtain, such as porosity, permeability and capillary pressure curves (Ravlo and Arland, 2014). It is to be noted that Caubit et al. (2008) reported that when these parameters are well matched, the relative permeability curves (which are significantly more difficult to measure) could be considered as reliable.

3.3.5 Multi-scale pore network modeling

As mentioned before, one of the most severe problems in pore-scale modeling of geological materials is dealing with the multiple spatial scales inherent to the pore structure of many natural rocks. This means that often,

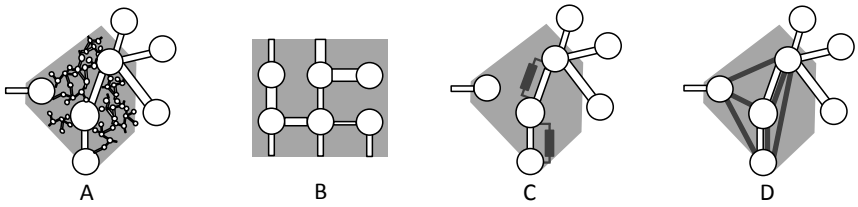

Figure 3.15: Model A takes individual micro-pores into account, e.g. Jiang et al. (2013). In model B a cubic-lattice based network is embedded in a microporous matrix (Bekri et al., 2005), model C is image-based but only takes into account microporosity in parallel to throats in the macro-pore PNM (Bauer et al., 2012), and model D takes microporosity both serial as parallel microporosity into account in an upscaled fashion (chapter 4 of this thesis). Microporous regions are depicted in dark gray.

not all pores are captured in one single imaging experiment, due to finite resolution and sample volume of these experiments. However, the presence of multiple pore scales in rocks can severely influence a rock's transport properties, an effect which is notably important in carbonates and tight-gas sandstones (Mehmani and Prodanović, 2014).

Even if one finds a way to merge data from multiple experiments, taking all relevant pore sizes into account in simulations remains hard, as the necessary resolution of such a model is dictated by the smallest pores of importance, while the minimal size of the model is dictated by the representative elementary volume of the medium. The discrepancy between these scales, which often amounts to several orders of magnitude, poses computational problems. PNMs are currently probably the most suitable technique for multi-scale simulations of this kind, because these models describe individual network elements with infinite resolution (i.e. pores of indiscriminate size can be described without loss of detail) and are very computationally efficient. In this section, we will give an overview of PNMs specially developed to deal with multi-scale simulations. These models, presented schematically in Figure 3.15, are often referred to as dual pore network models (DPNMs). In this thesis, micro-pores are defined ad-hoc as pores smaller than the resolution of the imaging experiment performed to characterize the larger pores (macro-pores) in the sample under investigation. Typically, in geological applications using micro-CT, micro-pores are pores with sizes smaller than approximately 1 to a few μm.

Jiang et al. (2013) proposed a work flow to join PNMs extracted from images at different resolutions. A PNM of indiscriminate volume representative of the microporosity is stochastically created based on a small network extracted from high-resolution imaging data (Jiang et al., 2011), thereby circumventing the resolution-size trade-off of the experimental technique used to image the micro-pore space. A PNM of the macro-pores is then merged with the microporosity network by characterizing the cross-scale connection structure between the two networks (Figure 3.15A). Theoretically, networks of more than two scales can be fused using this methodology. However, a disadvantage of this method is that the number of network elements can quickly become computationally prohibitive since each individual micro-pore is taken into account separately. A similar approach is followed by Mehmani and Prodanović (2014) and Prodanović et al. (2014). They use a less strict approach to generate the microporosity, but investigate the influence microporosity has on transport properties in general terms. Therefore, they pay attention to the location of microporosity with respect to the macro-pore space, by taking into account information on its genesis. They distinguish a clear difference between the behaviour of a system where microporosity acts in series to the macro-pores (intergranular or pore-filling microporosity) and a system where it acts in parallel (intragranular or dissolution microporosity).

Acknowledging the computational difficulties of treating microporosity as a network of individual micro-pores, researchers at IFPEN (France) have developed an approach where the macro-pores are treated with a PNM approach, while micro-pores are treated as blocks of continuous porous medium, characterized by for example a porosity, a permeability and a capillary pressure curve (Moctezuma et al., 2003; Bekri et al., 2005; Youssef et al., 2008; Bauer et al., 2011, 2012). Bekri et al. (2005) built a DPNM by representing the large pores as a cubic-lattice based PNM, which they supplement with conductivities due to microporosity in the matrix (Figure 3.15B). The microporosity is considered to be a continuum porous medium, acting in parallel to the cubic PNM. They allow large pores to be drained through micro-pores when a breakthrough capillary pressure is exceeded. Bauer et al. (2011, 2012) extracted image-based networks of the macroporosity from micro-CT images of carbonate samples and added cubic blocks of microporosity in parallel to a user-defined percentage of macro-throats in this PNM (Figure 3.15C). Although their method is largely image-based, micro- and macroporosity

were considered to conduct only in parallel. Contact surface areas of macro-pores with microporosity, necessary to calculate microporous conductivities, were based on the total contact surface area measured over the entire micro-CT scan.

In order to allow a general arrangement of microporosity in the network model, i.e. to let it act both in parallel as in series to the macro-pore network, a new network model which uses a similar approach of treating the microporosity as a continuous porous medium has been developed during the course of this PhD (Figure 3.15D). This model is explained in the following chapters (4 to 6).

4

Multi-scale network extraction and drainage simulations

4.1 Introduction

As stated in the previous chapter, pore scale modeling of transport properties in geological materials has gathered large momentum over the last few years, yet modeling multi-phase flow in samples with wide pore size distributions has remained an important outstanding issue. Broad pore size distributions, stretching from the scale of nanometres to tens of micrometers and sometimes even to millimetres, are for example found in many types of carbonates and clay-rich sandstones, which are media of considerable economic and scientific importance (e.g. hydrocarbon extraction and CO_2 sequestration in carbonate reservoirs or in tight gas sandstones). Most classical empirical relations (e.g. Archie's law and the Brooks-Corey parametrization of relative permeability, see chapter 2) fail in these cases, increasing the importance of simulations.

When a rock with a broad pore size distribution is investigated with a 3D imaging technique such as micro-CT scanning, it is often not possible to visualize pores of all scales present in one experiment due to the

resolution/sample size trade-off. The resolution/size trade-off, both in imaging and modeling, makes that pore network models are likely the most suited models to be extended towards multi-scale applications, due to their computational efficiency and their infinite resolution. Previous efforts towards this goal are reviewed in chapter 3 (section 3.3.5).

In this chapter, we treat a novel multi-scale pore network model in which the microporosity is treated as a continuous porous medium and is allowed to act both in parallel as in series to the macropore network. This is important, as serial microporosity produces very different effects than parallel microporosity, and its impact is harder to estimate a-priori (Mehmani and Prodanović, 2014), yet such approaches were not treated before in the literature. In this modeling work flow, the connectivity added by microporosity is derived from micro-CT information by segmenting the regions with unresolved porosity, as explained in section 4.2.1. A model for the conductivity of microporous connections was developed based on local data measured on the micro-CT image. Our dual pore network modeling (DPNM) method allows macropores to be drained if they are connected to microporosity, based on percolation theory. Section 4.2.2 treats the DPNM extraction in detail, while the drainage simulations performed on these DPNM are discussed section in 4.2.3. In section 4.2.4 we describe how the networks which were used for validation (an artificial network based on a sphere packing and networks extracted from Estaillades and Savonnières limestone) were set up, and the results from this validation are shown in section 4.3. This section also contains a first, exploratory sensitivity study on the dependence of the capillary pressure and relative permeability curves of the investigated carbonates on the microporosity's properties (this sensitivity is further explored for more rock samples in chapter 6). Finally, section 4.4 contains conclusions and offers an outlook on future research.

This chapter is based on a publication in Advances in Water Resources: Bultreys et al. (2015c), *"Multi-scale, micro-computed tomography-based pore network models to simulate drainage in heterogeneous rocks"*. Furthermore, it incorporates elements (simulations on the Savonnières limestone and a sensitivity study on the microporosity properties) from a peer-reviewed technical paper which was presented at the International Symposium of the Society of Core Analysts (SCA): Bultreys et al. (2015b), *"A multi-scale, image-based pore network modeling approach to simulate two-phase flow in heterogeneous rocks"*.

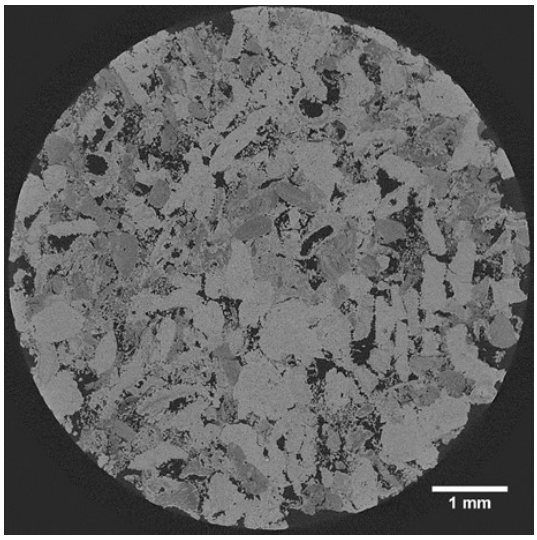

Figure 4.1: Reconstructed slice from a micro-CT scan of Estaillades limestone, with a voxel size of 3.1 μm. The sample's diameter is 7 mm. Dark grey regions contain sub-resolution microporosity, while light grey grains are solid calcite.

4.2 Materials and methods

4.2.1 Imaging microporosity

In a micro-CT experiment, the partial volume effect will ensure that, in a mono-mineralic rock, regions with pores smaller than the scan's resolution will show up less bright than solid regions. This is due to the lower effective material density in the former regions. An example of such a micro-CT scan can be found in Figure 4.1. In a multi-mineralic rock, differentiating a micro-CT image of the dry rock and a micro-CT image of the rock vacuum-imbibed with a strongly attenuating contrast liquid can allow to visualize microporous regions (Boone et al., 2014; Knackstedt et al., 2006; Long et al., 2013). Therefore, micro-CT scans can be used to investigate the connectivity of macropores to microporous zones, even if the resolution is insufficient to investigate the geometry or connectivity of individual micropores.

4.2.2 Multi-scale network extraction

Work flow

To build a pore network model which incorporates porosity at multiple spatial scales that cannot be captured in one single imaging experiment, we start with performing a three-phase segmentation of a micro-CT-based pore space image (either a dry micro-CT scan for a mono-mineralic rock or a difference image for a multi-mineralic rock). During this step, pore voxels, solid voxels and microporous voxels (voxels which contain pores below the image resolution) are distinguished. The second step in our method is the extraction of a classical PNM from the macropores (i.e. the space made up of pore voxels in the segmented image). Next, the microporous voxels are clustered into connected regions. By deciding for each macropore to which microporous regions it is connected, we assess the connectivity between macropores caused by microporosity, assuming the microporosity percolates (otherwise it can be considered as solid for transport calculation purposes). Other experimental methods can be used to validate this assumption (e.g. SEM or FIB-SEM imaging). This connectivity is then included in the network and taken into account in the drainage simulations. The different steps in the network extraction are treated in more detail in the remainder of this section.

Macropore network extraction

To extract the network representing the macroporosity, a maximal ball network extraction method was used (Delerue et al., 1999; Silin et al., 2003; Silin and Patzek, 2006; Monga et al., 2007). We employ the algorithm developed at Imperial College (Dong and Blunt, 2009). The method is based on the identification of so called maximal balls (MB). These are the largest inscribed spheres centred on each pore voxel in the image that just touch the boundary of the pore space. By using this concept, constrictions and dilations in the pore space are found and classified as pores and throats in the PNM, respectively. For more details regarding the network generation, we refer to chapter 3 (section 3.3.2) and to the aforementioned publication. During the process, each pore voxel in the image is assigned to a specific pore or throat in the corresponding PNM. The PNM extracted from the macroporosity with the MB method will henceforth be referred to as the macropore network.

Microporous connections

To supplement the macropore network with the appropriate connectivity provided by the microporosity, connected clusters of microporous voxels are first identified. In our method, this is performed in Morpho+ (Brabant et al., 2011), an image analysis package originally developed at UGCT and currently commercially distributed under the name Octopus Analysis (Inside Matters, Belgium). Subsequently, we calculate for each node in the macropore network to which microporous clusters it borders in the segmented micro-CT image. Two nodes touching the same microporous cluster are assumed to be connected through the microporosity. A special link is added between any two such pores. This link, henceforth called micro-link, will be used in the network simulation software to represent the transport through the microporous phase between the two nodes it connects. Note that micro-links are added completely independent of the two nodes already being connected by a throat in the macropore network. Therefore, microporous connectivity acting both parallel and serial to macroporosity is automatically taken into account. The extracted multi-scale networks consist of three types of network elements: nodes (pores), links (throats) and micro-links.

Contact surface areas

Since the conductivity of the microporous connection between two macropores depends on the local contact surface area between each of these nodes and the microporous phase (aside from its dependence on the bulk properties of the microporous zones), contact surface areas with microporous regions are measured for each pore individually. However, simple voxel face counting is known to systematically overestimate the surface area of an object due to voxelization effects (Wildenschild and Sheppard, 2013). Instead, a surface triangulation can be performed. In order to do so, we use a marching cubes (MC) algorithm (Brabant et al., 2011). The MC algorithm estimates surface areas of discrete binary images by assigning a surface area weight to local 2x2x2 configurations of voxels, and then summing these contributions to obtain the surface area of the digitized object (Lindblad, 2005). The MC algorithm is not the most accurate triangulation algorithm (for an investigation on the error produced by this method see Dalla et al. (2002), for more advanced methods see Lang et al. (2001) and Ohser and Mücklich (2000)), however,

its simple implementation and its efficiency make it attractive for our purposes. Standard surface generation algorithms have the obstacle that they are intended for use with two-phase images (Wildenschild and Sheppard, 2013). To calculate the contact surface area between a particular pore A and a particular microporous cluster B, the MC algorithm can be considered to run on a 3-phase image, consisting of voxels belonging to pore A, to cluster B, or neither to pore A or cluster B. A similar problem is encountered in surface area calculations in micro-CT experiments where two-phase flow in a rock is visualized. The solution offered by Porter et al. (2010) is to use linear combinations of the areas of isosurfaces in the image. This approach is applied to every pore-microporous cluster contact, running the algorithm only in the relevant volume around the pore (the pore's bounding box extended by one voxel in all dimensions). The algorithm was prepared for shared memory parallelization with OpenMP for increased computational efficiency.

4.2.3 Drainage simulations

MicroPoreFlow Solver

To calculate capillary pressure curves, (relative) permeabilities, formation factors and resistivity index curves during drainage, the network simulator developed by the group of Prof. Martin Blunt at Imperial College (Blunt et al. (2002); Valvatne and Blunt (2004), freely available online) was extended to work with the multi-scale networks developed in this work. We have named the adaptation of the simulator code microPoreFlow. To simulate the displacement of the wetting fluid by the non-wetting fluid, an invasion percolation algorithm is performed (see chapter 3, section 3.3.3). As stated there, the flow rate is assumed to be infinitesimal during the displacement calculation, rendering the viscous pressure drop over the network negligible. The model assumes that pores and throats have circular, triangular or square cross sections, depending on their shape factor. Non-circular pores and throats retain wetting films in the corners during drainage, strongly increasing the wetting-phase connectivity in the network. At any point during the displacement, the saturation of the macro-network can be calculated by using the prevailing capillary pressure to find the interface curvatures in every network element. Flow rates can be solved by imposing a potential drop across the length of the network and assuming mass (or electrical charge) conservation in every pore. As

shown in chapter 3, this translates into a linear system which can be solved for the pressure in each pore (Valvatne and Blunt, 2004) (equations 3.3 and 3.4).

To include the micro-links in the transport calculations on a multi-scale network, we consider the microporosity as a continuous porous medium. This means that the petrophysical properties of the microporosity have to be provided as input, as opposed to being calculated directly as in the approaches of Jiang et al. (2013); Roth et al. (2012) and Prodanović et al. (2014). The advantage, however, is that individual micropores do not have to be taken into account, greatly reducing the computational demands and allowing to include more rock heterogeneity in the simulations. We use the constitutive equations and provide the necessary petrophysical properties for the microporosity as input to the network solver:

- Porosity (ϕ)
- Permeability (K)
- Formation factor (F)
- Break-through saturation (S_b)
- Capillary pressure curve (P_c-curve)
- Relative permeability curves ($K_{r,w}$ and $K_{r,nw}$)
- Saturation exponent (n)

At each capillary pressure for which the transport properties are calculated, the saturation of the microporous volume present in the micro-CT scan is calculated. Furthermore, we allow the invasion of a pore with non-wetting fluid if it is connected by a micro-link to a pore filled with non-wetting fluid, using a breakthrough-pressure approach. These topics are discussed in more detail in the following two sections. To find the flow properties of the DPNM, the hydraulic or electrical conductances (the coefficients g_{ij} in equation 3.4) of all microporous connections are calculated. These calculations are described in the last part of this section. Once the micro-link properties mentioned in the previous paragraph have been determined, the inclusion of micro-links into the network solver framework is conceptually straightforward. When a micro-link is parallel to a macropore throat, their conductances are summed.

Saturation

To find the saturation of the multi-scale network, the saturations of the macroporous and the microporous volumes are calculated separately. The calculation of the macroporous saturation is described in Valvatne and Blunt (2004). The volume of the microporous phase is calculated during the network extraction, and its porosity is supplied as input. In further research, we will attempt to derive this porosity estimate directly from micro-CT grey values (Knackstedt et al., 2006; Long et al., 2013). These local values could also be used to estimate local microporous permeability and electrical conductivity input values. The saturation of the microporous volume in the micro-CT scan is calculated from the capillary pressure curve for the microporosity which is supplied as input to the network solver. Such an input capillary pressure curve can be estimated from a representative model of the microporosity. Alternatively, for some cases, an estimation can be made based on a mercury intrusion capillary pressure curve for the whole rock, as we show in section 4.2.4. However, the latter is not in general a trivial or well-justified process.

Microporous breakthrough pressure

In a classical PNM simulation, (groups of) macropores which are disconnected from the non-wetting phase injection face in the macronetwork will remain filled with wetting phase at all times during a drainage simulation. However, when these pores are connected to the injection face through microporous connectivity, they could be filled with the non-wetting phase after the microporous connection of interest is invaded first. Following the ideas in Bekri et al. (2005), we assume a breakthrough capillary pressure for this to happen. Invasion of macropores through microporosity is only of importance when invasion through neighbouring macroporous throats is impossible, as we assume the microporosity to have smaller radii and therefore higher intrusion pressures than the throats in the PNM.

In Bekri et al. (2005), one breakthrough capillary pressure is assumed for all macropores in a lattice-based network to be invaded. In reality, not all macropores are expected to drain instantaneously and simultaneously when a certain capillary pressure is exceeded. Instead, we try to mimic the behaviour of a network model where all individual micropores are

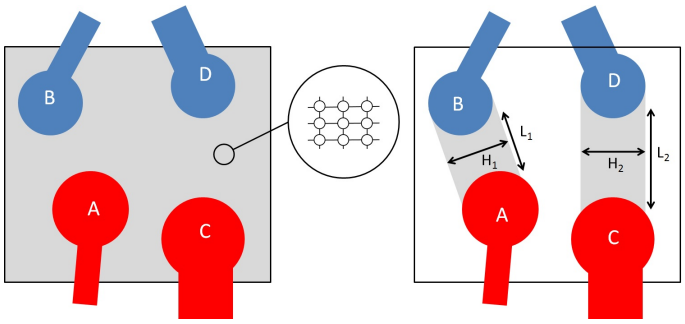

Figure 4.2: Illustration of the non-wetting phase breakthrough model for the microporosity. Pore A and C are filled with non-wetting phase, while pores B and D are filled with wetting phase. All pores touch a microporous matrix (in grey). This matrix (left figure with inset) is considered as a cubic network of micropores to find the dependence of the breakthrough capillary pressure of each micro-link on its length (L_1 and L_2) and approximate width (H_1 and H_2), based on percolation theory (uttermost right figure).

explicitly taken into account in an invasion-percolation scheme, without actually having to do so. Consider the situation in Figure 4.2. One can assume the microporosity to be represented by a cubic-lattice-based network, connected to macropores A, B, C and D at the macropore borders. The drainage of this microporosity network will start at the micropores which neighbour macropores A and C. If we consider the parts of the network in the zones labelled 1 and 2 as separate networks, it is clear that the non-wetting phase will, statistically speaking, percolate through zone 1 and reach pore B before (meaning at lower non-wetting phase saturation) it percolates through zone 2 to reach pore D. If the characteristic length of the micronetwork is sufficiently small compared to the domain size of the microporous region, we can assume that percolation theory is valid. For invasion-percolation in a network which fills a cubic domain with side length L, the non-wetting phase saturation S_b at which non-wetting phase percolation first occurs depends on the finite size of the micronetwork (Blunt et al., 1992; Wilkinson and Willemsen, 1983):

$$S_b \sim L^{-\beta/\nu} \tag{4.1}$$

where critical exponents β and ν equal 0.41 and 0.88 in 3D, respectively (Sahimi, 2011).

However, when looking at for example the zone between pores A and B in Figure 4.2, it should intuitively be clear that during drainage, the microporosity's non-wetting phase saturation at breakthrough should decline with H_1 (at constant L_1) and rise with L_1 (at constant H_1). We therefore approximate the geometry of the microporosity domain represented by each micro-link as a cuboid with height H and square base with side length L (Figure 4.2 illustrates this in 2 dimensions). For each micro-link, the height is set equal to the length of the connection and the square base is set to match the average of the micro-link's two pore-micropore contact surface areas. The breakthrough non-wetting saturation in invasion-percolation corresponds to the density of the spanning cluster in random percolation (the probability that a pore belongs to the percolating cluster right at the percolation threshold) (Marrink and Knackstedt, 1999). To calculate this density at breakthrough in the cuboid geometry, characterized by the aspect ratio H/L, we can discern two cases. For $H < L$, the following relation, found by finite-size scaling arguments, holds (in three dimensions, up to first order) (Monetti and Albano, 1991):

$$S_b \cdot L^{\beta/\nu} \sim \left(\frac{L}{H}\right)^2 \tag{4.2}$$

Marrink and Knackstedt (1999, 2000) specifically investigated the case where $H > L$, and found the following scaling behaviour:

$$S_b^{1/\beta} \cdot H^{1/\nu} \sim \sqrt{\ln\left(\frac{L}{H}\right)} \tag{4.3}$$

with β equal to 0.41. To make S_b scale like equation 4.1, 4.2 and 4.3 in their respective domains of applicability, we use the following formulas to calculate an S_b-value for each micro-link:

$$S_b = c \cdot L^{-\beta/\nu} \cdot \left(\frac{L}{H}\right)^2, L \leq H \tag{4.4}$$

$$S_b = c \cdot H^{-\beta/\nu} \cdot \left(1 + \sqrt{\ln\frac{L}{H}}\right)^{\beta}, L \geq H \tag{4.5}$$

In equation 4.5, the sum between the brackets makes sure that the formula gives the same results as equations 4.3 and 4.4 when $H = L$. In these formula, c is a calibration parameter to be determined a-priori. Our simulations therefore require the input of the breakthrough saturation of a micro-link with a specified geometry, from which c can be calculated using equation 4.4 or 4.5. Although this value is not at all trivial to assess, it can in principle be calculated if one has a representative network for the microporosity. At the beginning of the simulation, the breakthrough non-wetting saturation is calculated for each micro-link. Subsequently, the matching breakthrough capillary pressure is found using the input capillary pressure curve of the microporosity. Note that in this approach, we neglect the correlations and the heterogeneity present in the microporosity network.

Micro-link conductivity

To calculate the conductivity associated with a micro-link, we assume Darcy's law extended to two-phase flow for the hydraulic case and Archie's law for the electrical case, stated in the introduction (equations 2.10 and 2.14-2.15, respectively) and reformulated here for the case at hand in equations 4.6, 4.7 and 4.8:

$$q_p(S_w) = -\frac{1}{\rho_{h,p}(S_w)} \cdot \frac{(P_o - P_i)}{L} \tag{4.6}$$

$$\rho_{h,p}(P_c) = \frac{\mu}{K \cdot K_{r,p}(S_w)} \tag{4.7}$$

$$\rho_e(P_c) = R_w \cdot F_{micro} \cdot S_w^{-n} \tag{4.8}$$

with p the phase of interest (w or nw), q_p the flux of phase p, $\rho_{h,p}(S_w)$ the hydraulic resistivity of the porous medium to phase p at wetting phase saturation S_w, K the medium's permeability, $K_{r,p}$ the relative permeability for phase p, P_o the outflow pressure, P_i the inflow pressure, L the distance between the in- and outflow surfaces, $_p$ the viscosity of phase p, $\rho_e(S_w)$ the electrical resistivity of the rock at saturation S_w, R_w the resistivity of the wetting fluid, F_{micro} the formation factor and n the saturation exponent.

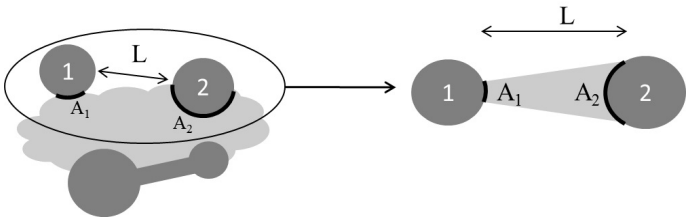

Figure 4.3: Schematic depiction of the truncated cone model. A microporous cluster is depicted in light grey, while neighbouring macroporous network elements are depicted in dark grey. L is the distance between the macropores labelled 1 and 2, A_1 and A_2 are the contact surface areas of the respective pores with the microporous cluster. The conductivity from pore 1 to pore 2 through the microporous cluster is modelled as the conductivity through a truncated cone with length L and bases having surface areas A_1 and A_2, connecting the pores in question.

To calculate the hydraulic conductivity of a connection, the permeability and the relative permeability curve of the microporous phase are supplied as input. To compute the electrical conductivity, the formation factor and the saturation exponent of the microporous phase are given as input. The geometric shape of the microporous connection between the two macropores in question then still has to be determined. Following the same approach at the roots of pore network modeling itself, an idealized shape is assumed. Since a 3D shape which connects two different contact surface areas is needed, we treat microporous connections as truncated cones in a first approach (see Figure 4.3). The micro-link's conductivity g_{ij} can then be calculated as:

$$g_{ij} = \frac{\sqrt{A_i \cdot A_j}}{\rho_{micro}(S_w) \cdot L_{ij}} \tag{4.9}$$

with A_1 and A_2 the contact surface areas of the microporous cluster to pores i and j, and ρ_{micro} the resistivity of the microporous phase, either hydraulic as defined in equation 4.7 or electrical as defined in equation 4.8. The truncated cone shape is preferred over a cuboid with the average of the two contact surface areas as base, as one can expect it to have better noise characteristics when one of the two contact surface areas is very small.

It is not trivial to assess the microporosity's input parameters (permeability, relative permeability, formation factor and saturation

exponent) needed to calculate the conductivities in equation 4.9, but in principle one could calculate estimated values if one can generate a representative (network) model of the microporosity. In some cases, a crude guess can be obtained by using empirical relations to describe the microporosity, e.g. Kozeny-Carman and Brooks-Corey relations for (relative) permeability. It should be noted that using the truncated cone shape, we are neglecting the tortuosity of the connection between the macropores (but not the tortuosity at the scale of individual micropores) and we are not taking into account any geometric details about the bulk of the microporous cluster, which can lead to erroneous local conductivities. These issues should be addressed in future work.

Micro-link cut-off length

One extra parameter was found necessary to obtain realistic results: a cut-off length for the micro-links. All micro-links longer than this length are removed. The need for the cut-off can be understood by taking into account the simplifications made when modeling the flow through the microporosity as flow through truncated cones made of continuous porous medium. The length of these connections is underestimated by taking the distance between pores as length of the truncated cone instead of using the length of the tortuous path through the microporous regions between the pores. Furthermore, we are not taking into account properties of the bulk of the microporous region (e.g. constrictions or dilations of the regions, along the tortuous path). The larger the distance between two pores, the larger the error in the path length will typically be, and the larger the probability that there are constrictions along the way. Neglecting the bulk properties can therefore result in a much larger volume available for flow when one counts the total volume of the truncated cones in the model, compared to the real volume of the microporous phase present in the sample (we repeat here that the calculation of saturations is based on the latter volume). The effect on the transport properties is a severe overestimation of both electrical and hydraulic conductivity through the microporosity if all micro-links are retained. Most long micro-links will only provide connectivity parallel to already existing paths formed by chains of shorter micro-links. Therefore, a cut-off length should be chosen long enough so that global pore-to-pore connectivity is not altered, but short enough so that the conductivity through microporosity is not severely overestimated. The former length scale is characteristic of the

separation between pores in contact with the same microporous region. Further research should point out if more intricate conductivity models, or alternatively, the use of a skeleton of the microporous phase, can remove the need for the cut-off length parameter. When removing micro-links which are longer than the cut-off length, the real volume of the microporous phase that was present in the micro-CT scan, which is used to calculate the network's saturation, is not altered.

4.2.4 Networks used for validation

Artificial network model

As a first and theoretical test of the newly developed model, a validation based on an artificial network is presented here. The novel DPNM are unavoidably a less detailed representation of porous media than DPNM in which individual micropores are taken into account. The artificial network test indicates that our method is nevertheless able to capture much of the behaviour of the latter models, justifying the loss of detail in our simulations for the sake of computational efficiency. In particular, the capability to include serial microporous connectivity is investigated, an important feature which to our knowledge has not been incorporated into unstructured DPNM carrying upscaled properties before.

Two-scale pore networks based on an artificial sphere packing were generated by Mehmani and Prodanović (2014) to study the effect of interparticular and intraparticular microporosity on transport properties. A network in which 50 percent of the macropores were clogged and filled with micropores (representing e.g. clay-filled macropores) was made available by the authors. The microporosity was generated by downscaling the original network five times. The radii of the packed spheres were set to 100 μm and the complete network was then scaled accordingly, for numerical reasons. For more details regarding the network generation we refer to the aforementioned publication. This network was transformed into a DPNM with upscaled micro-links by removing the micropores, clustering the clogged macropores into connected regions and reconnecting any two remaining macropores which border the same clay regions (Figure 4.4). For each connection, the pore-micropore contact surface areas were determined as the cross-sectional areas of the macro-pores which, before clogging, linked the two connected pores to

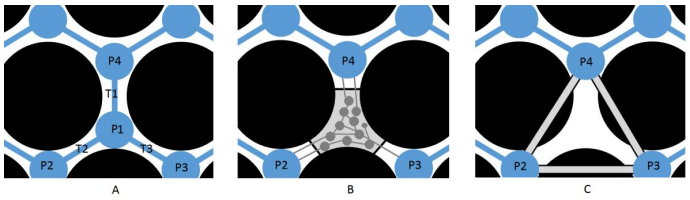

Figure 4.4: In A, a schematic representation of the original sphere packing-based network is drawn in blue, the sphere packing is black. In B, pore P1 (in light grey) has been clogged and replaced by micropores (dark grey). The equivalent network with micro-links (light grey) is shown in C.

Microporous property	Value
ϕ_{micro}	0.38
K_{micro} (mD)	533
F_{micro}	6.5
S_b at $L = H = 400$ µm	0.16

Table 4.1: Input properties for the microporosity in the artificial network simulation.

their neighbours in the clay zone they both border. For example, in Figure 4.4 the contact surface areas of the micro-link connecting pores P2 and P3 would be determined from the cross-sectional areas of throats T2 and T3. The lengths of the connections were found as the shortest path length between the two connected pores, measured along the graph represented by the clogged macropores and throats in the neighbouring "clay" region. For example, in Figure 4.4, the length of the micro-link connecting $P2$ and $P3$ is calculated as the sum of the lengths of throat $T2$ and $T3$.

To calculate the DPNM's transport properties, the micro-links' petrophysical properties were determined from single-scale PNM simulations on the parent network of the microporosity (i.e. the original network without clogging, but downscaled five times). These properties can be found in Table 4.1. The non-wetting phase saturation at which breakthrough occurs in the microporosity was set at 0.16 for a cubic microporosity domain with a side length of 400 µm, based on the $K_{r,nw}$-curve of the parent network with this length. The medium was assumed to be strongly water-wet, with a contact angle of 0°.

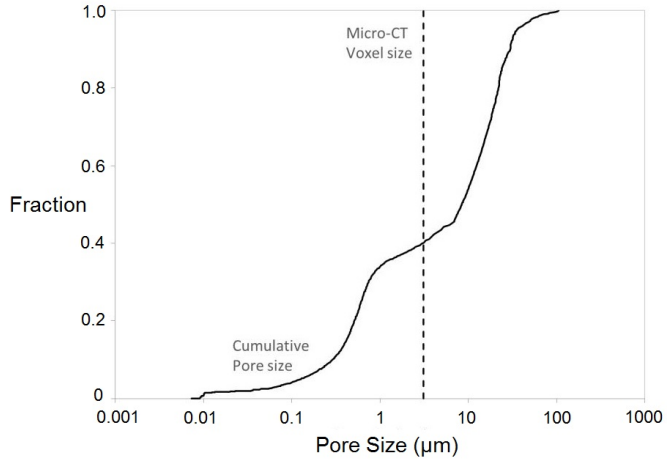

Figure 4.5: The cumulative pore size distribution of Estaillades limestone as measured with MIP. The voxel size of the micro-CT scan (3.1 μm) used to extract the network from lies in between the two modi of the pore size distribution.

Estaillades limestone

To illustrate the work flow and to perform a further validation of the network extraction and simulation method, a micro-CT scan of Estaillades limestone was performed. The two-phase flow properties of Estaillades, a French limestone, have been extensively studied and the rock has often been used as a test case for pore scale modeling of carbonates with a bimodal pore size distribution (Bauer et al., 2012; Dautriat et al., 2009; Gharbi and Blunt, 2012; Han et al., 2007; Moctezuma-Berthier et al., 2002; Prodanović et al., 2014; Tanino and Blunt, 2012; Youssef et al., 2008). This mono-mineralic, calcitic rock is composed of debris of fossils called "red algae" and calcic shells embedded into a microsparitic cement (Le Guen et al., 2007). It contains two types of pores: intergranular macropores and intra-granular micropores, found the red algae grains (Youssef et al., 2008). The pore size distribution obtained from a Mercury Intrusion Porosimetry (MIP) experiment can be found in Figure 4.5.

An Estaillades sample with a diameter of 7 mm was scanned with UGCT's HECTOR micro-CT scanner (developed in collaboration with XRE bvba). HECTOR's detailed set-up can be found in Masschaele et al. (2013). In this study, Estaillades was scanned using an accelerating voltage of 100 kV and a target power of 10W. 2800 projections were made, for each

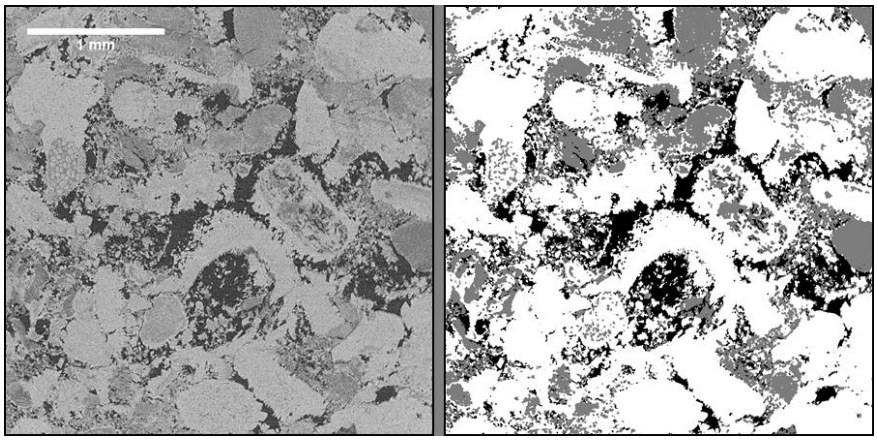

Figure 4.6: The image on the left shows a slice from a cropped image obtained from the full micro-CT scan of Estaillades (1000x1000x1001 voxels). The corresponding slice from the segmentation of this image which was used to extract the DPNMs from can be seen on the right. Pore space voxels in this image are black, microporous voxels are grey and solid voxels are white.

projection the detector was illuminated for 2 seconds. The reconstructed voxel size was 3.1 μm. A reconstructed slice of the scan is shown in Figure 1. The three-phase segmentation was performed by extracting the pore space and the solid grains using hysteresis thresholding (in combination with a bilateral noise filter) in Octopus Analysis (Brabant et al., 2011). The partial volume effect which causes the intermediate grey value of the microporous regions in the images, also occurs at the interface of solid grains and macropores. Therefore, the three phase segmentation appears to contain a lot of pore lining microporosity. To alleviate this artefact, a closing operation was performed on the microporous phase using VSG's Avizo software. This removed most of the pore lining microporosity, without removing an excessive amount of the real microporous regions. Figure 4.6 shows the segmented image next to its corresponding slice in the original CT scan.

A DPNM was extracted from a 1000x1000x1001 voxels large subset of the image (Figure 4.7). The image contains 32 % microporous voxels and 11.8 % pore voxels. Network characteristics are shown in Table 4.2 and Table 4.3. Clustering the microporous phase into connected regions showed that most of the microporosity in the image is contained in one sample spanning cluster (Figure 4.7, top right). This is problematic, as it can lead to an

Macropore PNM property	Pores	Throats
Amount	92398	207216
Average radius (μm)	6.3	2.7
Average length (μm)	-	9.6
Maximum length (μm)	-	115.8
Average coordination number	4.5	-
Maximum coordination number	206	-

Table 4.2: Properties of the classical PNM extracted from Estaillades (before rescaling the pore and throat radii)

	PNM, Classical	DPNM, 30 μm	DPNM, 70 μm	DPNM, 90 μm
Number of micro-links	0	34764	408920	772462
Average micro-link coordination number	-	0.75	8.9	16.7
Average total coordination number	4.5	5.2	13.3	21.2

Table 4.3: Dual pore network properties, for the DPNM different cut-off lengths are indicated.

excessive amount of micro-links. Therefore, this is an additional reason for the need of a micro-link cut-off length (note that this problem is alleviated when working with smaller images). The largest cut-off distance imposed for the network extraction here was 93 micron (or 30 voxels), resulting in approx. 800 000 micro-links (Figure 4.7, bottom). In the future, alternative ways of reducing the number of micro-links will be explored, for example by splitting microporous clusters using a watershed algorithm. However, since many of the microporous regions in Estaillades are very irregularly shaped, this approach was not readily executed in this work.

Petrophysical input parameters for the microporosity in the Estaillades sample were assessed based on literature (Bauer et al., 2012) and are summarized in Table 4.4. Note that these input variables are hard to assess and are only rough estimates. However, the aim of this work is to test whether a dual scale network of the proposed form is able to capture general trends of transport properties seen in real carbonates. Future work will focus on better determination of these parameters. The capillary pressure curve of the microporosity was assessed based on an MIP

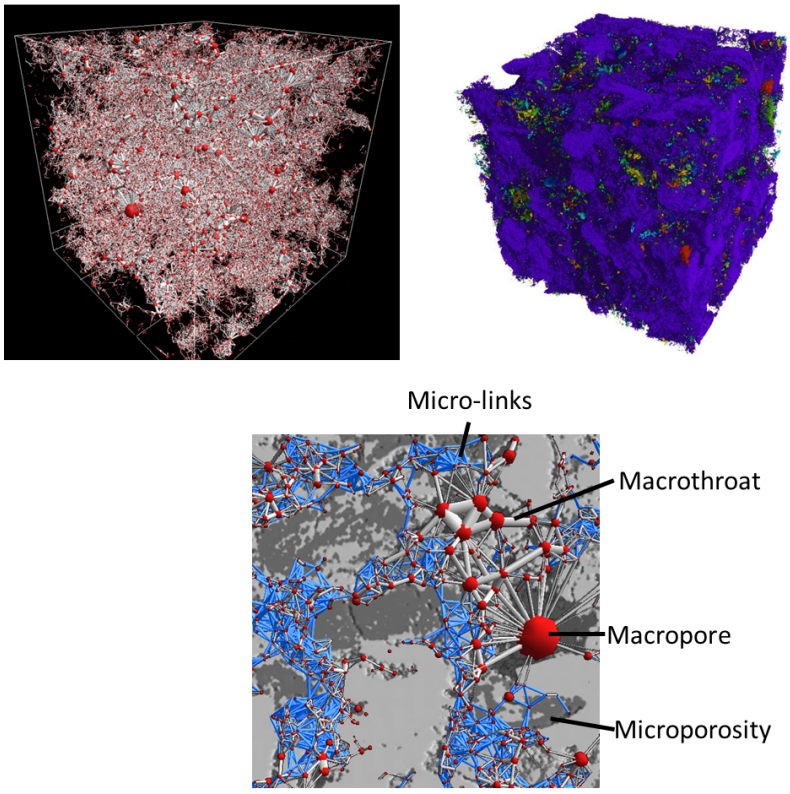

Figure 4.7: A rendering of the macronetwork extracted from Estaillades (top left), a rendered 3D image of the microporous connected clusters in this sample (top right) and a close-up of a part of the resulting DPNM on top of a 3D render of the segmented micro-CT scan (bottom). In the middle image, each cluster is shown in a different colour. The purple cluster is seen to span almost the entire sample (cube side length in A and B is 3.1 mm). In the right image, microporous regions and micro-links are rendered in blue, and the cut-off distance for micro-links was 93 μm.

Microporous property	Value
ϕ_{micro}	0.36
K_{micro} (mD)	8
F_{micro}	7.72
n_{micro}	2
S_b at $L = H = 300$ µm	0.3

Table 4.4: Input properties for the microporosity in the Estaillades network simulation.

experiment. A cut-off pressure was selected, defining the part of the curve which is attributed to microporosity in the system. This pressure can therefore be related to the resolution of the micro-CT scan used to extract the network. A cut-off pressure which translates to a pore diameter of 4.4 µm was selected based on a visual inspection of the MIP curve (corresponding to the onset of the influence of microporosity on the curve). This means that pores with a diameter of up to 1.4 times the voxel size of the micro-CT scan are considered as microporosity. The part of the MIP curve above the pressure cut-off was rescaled to the full saturation range of zero to one, and this curve was used as P_c-curve of the microporosity. Note that this approach of finding the capillary pressure curve would produce errors for carbonates in which many large pores can only be invaded through microporous regions due to the ink-bottle effect in the MIP measurement. In that case, a network model of the microporosity can be built using high resolution imaging techniques such as FIB-SEM, which can then yield a capillary pressure curve through network simulations. The microporosity's relative permeability curves were assessed by PNM simulations on a regular cubic network with similar pore size distribution (see Figure 4.5) as the microporosity. Both macro- and micropores were assumed to be strongly water-wet, with a contact angle of 0 °.

Savonnières limestone

Further validation was performed on Savonnières limestone. This is a layered oolithic limestone belonging to the Oolithe Vacuolaire, a stratigraphical unit which also includes Brauvilliers stone (among other varieties) (Derluyn et al., 2013). Its pore structure contains 4 types of porosity: inter-granular and intra-oolithic microporosity, and

inter-granular and micro-connected macroporosity (hollow ooliths) (Roels et al., 2001). The hollow ooliths are only connected to the other macro-pores by microporosity in the oolith-shells. Depending on local variations, the permeability ranges from 115 mD to more than 2000 mD (based on TinyPerm mini-permeameter measurements), and porosity ranges from 22 % to 41 %.

A Savonnières sample of 6 mm diameter was imaged with UGCT's HECTOR micro-CT scanner (Masschaele et al., 2013) at an accelerating voltage of 120 kV and a target power of 10 W. 2400 projections (illumination time 1s) were acquired, resulting in a scan with 3.8 µm voxel size. A 1000x1000x1000 subsection was segmented with a gradient watershed thresholding algorithm in Avizo (FEI, France), after performing an anisotropic diffusion filter. The gradient watershed algorithm is a three-phase segmentation method, resulting in less spurious edges in the microporous phase than the repeated application of a two-phase segmentation algorithm (Schlüter et al., 2014). Similarly to the Estaillades case, remaining noise and edges in the microporous phase were subsequently removed by applying a majority filter in Avizo. A dual pore network model was then extracted with the methodology outlined in section 4.2.2 (Figure 4.8).

The input capillary pressure curve for the microporosity was based on the pore size distribution for Savonnières, which was determined from SEM imaging by Roels et al. (2001). The input K_r-curve and BCP were assessed by simulations on an artificial, simple-cubic network with this throat size distribution. The other microporosity input properties (Table 4.5) were based on Roels et al. (2001). Like in the Estaillades case, the microporosity properties used here are crude estimates, which require further work to be improved. Nevertheless, the simulations allow to investigate whether the method yields generally realistic results, and are useful to investigate the dependence of the two-phase flow properties on the microporosity.

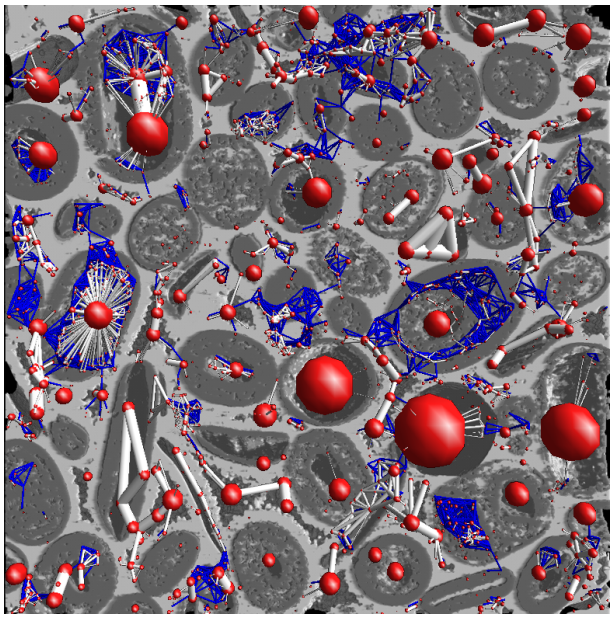

Figure 4.8: Illustration of DPNM extracted from Savonnières limestone. Microporous zones are in dark grey, micro-links in blue.

Microporous property	Value
ϕ_{micro}	0.35
K_{micro} (mD)	4.1
F_{micro}	8.2
n_{micro}	2
S_b at $L = H$ = 100 µm	0.3

Table 4.5: Input properties for the microporosity in the Savonnières network simulation.

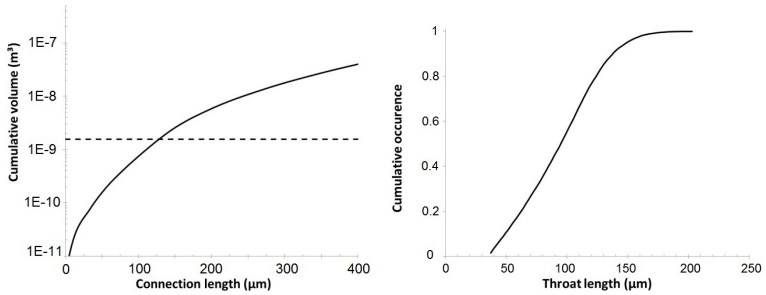

Figure 4.9: The cumulative volume of the micro-links (calculated as the volume of truncated cones) plotted versus the micro-link length is shown on the left. The dashed line shows the total volume of the clogged macropores. The figure on the right shows the cumulative throat length distribution of the original sphere-packing based macropore network, before any pores were clogged.

4.3 Results and discussion

4.3.1 Artificial network model

After converting the network with individual micropores to a DPNM with micro-links and supplying the microporosity properties, drainage simulations were performed with microPoreFlow. We first address the issue of the cut-off length for the micro-links. Figure 4.9 (left) shows the volume of the truncated cones which represent the micro-links, compared to the real microporous phase volume in the model. Removing micro-links longer than 130 µm leads to a correct microporosity volume in the truncated cones compared to the volume of clogged macropores. To describe the characteristic length of the separation between pores in contact with the same microporous region, we look at the throat length in the original macropore network without clogging in a first approach (see Figure 4.9, right). We will show results for cut-off lengths between 130 µm, which corresponds to the correct microporous volume, and 400 µm, for which any two macropores touching the same clogged pore are reconnected, as the maximum distance between any two pores in the original network is 200 µm (see figure Figure 4.9, right).

It is to be noted that after clogging 50 % of the macropores, the macropore network does not percolate any more. This means that transport where macro- and microporosity conduct in series is of crucial importance. Single phase flow properties of the investigated DPNM are summarized in

Network		K (mD)	F	#network elements
DPNM, cut-off:	130 μm	238	103.6	9662
	225 μm	531	22.2	13307
	400 μm	1069	7.6	29004
PNM individ. micropores		245	49.0	363749
Microporous parent PNM		553	6.5	-

Table 4.6: Single phase transport properties for the artificial DPNM with micro-connections and with individual micropores, as well as the properties of the parent network for the microporosity in the latter case.

Network		Relative error K (%)	Relative error F (%)
DPNM, cut-off:	130 μm	2.86	111.43
	225 μm	116.73	54.69
	400 μm	336.33	84.49

Table 4.7: Relative error of single phase transport properties for the artificial DPNM with micro-connections, compared to networks with individual micropores as ground truth.

Table 4.6. A cut-off of 400 μm is seen to severely overestimate conductivities. A cut-off of 130 μm results in an overestimated formation factor, while it assesses the permeability rather well. This is caused by the microporosity parent network's high permeability. The deviations in table 4.6 are caused by the oversimplified truncated cone model, the assumption of perfect coupling between pores and micropores, and the assumption that microporous regions are homogeneous enough to be replaced by micro-links with a single set of petrophysical parameters. Overall, the single phase results are within the same order of magnitude as the fully resolved network model. The relative errors of the DPNM approach compared to the fully resolved network model are shown in Table 4.7.

Figure 4.10 shows the capillary pressure curves calculated on the networks with micro-links and on the network with individual micropores. The capillary pressure curve calculated with cut-off length 400 μm is not reported, as it falls on top of the curve with cut-off 225 μm. This means that the global connectivity of the DPNM does not significantly increase any more once the cut-off length is larger than 225 μm, indicating that this would be a good choice for the cut-off. While some of the detailed P_c-behaviour is not captured by the DPNM with micro-links, the curves

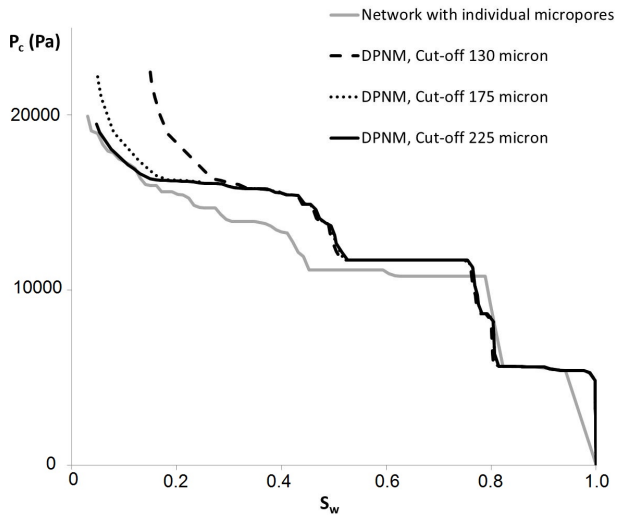

Figure 4.10: Capillary pressure curves of the calculated with our dual PNM are in good agreement with those calculated on the original artificial network with individual micropores (Mehmani and Prodanović, 2014), if the applied cut-off length for micro-links is 225 μm or larger.

show good agreement.

Relative permeability curves and resistivity index curves calculated on the networks with cut-offs 130 μm, 225 μm and 400 μm are shown in Figure 4.11. The network with a 225 μm cut-off is seen to reproduce the resistivity index very well. Qualitatively, the resistivity index curve and the wetting phase relative permeability agree very well, however, the oil permeability is underestimated. This may be related to the fact that micro- and macroporosity can be only weakly coupled in the network with individual micropores, while we assume them to be perfectly coupled. Another possible cause is the fact that the difference between the length scales of the networks is only a factor 5. This means that domains of microporosity are not appropriately described as a continuous porous medium with a single set of petrophysical properties, since some microporous regions may only contain a few micropores. Both these effects result in an overestimation of the microporous conductivity. A crude correction is provided by lowering the permeability of the microporous phase to 172 mD, so that the permeability of the DPNM with cut-off 225 μm matches the permeability of the network with individual

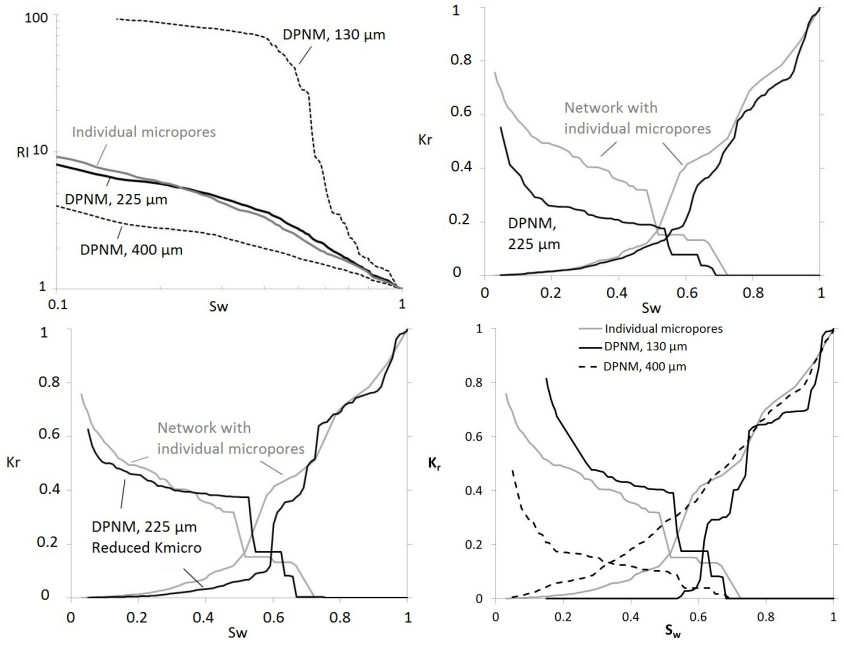

Figure 4.11: The resistivity index curves (top left) calculated with our method show good agreement with the original artificial network with individual micropores, if the cut-off length is around 225 µm. Too small cut-off lengths result in overestimation of the RI, while too large cut-offs result in an underestimation. Relative permeability curves calculated with our method (cut-off length 225 µm.) show fair agreement (top right), although the non-wetting relative permeability is underestimated. Reducing the input permeability of the microporous phase so the single phase permeability matches the network with individual micropores counters this effect (bottom left). Results at other cut-off lengths are shown at bottom right.

micropores. The relative permeability results for this case are shown in Figure 4.11, and provide a much better qualitative agreement for the non-wetting phase. Further research should point out how to appropriately calculate the permeability and relative permeability of the microporous phase, taking into account coupling effects. Note that relative permeability results of the original network differ somewhat from Mehmani and Prodanović (2014) due to different assumptions regarding film flow and volume in throats. By using the approach of micro-links with upscaled properties, the amount of network elements in these simulations was reduced by almost a factor of 30 (Table 4.6), while it was still possible to obtain good results from a network which does not percolate when the microporosity is not taken into account. Furthermore, increasing the difference in length scale between macro-and microporosity (a factor of 5 in the simulations presented here) would have no influence on the amount of network elements in our method. This is important, as the length scales can differ by several orders of magnitude in real rocks, quickly making it impossible to take individual micropores into account.

4.3.2 Estaillades limestone

After the extraction of the dual scale network from the 1000x1000x1001 micro-CT image of Estaillades limestone, drainage simulations were performed with microPoreFlow. Table 4.8 summarizes results for the single phase properties compared to experimental values obtained from literature (Bauer et al., 2012) and from our own measurements (porosity based on an MIP experiment and permeability on the average of 15 measurements with a TinyPerm II portable probe permeameter on the 5x5x5 cm block from which the 7 mm diameter sample was cored). Relative errors of the predicted transport properties can be found in Table 4.9. Properties of the classical PNM can be found in Table 4.2. The classical PNM clearly underestimates the permeability, overestimates the formation factor, and only represents about half of the pore space present in the rock. To correct for the permeability underestimation and the error in the P_c-curve (see further), all pore and throat radii were multiplied by 1.25 and the porosity was increased to 13.9 percent. This modification was also done on the macronetworks of the DPNM extracted with different cut-off lengths for the microporous connections (Table 4.3), because in this validation work we want to reduce the error in the macronetwork as much as possible in order to facilitate the assessment of the influence of

Transport property	ϕ (%)	k (mD)	F
Experimental[1]	25	273 ± 16	24 ± 0.24
Experimental[2]	23	260 ± 60	-
Classical PNM	11.5	114	58
Classical PNM, radii x 1.25	13.9	281	36.8
DPNM, cut-off length 30 μm	25.5	281	35.5
DPNM, cut-off length 65 μm	25.5	289	19.3
DPNM, cut-off length 70 μm	25.5	292	16.8
DPNM, cut-off length 90 μm	25.5	303	9.7

Table 4.8: Single phase transport properties of the classical PNM and the DPNM extracted from Estaillades, compared with experimental values ([1] from Bauer et al. (2012) and [2] from our own measurements).

Transport property	Relative error k (%)	Relative error F (%)
Classical PNM	58.2	141.7
Classical PNM, radii x 1.25	2.9	53.3
DPNM, cut-off length 30 μm	2.9	47.9
DPNM, cut-off length 65 μm	5.9	19.6
DPNM, cut-off length 70 μm	7.0	30.0
DPNM, cut-off length 90 μm	11.0	59.6

Table 4.9: Relative errors of single phase transport predictions, calculated with the classical PNM and the DPNM extracted from Estaillades, compared to experimental values (from Bauer et al. (2012)).

the micro-links. Anchoring the network on experimental data which is relatively easy to obtain can improve the reliability of multi-phase flow predictions (Sorbie and Skauge, 2011). By using DPNM with an appropriate cut-off length, it is possible to get a better estimate of the formation factor after adjusting the pore and throat radii to match the permeability. Note that the microporosity in Estaillades has a negligible effect on the permeability.

Figure 4.12 shows the capillary pressure curve results for the classical PNM, the classical PNM with added passive microporosity (meaning it remains water-filled at all times and has zero conductivity) and the DPNM (with cut-off length 65 μm). The DPNM qualitatively agree with the experimental curve, whereas the classical PNM do not show the same qualitative trend as the experimental curve because the microporosity

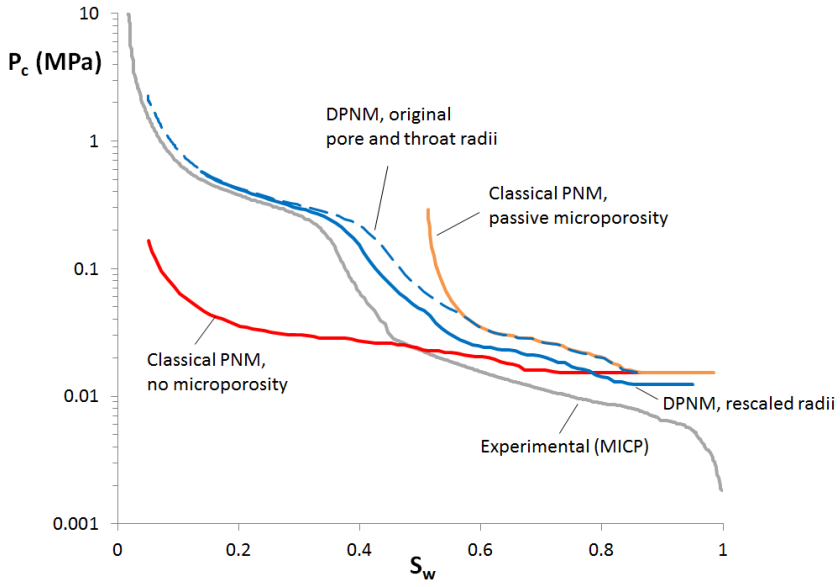

Figure 4.12: P_c-curves calculated with DPNM show better agreement with the experimental data (from an MIP experiment, pressures were rescaled to represent an oil-water system) than those calculated with classical PNM. Increasing all pore and throat radii by 25 percent improves the capillary pressure prediction. The DPNM used here had a microporous cut-off length of 65 μm.

which makes up approximately 50% of the total pore space is either ignored or not invaded. For clarity, only the results of the DPNM with a cut-off length of 65 µm are shown, because the cut-off length had a negligible effect on the P_c-curve simulation for this particular sample.

Figure 4.13A shows drainage relative permeability calculated with the classical network and with the DPNM, compared to experimental measurements from Ott et al. (2015). The curves obtained with DPNM are in qualitative agreement with experimental results (Moctezuma-Berthier et al., 2002; Ott et al., 2015). When plotting the curves calculated with a classical PNM which includes passive (non-conducting) microporosity (Figure 4.13B), it becomes clear that this is mostly due to the effect the microporosity has on the saturation rather than on its effect on the conductivity of both phases through the medium. Since in Estaillades, the microporosity remains water filled until the macroporosity is almost completely desaturated, there is a tendency to compress both the wetting

and non-wetting relative permeabilities to the right of the graph as compared to the classical PNM simulations. This has the effect of shifting the cross-over point to higher saturations, as well as increasing both relative permeabilities at this saturation, corresponding well with the results of Prodanović et al. (2014). We note further that adding conductive micro-links has a rather small effect on the curves, with the exception of removing the non-physical situation of having a relative permeability of 1 at a non-zero saturation. The small influence can be explained by the existence of a well-connected macro-pore network in Estaillades, meaning that macro- and micro-networks act more or less in parallel (Bauer et al., 2012; Han et al., 2007; Prodanović et al., 2014). Differences between the simulations and the experimental results in Figure 4.13A (as well as those in (Moctezuma-Berthier et al., 2002)) are expected to arise due to sample heterogeneity and scale dependence of the experiments (our simulations are performed on a network of 3.1 x 3.1 x 3.1 mm, while the plotted experimental measurements were performed on cylinders of 3.8 cm diameter and 5 cm length).

Figure 4.14A shows the resistivity index (RI) curves calculated with the network models compared to the experimental results obtained by Han et al. (2007). Estaillades is known to show non-classical electrical behaviour, characterized by a double-bending RI curve. The bending-up is caused by wetting phase in the macropore network becoming disconnected during the invasion. When the wetting phase saturation is lowered further, the curve bends down again when the microporosity starts to drain and the wetting films in the intergranular pores become the dominant pathway for the electrical current (Fleury, 2002; Han et al., 2007). This behaviour, inherent to rocks with dual scale pores which act mainly as parallel networks, is clearly not captured in the classical PNM. The DPNM are able to reproduce double-bending and give good qualitative results, but these results depend on the cut-off length for the microporous connections (Figure 4.14D). When the cut-off length becomes larger and the number of microporous connections increases, the microporosity dominates the transport sooner in the drainage process, thereby reducing (or even eliminating) the bending-up of the RI curve. This suggests that the electrical transport through long-range micro-links is overestimated.

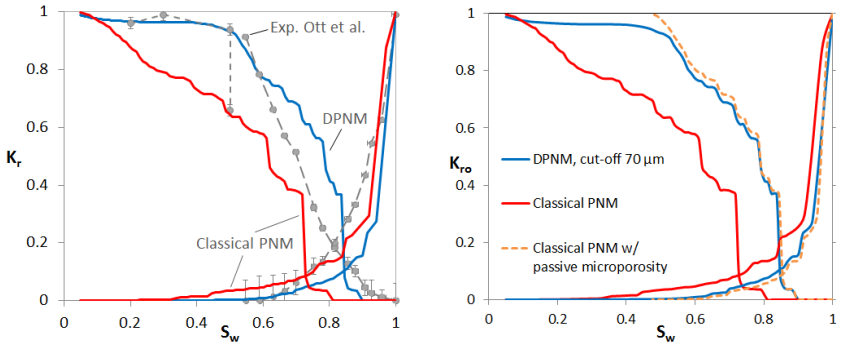

Figure 4.13: Estaillades drainage relative permeability calculated with classical PNM and DPNM. For the relative permeability, only results from a DPNM with microporous cut-off length of 70 µm are shown, as the cut-off length had very little influence on these curves. Experimental results are brine-decane relative permeability measurements from (Ott et al., 2015) (steady-state measurement SS1 and unsteady-state measurements with the porous plate method.

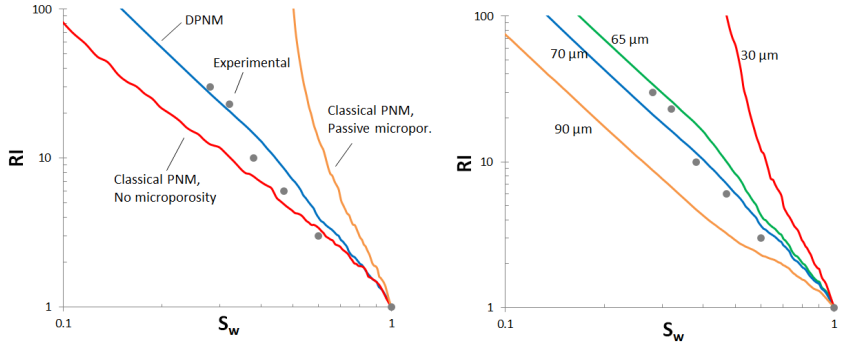

Figure 4.14: Drainage resistivity index curves calculated with DPNM with different micro-links show double bending behaviour characteristic to certain carbonates where micro-and macroporosity act mostly as parallel conduction paths. Figure A shows results calculated with a DPNM with micro-link cut-off length 67.5 µm, compared to results from classical experiments and experimental results estimated from the graph published in Han et al. (2007). Figure B shows the influence of the cut-off length on the DPNM results.

4.3.3 Savonnières limestone

Single phase transport predictions calculated with the classical PNM and the DPNM extracted from Savonnières can be found in Table 4.10. In this Table, permeability calculations are compared to experimental values performed with a minipermeameter (TinyPerm II). The predictions are in the same order of magnitude as the experimental results, but it should be noted that the heterogeneity of Savonnières can be expected to significantly influence this comparison.

In the investigated Savonnières sample, isolated macropores in hollow ooliths make up 30 % of the macropore space. As these pores are only connected through microporosity, they are not taken into account when calculating transport properties with conventional, single-scale PNM. The P_c-curve simulated with the DPNM therefore shows better qualitative agreement to the experimental P_c-curve (scaled from an MIP experiment on a different Savonnières sample) than the single-scale PNM (Figure 4.15). The hollow ooliths start to drain at $S_w = 0.61$, when nearly all inter-granular macropores have been filled with non-wetting phase. The K_r-curve (Figure 4.15) is in qualitative agreement with measurements on Brauvilliers limestone (Moctezuma-Berthier et al., 2002), which has a similar lithology than Savonnières but is tighter. The saturations at the cross-over K_r and at the onset of non-wetting phase flow are in better agreement with the DPNM than with the PNM, mostly due to the inclusion of the wetting saturation in microporosity. In the multi-scale network, the inter-granular macropores dominate the $K_{r,nw}$ behaviour ($K_{r,nw} = 0.83$ at $S_w = 0.61$). At $S_w < 0,61$, $K_{r,nw}$ bends down due to the lower importance of the microporosity/hollow ooliths pore system for the conductivity. In the RI-simulation (Figure 4.15), the bending-up behaviour at $S_w = 0.3$ in the single-scale simulation contradicts the classification of Brauvilliers as a texture III rock characterized by a double bending RI (Han et al., 2007). In the DPNM simulation however, the curve weakly bends up until reaching the macropores' percolation threshold ($S_w = 0.61$), and bends down when the pressure is further increased because the wetting films in the macropores become the dominant electrical pathways when the microporosity drains. The weakness of the bending-up may be an artefact of the selection of the length cut-off parameter. The simulations on Savonnières illustrate how our DPNM can be used when microporosity provides both parallel and serial connectivity to macroporosity.

Transport property	k (mD)	Rel. error k (%)	F
Experimental	903	-	-
Classical PNM	244	73.0	85.7
DPNM	268	70.3	13.5

Table 4.10: Single phase transport predictions, calculated with the classical PNM and the DPNM extracted from Savonnières, compared to experimental values for the permeability (experimental formation factor values were not available). It should however be noted that the heterogeneity of Savonnières can be expected to significantly influence this comparison.

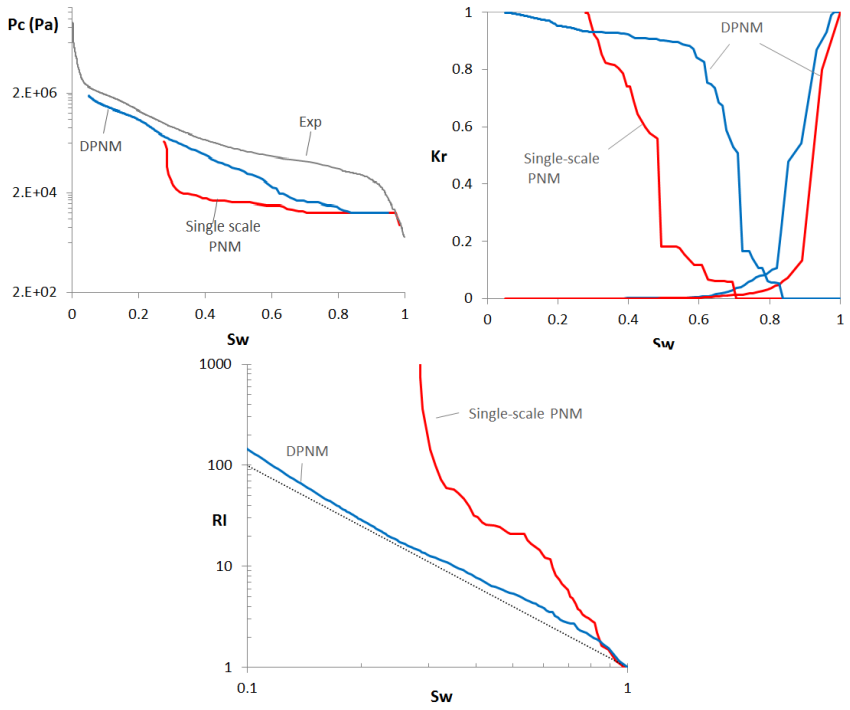

Figure 4.15: P_c-curve (top left), K_r-curves (top right) and RI-curve (bottom) for drainage of Savonnières, calculated with a single scale maximal ball based PNM and with the proposed DPNM. The experimental P_c-curve is obtained from an MIP measurement on a different, likely more porous Savonnières sample.

4.3.4 Sensitivity of P_c and K_r on microporosity properties

Influence of the microporosity's permeability

The microporosity's permeability was varied over 4 orders of magnitude for the Estaillades and the Savonnières networks (Figure 4.16), while keeping all other parameters constant. With increasing microporous permeability, the non-wetting phase relative permeability decreases and the wetting phase relative permeability increases. This is due to the increasing importance of fluid flow through microporosity, which is only invaded by the non-wetting phase at $S_w < 0.5$ for Estaillades and $S_w < 0.6$ for Savonnières. The behaviour fits well with the observation that non-wetting phase mobility is enhanced and wetting phase mobility decreased by the existence of high-permeability pathways (Bekri et al., 2002), in this case caused by the macroporous network.

Influence of the microporosity's breakthrough saturation

To test the influence of the input breakthrough saturation (and equivalently BCP) on a network where a significant amount of micro-links conduct in series to macro-throats, this parameter (defined for a 100x100x100 μm geometry) was varied for simulations with the Savonnières network (the influence of this parameter is expected to be negligible for Estaillades, as nearly all macro-pores are drained before the microporosity is invaded). Drainage results for the different breakthrough saturations (Figure 4.17) show identical P_c-curves and K_r-curves for S_w down to 0.6, as macro-pores cannot be invaded through micro-links as long as the capillary pressure is below the microporosity's intrusion capillary pressure. The well-connected macro-pores are thus drained first. Below S_w = 0.6, P_c and K_r curves show minor differences, related to the fact that disconnected macro-porosity (mostly hollow ooliths) start to fill at different capillary pressures for different microporous breakthrough saturations. The results show that this parameter is of particularly minor importance to the K_r-calculations in this network, if the pore sizes of the microporosity and the macroporosity do no significantly overlap.

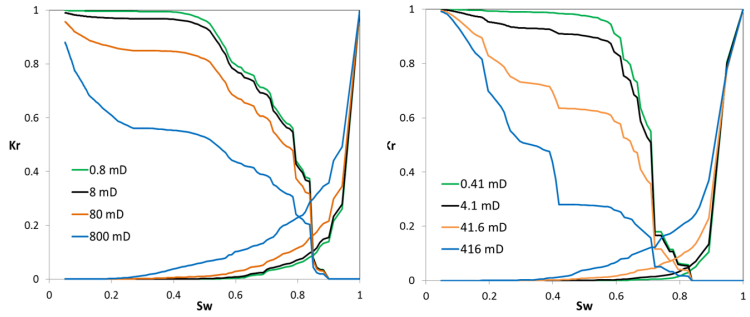

Figure 4.16: Relative permeability results from drainage simulations on the multi-scale Estaillades (left) and the Savonnières (right) networks, with different input properties for the microporosity's permeability.

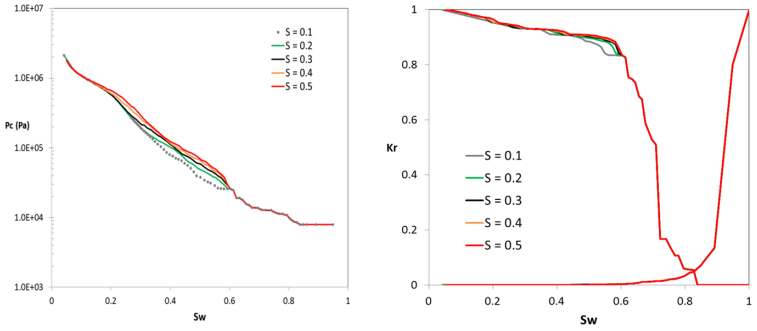

Figure 4.17: Cumulative pore size distributions and multi-scale drainage capillary pressure curves for different input microporosity P_c-curves in Savonnières.

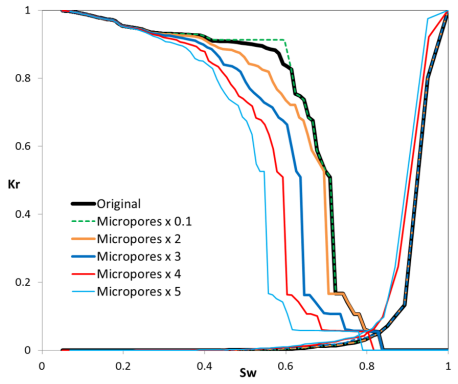

Figure 4.18: Drainage relative permeability curves calculated on the multi-scale Savonnières network with different microporosity P_c-curves as input. These input P_c-curves correspond to scaling of the throat sizes in the microporosity with different factors. The permeability of the microporosity was kept constant, to allow better interpretation of the results.

Influence of the microporosity's input capillary pressure curve

To assert how the microporosity's pore size distribution affects the drainage behaviour in a multi-scale carbonate, the input capillary pressure curve in the Savonnières simulation was varied while keeping the other input parameters constant (like in the previous section, this discussion is focussed on the case of Savonnières, as in the Estaillades case the micro- and macro-pore networks are coupled fully in parallel). Results with input capillary pressure curves corresponding to a scaling of the microporous throat sizes with factors 0.1, 2, 3, 4 and 5 were compared. Size distributions for micro-and macroporosity are shown in Figure 4.18. When microporous throat sizes are scaled with a factor 3 or more, there is significant overlap with the throat sizes of the macroporous network. This is an interesting test case, as it indicates how the model responds to situations where there is no clear distinction between the peaks in a rock's multimodal pore size distribution, or when the resolution of the imaging method (in this case micro-CT) cannot be tuned to a value in between the peaks. Scaling factors larger than 5 were not tested, as microporosity with throat sizes larger than the macroporosity would be non-physical.

When microporosity is scaled with a factor 0.1, all well-connected macropores are filled before the microporosity is invaded. This is clearly reflected

in the P_c-curve by a strong increase in the capillary pressure at S_w = 0.6. The new flow paths which are opened to non-wetting phase flow below this saturation are less efficient, as they are associated with drainage of macro-pores which only contribute to the flow through connections with low-permeability micro-links. In the $K_{r,nw}$-curve (Figure 4.18), this point in the drainage sequence is characterized by a sharp bend. The influence on $K_{r,w}$ is much smaller, as the wetting phase flow becomes dominated by passage through wetting films in the (fully drained) well-connected macro-pore network.

For scaling factors larger than 1, the rise in the K_r,nw-curve shifts to lower wetting saturations (Figure 4.18). This behaviour can be analysed by looking at the relative permeability behaviour of the macro-pore network separately (classical network in Figure 4.15). Due to its heterogeneous nature, the relative permeability of the macro-network has a sharp increase at a (macroporous) wetting saturation of 0.5. At this point, 70 % of the well-connected macro-pore space has been drained. The slight shift for the multi-scale simulation with scaling factor 2 (Figure 4.18) can then be explained by taking into account that the microporosity's invasion capillary pressure is reached at S_w = 0.72 for this simulation. Therefore, at a given total wetting saturation below 0.72, the wetting saturation of the well-connected macro-network is higher than in the multi-scale simulation with the original microporosity's throat sizes (due to drainage of microporosity and, at lower saturation, of isolated macro-pores). For larger scaling factors, the microporosity also starts to significantly affect the invasion sequence of the well-connected macro-pores, due to the increased overlap in microporous and macroporous throat sizes. For scaling factor 3, the strong increase in permeability (at total S_w = 0.65) only happens when 82 % of the well-connected macro-pore space has been drained (compare to 70 % in the original multi-scale network). This means that the well-connected macroporosity is drained through macro-throats and micro-links concurrently, and suggests that pores are not strictly drained in order of decreasing size of their connected macro-throats. More validation work is needed to investigate the physical relevance of the model in such situations.

4.4 Conclusions and outlook

Understanding the multi-phase flow properties of rocks with broad pore size distributions is an important problem in reservoir engineering and hydrology. The complexity of these media does not only make it difficult to simulate two-phase flow, it also often causes the classical relationships describing these phenomena to fail. We use the concept of micro-links, connections which represent the upscaled transport properties of microporosity, to develop a novel type of micro-CT image-based dual pore network model (DPNM) to investigate two phase flow in multi-scale porous media. The computational demands of these DPNM do not depend on the length scale of the micropores, making it feasible to investigate much larger volumes of real microporosity-containing rocks than would be possible when one tries to take individual micropores into account explicitly. Furthermore, the method takes microporous transport both parallel and serial to macroporous transport into account. We show that the new technique is able to reproduce much of the drainage flow behaviour shown by a considerably more detailed DPNM representation (with individual micropores). To this end, the method was tested on an artificial pore network generated from a sphere packing (Mehmani and Prodanović, 2014). While it may be difficult to reproduce absolute, single phase properties exactly, we show that it is possible to gain good estimates of the multi-phase properties using the less detailed approach.

The power of our DPNM method is illustrated by extracting a network from 10^9 voxels counting micro-CT datasets of Estaillades and Savonnières, two complex, bimodal carbonate rocks. Drainage results compare well to experimental results, indicating that this method is a promising tool for the investigation of pore-scale two-phase flow properties in multi-scale porous media. The presented simulations illustrate how the model can help to understand the influence of microporosity on transport properties, by investigating the influence of microporosity properties. Despite the advantages of DPNM with micro-links, we note the need for further research, mainly into better ways to determine the microporosity's petrophysical parameters, and into more advanced conductivity models to describe the transport through microporous zones in the model. The difficulty of describing for example (relative) permeability, capillary pressure and non-wetting breakthrough saturation of the microporous phase can be a bottleneck in multi-scale

modeling. Another weakness of the current implementation of our DPNM with micro-links is the need to include a maximum length for connections between pores through microporosity, in order not to overestimate the conductivity through the microporous phase. The need for this non-physical, user-defined parameter is brought forth by oversimplifications in the conductivity model we have employed (which assumes perfect coupling between macro-pores and microporous zones and which does not take into account the tortuosity of a micro-link). Further developments in the assessment of petrophysical properties and transport models are expected to increase the reliability of the method, while reducing the dependency on operator-supplied parameters. Next to the necessity of these developments, it is also important to highlight the need for adequate imaging, image processing and image analysis procedures (including classical pore network extraction) to digital rock physics approaches like ours.

5

Multi-scale imbibition simulations

5.1 Introduction

In this chapter, the image-based multi-scale PNM presented in chapter 4 is extended to simulate secondary imbibition in homogeneous and mixed wettability conditions. Secondary imbibition is a process of crucial importance in for example hydrocarbon production, where water is often injected to maintain reservoir pressure and to sweep the oil towards a production well during secondary recovery. In CO_2 sequestration, it takes place when the CO_2 plume migrates under influence of gravity (Krevor et al., 2015). In environmental remediation, it is important to study pollutant spreading and NAPL remediation by water flooding.

During secondary imbibition processes, the distribution of the wettability in rock samples plays an important role. It is influenced by the mineralogy, pore size, pore shape, and the saturation history. While many reservoir and aquifer rocks consist primarily out of water-wet minerals like quartz, calcite and dolomite, other constituent minerals can have different wettabilities (Buckley et al., 2007). Furthermore, when crude oil and certain non-aqueous phase liquids (NAPL) are in direct contact with a mineral surface after drainage, polar compounds (e.g. asphaltenes) may

precipitate and render the mineral surface oil-wet (Powers et al., 1996). Water films that remain stable after drainage can preserve the mineral's initial wettability by protecting it from direct contact with wettability-altering fluids. Skauge et al. (2007) showed that mixed-wet reservoir samples can be subdivided into three classes: fractionally-wet (FW), mixed-wet large (MWL) and mixed-wet small (MWS). In the FW case, the spatial distribution of the wettability is random with respect to pore size, in the MWL case the large pores are oil-wet, and in the MWS case the small pores are oil-wet. Similar wettability distributions could arise in aquifer rocks or in soils which are brought into contact with NAPLs (Al-Futaisi and Patzek, 2004). As imbibition is an ill-defined concept in mixed-wet porous media, we will rather refer to this invasion process as secondary water flooding, which takes place after primary oil flooding. Note however, that the terms "oil" and "water" are used as arbitrary designations of two immiscible fluids, and could readily be replaced by e.g. CO_2, gas, air, non-aqueous phase liquid (NAPL) and brine.

In section 5.2, we discuss the rules we have implemented to simulate imbibition in the pore network models introduced in the previous chapter. The method is tested by performing simulations on artificial networks extracted from a sphere packing and on a network extracted from a micro-CT scan of Estaillades limestone (section 5.3). The results from these tests are shown in section 5.4. Finally, section 5.5 contains conclusions and an outlook on further research. This chapter is based on a publication in Water Resources Research: Bultreys et al. (2016d), *"Simulating secondary water flooding in heterogeneous rocks with variable wettability using an image-based, multi-scale pore network model"*.

5.2 Secondary water flooding simulations

As introduced in chapter 2 (section 2.2.2), multiple pore filling mechanisms take place during quasi-static secondary water flooding (after primary oil flooding). Piston-like displacement, snap-off and cooperative pore body filling have to be considered (Lenormand and Zarcone, 1984). Piston-like displacement is equivalent to the filling of throats during drainage: a terminal meniscus moves through a throat. Snap-off takes

place when water films in corners swell so strongly that the fluid configuration becomes unstable. While piston-like displacement is always favoured over snap-off when it is possible, snap-off is important because no adjacent network elements have to be filled with water for it to happen. It can therefore strongly decrease the connectivity of the retreating oil phase, resulting in high amounts of capillary oil trapping. Snap-off proceeds preferentially in narrow, strongly water-wet throats.

Cooperative (pore body) filling is the process through which water-wet pores are invaded with water. The associated entry pressure is determined by the largest radius of curvature which has to be achieved by the fluid-fluid interface to enter the pore. This pressure is therefore influenced by the amount of neighbouring pore throats which are filled with oil. It is notably difficult to calculate, as the exact spatial arrangement of these throats is hard to take into account. To replicate the qualitative behaviour seen in micromodel experiments, the entry pressure is calculated with parametric models (Blunt, 1998; Øren et al., 1998), ranking pore filling events with many neighbouring oil-filled throats as unfavourable, e.g.:

$$P_c = \frac{2\sigma \cos\theta_a}{r + \sum_{\forall i} C_i x_i r_i} \tag{5.1}$$

with σ the interfacial tension, θ_a the advancing contact angle, r the pore size, i running over all neighbouring oil-filled throats, C_i input parameters, x_i random numbers and r_i the radii of neighbouring oil-filled throats. Cooperative pore filling becomes more important to the overall network behaviour as the network becomes more weakly water-wet and exhibits more homogeneous pore sizes, making these situations harder to simulate.

For all pores and throats in the network, capillary entry pressures for each of the eligible transport mechanisms can be calculated using the equations in Valvatne and Blunt (2004). Network elements are then invaded in order of decreasing capillary entry pressure. Below, we describe how this algorithm was adapted to take the micro-links in the multi-scale model into account.

5.2.1 Saturation, wettability and conductivity

To simulate secondary water flooding, P_c - and K_r-curves which are representative of water flooding in the microporosity are provided as input to the model. The model thus uses different sets of microporous P_c - and

K_r-curves during water and oil flooding, in order to take hysteresis into account. The saturation and micro-link conductivities can then be calculated in the same way as during primary oil flooding.

The model can take into account wettability alteration in parts of the pore space which have been in contact with oil as a result of primary oil flooding. In macro-pores, the approach presented by Valvatne and Blunt (2004) (following Kovscek et al. (1993)) is taken. The same algorithm is used to calculate the microporosity's water flooding P_c - and K_r- curves on single-scale networks with the desired wettability. The microporosity's wettability behaviour is thus set during these single-scale calculations, and encoded in the input values used for the multi-scale simulations. This is also the case for wetting film flow in the microporosity: the presence of wetting films influences the capillary pressure and relative permeability curves of the microporosity, and is therefore taken into account in the multi-scale simulations.

5.2.2 Filling sequence

Piston-like pore filling from a neighbouring micro-link

To determine the invasion sequence of the multi-scale network during secondary water flooding, we have to take into account possible piston-like invasion of macro-pores with water, starting from terminal water menisci in a neighbouring zone of microporosity, i.e. piston-like invasion from a micro-link. A representative pore network model of the microporosity could be used to try to determine a critical wetting saturation (and capillary pressure) for such a terminal meniscus to exist in the microporosity. When the microporosity's water saturation just exceeds this value, a neighbouring oil-filled pore could be invaded if its (piston-like) invasion capillary pressure were higher than the current network capillary pressure, i.e. the microporosity's critical percolation capillary pressure. This is rarely the case if the microporosity is water-wet, as its smaller pore sizes cause it to imbibe with water at high capillary pressure. The order in which eligible macro-pores fill is then determined by macro-pore properties (size and contact angle) rather than by properties of connecting micro-links.

If the microporosity is water-wet, a micro-link's critical P_c may only be lower than the invasion capillary pressure of a connected macro-pore when

the micro-pores reach the size of the smallest macro-pores. In this case, we are presented with a similar difficulty as during drainage: if we define a single critical P_c for all micro-links, all macro-pores with invasion capillary pressure higher than this value would be invaded simultaneously, while we are interested in determining the *order* of filling. Like for primary drainage, we again look at the behaviour of a network with individual micro-pores, and conceptually treat the micro-links as if they were filled with a regular network of small pores and throats. To determine the capillary pressure at which a water cluster percolates this regular network, the possible invasion patterns which may occur during imbibition have to be taken into account. These emerge as a result of the competition between snap-off, piston-like displacement and cooperative pore filling. Depending on the presence of wetting films, the contact angles and the pore and throat radii, the invasion in a quasi-static network follows a percolation, invasion percolation, frontal advance or cluster growth pattern (Blunt, 2016). Finite size scaling relations, like the ones used to determine the order of macro-pore filling during drainage, are only applicable for percolation and invasion percolation.

If we assume the microporosity to be strongly water-wet and significantly heterogeneous in pore size, the invasion pattern under water-wet conditions in this network may be described as percolation (with trapping) (Blunt, 2016). We therefore assume that finite size scaling can be used to determine the micro-link's critical water saturations. The order of filling of macro-pores can therefore be determined in a similar way as during drainage, and is related to the geometry of the microporous regions (similarly to equation 4.2 and 4.3).

If the microporosity is oil-wet, it tends to be filled with water at very low capillary pressures. This is effectively a drainage scenario, the invasion pattern is invasion percolation, and the finite size scaling relations are therefore applicable.

The algorithm described here may not be appropriate if the microporosity is homogeneous and has pore sizes close to those of the macroporosity, particularly for contact angles close to 90 °. In this case, the micro-links may be critical to determine the invasion sequence of the multi-scale network, yet the invasion pattern in the microporosity itself is likely strongly influenced by cooperative pore filling, resulting in cluster growth (in the strongly water-wet case) or frontal advance (in the weakly water- or oil-wet case), which cannot be described as a percolation process (Blunt,

2016). However, in most intended applications of this model (i.e. heterogeneous natural rocks), the microporosity is significantly heterogeneous and consists of much smaller pore sizes than the macroporosity. In other cases, direct multi-scale methods and PNMs with individual micro-pores may be more appropriate.

Connectivity of the retreating oil phase

Microporosity does not only provide pathways for the invading water phase to invade macro-pores, it may also allow pathways for the retreating oil phase to escape from macro-pores, potentially lowering the amount of oil trapping. These pathways are however only available as long as oil percolates through the microporosity. For simplicity, a single cut-off capillary pressure is determined for all micro-links during water flooding: the capillary pressure at which the microporosity's oil relative permeability reaches zero.

Cooperative pore filling

We consider how the capillary entry pressure of a water-wet pore body is influenced by the presence of an oil-filled microporous zone connected to it, i.e. how should micro-links be taken into account when considering cooperative (macro-)pore filling? To explore this issue, we can investigate the model situation of a two-dimensional pore connected to three throats and one microporous zone in figure 5.1. The critical curvatures for different cooperative pore filling scenarios in this simple 2D case were determined using a level-set method (Prodanović and Bryant, 2006). When all but one of the connections are water-filled (the I_1 case), the smallest curvature which has to be achieved is determined by the inscribed radius of the pore. The influence of the microporous zone on the critical curvature can be neglected, taking into account that pore shapes are already strongly simplified during pore network extraction.

If the microporous zone is oil-filled along with one of the throats adjacent to it (the $I_{2,m}$ case), the critical curvature and the corresponding capillary entry pressure are decreased compared to I_1. However, the curvature lowering effect is much weaker than in the case where two adjacent throats are oil-filled (I_2), due to the roughness of the microporous interface. If the

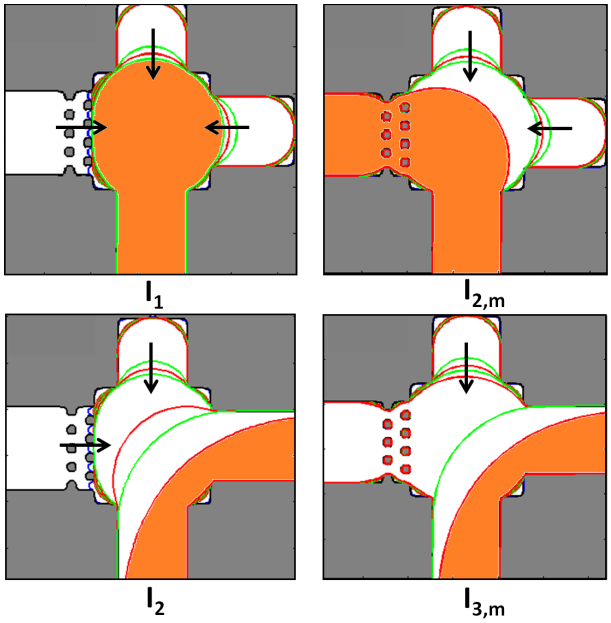

Figure 5.1: Level-set simulations (Prodanović and Bryant, 2006) of cooperative pore filling during water flooding, in the situation of a pore with three neighbouring throats and a neighbouring microporous zone (oil coloured orange). In the I_1 case, only one of the pore's neighbouring throats is oil-filled: the pore invasion is equivalent to piston-like advance. In the $I_{2,m}$ case, the invasion pressure is altered due to the oil-filled microporosity, yet the effect is much smaller than in the I_2 case, where two neighbouring throats are oil-filled. In the $I_{3,m}$ situation, the invasion pressure is not affected by the neighbouring microporosity.

size difference between the macro-pore and the micro-pores would further increase, the critical curvature in the $I_{2,m}$ scenario would eventually equal that during I_1, as the interface with the microporosity would resemble a rough pore wall. While the roughness of this surface might alter the contact angle there, and thus influence the curvature, we assume this effect to be negligible compared to simplifications regarding the pore shape and the cooperative pore filling model (equation 5.1). Therefore, we assume that neighbouring oil-filled micro-links do not lower the invasion pressure of a macro-pore. Micro-links are thus not considered when summing over the pore's neighbouring oil-filled throats in equation 5.1. Figure 5.1 shows that this approach is equally valid for the $I_{3,m}$ case, where two of the throats and the microporous region are initially oil-filled, as this case yields the same critical curvature as I_2.

5.3 Networks used for validation

5.3.1 Wettability distribution

As discussed in the introduction of this chapter (section 5.1), the wettability in geological materials is often distributed heterogeneously throughout the pore space, in which case it may follow the FW, MWL and MWS mixed-wettability distributions. We investigated whether the influence of these wettability distributions on the multiphase flow properties can be captured in our model, by altering the wettability of macro- or micro-pores which are in contact with oil after primary drainage. To simplify the interpretation of the results, primary oil flooding was performed with a receding contact angle of 0° in all cases. Then, before water flooding, the advancing contact angles were randomly distributed in all network elements in the ranges shown in table 5.1. The validation simulations were run for uniform (strongly and intermediately water- and oil-wet) and non-uniform (mixed strongly and intermediately water- and oil-wet) wettability.

5.3.2 Artificial networks

Two artificial networks were used to compare our model to a reference model with individual, resolved micro-pores, which provides a more

	Microporosity	Macroporosity
Strongly water-wet (SWW)	0°- 30°	
Intermediately water-wet (IWW)	70°- 90°	
Strongly oil-wet (SOW)	150°- 180°	
Intermediately oil-wet (IOW)	90°- 110°	
Strongly fractional-wet (SFW)	0°- 30°(50 %) or 150°- 180°(50 %)	
Intermediately fractional-wet (IFW)	70°- 90°(50 %) or 90°- 110°(50 %)	
Strong mixed-wet large (SMWL)	0°to 30°	150°to 180°
Strong mixed-wet small (SMWS)	150°to 180°	0°to 30°
Intermediate mixed-wet large (IMWL)	70°to 90°	90°to 110°
Intermediate mixed-wet small (IMWS)	90°to 110°	70°to 90°

Table 5.1: Advancing contact angles are assigned randomly within these ranges, for different wettability scenarios.

detailed description of the pore space but is also significantly more computationally demanding (figure 5.2). Since all the upscaled properties of the microporosity are exactly known in this case, the networks can be used to answer the question whether a multi-scale PNM with upscaled properties can replicate the behaviour of a full PNM description of the pore space. The artificial networks were provided by Mehmani and Prodanović (2014), and their generation is outlined in chapter 4 (section 4.2.4). Here, we use two reference networks, in which respectively 20 % and 50 % of the macro-pores were removed and replaced by micro-pores. The amounts of macro-pore filling were chosen to represent the situations where the macroporosity percolates the network, yet the influence of microporosity is already important (20 % pore filling), and where the macroporosity does not percolate any more, meaning that fluids need to pass through the microporosity to flow through the network (50 % pore filling). As described in detail in chapter 4.2.4, equivalent PNM with micro-links were extracted from these fully resolved PNMs by removing the micro-pores and reconnecting the macro-pores which neighbour microporous regions by micro-links (figure 5.2). The input parameters for the microporosity were determined with single-scale simulations on the microporosity's parent network and can be found in appendix A. Long micro-links ($> 225\mu m$) were removed (see discussion on the cut-off length for micro-links in chapter 4). To calculate cooperative pore filling invasion pressures in both the reference networks and the equivalent networks with micro-links, equation 5.1 was used, with C_1 = 0.0, C_2 =

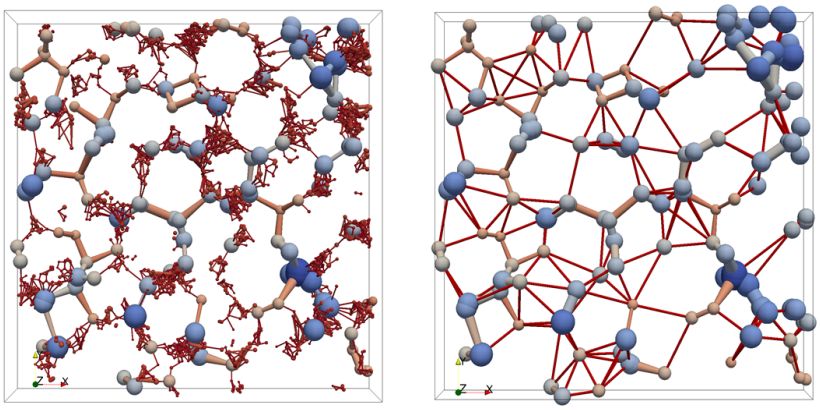

Figure 5.2: Small 2D subsection of the artificial networks: on the left the reference network with individual micro-pores and on the right the equivalent network with micro-links

0.5, C_3 = 1.0, C_4 = 2.0, C_5 = 5.0 and $C_{\geq 6}$ = 0.0. These are typical values used by Øren et al. (1998), with the exception of $C_{\geq 6}$, which was set to zero to avoid unrealistically low invasion pressures in macro-pores which are connected to many small, oil-filled micro-throats.

5.3.3 Estaillades network

In this chapter, we present simulations on the multi-scale PNM extracted from Estaillades limestone (section 4.2.4) as a first test of the feasibility and suitability of the model to perform image based water flooding simulations. The petrophysical input parameters for the microporosity were estimated based on literature (Bauer et al., 2012) and on analysis of the MIP experiment. The microporosity's input relative permeability curves for different wettabilities were calculated on a cubic, randomly generated network with pore and throat size distributions matching the MIP experiment. Like for drainage simulations (section 4.3.2), assessing the upscaled flow properties of the microporous phase is in general very challenging. Here, only rough estimates of these properties are made, as the aim of this work is to test whether general trends of water flooding behaviour in complex rocks can be predicted. Further work should be done to increase the reliability and precision of the estimates. The input parameters can be found in appendix A. To calculate cooperative pore

filling pressures on this network, the model from Blunt (1998) was used. This model is similar to the one in equation 5.1, but it allows to relate the input constants to the permeability of the sample (C_1 = 0 and C_i = $0.03/\sqrt{K}$ for $i > 1$,Valvatne and Blunt (2004)) and it allows for negative capillary entry pressures in pores with contact angles below 90°.

5.4 Validation and discussion

5.4.1 Artificial networks

Uniform wetting

Under strongly water-wet conditions, the microporosity is imbibed first and the invasion pressure for macro-pores is determined by their own radius, rather than by the properties of neighbouring water-filled microporosity. This behaviour is well-captured by our model, resulting in a very good agreement in P_c, K_r and RI with the reference networks (Figure 5.3). This is also the case for the strongly oil-wet case (Figure 5.4). While water films are present in the corners of the pores and throats in SOW, snap-off in oil-wet elements is suppressed and can only take place at very low capillary pressure. The SOW case is therefore essentially an invasion-percolation-like drainage process, for which a good agreement was already shown in chapter 4.

As explained in section 5.2.2, the invasion sequence is more difficult to simulate under intermediate wetting conditions (contact angles close to 90°), because the importance of cooperative pore filling is then larger. While the predicted transport properties are in qualitative agreement, there is a discrepancy in the residual oil saturation when there is a high amount of microporosity present in IWW (the 50 % clay-filling case in Figure 5.5). In this case, the connectivity of the retreating oil phase through the microporosity is crucial. As the microporosity in the reference network is very homogeneous (being extracted from a packing of equal spheres), the invasion pattern of these pores in the IWW case tends towards frontal advance, which is not captured in the network with upscaled microporosity properties. Figure 5.6 shows a comparison of the displacement pattern in a strongly and a weakly water-wet network. Due to frontal advance, oil flow paths are closed off sequentially rather than

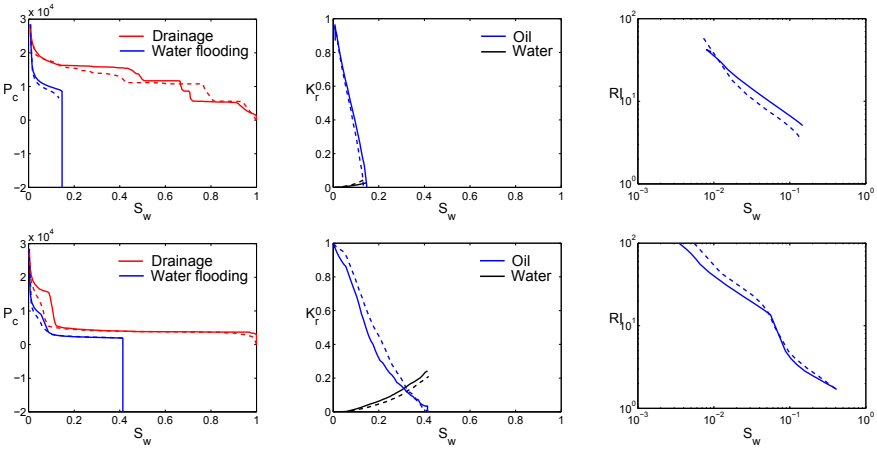

Figure 5.3: Capillary pressure, relative permeability and resistivity index curves from secondary water flooding simulations in the strongly water-wet case (SWW). These results were calculated on the artificial network where 50 % (top row) and 20 % (bottom row) of the macro-pores were removed and replaced by microporosity. Broken lines are the reference network, full lines represent the model presented in this chapter.

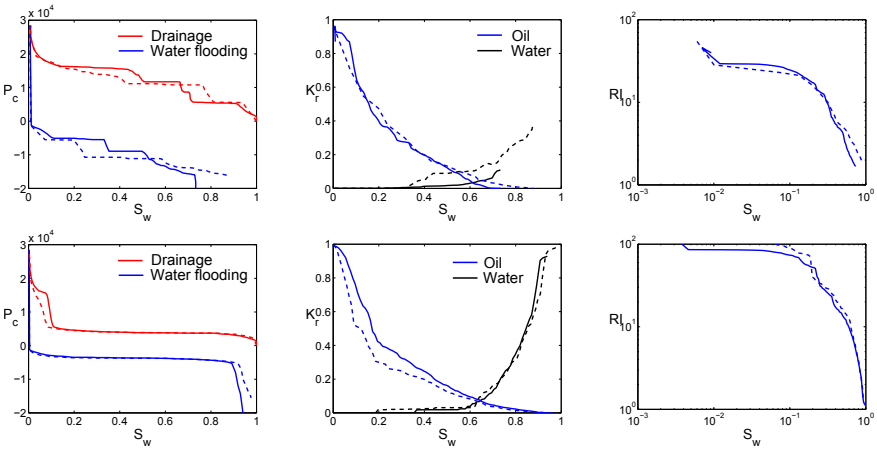

Figure 5.4: Capillary pressure, relative permeability and resistivity index curves from secondary water flooding simulations in the strongly oil-wet case (SOW). These results were calculated on the artificial network where 50 % (top row) and 20 % (bottom row) of the macro-pores were removed and replaced by microporosity. Broken lines are the reference network, full lines represent the model presented in this chapter.

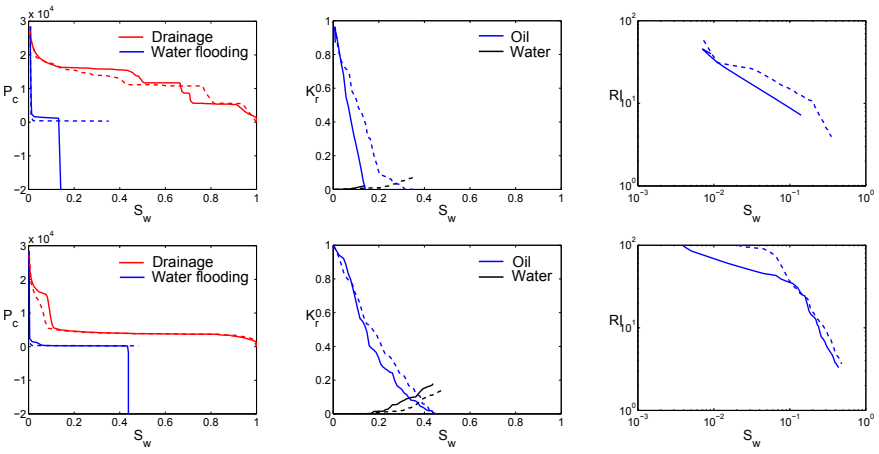

Figure 5.5: Capillary pressure, relative permeability and resistivity index curves from secondary water flooding simulations in the intermediately water-wet case (IWW). These results were calculated on the artificial network where 50 % (top row) and 20 % (bottom row) of the macro-pores were removed and replaced by microporosity. Broken lines are the reference network, full lines represent the model presented in this chapter.

simultaneously, resulting in a lower residual oil saturation. However, more heterogeneity is generally expected in natural porous media, suggesting that this problem does not occur as strongly in simulations on real rock geometries. Nevertheless, the lack of a rigorous description of cooperative pore filling is expected to render these results less reliable than the strongly wetting simulations. Note that this is also the case for PNM with individual micro-pores, and is not (only) related to the description of the microporosity. Results for the IOW case can be found in Figure 5.7, and show a higher amount of trapped oil than the SOW simulations, due to the decreased stability of oil layers for contact angles closer to 90 °.

Non-uniform wetting

When strongly oil-wet pores and throats are assigned randomly in the reference network (SFW), water-wet micro-pores and micro-throats have the highest invasion capillary pressure, followed by respectively water-wet macro-pores and throats, oil-wet macro-pores and oil-wet micro-pores. Water-wet micro-pores and micro-throats are thus filled with water first. Due to the small difference in scale between the micro-and macroporosity,

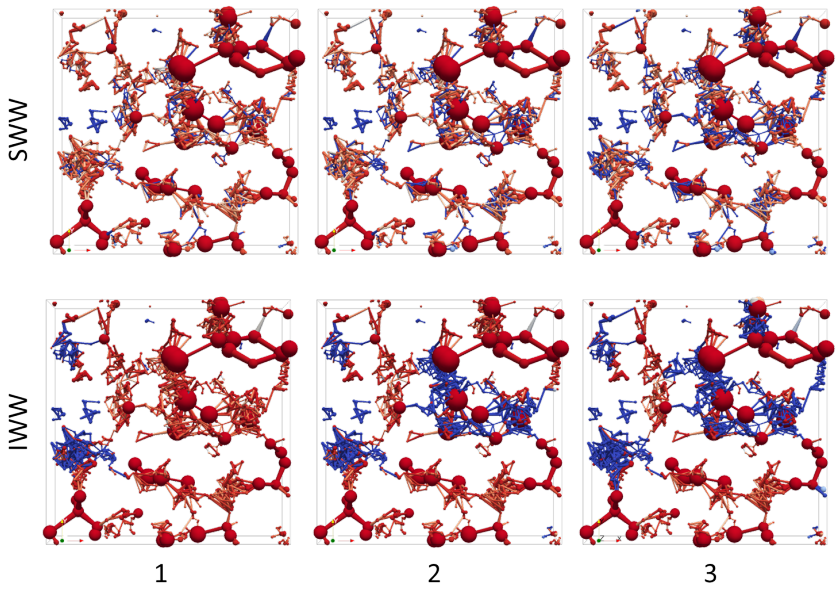

Figure 5.6: This filling sequence (three selected capillary pressure steps) in a small section of the reference network during water flooding illustrates that the water invasion of microporosity is homogeneously spread over the network during SWW, while zones of microporosity tend to fill sequentially when the network is less strongly water-wet (IWW). This is caused by snap-off being the dominant displacement mechanism in the former case, while cooperative pore filling has a strong influence in the latter. In this figure, water is rendered in blue, oil in red.

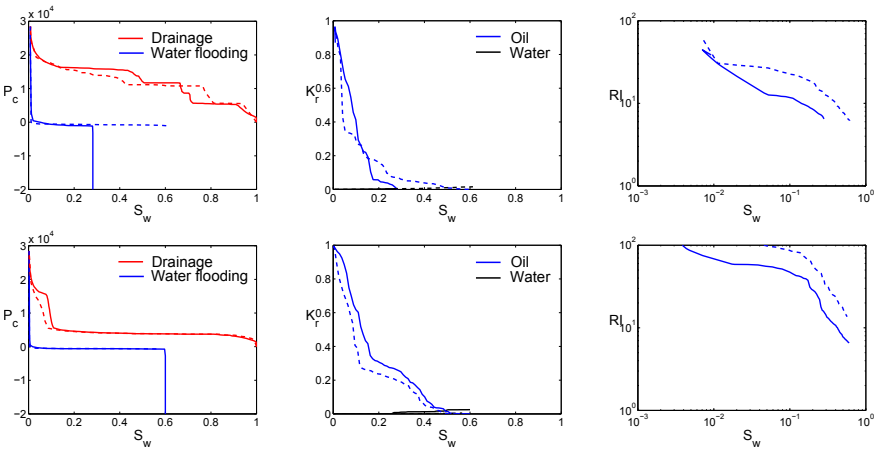

Figure 5.7: Capillary pressure, relative permeability and resistivity index curves from secondary water flooding simulations in the intermediately oil-wet case (IOW). These results were calculated on the artificial network where 50 % (top row) and 20 % (bottom row) of the macro-pores were removed and replaced by microporosity. Broken lines are the reference network, full lines represent the model presented in this chapter.

macro-pores in the reference network are often connected to a microporous region by only a few microthroats. Snap-off in a small number of water-wet microporous network elements can therefore cut off the oil flow in a zone of microporosity, leading to oil trapping in neighbouring macro-pores. This effect is not captured in the networks with upscaled microporosity, as the microporosity properties provided as input are calculated on a larger network of micro-pores, with many network elements connected to the in- and outlet. This leads to the observed underestimation of the amount of trapped oil compared to the reference network (Figure 5.8), while the capillary pressure and relative permeability qualitatively agree up to $S_w = 1 - S_{or}$. In most intended applications of this model, the scale difference between macro-and microporosity is larger, as these situations are indeed the strength of the model compared to networks with individual micro-pores. In this case, the observed sparse cross-scale connectivity effect is less likely to be an issue, although a thorough characterization should be performed to point out these connectivity properties on a case-by-case basis.

The SMWL scenario (Figure 5.9) is similar to the SWW case: the intrusion capillary pressure of the macro-pores and macro-throats is decisive for the

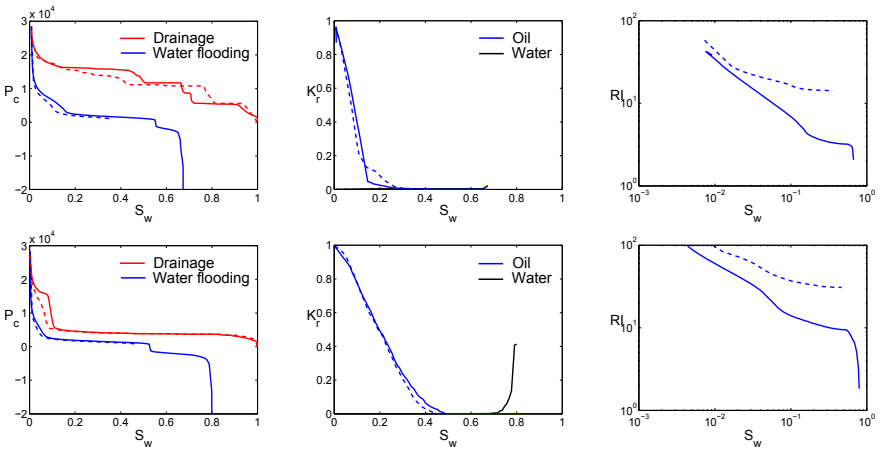

Figure 5.8: Capillary pressure, relative permeability and resistivity index curves from secondary water flooding simulations where the pores are randomly assigned strongly-oil or water-wet (SFW). These results were calculated on the artificial network where 50 % (top row) and 20 % (bottom row) of the macro-pores were removed and replaced by microporosity. Broken lines are the reference network, full lines represent the model presented in this chapter.

filling sequence, and the results therefore fit very well. The microporosity is filled with water first. When there is a high amount of pore-clogging clay (e.g. in the case where 50 % of the pores were clogged), the oil does not percolate through the network after this has happened. This leads to a high amount of trapped oil. When there is a lower amount of microporosity, the oil remains connected to the outlet through films in the oil-wet macro-pores and throats, leading to a very little oil trapping. When the small pores are oil-wet (the SMWS case, Figure 5.10), the microporosity essentially undergoes a drainage process, leading again to qualitative agreement with the reference network, similar to the SOW case. It is then no surprise that the model performs well, yet slightly worse, in the IMWS and IMWL cases, as these relate to SMWL and SMWS like IWW and IOW relate to SWW and SOW. Similarly, the IFW prediction is less good than the SFW case. The same arguments regarding homogeneity of the microporosity are valid here. Results for IFW, IMWS and IMWL can be found in appendix A.

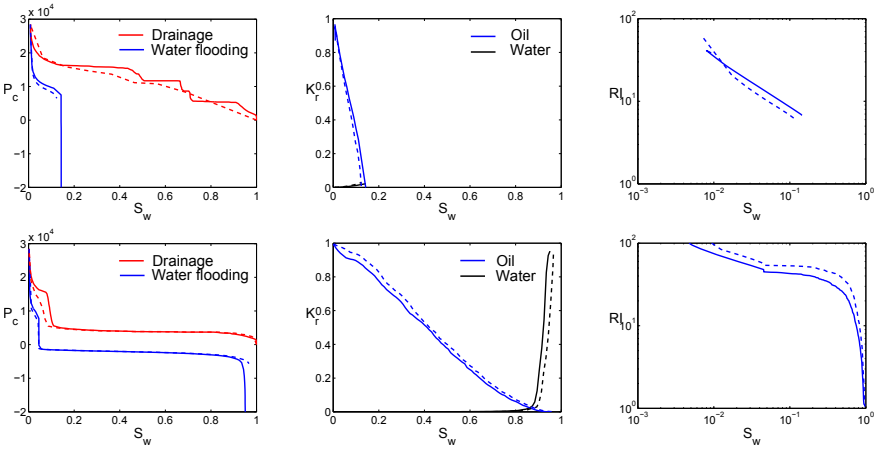

Figure 5.9: Capillary pressure, relative permeability and resistivity index curves from secondary water flooding simulations where the macro-pores are strongly oil-wet and the micro-pores strongly water-wet (SMWL). These results were calculated on the artificial network where 50 % (top row) and 20 % (bottom row) of the macro-pores were removed and replaced by microporosity. Broken lines are the reference network, full lines represent the model presented in this chapter.

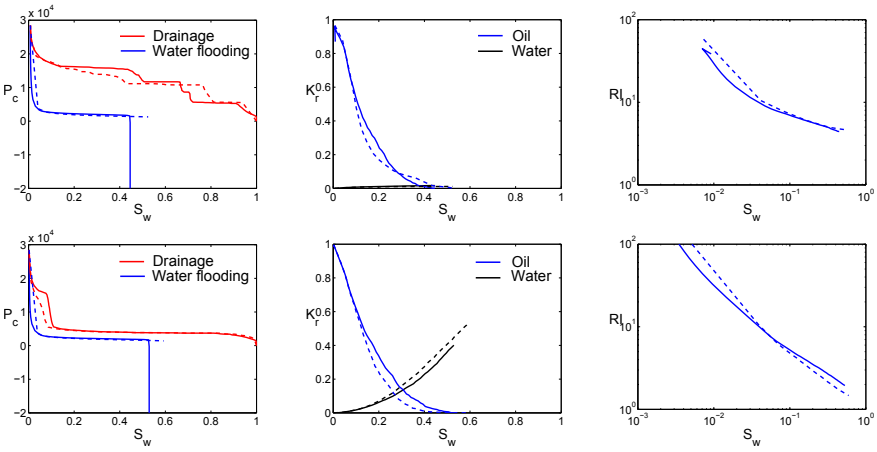

Figure 5.10: Capillary pressure, relative permeability and resistivity index curves from secondary water flooding simulations where the macro-pores are strongly water-wet and the micro-pores strongly oil-wet (SMWS). These results were calculated on the artificial network where 50 % (top row) and 20 % (bottom row) of the macro-pores were removed and replaced by microporosity. Broken lines are the reference network, full lines represent the model presented in this chapter.

Computational performance

The simulations on the artificial network models do not only allow to compare the model results to those obtained with a network with individual micro-pores, they also allow to compare the performance of the models. Using a single core of an Intel Sandy Bridge 2.6 GHz processor, our model took approximately 14 s and 35 s to perform the full SWW and SOW simulations on the network where 50 % of the macro-pores where filled with clay, respectively. Using the same infrastructure and solver precision, the model with individual micro-pores ran for approximately 9 and 34 minutes. Our model needed to store less than 15000 network elements, compared to more than 318000 network elements for the model with individual network elements. The calculation time and memory requirements of our model are independent of the scale difference of the micro-pores and the macro-pores, and in real geological porous materials this scale difference is often larger than a factor of 5 (as is the case in the artificial networks). In Estaillades for example, a factor 100 would be more appropriate. We can thus expect an even larger performance gain for image-based simulations on real rocks.

5.4.2 Estaillades network

Results of SWW and IWW water flooding simulations in the Estaillades network can be found in figure 5.11. The IWW simulation shows good general agreement with the imbibition relative permeability measurements on Estaillades in Moctezuma-Berthier et al. (2002). The results are also in excellent accordance with Tanino and Blunt (2012), who report a trapped oil saturation of 0.37 and an endpoint $K_{r,w}$ of 0.081 in a fresh (i.e. unweathered and without having been in contact with crude oil) Estaillades sample with initial water saturation of 0.04. As can be seen in figure 5.11, the inclusion of microporosity in the multi-scale simulations has a significant effect, compared to simulations on the single-scale network of the macroporosity.

Recent measurements by Al-Menhali and Krevor (2016) indicate a residual non-wetting saturation (of CO_2 and N_2 in their case) of around 0.25 for initial non-wetting saturations around 0.42, for a water-wet Estaillades sample. At this initial saturation, almost the complete macroporosity network is drained (about 50 % of the total pore volume),

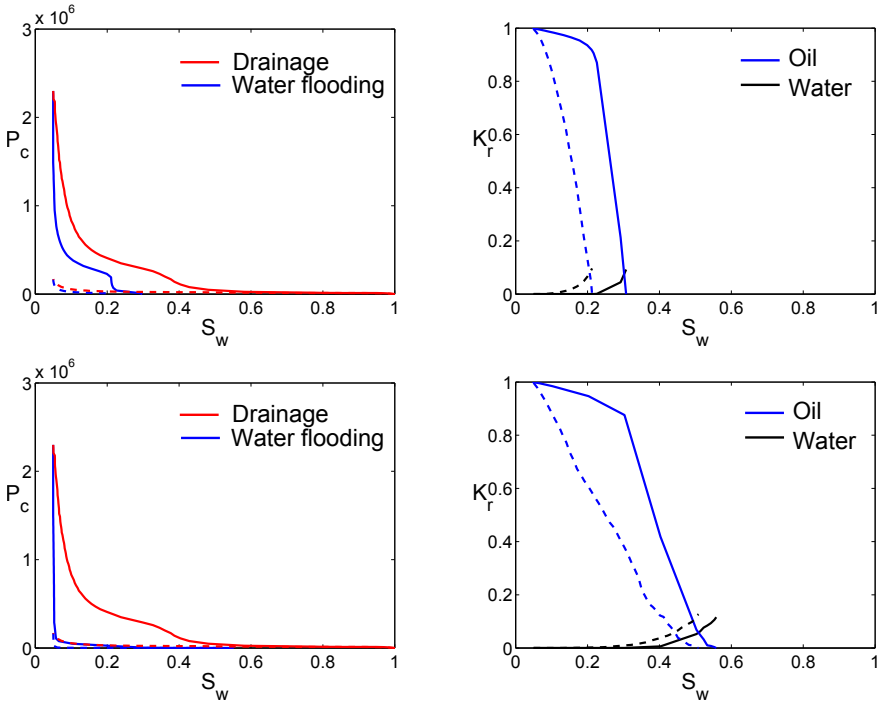

Figure 5.11: Capillary pressure and relative permeability curves from secondary water flooding simulations where the Estaillades network was assumed strongly water-wet (SWW, top row) and intermediately water-wet (IWW, bottom row). Full lines are simulations on the multi-scale network model, broken lines are simulations on the single-scale network representing the macroporosity, which neglects the presence of microporosity.

while the microporosity likely remained water-filled. This indicates that the macroporosity's trapping efficiency (the volume of trapped oil relative to the oil present at the start of water flooding) was around 55 %. This corresponds well to the IWW simulation, in which the macroporosity had a trapping efficiency of 50 %. The much higher amount of total oil trapping seen in the SWW simulation is mostly related to more trapping in the macroporosity (efficiency 81 %). Due to the well-connected nature of the macroporosity, this efficiency is hardly influenced by the presence of microporosity: simulations on single-scale macroporosity networks yielded nearly identical macroporosity trapping efficiencies in both SWW and IWW. The better agreement of the IWW case with the experiments is thus not an effect brought forth by the novel multi-scale algorithm, but is supported by well-validated single-scale networks (Gharbi and Blunt, 2012; Blunt et al., 2013). This supports the assumption that intermediately water-wet simulations are indeed closer to reality for Estaillades, which may be an artefact due to the imprecise cooperative pore filling algorithms employed here. Better deterministic models, based on the local arrangement of pores and throats, are being developed (Ruspini et al., 2016a).

Experimental water flooding relative permeability measurements on oil-wet or mixed-wet carbonate rocks are scarce in the literature. We therefore compare results obtained with the Estaillades model to experiments performed on other carbonate rocks with bimodal pore size distributions. While a quantitative match should therefore not be expected, this comparison allows to assess wettability trends, and therefore provides further indication that the model can help to increase insight into the flow properties of such heterogeneous carbonate rocks. Figure 5.12 shows intermediate- and mixed-wet simulations compared to experimental measurements performed by Al-Sayari (2009). In the experiment, relative permeabilities were measured on a Middle-Eastern carbonate sample with a dual pore system, a porosity of 32 % and a permeability of 111 mD. The rather high permeability and a distinguishable peak of microporosity in the MIP experiment performed by Al-Sayari and co-workers suggests that at least part of the macroporosity in this sample is well-connected. This is similar to Estaillades, in which the microporosity conducts mainly in parallel to the macroporosity.

Al-Sayari (2009) performed experiments on reservoir samples cleaned with toluene, and on samples of which the wettability was altered by

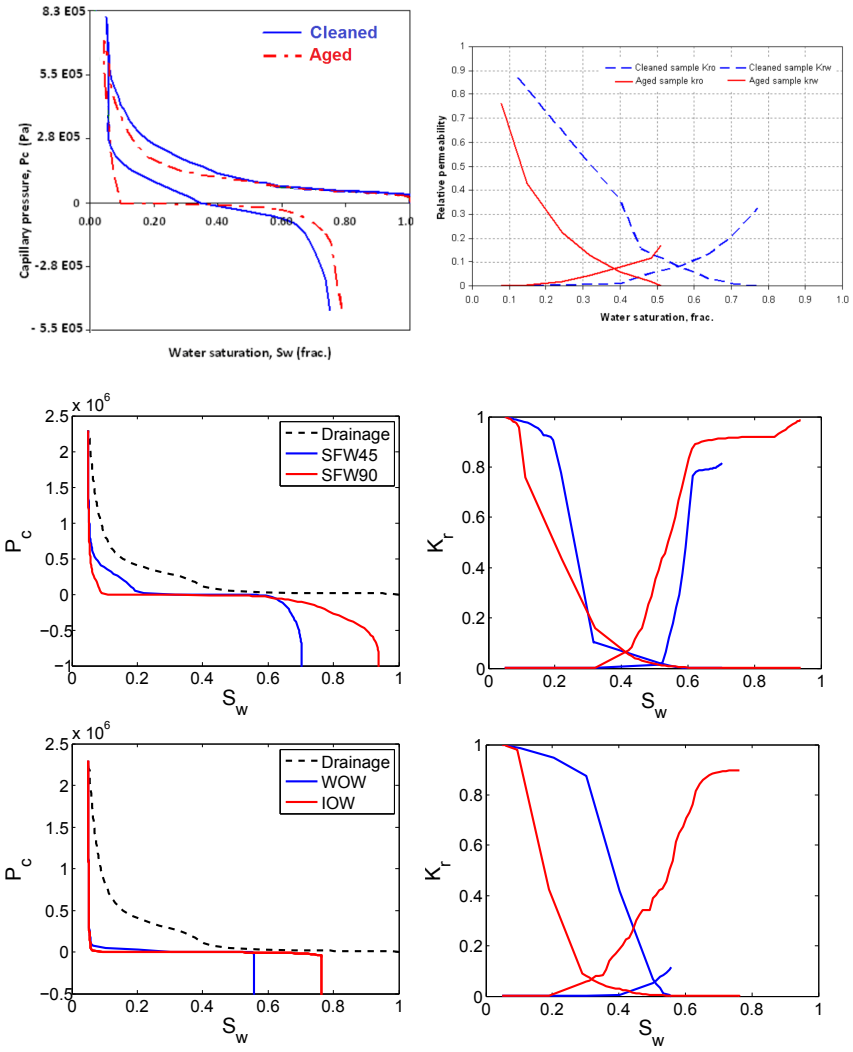

Figure 5.12: The top row shows experimental capillary pressure and water flooding relative permeability measurements on middle-eastern carbonate rocks from Al-Sayari (2009) (cleaned cores in blue and aged cores in red). On the middle row, mixed-wet water flooding simulations on Estaillades are presented. Here, we compare the situations where 45 % and 90 % of the invaded pore volume is rendered oil-wet (SFW 45 % in blue and SFW 90% in red). On the bottom row, we compare intermediately-water-wet water flooding on Estaillades (IWW, blue) to the intermediately-oil-wet situation (IOW, red).

contact with crude oil after cleaning. The experiments by Al-Sayari prove that the cleaned and wettability-altered rock are not respectively strongly water- and oil-wet, but rather intermediate or mixed wet (figure 5.12). We have performed fractionally-wet simulations where the wettability of 45 % or 90 % of the drained pore space was changed to strongly oil-wet. Contrary to the simulations on the artificial PNM, pores which are rendered oil-wet were spatially correlated: oil-wet patches have an average diameter of 7 pores. This is more realistic (Blunt, 2016): it results in a larger connectivity of the oil-wet regions, which now span the length of the network. The fractionally-wet results (figure 5.12) are compared to intermediately-wet results (IWW for the cleaned rock and IOW for the wettability-altered rock). The fractionally-wet case shows very good qualitative agreement to the experimental P_c measurement and reproduces the general trend in relative permeability (lower $K_{r,o}$ and higher $K_{r,w}$ after wettability alteration). The intermediate-wet simulations fit the experimental P_c worse, as they fail to reproduce the spontaneous imbibition on the one hand and the forced imbibition at high negative pressures, associated with oil-wet micro-pores, on the other hand. The relative permeability curves on the other hand qualitatively agree with the experimental results. Both the fractionally-wet as the intermediate-wet simulations predict lower residual oil saturations for the more oil-wet cases. This is not seen in the experiment, because the employed steady-state technique was not able to probe the layer-drainage regime where $K_{r,o}$ is very low, as noted in Al-Sayari (2009).

While the simulations presented here provide an example of how network investigations can help us investigate the link between pore scale properties and effective transport behaviour, it should be noted that the simulations were performed on a different rock type than the experiments, and so the quantitative properties (e.g. the fraction of oil-wet pores) do not necessarily reflect reality. Furthermore, the effect of the wettability alteration by contact with crude oil is likely more complicated than the simple scenarios applied here (Kallel et al., 2015).

5.5 Conclusion

In this chapter, we show that the multi-scale pore network model presented in chapter 4 can be expanded to simulate the important process of water

flooding (i.e., secondary water flooding if the sample is water-wet). We show that this model is able to adequately reproduce the behaviour of a sphere-packing based PNM with individual micro-pores in the strongly and intermediately water-and oil-wet cases (SWW, IWW, SOW and IOW). Furthermore, good results were obtained for mixed wettability, in the cases where the wettability is distributed randomly with respect to pore sizes (SFW and IFW, for strong and intermediate wetting respectively), where the microporosity is water-wet and the macroporosity is oil-wet (SMWL and IMWL), and vice-versa (SMWS and IMWS). The power of the approach is further illustrated by performing simulations on a network extracted from a micro-CT scan of Estaillades limestone. These results show good agreement with experimental measurements of non-wetting phase trapping and relative permeability in water-wet Estaillades and reproduce general wettability-alteration trends observed in mixed-wet carbonate rocks. Note that we merely use the terms "oil" and "water" to refer to arbitrary immiscible fluids, and that the method is thus applicable to a wide range of two-phase flow problems in geological porous materials, e.g. subsurface CO_2-sequestration and NAPL-intrusion and remediation in soils and aquifers.

Despite these good results, a number of difficulties related to both the description of the microporosity as the general pore network modeling approach remain. The most important limitations are the high amount of user-defined parameters in the model (including a micro-link length cut-off parameter), uncertainties brought forth by the imaging and the image segmentation, the difficulty of obtaining a representative network for the microporosity to calculate its upscaled transport properties, and the problem of describing cooperative pore filling in a PNM. Furthermore, the multi-scale model may have difficulties when the microporosity is homogeneous and when the difference between the scales of the macroporosity and the microporosity is small, due to a misrepresentation of the filling sequence in the microporosity under these conditions. Therefore, it is our opinion that multi-scale network models like the one presented here can currently not be regarded as truly predictive, but are nevertheless very useful to investigate trends in two-phase flow properties brought forth by the rock's pore structure and wettability.

6

The influence of microporosity on relative permeability in heterogeneous rocks

6.1 Introduction

As outlined in Chapter 3 (section 3.3.5) multi-scale PNMs have been developed over the last few years, including during this PhD. However, Chapters 4 and 5 of this thesis and most work in the literature focus on the methodological aspects, and few studies applied these recent developments to study how multi-scale pore geometries lead to qualitatively anomalous two-phase flow properties in a range of natural rocks. This is especially the case for tight materials and for rocks which contain microporosity with pore sizes two or three orders of magnitude smaller than the macroporosity, as often found in natural rocks. In this Chapter, we investigate the capillary pressure and relative permeability behaviour of three outcrop carbonates and two tight reservoir sandstones with wide, multi-modal pore size distributions. We apply our multi-scale pore network algorithm to examine how the drainage and imbibition properties of these complex rock types are influenced by the connectivity

of macro-pores to each other and to zones with unresolved small-scale porosity. Given the experimental difficulty of thoroughly characterizing the microporosity, we follow a similar approach as Prodanović et al. (2014) to investigate its influence in the model: rather than using the real pore space geometry, we use artificial networks extracted from a random sphere packing as a proxy. Following this approach, we investigate the sensitivity of the two-phase flow properties on the microporosity structure by comparing simulations on one sample with different microporosity properties. Furthermore, the influence of the macro-pore network and the coupling between the scales is investigated by comparing simulations on the different samples with the same microporosity properties. Finally, we consider the influence of mixed wettability during water flooding, assuming different wettability distributions for the micro- and macroporosity. Predictive simulations (i.e. with a focus on precisely matching the simulations to experimental P_c and K_r measurements) require a detailed characterization of the microporosity, and are thus not presented here, but need further research. In this Chapter, we rather seek to qualitatively explain the behaviour of the investigated samples and illustrate the use of the multi-scale pore network model on a wider range of samples then previously shown. This Chapter is based on a publication in the Journal of Geophysical Research: Bultreys et al. (2016c), *"Investigating the relative permeability behavior of microporosity-rich carbonates and tight sandstones with multi-scale pore network models"* (In press at the moment this thesis was presented).

In the following, Section 6.2 contains an overview of the samples (6.2.1) and the imaging work flow (6.2.2). The drainage and imbibition simulations on these networks are treated in Section 6.2.3. Results are presented in Section 6.3, followed by a general discussion in Section 6.4 and conclusions in Section 6.5.

6.2 Materials and methods

6.2.1 Sample description

In this Chapter, five samples were investigated: three French outcrop carbonates (Estaillades, Savonnières and Massangis Jaune) and two tight sandstones (a tight gas sandstone from the Wilcox Formation in Texas,

USA, and a tight sandstone from the Knorringfjellet Formation on Spitsbergen, Svalbard, which is under consideration as a CO_2-storage reservoir). By making the analogy to electrical current in circuits, multi-scale networks can be analysed by conceptually treating macro-pore networks and microporosity as conducting in parallel (i.e. flow from one macro-pore to another can proceed through independent macroporosity and microporosity pathways) or in series (all flow from one macro-pore to another has to pass through microporosity) (Mehmani and Prodanović, 2014). The samples were selected because of their multi-modal pore size distribution, and because they are characterized by pore topologies which range from very highly connected macro-pores coupled in parallel with microporosity (Estaillades) to very poorly connected macro-pores which can only be reached through serially-coupled microporosity (the tight sandstones). The Savonnières and Massangis samples represent intermediary situations. In the following, each of the samples is discussed in more detail.

Estaillades limestone is a mono-mineralic, calcitic grainstone with a porosity around 25 % and a permeability around 250 mD (Bauer et al., 2012). Its porosity with bimodal pore sizes consists of intergranular macro-pores and intra-granular micro-pores with pore sizes smaller than approximately 1 μm, found in fossil grains (Youssef et al., 2008). Micro- and macroporosity each make up about half of the pore volume. The macro-pores are well connected to each other, resulting in the rock's rather high permeability. The microporosity thus conducts fluids mainly in parallel to the macro-pores. Estaillades has been used frequently as a test case for pore scale modeling and experiments, such as relative permeability studies (Moctezuma-Berthier et al., 2002; Gharbi and Blunt, 2012; Prodanović et al., 2014; Bauer et al., 2012; Ott et al., 2015). This is the same sample as the one discussed in Chapters 4 and 5, where our model's relative permeability predictions for drainage and imbibition were compared to experimental data and found to match well.

Savonnières is a mono-mineralic, layered, oolithic grainstone with a porosity of 22 % to 40 % and a permeability ranging from 115 to more than 2000 mD, depending on local variations (Derluyn et al., 2014). The porosity consists of four pore types: intergranular and micro-connected macroporosity (hollow ooids), next to intergranular and intra-ooidic microporosity. The hollow ooids are only connected to the other macro-pores by microporosity in the ooid-shells (Roels et al., 2001). This

sample was also inspected in Chapter 5.

The Massangis Jaune variety of the Massangis limestone is an ooid-dominated grainstone containing detrital micrite and bioclasts. Within the bulk of this rock, patches of several cubic centimetres with a different microstructure and a lower porosity occur seemingly randomly (Boone et al., 2014). The bulk, from which the sample was selected, has a porosity of 11.6 % (measured by mercury intrusion porosimetry (MIP) to avoid averaging the porosity of the bulk and the patches) (Boone et al., 2014). It contains interparticular moldic macro-pores due to dedolomitization. The macro-pore network may or may not percolate, depending on the local amount of (de)dolomitization. Depending on this, permeability can range from 70 mD (measured by portable permeameter) to values on the order of 0.03-0.07 mD (Casteleyn et al., 2010; Makhloufi et al., 2013). Microporosity can be found in the partially dissolved dolomite lining the moulds and in local ooids.

The Wilcox tight gas sandstone is a plagioclase arkose, and thin section analysis indicated that the rock contained 2.9 % of primary porosity and 3.1 % of secondary porosity in the form of micro-pores in clay clasts and dissolved feldspars (Mehmani et al., 2015a). An experimental permeability measurement is at present not available. MIP experiments show a high intrusion pressure, and point to a non-percolating macroporosity network, which is however connected by the microporosity (Mehmani et al., 2015a).

The sandstone sample from the Knorringfjellet formation was cored from a depth of 681 m in drill hole 4 of the Longyearbyen CO_2 Lab project (Van Stappen et al., 2014). The sample was measured to have a porosity of 7.54 %, another sample from the same sandstone bed had a porosity of 8.73 % and a permeability of 0.07 mD (Braathen et al., 2009). In accordance with this low permeability, the pore size distribution from MIP (Van Stappen et al., 2014) shows a dominant peak between 100 and 500 nm, associated with secondary porosity in illite clay.

6.2.2 Imaging and image processing

All samples with the exception of Wilcox were micro-CT scanned at Ghent University's Centre for X-ray Tomography (UGCT). Estaillades, Savonnières and Knorringfjellet were scanned with the HECTOR scanner Dierick et al. (2014), Massangis was scanned with the set-up described in

Masschaele et al. (2007), and the Wilcox image (which is available from the Digital Rocks Portal (Prodanovic et al., 2015; Mehmani et al., 2015b)) was generated and provided by Ayaz Mehmani and Maša Prodanović (Mehmani et al., 2015a). Samples were cylindrical and ranged in diameter from 2.5 to 7 mm. Sample sizes and detailed scanning parameters of the samples scanned at UGCT can be found in Table 6.1.

Tomographic reconstruction was performed with Octopus Reconstruction software (Inside Matters, Belgium). Approximately inscribed cubes were cropped from the cylindrical samples. These 3D images were noise filtered and then segmented into three phases: pore voxels, solid voxels and voxels which contain unresolved porosity (i.e. microporous voxels). Noise filtering, segmentation and post-processing methods were carefully tuned to each individual sample, in order to obtain the best achievable result (by visual inspection). Applied noise filters include anisotropic diffusion and non-local means filtering, both implemented in Avizo (FEI, France), while the applied segmentation methods were hysteresis thresholding and watershed segmentation (Schlüter et al., 2014). The segmented images were post-processed with majority filters and thinning operations to remove spurious noise voxels and to alleviate artefacts caused by the erroneous classification of border voxels between pore and solid as microporous. Image processing was performed in Avizo (FEI, France), Octopus Analysis (Inside Matters, Belgium) and Fiji. Details of the applied image processing operations are provided in Table 6.1.

The segmentation work flow clearly introduces operator bias (Wildenschild and Sheppard, 2013), especially since segmentation of the microporous voxels was challenging in all samples. It should be noted that the segmentation significantly affects the extracted network models and the resulting simulation results, and can in fact be one of the pitfalls to obtaining reliable results by image-based pore scale modeling. While fully or partially automated multi-phase segmentation methods exist and are in constant development (Iassonov et al., 2009; Schlüter et al., 2014), these methods are not easily available and not always applicable to the problem at hand. Thus, like in most practical applications of micro-CT-based modelling, the problem of non-unique segmentation persists here. Nevertheless, comparison of model results to experimental data is in qualitative agreement for Estaillades and Savonnières (see Chapters 4 and 5) and makes the simulation results on the other rocks plausible (here, there were either no experimental results available for the exact same

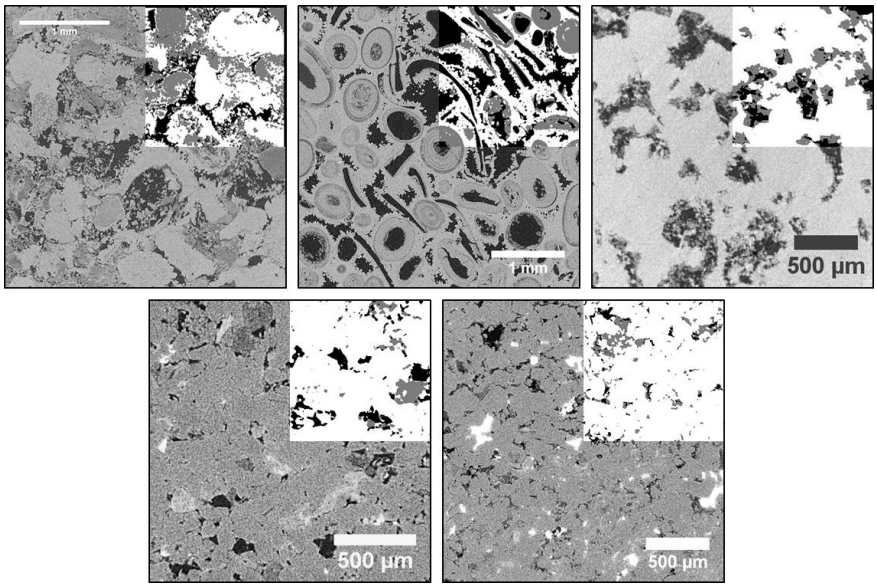

Figure 6.1: Micro-CT datasets of Estaillades, Savonnières and Massangis Jaune (top, left to right); Wilcox and Knorringfjellet (bottom, left to right) from which the networks were extracted. In the top right corner, a quarter of the corresponding slice from each segmented dataset is overlaid. In the segmentations, solid voxels are displayed in white, microporous voxels in grey and pore voxels in black.

sample, or there were no simulations performed with representative microporosity properties, see Section 6.3). Furthermore, note that our main interest here is not to replicate the exact petrophysical properties of the samples at hand, but rather to obtain pore structures which are representative for those found in natural porous media, and to investigate the link between these structures and the resulting relative permeability behaviour in a more general sense. Example slices showing the original micro-CT image and the segmentation of each sample can be found in figure 6.1.

6.2.3 Simulations

To investigate the dependence of the samples' relative permeability curves on the microporosity's properties, we generated three artificial microporosity PNMs. Note that these are not representative of the

Table 6.1: Sample sizes and scanning parameters of the six samples. Filtering, segmentation and post-processing were performed in Avizo, except where indicated with an asterisk, in which case Octopus Analysis was used. "AD" stands for Anisotropic Diffusion, "NLM" for Non-Local Means.

	Estaillades	Savonnières	Massangis	Wilcox	Knorringfjellet
Sample size (mm)	7	6	3.3	2.5	4
Voxel size (μm)	3.1	3.8	4.54	2.7	2.75
Scanner	HECTOR	HECTOR	Masschaele et al. 2007	-	HECTOR
Accelerating voltage (kV)	100	120	100	-	110
Target power (W)	10	10	8	-	10
Projections	2800	2400	1200	-	2500
Illumination (s)	2	1	4	-	2
Noise filter	Binormal*	AD	AD	AD	NLM
Image segmentation	Hysteresis*	Watershed	Hysteresis	Watershed	Watershed
Post-processing	Thinning*	Majority	Majority	Despeckle*	Despeckle

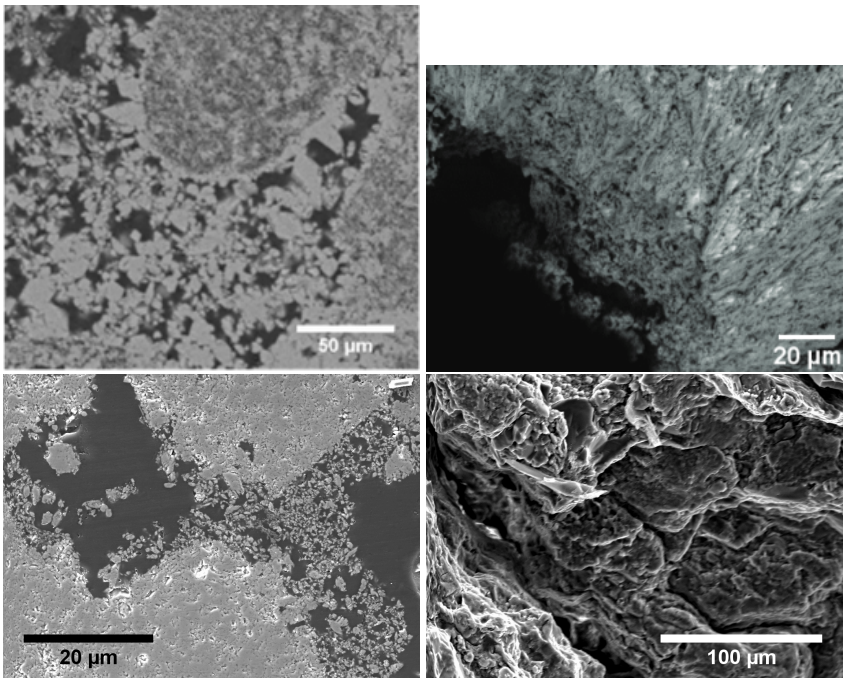

Figure 6.2: Scanning electron microscopy images of the microporosity in Estaillades, Savonnières, Massangis and Knorringfjellet (top to bottom, left to right), illustrating porosity features that are unresolved in the micro-CT scans. The Savonnières image is from Derluyn (2012). SEM images of Wilcox were not available at the time of writing.

microporosity in the investigated samples, and the multi-scale PNMs will thus not necessarily yield results that compare well to the samples' experimental petrophysical properties. The artificial networks' properties were set to investigate the influence of the microporosity's average pore size (permeability and capillary pressure) and more detailed structure (relative permeability) on the behaviour of the multi-scale networks. While this work is not aimed at thoroughly characterizing the microporosity in the presented samples, but rather at understanding the influence microporosity has on relative permeability behaviour in a broader sense, SEM images that visualize the microporosity in all samples except Wilcox can be found in figure 6.2.

To extract the single-scale microporosity PNM, we first generated a random sphere packing and extracted a PNM from it to obtain a realistic, yet general, porous medium topology. Then, the radii of the pores and

throats in this sphere packing-based network were changed according to normal distributions. In the first microporosity network (M1), the throat radii were drawn from a normal distribution with a mean of 120 nm and a standard deviation of 50 nm. The second microporosity network (M2) had an equally wide throat size distribution, but a mean throat size of 800 nm. The third microporosity network (M3) had a binormal throat size distribution, with 75 % of the pores distributed around 120 nm and 25 % around 800 nm (standard deviation of both normal distributions was 50 nm). Pore radii were adjusted after setting all throat radii, so that for each pore the ratio of its radius to the average radius of its connecting throats was preserved from the sphere packing-based network. Similarly, the throat lengths were adjusted to preserve the ratio between each throat's length and radius.

After generating the microporosity networks, primary oil flooding and secondary water flooding simulations were performed on these single-scale networks to obtain input parameters for the multi-scale simulations. In the oil flooding simulations, the contact angles were distributed between 30° and 60°. Due to the equally wide throat size distribution, M1 and M2 produced very similar K_r-curves, yet they had different permeabilities (0.2 mD vs 9.2 mD) and P_c-curves. The M3 network had a permeability close to that of M2 (7.5 mD), but yielded different P_c and K_r-curves. The single-scale microporosity network's P_c and K_r-curves are included in Appendix B, together with the other microporosity properties which are provided as input to the multi-scale simulations.

For the water flooding simulations, it is important to take into account the different wettability alteration scenarios which can cause non-uniform wetting by absorption of polar compounds from the oil phase on mineral surfaces (Skauge et al., 2007; Buckley et al., 2007). As introduced in Chapter 5, the small pores may become oil-wet while the large ones remain water-wet (the "mixed-wet small" or MWS case), or vice versa (the "mixed-wet large" or MWL case), or the oil-wet pores may be uncorrelated to size (the fractionally-wet or FW case).

Multi-scale water-flooding simulations were performed for the water-wet (WW) case and for the three mixed-wet cases, by setting the appropriate contact angles in the macro-pores and selecting the appropriate input properties for the microporosity. Oil-wet pores were assigned contact angles randomly distributed between 120° and 150°, water-wet pores

between 30° and 60°. In the MWS simulations for example, the macro-pores and throats were assigned contact angles between 30° and 60°, and the input properties for the microporosity were calculated on single-scale microporosity networks with contact angles between 120° and 150°. To account for all wettability scenarios, the secondary water flooding on the microporosity networks was thus performed for three different wettability cases: water-wet, oil-wet and fractionally wet (50 % volume of oil-invaded pores remained water-wet and 50 % became oil-wet). In the fractionally wet simulations, the oil-wet pores were distributed randomly with respect to the pore/throat size, but were spatially correlated as this tends to be more realistic (Blunt, 2016). In this case, the oil-wet regions had a size of 10 pores across. For brevity, we do not show fully oil-wet results, as these give similar results to the primary drainage simulations, only with water as the invading phase.

6.3 Results

6.3.1 Network characteristics

The network characteristics of the extracted PNM are useful to analyse the pore structure of the samples. Table 6.2 summarizes the properties of the five extracted PNM. Next to the coordination number (CN), which represents the average amount of macro-throats connected to a macro-pore, we also look at the size of the largest connected macroporosity cluster, the percentage of pores connected to microporosity, the percentage of macro-throats with a parallel micro-link, and the amount of micro-links in the minimal spanning forest (MSF) of the network. The MSF is a concept adapted from graph theory. Consider the multi-scale network as a graph made of vertices (pores) and links (macro-throats or micro-links). The MSF is the sub-graph with exactly one path between any two connected vertices in the multi-scale network, with the minimum total length travelled through micro-links. The percentage of micro-links in the MSF expresses the importance of microporosity coupled in series with macroporosity in the multi-scale network, because the MSF is the sub-graph without loops which only contains the shortest possible micro-links that are absolutely necessary to appropriately connect all the pores. The MSF was calculated using Kruskal's algorithm (Kruskal, 1956).

Analysing the volume of the largest connected cluster of macroporosity (i.e. ignoring the micro-links) shows that nearly all of the macroporosity is connected in the Estaillades case. Estaillades is the most well-connected network investigated here, with an average macroporosity coordination number (CN) of 4.46. Micro- and macroporosity will thus act as two parallel pore systems during the flow simulations (71 % of macro-throats have a micro-link in parallel), which are connected to each other at most pores (91 % of pores are connected to microporosity). This results in a rather high permeability, which has a weak dependence on the properties of the microporosity (table 6.2). Only 4 % of the MSF consists of micro-links, meaning that serially coupled transport through the microporosity is of minor importance in this sample.

In Savonnières, the macroporosity falls into two categories: well-connected macro-pores (60 % connected into one single macro-pore cluster) and isolated macro-pores within hollow ooliths (30 % of the macro-pore space). The latter are however connected to the large macro-pore cluster by micro-links in the multi-scale network. Even when disregarding the isolated pores, the connectivity is lower than in Estaillades (CN 3.5). The well-connected macroporosity dominates the permeability, and in these pores we can expect a similar behaviour as in the Estaillades' network. In Savonnières, 95 % of macro-pores are connected to microporosity, and 79 % of macro-pores have a micro-link coupled in parallel, which is comparable to Estaillades. However, 16 % of the MSF consists of micro-links that serially connect 30 % of the macroporous volume to the rest of the pore space. The pathways through microporosity do not represent a strong contribution to the flow rates, as indicated by the weak dependence of the permeability on the microporosity type. However, the hollow ooid pores may be important potential sites for capillary trapping.

The Massangis sample lies on the transition from parallel-dominated to serial-dominated flow, due to the pore-lining microporosity which may or may not block the passage between neighbouring pores and therefore results in a lower CN than in Savonnières and Estaillades (2.6). Due to the pore-lining nature of the microporosity, nearly all macro-pores (i.e. 99 %) are connected to microporosity, and most macro-throats have a parallel micro-link (92 %). Similarly to Savonnières, 16 % of the MSF consists of micro-links. However, the structure of the network is different: there are multiple, still relatively large clusters of connected macroporosity, each of

which does not percolate the sample. The introduction of a relatively small amount of micro-links, which represent serially coupled microporosity, reconnects the isolated clusters and provides percolation. By its very nature however, the serially coupled microporosity dominates the permeability, as evidenced by the permeability's strong dependence on the microporosity's properties.

In both tight sandstone samples, clusters of connected macro-pores are small: the largest clusters only make up about 5 % of the macroporosity volume in both samples. This is associated with very low CN. Wilcox has the lowest amount of macro-pores connected to microporosity of all investigated samples (65 %) and accordingly the lowest amount of macro-throats with parallel micro-links. The amount of (serial) micro-links in the MSF is higher than in the investigated carbonates, yet still only makes up 22 % in Wilcox and 28 % in Knorringfjellet. Nevertheless, the flow behaviour in the tight sandstones is strongly dominated by serial coupling, due to the isolated nature of connected clusters of macroporosity. This is evidenced by the strong dependence of the permeability on the microporosity type. Knorringfjellet has the smallest pore and throat sizes and is the tightest sample investigated here. It should be noted however that the absolute permeabilities are influenced by the micro-link cut-off length, and are thus to be taken as an indication of the order of magnitude of the permeability associated with these networks.

6.3.2 Oil flooding simulations

Capillary pressure and relative permeability results from the oil flooding (i.e. primary drainage) simulations can be found in figures 6.3 and 6.4. Estaillades and Savonnières display similar behaviour: the capillary pressure curves show that the well-connected macroporosity is almost completely drained first, followed by the microporosity. This results in a rapidly increasing $K_{r,o}$. In Estaillades, microporous flow paths have a negligible influence on the flow rates, resulting in very small differences in the network's relative permeabilities calculated with M1, M2 and M3 microporosity. The qualitative behaviour fits well with experimental measurements on Estaillades samples, performed by Ott et al. (2015) and Moctezuma-Berthier et al. (2002). In Savonnières, the influence of the microporosity type is larger, because the micro-connected macro-pores

Table 6.2: Network properties

	Estaillades	Savonnières	Massangis	Wilcox	Knorringfjellet
Voxel size (μm)	3.1	3.8	4.53	2.7	2.75
Network size (voxels)	1000x1000x1001	1000^3	501x482x600	630^3	800^3
Number of nodes	92398	30155	13126	13752	27579
Number of links	207216	45017	17466	11664	18991
Average CN	4.46	2.95	2.62	1.66	1.18
Largest macro-pore cluster volume (%)	95.3	59	24.1	5.3	4.8
Macro-throats with parallel micro-link (%)	70.5	78.9	91.5	56.5	79.4
Pores connected to microporosity (%)	91.4	95.5	99.1	64.8	87.0
Micro-links in minimal spanning forest (%)	3.6	15.8	15.6	21.6	28.2
Total porosity (%)	20.1	34.2	9.5	6.8	4.1
Microporosity fraction of pore space(%)	43.4	34.4	38.9	33.3	49.6
Permeability M1 (mD)	120.4	109.1	0.44	0.02	0.008
Permeability M2 (mD)	131.5	128.3	5.38	0.5	0.27
Permeability M3 (mD)	134.7	134	6.6	0.64	0.36

can add extra flow paths. As the permeability of the microporosity increases ($k_{M1} << k_{M3} < k_{M2}$), the importance of these flow paths to the full multi-scale network's permeability increases. Therefore, the situation where the well-connected macroporosity cluster is fully drained ($S_w \approx 0.5$) does not correspond to $k_{r,o} \approx 1$ for M2 and M3, and $k_{r,o}$ thus rises more slowly in these cases than in the M1 case. For the same reason, $k_{r,w}$ falls less quickly in simulations with M2 and M3. Note that the microporosity type influences the pressure at which the micro-connected macro-pores are invaded, causing the P_c curves for M2 and M3 to cross each other.

The two-phase flow behaviour of Massangis and the tight sandstones depends more strongly on the microporosity type. The P_c-curves for Massangis are less flat than those of the tight sandstones. This is caused by the fact that after invading a cluster of macroporosity, the oil percolates through short neighbouring micro-links at fairly low breakthrough capillary pressures, allowing it to invade a next macroporosity cluster. The pore-lining nature of the microporosity in this sample, which clogs pore throats connecting large clusters of macro-pores, thus allows a large part of the macroporosity to be drained while the microporosity still has a high water saturation. In the tight sandstones, the macroporosity is so poorly connected that oil percolation through a few short micro-links has a very small effect. The micro-links' breakthrough pressures thus strongly dominate the P_c-curves.

In Massangis, the $k_{r,w}$-curve is still relatively similar to Estaillades and Savonnières, because at high S_w (>0.8) the decrease of the water flow rate is dominated by the drainage of macro-pores. The high and relatively constant water content in the microporosity during this part of the drainage process allows water to percolate the sample. The $k_{r,o}$ however shows a more similar behaviour to that of the tight sandstones. Oil only starts flowing at much lower S_w than in the other carbonates, but $k_{r,o}$ then rises more quickly. This is related to the oil relative permeability of the microporosity, which does not allow oil flow if the water saturation in the microporosity is high. Note that for the same reason, $k_{r,o}$ is lower for tighter microporosity types in Massangis (contrary to the behaviour for Estaillades and Savonnières).

In the tight sandstone samples, the water relative permeability drops down very quickly during drainage, and the so-called "permeability jail" behaviour emerges (Shanley et al., 2004; Cluff and Byrnes, 2010): there is

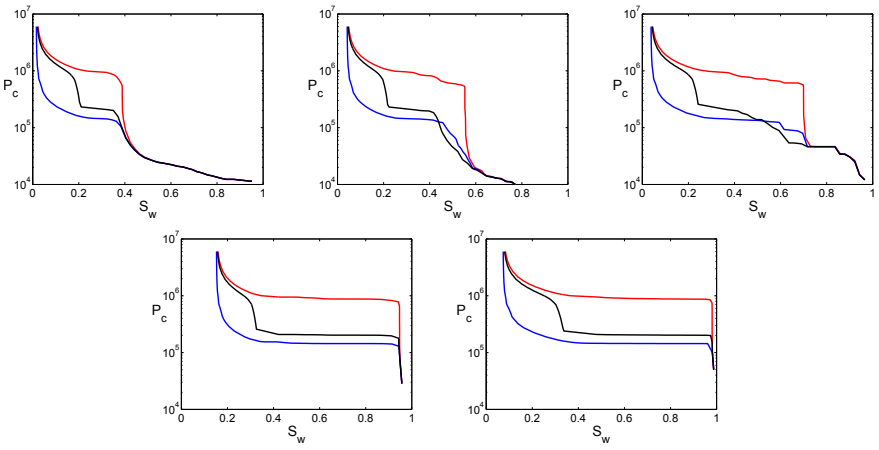

Figure 6.3: Drainage capillary pressure curves for Estaillades, Savonnières and Massangis Jaune (top, left to right); Wilcox and Knorringfjellet (bottom, left to right). M1 in red, M2 in blue and M3 in black.

a large range of the saturation over which both fluids appear immobile, at least within laboratory time frames. This behaviour has been observed experimentally in tight sandstones (Shanley et al., 2004; Cluff and Byrnes, 2010). The fast decrease of the $k_{r,w}$-curve, which is commonly seen in experiments on tight reservoir rocks, occurs in the network because all the macro-pores and throats connected to the inlet are drained first, strongly reducing the flow of water through the network. In core flooding experiments, a similar behaviour can be expected, but water flow might be higher if the microporosity connects throughout the sample. Very rapidly decreasing permeabilities to water were observed experimentally in samples from the same drill hole in the Knorringfjellet Formation (Farokhpoor et al., 2010, 2013), indicating that this is indeed qualitatively realistic behaviour for the investigated samples.

6.3.3 Water flooding simulations

After primary oil-flooding, secondary water-flooding simulations were performed on the five samples. The P_c- and K_r-curves for the water-wet case can be found in figures 6.5 and 6.6, respectively. Comparing the simulations with different microporosity input properties, we see only a minor influence of the microporosity's permeability and input P_c-curve on the resulting K_r-curve, as evidenced by the small difference between the

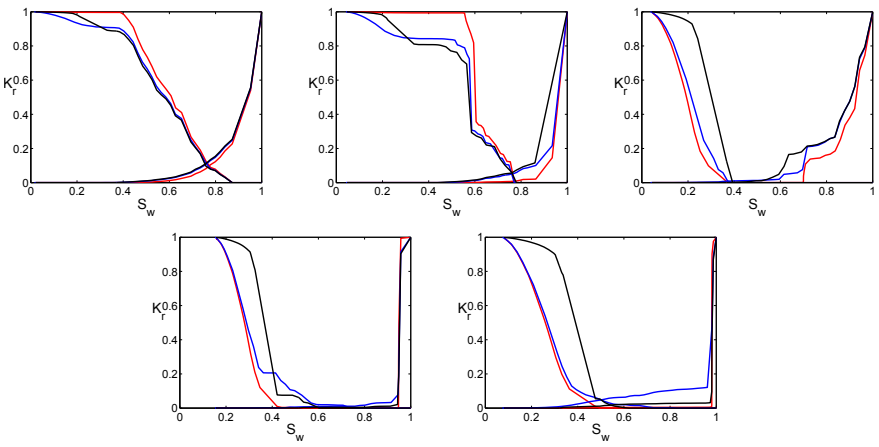

Figure 6.4: Drainage relative permeability curves for Estaillades, Savonnières and Massangis Jaune (top, left to right); Wilcox and Knorringfjellet (bottom, left to right). M1 in red, M2 in blue and M3 in black.

simulations with M1 and M2 microporosity. In the Massangis and the tight sandstone samples, where serial coupling between macroporosity and microporosity is important, there is a stronger dependence on the microporosity's K_r-curve than in the Estaillades and Savonnières samples. This can be seen by comparing the simulations with M3 to those with M1 and M2, taking into account that M1 and M2 have very similar K_r-curves, which differs from that of M3. All samples show rather high residual oil saturations and low end-point water relative permeabilities. Comparing the trapping efficiencies (the amount of trapped oil over the initial oil saturation at the start of water flooding) for the water-wet case with M1 microporosity in figure 6.9 shows that there is less trapping in the well-connected samples (Estaillades en Savonnières), because oil can escape from the macroporosity. In the other samples, all oil initially present in macro-pores is trapped, while the amount of trapping in micro-pores is fully determined by the input properties of the microporosity.

Figures 6.7 and 6.8 show results for simulations under different wettability circumstances (water-wet, mixed-wet small, mixed-wet large and fractional-wet) with M1 microporosity. Simulations with M2 and M3 yield similar results and can be found in Appendix B. In the MWS case, the macro-pores are filled with water before the microporosity. For this wettability type, the lowest trapping efficiencies in the macroporosity are

found when macro-pores are well-connected and have a high CN (e.g. Estaillades) or when many macro-throats have micro-links coupled in parallel, allowing more oil to escape through microporous pathways (e.g. in Massangis). Even though Wilcox has a higher CN than Knorringfjellet, it has a higher overall trapping efficiency in this case, due to having a lower amount of pores connected to microporosity and a lower amount of parallel micro-links. Note that at the end of the simulations, all the oil in microporosity is trapped in our model, because it does not take into account that there may exist percolating flow paths entirely through microporosity. In samples where this is the case, forced water-flooding could lead to very low residual oil saturations, but recovery would take place very slowly once the water saturation rises above the end points of the simulations presented here.

The MWL wettability scenario leads to strongly reduced residual oil saturations compared to the water-wet case in the Estaillades and Savonnières samples, due to the existence of oil films in the macro-pores and throats, which percolate the sample and allow the oil to escape. This fits with the observations made by Skauge et al. (2007), who found lowest residual oil saturations in MWL and highest in MWS cores of 13 different North Sea reservoirs, and is supported by Gharbi and Blunt (2012). In the tight samples on the other hand, the macroporosity does not percolate the sample, and therefore the oil films which only exist in the oil-wet macroporosity do not allow the oil to escape.

For all samples except Estaillades, the FW case gives the lowest amount of trapping (in Estaillades, the MWL case allows nearly all oil to escape, as explained in the previous paragraph). This is due to the fact that parts of the macro- and microporosity are invaded with water alternately, while other parts are still oil filled. Therefore, oil can flow through an interconnected network of both pore types until high water saturations.

6.4 Discussion

6.4.1 Oil flooding

The results in Section 6.3.2 indicate that the multi-phase flow properties of rocks with a dual porosity depend greatly on the connectivity structure of the macro-pores. When a significant part of the macro-pores are strongly

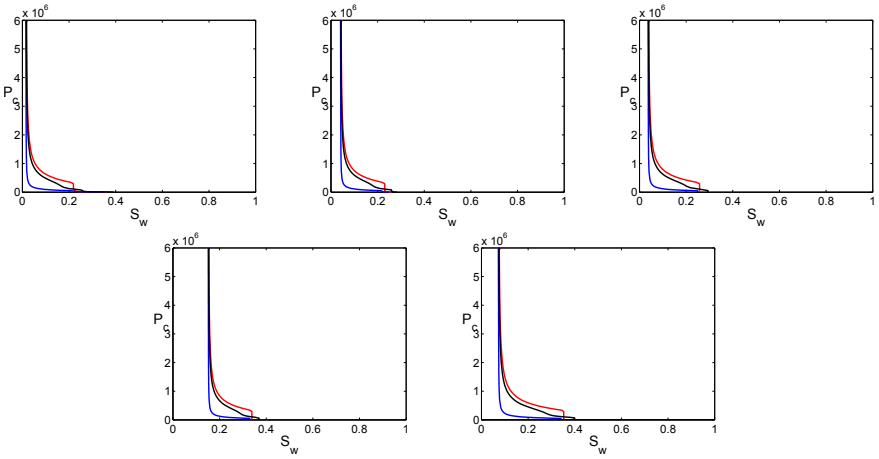

Figure 6.5: Fully water-wet imbibition capillary pressure curves for Estaillades, Savonnières and Massangis Jaune (top, left to right); Wilcox and Knorringfjellet (bottom, left to right). M1 in red, M2 in blue and M3 in black.

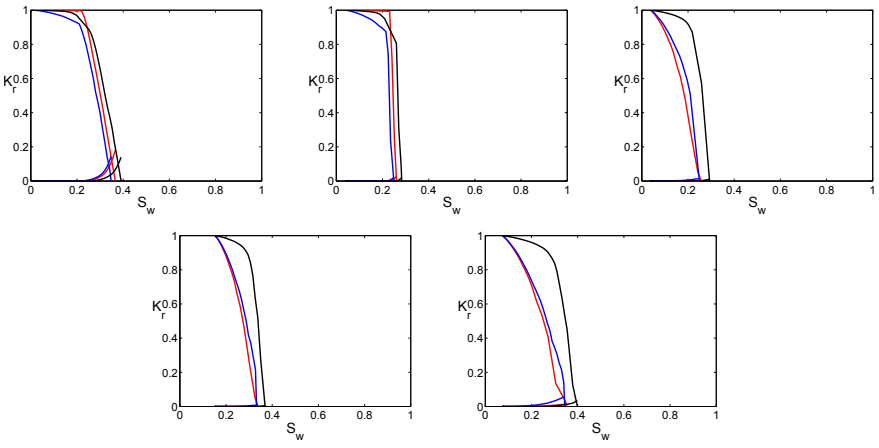

Figure 6.6: Fully water-wet imbibition relative permeability curves for Estaillades, Savonnières and Massangis Jaune (top, left to right); Wilcox and Knorringfjellet (bottom, left to right). M1 in red, M2 in blue and M3 in black.

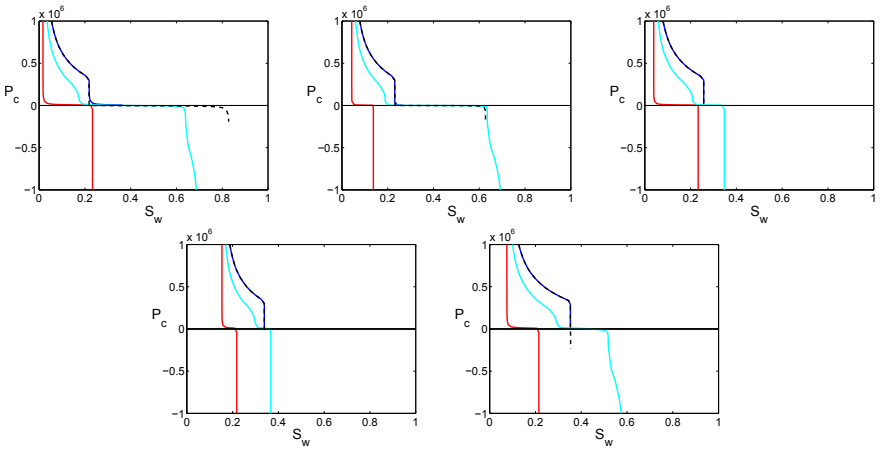

Figure 6.7: Water flooding capillary pressure curves in Estaillades, Savonnières and Massangis Jaune, Wilcox and Knorringfjellet (top to bottom, left to right) for the M1 case. SWW in blue, MWS in red, MWL in black and FW in cyan.

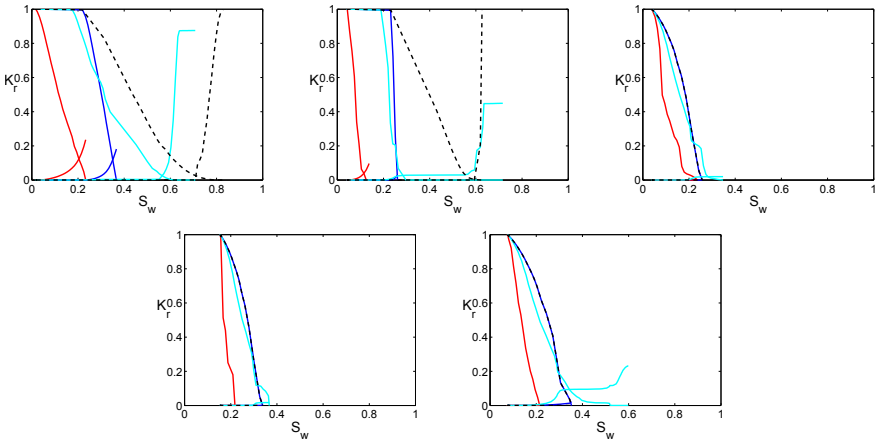

Figure 6.8: Water flooding relative permeability curves in Estaillades, Savonnières and Massangis Jaune, Wilcox and Knorringfjellet (top to bottom, left to right) for the M1 case. SWW in blue, MWS in red, MWL in black and FW in cyan.

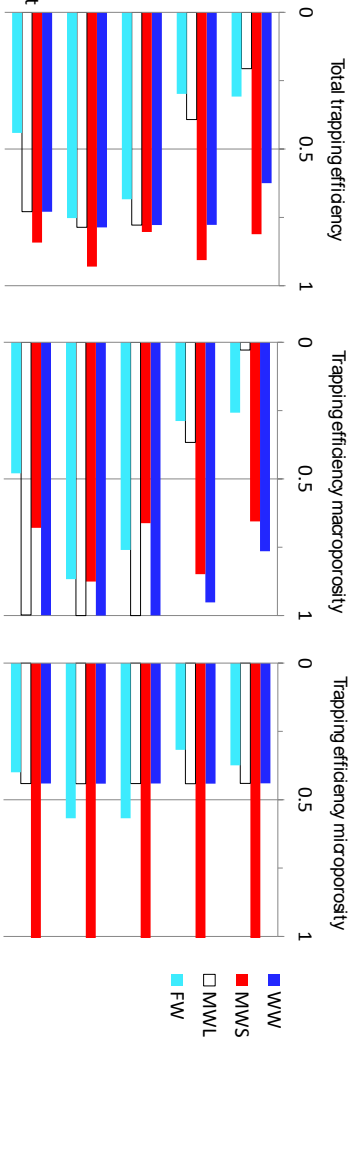

Figure 6.9: Trapping efficiencies (amount of trapped oil over amount of oil which could be introduced in the sample during primary drainage) for Estaillades, Savonnières and Massangis Jaune, Wilcox and Knorringfjellet, in the MI case, for the full network (left), the macroporosity (middle) and the microporosity (right).

connected to each other, as indicated by a high CN and large connected clusters of macro-pores, the flow through microporosity is likely small compared to the total flow. In this case, the microporosity is coupled mainly in parallel to the macro-pores, and will remain water-filled until nearly all macro-pores are drained. In such rocks (e.g. Estaillades), the influence of the microporosity on the drainage relative permeability curves is mostly limited to its impact on the saturation, i.e. the curves shift to the right in the graph. Since microporosity tends to retain water, fluid flow through it also tends to lower $K_{r,o}$ and increase $K_{r,w}$. Logically, this effect is stronger when the permeability of the microporosity is larger, yet in most cases where micro-pores are significantly smaller than macro-pores, it may be regarded as a rather small perturbation. The Savonnières simulation shows that when a well-connected part of the macroporosity is connected to a small or moderate amount of macro-pores which can only be reached through microporosity, this perturbation may be larger, and the influence of the microporosity's presence on the P_c-curve can be harder to predict. This was also found by Mehmani and Prodanović (2014). The inclusion of such "micro-connected" macro-pores is characterized by a decrease of the CN and an increase in microporosity flow paths connected in series to macro-pores. The latter can be characterized by the amount of micro-links in a minimal spanning forest of the network.

If the presence of microporosity reduces the connectivity of macro-pores, e.g. if it is pore filling or pore lining and sufficiently thick, serial coupling of macro- and microporosity may start to dominate the behaviour. While the CN is in these cases typically rather low and the minimal spanning tree of the network contains a significant amount of connections through microporosity, the most salient feature of such networks is that the macroporosity consists of several clusters, which are only connected to each other through microporous connections. This is the case in the Massangis, Wilcox and Knorringfjellet samples. The drainage oil relative permeability in these networks remains very low until most macro-pores are drained, and only rises at saturations associated with high capillary pressures. Macro-pores are drained at the lowest capillary pressure for which oil can percolate through the microporous regions that connect them to the inlet face of the network. When this capillary pressure is reached, the water saturation decreases, yet the oil flow rate does not increase immediately, as the microporosity's relative permeability to oil is likely very low right at the percolation threshold. The onset of the oil flow thus depends strongly on the microporosity's oil breakthrough saturation and

relative permeability curves. The lower the oil saturation in the microporosity at which oil can percolate through it and invade a neighbouring macro-pore, the later the onset of the oil flow in the multi-scale network occurs. This is caused by the fact that a lower oil breakthrough saturation in the microporosity causes a higher water saturation (and correspondingly a lower $K_{r,o}$) in the microporosity at the same total water saturation of the sample. The relative permeability to water in these rocks is more strongly influenced by the connectivity of the macro-pores: lower connectivities tend to result in a very fast $K_{r,w}$ decrease, as the drainage of a few macro-pores at the inlet face of the network then blocks water flow paths. In the investigated tight sandstones, the $K_{r,o}$ and $K_{r,w}$ behaviour results in a permeability jail. The occurrence and the width of the permeability jail depends on the microporosity's properties, on its volume relative to the macroporosity, and on the arrangement of microporous zones in the multi-scale pore space. The jail tends to widen when the scale difference between the macro-and micro-pores increases, as finite size scaling lowers the microporosity's breakthrough oil saturation for decreasing microporosity pore sizes. This observation could partially explain the observations of Cluff and Byrnes (2010): the width of the permeability jail in tight sandstones tends to increase with decreasing permeability. While these authors ascribe the observed permeability jail to the occurrence of slit-shaped pore throats, our results suggest that the behaviour could also be influenced by pore-blocking microporosity in the form of e.g. clays.

6.4.2 Water flooding

In the water-wet case, all the investigated samples showed rather high residual oil saturations and low end-point water relative permeabilities. This is due to the heterogeneity of the investigated samples: the smallest pores are invaded with water resulting in low water flow rates, while the oil in the large pores has a high probability of being trapped. In the samples with well-connected macroporosity, the amount of trapping increased with decreasing CN, and was therefore lowest in Estaillades and highest in Massangis. For similar reasons, the end-point water relative permeability is highest in Estaillades and lowest in Massangis. These generic observations are confirmed by single-scale image-based network models extracted from carbonates (Gharbi and Blunt, 2012) and by experiments (Al-Sayari, 2009; Tanino and Blunt, 2012). In networks

where macro-pores exist in non-percolating clusters connected by microporosity (Massangis, Wilcox and Knorringfjellet in this Chapter), the model predicts that essentially all of the oil initially present in macroporosity is trapped. Differences in the amount of trapping thus result due to different ratios of macro-and microporosity present and due to the properties of the microporosity (i.e. the residual saturation of the microporosity as a separate porous medium). The properties of the macro-pores, e.g. the CN, seem to be less important in such cases. Measurements of residual non-wetting saturations in tight sandstones are rare in the literature, due to the experimental difficulty of performing these measurements (particularly at high initial non-wetting saturations). Qualitatively, the high residual saturations in the tight sandstone simulations are consistent with mercury drainage/imbibition measurements on Mesaverde low-permeability sandstones (Cluff and Byrnes, 2010).

When macro-pores are water-wet and micro-pores oil-wet (MWS), macro-pores are filled with water first, leaving a high amount of oil in the microporosity trapped. The amount of trapping in the macro-pores is strongly influenced by the connectivity (CN) of macro-pores and the persistence of oil flow paths through microporosity coupled in parallel to the macroporosity. In tight materials with very low CN (e.g. the tight sandstones investigated here), the latter can be the dominant factor. The MWS scenario is similar to the observation of Gharbi and Blunt (2012), who investigated fractionally-wet carbonate pore networks and found the highest residual oil saturation when there is a low amount of oil-wet pores; in this case, the oil films do not connect throughout the network to allow the oil to escape, but the water-wet regions fill with water first and surround the oil-wet parts.

If macro-pores are oil-wet and micro-pores water-wet (MWL), oil films in the macro-pores may lead to strongly reduced residual saturations. However, this is not the case for pores from which oil needs to pass through microporosity to escape (e.g. Massangis, Wilcox and Knorringfjellet networks, and the isolated pores in the Savonnières network). If these pores form the majority or all of the network, the relative permeability and residual saturation may not differ much from the water-wet case. In that case, the sample's relative permeability behaviour is dominated by the relative permeability of the microporosity, and essentially all of the oil in macro-pores is trapped because the retreating oil

in the micro-pores loses connectivity before (i.e. at much higher pressure) the macro-pores can be invaded with water. This can be important for practical applications, as certain clays may remain water-wet, leading to an MWL wettability distribution (Skauge et al., 2007).

In the case where randomly distributed patches of macro-and micro-pores are water- and oil-wet (FW), parts of the micro-and macroporosity are alternately invaded. When the inter- and intra-scale connectivity and size of the patches is favourable, this wettability type can lead to low residual saturations, as an interconnected network of macro-and microporous oil flow paths may exist.

As can be expected, the differences between the three mixed-wettability scenarios are larger for the rocks with multi-scale pore spaces investigated here, compared to the more homogeneous, single-scale rock investigated in Valvatne and Blunt (2004). This underlines the need for pore scale simulations on rocks with wide pore size distributions.

6.5 Conclusion

The capillary pressure and relative permeability behaviour of rocks with wide pore size distributions is in many cases still poorly understood. In this Chapter, the micro-CT based multi-scale pore network model presented in Chapters 4 and 5 was applied to study drainage and imbibition in two important classes of ”difficult” rocks: carbonates and tight sandstones. Aside from the intended insights into the flow behaviour, this sensitivity study is also motivated by the recent emergence of 3D imaging experiments with nm-resolutions, e.g. FIB-SEM (Keller et al., 2013; Hemes et al., 2015) and ptychography (De Boever et al., 2015; Holler et al., 2014). When considering such experiments, which are often expensive and difficult to perform, it is important to investigate the level of detail needed to describe or predict the effective flow behaviour. The results indicate that the microporosity properties have a larger and less predictable effect on the two-phase flow properties in networks where macroporosity and microporosity conduct more in series (e.g. in the investigated tight sandstones), compared to where they mainly conduct in parallel (e.g. in Estaillades and Savonnières carbonate). This concurs with earlier results from (Mehmani and Prodanović, 2014) on process-based network models.

The presented simulations allowed to qualitatively investigate how the total pore system influences the drainage behaviour. As the flow became more dominated by the microporosity due to the coupling of the different pore systems, we observed a later breakthrough of the non-wetting phase and a faster decrease of the wetting phase permeability in the model. Depending on the properties of the microporosity, this can result in a ”permeability jail”, meaning that both fluids are essentially immobile over a wide range of saturations. This behaviour, which has been described in the literature on tight gas sandstones (Shanley et al., 2004), seemed more likely to occur in the simulations when the macro-pores were poorly connected to each other, when there was a large scale difference between the macro- and micro-pores, and when the microporosity had a flat non-wetting phase relative permeability curve. Understanding the differences in the drainage behaviour between traditional reservoirs and tight systems is crucial in oil and gas exploration from unconventional reservoirs (Shanley et al., 2004).

In addition to primary drainage by oil flooding, we also investigated secondary water flooding (noting that the terms ”oil” and ”water” are used as arbitrary designations for immiscible fluids). The tight samples generally showed higher trapping efficiencies than the samples with well-connected macro-pores. Furthermore, the pore structure was seen to influence the response of the system to wettability alteration in different parts of the pore space. For example, simulations where only the macroporosity was oil-wet showed low residual oil saturations in the well-connected carbonates, while they did not result in a decrease of trapping in the tight sandstones. Such findings could prove important to understand the behaviour during wettability alteration by surfactants in fractured gas reservoirs (Kathel and Mohanty, 2013; Naik et al., 2015), where the goal is to increase recovery by spontaneous imbibition.

While the work presented here may contribute to the understanding of two-phase flow processes in carbonates and tight sandstones, care should be taken when generalizing the results, as the current investigation was based on a limited number of rocks. Furthermore, future work aimed at predictive modeling should focus on a number of remaining challenges. These are related to both the description of the microporosity, which should be based on experiments and incorporate the variability throughout the rock, as the general pore network modeling approach. The latter is faced with a high number of tuning parameters (including a length cut-off for the micro-links)

and incorporates simplifications (e.g. simplified pore shapes) which may not always be applicable. Further uncertainties arise from the micro-CT imaging and image segmentation, which are not straightforward in samples with multiple pore scales. Another subject in need of further research is how to include narrow slit-shaped pore throats between the macro-pores, which may fall below the image resolution of the micro-CT scans, and may cause connectivity between the macro-pores that is not well described by representing it as microporosity in the network.

Part III

Pore scale visualization

7

Advances in fast, laboratory-based micro-computed tomography

A theory is something nobody believes, except the person who made it. An experiment is something everybody believes, except the person who made it.

– Albert Einstein

This chapter treats the current state-of-the-art in fast laboratory-based micro-computed tomography, and the methodological advances we made at UGCT in this field. It forms an introduction to chapter 8, which describes the use of this technology to study the dynamics of drainage in rocks at the pore scale.

This chapter is based on a publication in Advances in Water Resources: Bultreys et al. (2016a), *"Fast laboratory-based micro-computed tomography for pore-scale research: Illustrative experiments and perspectives on the future"*

7.1 Introduction

As outlined in Chapter 3 (section 3.1), the recent increase in the availability of laboratory-scale micro-CT instrumentation has enabled many researchers to characterize the pore space of geomaterials in 3D on an almost routine basis, although a number of limitations in both the acquisition and the analysis of micro-CT data persist. For example, the acquisition time is typically on the order of 30 minutes to a few hours, the attainable spatial resolution is often on the order of 1 to a few microns and both depend on the size of the studied sample. While 3D pore space characterization is an essential part of any pore scale transport or degradation study, it does not provide insight into the dynamics of the processes under investigation. To avoid image blurring (and other motion artefacts), the imaged sample should remain unchanged during the micro-CT acquisition. Therefore, there is a need for fast, time-resolved 3D (i.e. 4D) imaging of a material's microstructure while such a process is taking place, as the only alternative is imposing quasi-static conditions by halting the process during every imaging experiment (Maire and Withers, 2014).

Extremely fast micro-CT imaging has become available at synchrotrons over the last few years, attaining even sub-second time resolutions (Mokso et al., 2010; Rack et al., 2010; Wildenschild and Sheppard, 2013; Maire and Withers, 2014). Some notable examples of pore scale imaging (in a geological context) at the sub-minute time scale of two-phase flow are provided by Berg et al. (2013); Hoogland et al. (2013); Youssef et al. (2013) and Armstrong et al. (2014b), and reactive flow was investigated by Menke et al. (2014). Other examples of fast imaging of porous media at synchrotron institutions can be found in Eller et al. (2011); Baker et al. (2012) and Sedighi Gilani et al. (2013). While synchrotron experiments are proving to be very valuable, the restricted accessibility of synchrotrons limits the amount of experiments which can be performed. Therefore, the development of laboratory-based fast (sub-minute) micro-CT scanning can prove important, as it would drastically increase the availability of 4D imaging with sub-minute time resolutions. Fast lab-based micro-CT would also allow researchers to prepare 4D experiments in the lab before performing them with higher temporal or spatial resolutions and with better image quality at a synchrotron. This would be of high value to help optimize the use of synchrotron beam time.

Despite the desirability of fast lab-based micro-CT, the much smaller X-ray flux in lab-based systems bounds the time resolution which can be attained. Just like an underexposed photograph appears noisy due to photon counting statistics, the restriction on the X-ray flux in laboratory sources limits the image quality for short acquisition times. Other complications which may occur are for example insufficient angular sampling, too long detector read-out times and limited rotation speed. Despite the fact that rather little attention has been given to this topic in the literature (with the exception of work performed by researchers at the Australian National University, e.g. Myers et al. (2011a,b); Sheppard et al. (2014)), advances in micro-CT hardware and in reconstruction and analysis software are starting to render sub-minute pore-scale experiments possible at laboratory set-ups. Figure 7.1 illustrates the progress in attainable spatial and temporal resolution in micro-CT over the years, both at synchrotron and in typical laboratory-sources (Maire and Withers, 2014).

In this chapter, we outline the current state of the art and the expected future development of fast lab-based micro-CT imaging. In section 7.2, we discuss the optimization of various hardware and software components. We illustrate the progress made in fast lab-based imaging by showing experiments that visualize advective/diffusive mass transport of a salt (CsCl) in a water-saturated Savonnières limestone (section 7.3) and, in the following chapter, drainage of a Bentheimer sandstone (Chapter 8). In both experiments, the acquisition time per full micro-CT scan was 12 seconds, with a voxel size of 14.8 μm. While, naturally, the data quality is not as good as what can be expected from similar experiments performed at synchrotrons, the experiments performed during this PhD work illustrate that many interesting aspects of transport processes in individual pores can be studied with fast lab-based micro-CT, even without applying special reconstruction algorithms. To our knowledge, these experiments are the fastest in-situ, lab-based pore-scale micro-CT measurements of this kind described in the literature until now. They simultaneously illustrate the use of fast 4D lab-based tomography in pore scale experiments and the current state of the art of this method.

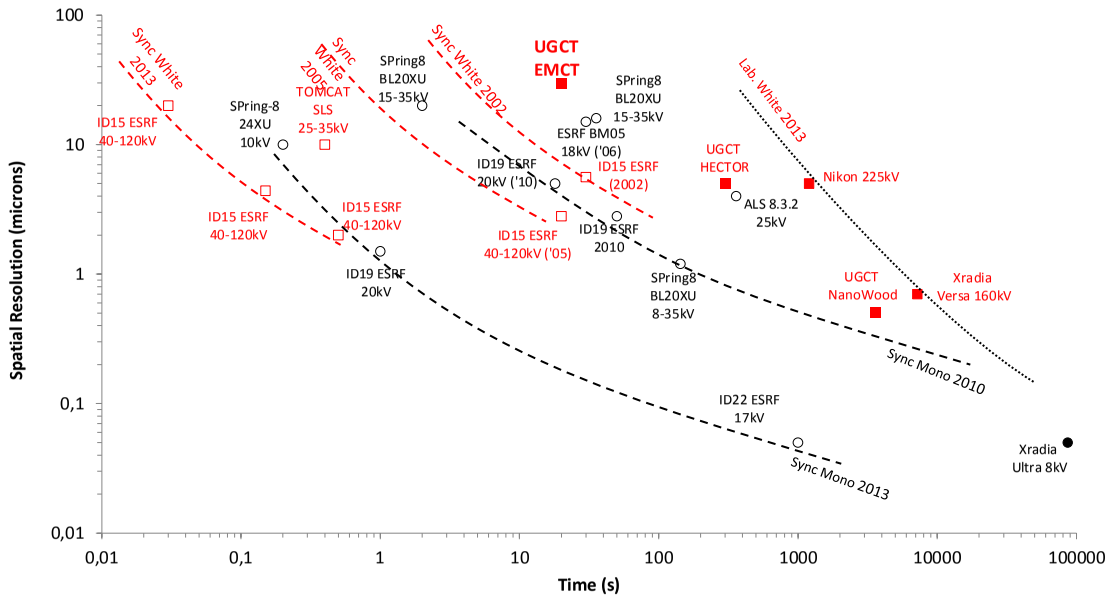

Figure 7.1: This figure (adapted from Maire and Withers (2014)) shows temporal and spatial resolutions attained at different synchrotron beam lines and lab set-ups. Open symbols denote synchrotron sources, while filled ones represent laboratory sources, squares denote polychromatic (white) beam and circles denote monochromatic scanners. In cases where the spatial resolution is not cited, an estimated resolution of twice the voxel size is used. We follow this convention to report the spatial resolution in our own experiments. The reported time is the time needed to gather 1000 projections.

7.2 Technological advances

In order to obtain a high-quality micro-CT scan, the accumulated X-ray dose in the detector during the acquisition of the projection images has to be sufficiently high, as the signal-to-noise ratio varies approximately as the square root of the amount of photons which hit the detector. In laboratory-based micro-CT systems, this sets a lower limit to the acquisition time, as the used X-ray flux emitted by the X-ray source is typically low compared to synchrotrons (taking into account also the necessary minimum distance between the source and the detector, due to considerations regarding image magnification, sample size and cone beam artefacts). The limitations of these sources with respect to dynamic imaging are explained in the first part of section 7.2.1, as well as technological developments which might mitigate these limitations in the future. Other limitations on the image acquisition may be posed by the X-ray detector, which is discussed next in section 7.2.1. During dynamic experiments on porous materials, the sample conditions are usually controlled in some way (e.g. applying mechanical loading, imposing (reactive) fluid flow, controlling temperature and humidity). Therefore, the sample usually has to be contained in a cell or a similar set-up. These cells can affect the image quality, and should therefore be designed carefully. The final part of section 7.2.1 treats this challenge.

After discussing the hardware challenges, we treat the possibilities of smart image reconstruction and analysis to compensate for low image quality (section 7.2.2). Fast scans, acquired while dynamic processes are going on in the pore space, can and should be supplemented with as much prior information as possible. In many experiments, prior information about the pore geometry can be acquired with a long, high-quality scan while the sample is in static conditions. Other prior information might pertain to the dynamic process itself, for example, in immiscible two-phase flow experiments the assumptions of incompressible fluids and the presence of only three material phases can improve reconstructions with a limited number of projections (Myers et al., 2011b). By scanning faster, the quality will typically decrease, hence approaches using a priori information gain importance. Another principle which we expect will prove important in the future, is the incorporation of the time dimension in the image analysis. On the one hand, there is a need for software tools which allow researchers to track changes in their sample over time (e.g.

deformation of a sample, velocities of fluid interfaces) and help them to make sense of the typically huge amount of data they acquire during a dynamic experiment. On the other hand, truly treating micro-CT time series data as 4D datasets may improve image analysis results, as it allows to incorporate more information. However, one thing is certain: 4D data analysis is computationally intensive, both when it comes to data storage as processing. Section 7.2.2 treats these challenges and opportunities.

7.2.1 Hardware evolutions

X-ray sources

X-ray sources in laboratory-based micro-CT set-ups are typically micro-focus X-ray tubes, in which an electron beam is focused on a very small focal spot on the anode target. When the electrons hit the target after being accelerated by a high-voltage electric field, they create X-rays through their interaction with the anode material. The main limitation of laboratory-based micro-CT in the scope of fast image acquisition is posed by the X-ray source. Unlike synchrotron sources, which exhibit very high brilliance, traditional laboratory sources have a limited X-ray output due to the power dissipation limitation when the electrons hit the anode target, implying longer acquisition times. Indeed, the energy efficiency of X-ray production in the form of Brehmsstrahlung in this set-up is only about 1 %, and a large portion of electron beam energy is deposited as heat. The power density limit of approximately 2W/μm ^{2} in the target is close to the fundamental limit at which material vaporization starts taking place, despite efforts of rotating anode systems (Wildenschild and Sheppard, 2013). As a result, the maximum achievable X-ray flux in laboratory systems is strongly correlated with the achieved focal spot size, and hence inversely correlated to the achievable image resolution. This resolution is important to resolve a pore space with sufficient detail (typical geological pore-scale micro-CT studies employ resolutions of (1 μm)^3 to (20 μm)^3 with acquisition times increasing strongly for higher resolutions, see Figure 7.1).

Recently, the invention of the liquid metal-jet X-ray source has mitigated the power density limit in laboratory X-ray sources. In this set-up, the anode target is a thin jet of liquid metal, hence renewing the target material constantly to avoid vaporization. The liquid metal-jet tubes are commonly

used for X-ray diffraction (e.g. King et al. (2013); Kaminski et al. (2014)), but have also proven their value for high-resolution X-ray imaging (Lundström et al., 2012; Bartels et al., 2013; Larsson et al., 2013; Zhou et al., 2013). For the imaging of pore-scale dynamics, their applicability can be limited by the lower limit of the focal spot size (approximately 5-6 μm) and the low energy of the generated X-rays, caused by the low atomic numbers of the materials used as liquid metal. Recently, a set-up using Indium (characteristic Kα energy 24.2 keV) has also been used for hard X-ray imaging (Larsson et al., 2011; Espes et al., 2014). When spatial resolutions better than 5-6 μm (hence smaller focal spot sizes) are required, transmission-type X-ray tubes need to be used. Nowadays, several manufacturers offer transmission targets on diamond substrate, allowing for an improved heat dissipation as compared to conventional beryllium substrates. Nevertheless, the highest achievable output power is relatively low due to the absence of direct, active cooling.

Other alternative X-ray sources are based on inverse Compton-scattering (Eggl et al., 2015; Graves et al., 2014). While such sources may become more accessible in the future, they are not treated here in detail as they are currently still under development and not yet commercially available on a large scale.

X-Ray detectors

Due to the limited X-ray flux achievable with conventional laboratory-based sources, image acquisition should be as efficient as possible. In laboratory conditions, this usually means that large flat-panel detectors with thick scintillators need to be used. In recent years, the highest achievable frame rate of these systems has drastically increased to values ranging from several tens of frames per second for full-frame acquisition to several hundreds of frames per second for limited region readout, while several experimental detector systems perform even better (Krymski et al., 2003; Singh et al., 2013). At the same time, the increased availability of large amounts of fast computer memory allowed for the implementation of fast acquisition schemes, no longer limited by the processing speed of hard drives. These two developments have drastically increased the possibilities of fast and continuous CT scanning. When even higher scanning rates are needed, high-speed line detector systems are to be used. However, they can scan only one or several lines at a time,

drastically limiting the field-of-view and therefore the ability of these set-ups to create 3D images. For both detector types however, the temporal behaviour of scintillators may in some cases become an issue at high frame rates (i.e. cause detector lag).

As an alternative to flat-panel detectors with scintillators, direct or hybrid detector systems have been developed over the last few years. These detector systems have no scintillator screen, but convert the absorbed X-rays directly into electron-hole pairs. This detection method increases the response speed, and allows for energy discriminating possibilities based on pulse height analysis. The latter allows for energy-dispersive acquisition and for a drastic reduction of electronic noise. These systems have been reported to have frame rates in the kHz range (Dinapoli et al., 2010; Szczygiel et al., 2012). These very high frame rate detectors are primarily developed for synchrotron applications (Henrich et al., 2009; Johnson et al., 2014) such as ptychographic imaging (Guizar-Sicairos et al., 2014). Consequently, they often use Si as detecting material, given the low X-ray energy typically used in coherent diffractive imaging. Using materials such as CdTe, which have a larger efficiency at high X-ray energies (Koenig et al., 2012), the further developments of photon counting detectors may in the near future also benefit laboratory-based dynamic CT scanning.

Add-on equipment for sample conditioning

To investigate how fluids migrate through pores in a rock or how the minerals in the rock react over time, the geological sample needs to be subjected to controlled external conditions, e.g. mechanical loading (Bale et al., 2013), temperature (De Kock et al., 2013) or humidity, possibly combined with the injection of pressurized liquids or gasses (Boone et al., 2014). Specialized add-on equipment for the micro-CT set-up is thus needed in order to visualize the sample at the desired in-situ conditions. In this section, the limitations and challenges brought forth by this equipment, and more specifically by flow cells, are briefly highlighted. The main concerns related to such flow cell set-ups, especially for fast laboratory-based micro-CT imaging, are the size of the set-up and the materials out of which it is constructed. Lab-based micro-CT commonly achieves geometrical magnification by using conical X-ray beams. This means that the diameter of the flow cell should be small in order to achieve

high magnifications and correspondingly high resolutions (depending on the characteristics of the scanner) while simultaneously maximizing the use of the available X-ray flux (i.e. without having to increase the focus-detector distance more than necessary) (Cnudde and Boone, 2013; Sheppard et al., 2014). This is crucial to discriminate the pore network in the sample with sufficient detail. Furthermore, the parts of the cell which are in the field of view should attenuate the X-ray beam as little as possible to maximize the X-ray flux. At low cell pressures, low-cost plastics (e.g. PMMA) and epoxies (Herring et al., 2013; Pak et al., 2013) are suitable, as these have a low X-ray attenuation coefficient compared to most geological materials. However, to simulate reservoir conditions, high pressures (typically 100 - 500 bar) and temperatures (typically 50-200° C) are required. The steel alloys (e.g. hastelloy) which are typically used to build Hassler cells for flow experiments at these conditions are highly attenuating and therefore not suitable for X-ray micro-CT imaging. Instead, imaging experiments require miniature Hassler cells constructed out of weakly attenuating, strong materials like aluminium (Fusseis et al., 2014), carbon-based materials (Iglauer et al., 2011; Ott et al., 2012; Andrew et al., 2014), beryllium (Wildenschild and Sheppard, 2013) and special plastics like PEEK (Boone et al., 2014).

7.2.2 Software advances

Advances in reconstruction algorithms

In addition to specific requirements for acquisition hardware to optimize 4D scanning, major improvements can also be achieved by applying clever software algorithms, mainly in terms of tomographic reconstruction. The main challenge posed by laboratory-based fast CT is Poisson noise, induced by the limited X-ray flux. Additionally, structural changes of the scanned sample during a CT acquisition will cause motion blurring artefacts which deteriorate the reconstruction quality. Methods to cope with both motion blurring and poor image statistics are thus crucial in dealing with fast imaging of dynamic processes.

Currently, most tomographic reconstructions are performed using analytical filtered back-projection (FBP) methods, such as the Feldmann-Davis-Kress (FDK) algorithm (Feldkamp et al., 1984; Kak and Slaney, 1988). These algorithms have the advantage of being relatively

simple and fast in terms of computational complexity, but theoretically they are only valid in idealized cases (i.e. when enough projections are acquired). In the context of (dynamic) CT imaging, iterative reconstruction techniques (Herman and Lent, 1976; Andersen and Kak, 1984) have gained much interest. During iterative reconstruction, intermediate solutions of the reconstructed 3D object are incrementally refined by simulating projection images from this solution (by forward projection) and subsequently adapting it to better reproduce the experimental projections. Unlike analytical algorithms, the iterative techniques can incorporate a priori knowledge about the measured object, drastically decreasing the degrees of freedom in the reconstruction process. Furthermore, accurate models for specific physical and geometrical features of the acquisition process can be modelled into the reconstruction, opening the possibility to include corrections for imaging artefacts, e.g. beam hardening (De Man et al., 2001; Brabant et al., 2012). In general, a priori knowledge in CT leverages the spatial and temporal correlations which exists between neighbouring voxels in a volume throughout time. It can be implemented in several ways, e.g. by assuming the scanned object is only made up of a limited number of clearly separated materials, corresponding to an equally limited number of discrete gray values. This is typically done by a segmentation of the intermediate result before a forward projection is performed. In doing so, the final result can typically be obtained using fewer projection images, and no longer contains image noise. Furthermore, as image segmentation is in most cases the first step in 3D analysis, these reconstruction methods have the capability to make this processing step obsolete. Several reconstruction algorithms for this so-called discrete tomography have been developed in recent years (Herman and Kuba, 2007; Batenburg and Sijbers, 2011; Brabant et al., 2014). They differ mainly in the segmentation method, in the moment of the appearance of the segmentation in the flow of the algorithm, and in additional strategies to reduce noise effects in the segmentation of (partially) reconstructed volumes.

Another way of using prior knowledge is to incorporate information about the object's shape. The simplest approach is to provide an appropriate initial solution to the iterative reconstruction method. The drawback of this method is that this initial solution can become too dominant, obscuring details which are actually changing in time. Other, more advanced methods indirectly incorporate the initial solution by

reconstructing the difference between the initial volume and the temporally changing volume, as in prior image constrained compressed sensing (PICCS) (Chen et al., 2008; Lee et al., 2012). Indeed, the difference between these volumes will primarily highlight the regions of the volume which are structurally changing through time. One of the more accomplished iterative reconstruction methods for dynamic porous media applications so far has been developed at ANU, and combines the notion of compressed sensing (cfr. PICCS) with discrete tomography (Myers et al., 2011a,b, 2012). The method has been used for two-phase flow experiments and formulates the reconstruction as an optimization problem over all discrete two-grey level solutions which honour the static pore structure, while accommodating for the expected physical two-phase flow behaviour by adding extra regularization terms to the optimization cost function.

The dynamically evolving regions can also be estimated directly from the dynamic CT data itself, i.e. without introducing an initial solution (Van Eyndhoven et al., 2014). Finally, temporal correlations can be exploited by modeling the expected deformation of the object as a function of time (Mooser et al., 2013). However, computational feasibility limits the number of parameters, which restricts the deformation models to fairly global ones, affecting the object as a whole, e.g. affine deformations.

It should be clear that aforementioned methods are only valid within specific constraints. Discrete reconstruction methods are not applicable for complex multi-material objects where partial volume effects are important. They are however very well suited for the imaging of homogeneous structures which are changing in time, e.g. foams under compression. Methods which apply initial solutions on the other hand are well suited for the imaging of rigid structures in which small regions are changing in time, e.g. fluid flow through a geological sample. Vast, non-local, structural changes however are more difficult to correct for with these methods, in this case the reconstruction methods based on deformation models are more suitable. Next to alterations in the reconstruction step, some methods also rely on image pre-processing, by altering the projection. This is quite often the case for noise reduction methods or phase retrieval algorithms, some of which inherently include noise reduction. In filtered back-projection methods, the filter may also be adapted in order to reduce noise (typically at the expense of image sharpness).

4D image analysis

As the signal-to-noise ratio is of major concern in lab-based fast micro-CT, it may prove very important to make use of the redundancy of information in the time sequence when analysing the data. This way, it should be possible to improve the 3D analysis (see e.g. Russ (1999); Kaestner et al. (2008); Brabant et al. (2011); Wildenschild and Sheppard (2013)) at one fixed time point by incorporating information from other time points. For example, 4D filtering methods may be useful to reduce motion artefacts and even to compensate for noisy data. To our knowledge, very little work on this topic has been done in the context of high-resolution CT research. However, we see a large potential for methods which have recently been developed for medical imaging purposes, e.g. 4D filters designed for CT perfusion scans (Mendrik et al., 2010, 2015; Eklund et al., 2011) and for magnetic resonance imaging (Kosior et al., 2007; Gal et al., 2010).

Another key principle to improve the quality of the analysis is the use of high quality scans performed at initial or final states of the sample. For example, one can segment the pore space from a prior high quality scan and use it as an analysis mask for the dynamic scans (as demonstrated in Chapter 8). This rather simple approach is only applicable when the pore structure does not deform during the experiment and when the high-quality dataset can be spatially matched to the dynamic datasets (either by not moving the sample between acquisitions or by applying image registration algorithms, e.g. Zitová and Flusser (2003); Latham et al. (2008)).

Next to using redundant and prior information, 4D datasets call for algorithms to quantify a sample's evolution through time. In some cases it may be sufficient to perform 3D analysis on datasets of consecutive time steps and compare the results. It should be noted that in this case, it should be possible to script the process, which may cause problems when user-defined input parameters need to be varied for each time step. In many cases, it is interesting to quantify changes through time by tracking movement or deformation of structures in the sample. Methods to do this are often inspired by 2D digital image correlation, and referred to as digital volume correlation. However, this problem is not specific to laboratory-based micro-CT, as it is of interest in synchrotron-based and medical CT as well. For this reason, it is not treated here and the interested reader is referred to Chenouard et al. (2009, 2014); Coraluppi and Carthel

(2011); Fife et al. (2012); Maire and Withers (2014) and Maška et al. (2014).

7.3 An illustration: solute transport in Savonnières

In this section, we describe an experiment aimed at elucidating solute transport in heterogeneous rocks. In groundwater systems, mixing of reactants often limits (bio)chemical reactions (Rolle et al., 2012). In CO_2 sequestration and enhanced oil recovery, CO_2 dissolved in brine can trigger dissolution and precipitation of minerals in the host rock's pore space, in turn affecting this rock's mechanical and fluid flow properties (Ott et al., 2012). The transport phenomena and simultaneous chemical reactions in these processes are coupled, and one can therefore only begin to understand the dissolution and precipitation patterns and the resulting flow properties, if one also understands solute transport by advection and diffusion in the pore space. In heterogeneous media, particularly carbonates, the pore-level flow field can show significant channelling (Blunt et al., 2013). This implies that important differences in fluid chemistry can arise between the more stagnant regions and the channels with a higher advective transport rate, which in turn will influence the dissolution behaviour in the carbonate host rock. Depending on the balance between advection, diffusion and reaction rates, the dissolution reaction can cause the preferential flow channels to become increasingly wide. This behaviour is often referred to as worm-holing (Daccord et al., 1993), and can have important field-scale consequences (Gharbi et al., 2013).

We show the feasibility of imaging solute transport (diffusion and advection) in 3D in a carbonate at the pore scale. While some studies have investigated the imaging of solute transport (Clausnitzer and Hopmans, 2000; Fourar and Radilla, 2009; Ott et al., 2013; Koestel and Larsbo, 2014), to our knowledge this has not been undertaken before simultaneously at the pore scale and at the time scale shown here (12 seconds per scan). While the discussion will be restricted to one experiment (a single imposed flow rate), by varying the flow rate a detailed study of pore scale dispersion can be undertaken. Such studies may prove vital as a validation to solute transport modeling methods described by for example Ovaysi and Piri (2011) and Bijeljic et al. (2013b).

Materials and methods

In the experiment outlined here, transport of a tracer salt subject to diffusion and advection is investigated in the Savonnières limestone. As mentioned in Chapter 4 (section 4.2.4), this grain-supported limestone consists of ooids and shell fragments bound together by sparite. During diagenesis, some of these grain fragments were partially dissolved resulting in a pore network with well-connected pores between the grains (intergranular porosity) and secondary porosity inside the dissolved grains (intragranular porosity or vuggy porosity), which is connected to the rest of the pore network through microporosity (Roels et al., 2001). A sample with a diameter of 6 mm and a height of 17 mm was put in a Viton sleeve and set into a custom-built, low-cost PMMA flow cell (Figure 7.2). The flowcell was mounted on UGCT's Environmental Micro-CT scanner (EMCT, Figure 7.2), designed and built in-house in collaboration with X-Ray Engineering bvba (XRE, Ghent, Belgium). This scanner is specially developed to image samples under controlled environmental conditions or during dynamic experiments. To allow for the sample and the equipment connected to it with wires or tubing to remain static, the set-up has a rotating X-ray source and detector assembly on a gantry. This eliminates problems with flow instabilities caused by bending or twisting of the flow lines, and it helps avoid unwanted sample movement during the acquisition. Unlimited continuous rotation is possible because electrical power and safety interlocks are transmitted through slip-rings. The system is equipped with a standard micro-focus X-ray tube with integrated high-voltage power supply (maximum high voltage 130 kV, maximum power output 39 W, minimum spot size 5 μm). The detector is a CMOS flat-panel detector (1316 by 1312 pixels with a 100 μm pitch) with a thick, structured CsI scintillator. The GigE-interface permits frame rates of 30 fps at full resolution and 60 fps in 2x2 binned mode (and even more in panoramic mode). The scanner's source-detector combination, together with the applied smooth-scanning (rather than step-and-shoot) acquisition, allows for fast scanning. More details on EMCT's set-up are given by Dierick et al. (2014), although the rotation motor has since been upgraded to allow for faster image acquisition.

The sample was first saturated with water by flushing with CO_2 and subsequently with water. At this point, a first high-quality scan (Table 7.1) of the sample was performed to obtain geometric information of the sample's pore space. Preferential flow channels were then visualized by

Figure 7.2: A custom-built PMMA confining-pressure flowcell (left) allows the visualization of fluid flow in stone samples with a diameter of 6 mm and a height between 15 and 20 mm. UGCT's EMCT scanner (right) was built in collaboration with XRE. The flow cell is mounted on a stand which moves into the scanner from below. The gantry (with the source and detector mounted on it) rotates around the sample, while the sample remains static.

	High quality	Fast scans
Voxel size (µm)	7.4	14.8
Total time per scan	21 min	12 s
Binning of detector pixels	No	Yes (2x2)
Amount of voxels/scan	1314x1314x1311	657x657x656
Projection exposure time (ms)	550	20
Projections per 360° scan	2200	600
Accelerating voltage (kV)	80	130
X-ray source output (W)	8	16
Source-detector distance (mm)	365.0	365.0
Source-object distance (mm)	27.1	27.1

Table 7.1: Settings of scans performed in the solute transport experiment.

pumping a highly X-ray attenuating brine (containing 10 wt % CsCl) into a water-saturated sample at a flow rate of 0.6 ml/min. During pumping, fast scans were performed with settings outlined in Table 7.1. Projections were continuously acquired during a 5 minute time interval, during which the flow was not halted. The fast scans were recorded and processed with the proprietary 4D tools (XRE, Belgium) of the ACQUILA software. Tomographic reconstruction was performed with the FDK algorithm, implemented on the GPU.

Results and discussion

In Figure 7.3, the histogram of the reconstructed image intensity values of the macropore voxels (selected by applying the pore space mask) in the limestone is given for the different time steps. The peak at 0 seconds shows the distribution of the intensity values before brine injection. At this stage, all voxels included in the histogram (i.e. all voxels in the macro-pore space) are filled with pure water. This is also illustrated in the rendering in this figure, where at 0 seconds the image intensity values in the pore space are low and homogeneously distributed. During injection, the histogram shifts to the right and after 96 seconds, the intensity values are distributed in two peaks. This indicates a heterogeneous distribution of the CsCl concentration in the pore space of the limestone sample. The renderings show that most of the intergranular pore space contains a high CsCl concentration, while the intragranular pores in the dissolved ooids (Figure 7.3, dotted circle) still have a low CsCl concentration. In later time steps, the peak on the left side of the histogram starts to disappear. This corresponds to the gradual increase of the CsCl concentration in the intragranular pores, which can be seen in the renderings. After a long waiting time (e.g. after some hours), the histogram of the pore space voxels will again consist of one single peak, but centred around a higher average grey value than in the initial condition.

The results illustrate that the distribution of the brine in the intergranular pore space is mainly controlled by advection. In these pores, preferential flow paths can be found. The flow in the intragranular pores is more stagnant and the concentration of CsCl in this vuggy pore space is therefore mainly controlled by diffusion. As this section is merely intended as an illustration of the use of fast imaging to investigate pore scale processes, further analysis will not be shown here. Although the measurements presented here are clearly a good indication of CsCl-concentrations in the sample, further research needs to be performed to calibrate the image intensity values to exact concentration values.

7.4 Conclusion

Micro-CT scanning with a sub-minute time resolution is a very desirable experimental technique, both as an accessible stand-alone tool to

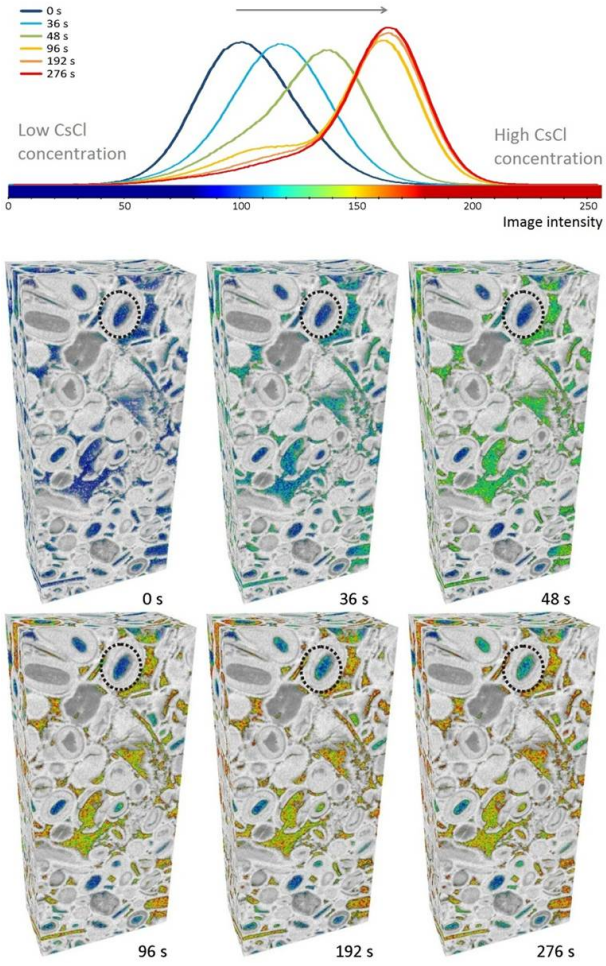

Figure 7.3: The graphs show the evolution of the image intensity histograms of (only) the pore space voxels in the Savonnières limestone sample during brine injection. High image intensities correspond to high CsCl-concentrations. The corresponding 3D renderings show the evolution of the CsCl concentration in the macropores. The dotted circle indicates an intragranular pore in which the flow is stagnant. Time series measurements were performed with the EMCT-scanner at an acquisition time of 12 seconds and a voxel size of 15 μm.

investigate dynamic pore-scale processes and to prepare experiments for much more restricted yet higher-quality synchrotron measurements. A number of difficulties, mainly related to the limited X-ray flux, have hampered the implementation of such set-ups. Future developments in X-ray source and detector technology (notably the improvement and implementation of liquid-metal jet sources and photon-counting detectors) may increase the attainable time resolution and improve the image quality and spatial resolution at short acquisition time. We also expect a significant contribution from advanced tomographic iterative reconstruction and 4D image analysis algorithms, which can compensate for the often limited image quality in fast scans by incorporating prior information about the pore structure or the physical processes transpiring in the pore space. Furthermore, progress is being made in automating 4D image processing and image analysis, making it more and more feasible to work with large, computationally intensive time-series datasets.

Despite the limitations, we illustrated the large potential of fast micro-CT scanning with a real-time imaging experiment to visualize pore scale solute transport of a tracer salt (CsCl) in a Savonnières limestone. This imaging experiment, performed by continuously imaging the process at an acquisition time of 12 seconds per full rotation, allows to study the location of stagnant and fast flow regions and the relative time scales of diffusion and advection in this stone. In Chapter 8, we will show that fast lab-based imaging is also very useful to investigate two-phase flow, and particularly to validate assumptions made in pore scale models like the one presented in Part II of this thesis.

As illustrated by the experiments described in this chapter and in Chapter 8, it is today becoming possible to study transport processes in geological samples at the pore scale in a laboratory-setting, without having to impose quasi-static conditions. We expect that with further improvements in image quality, real-time imaging with laboratory-based micro-CT scanners will be implemented much more widely. This would provide valuable feed-back to the pore scale modeling community and has the potential to strongly increase our understanding of porous media behaviour. In the long term, this may be beneficial to the management of geological reservoirs and aquifers, as well as to a wide variety of other issues involving porous materials (e.g. building stone deterioration, development of batteries and fuel cells, food engineering, textile engineering).

8

Real-time visualization of Haines jumps in sandstone

8.1 Introduction

As already introduced in Chapter 2 (section 2.2.2), the pore scale displacement process during slow, capillary-dominated drainage displays rapid interfacial jumps, usually called bursts or Haines jumps (Moebius and Or, 2014a). In the classical reasoning, such jumps correspond to the filling of a geometrical pore body, a local dilation in the pore space (Haines, 1930). These jumps often happen in cascades, which is explained as sequential filling of pores with lower entry capillary pressure than the first pore of the cascade. Haines jumps in individual pores have been found to happen on the millisecond time scale regardless of the externally imposed capillary number (Armstrong and Berg, 2013), while cascades typically have decay times of 0.5 to 2 seconds (Armstrong et al., 2014c). In the following, we define filling events as the filling of a pore or a number of pores before the invasion stops and continues elsewhere in the pore space. The frequency of filling events is controlled by the fluid injection rate.

The dynamics of the invasion process have been investigated by studying two-dimensional micro-models (Furuberg et al., 1996; Crandall et al., 2009; Moebius and Or, 2014b), acoustic emissions (Moebius et al., 2012), pressure measurements (Måloy et al., 1992) and electrical measurements (Haas and Revil, 2009). Despite these experiments a number of questions remain, notably regarding the suitability of quasi-static (invasion-) percolation models to describe the invasion sequence in natural porous media, which is subject to non-local inertial and viscous forces (Armstrong and Berg, 2013; Moebius and Or, 2014b). Full comprehension of drainage behaviour in geological porous materials requires direct three-dimensional observation of the evolution of the fluid configuration in real rock samples.

While fluid distributions have been visualized with lab-based micro-CT scanners in quasi-static two-phase flow experiments (Prodanović et al., 2007; Andrew et al., 2013, 2014; Herring et al., 2013; Aghaei and Piri, 2015), it is crucial not to interrupt the non-wetting fluid injection in order to investigate the properties of the filling events or the influence of dynamic effects (Wildenschild et al., 2001). At drainage rates representative of field-scale applications, this can be achieved with micro-CT acquisition times on the order of 10 to 30 seconds (Berg et al., 2013). Their argument is based on the observation from high-precision pressure measurements that at typical field-scale flow rates (capillary numbers on the order of 10^{-8}), a Haines jump take place every 10-20 s somewhere in the pore space. Therefore, it is statistically unlikely that two neighboring but separate Haines jumps take place within only a few seconds. Typical laboratory-based micro-CT experiments can be used to visualize slower processes in rocks, e.g. fluid-rock chemical reactions (Boone et al., 2014; Menke et al., 2015), but are too slow to study two-phase flow under dynamic conditions. In the fastest lab-based micro-CT work on two-phase flow presented in the literature before our work, a time resolution of 80s per scan was achieved (Myers et al., 2011a). Therefore, such real-time imaging experiments had only been performed at synchrotron facilities, e.g. the ground breaking study presented by Berg et al. (2013) visualized individual filling events with a time resolution of 16.8 s. Other notable examples of real-time synchrotron imaging of two-phase flow were presented by Youssef et al. (2013); Armstrong et al. (2014b); Andrew et al. (2015) and Rücker et al. (2015). The scarceness of synchrotron beam time however strongly limits the number of these studies. It is therefore very desirable to use the methodological

developments in fast laboratory-based micro-CT outlined in Chapter 7, which allow to perform these experiments at much lower cost.

In this Chapter, we present a fast lab-based micro-CT experiment during which drainage in Bentheimer sandstone was visualized with UGCT's custom-built EMCT scanner (presented in Chapter 7), while non-wetting fluid was continuously injected. During the experiment, the fluid distribution in the 3D volume was assessed every 4 seconds (with an acquisition time of 12 seconds per micro-CT reconstruction), allowing for the observation of the fluid arrangements before and after single-pore filling events. To illustrate how such an experiment can be used to investigate the validity of percolation theory to describe the invasion sequence, we propose a unique analysis of the observed drainage dynamics in terms of the filling of geometrical pores. Pores are identified directly on the images and tracked throughout the experiment. The statistical distribution of the sizes of filling events is used as a fingerprint for the invasion process and compared to percolation theory predictions.

This chapter is based on the following publication in Water Resources Research: Bultreys et al. (2015a), *"Real-time visualization of Haines jumps in sandstone with laboratory-based micro-computed tomography"*

8.2 Materials and methods

8.2.1 Experimental set-up

Bentheimer sandstone is a well-sorted German sandstone from the Early-Cretaceous with a high porosity (17 to 22 %) and permeability (1.5 to 2.5 D). A sample of this rock with a diameter of 6 mm and a height of 17 mm was put in a Viton sleeve and mounted into the PMMA flow cell shown in Chapter 7 (Figure 7.2). This cell was placed on UGCT's Environmental Micro-CT (EMCT) scanner (section 7.3). The flow cell thus remained static during the experiment, eliminating possible sample movement and flow instabilities caused by bending or twisting of the flow lines. During the imaging, a central part (height 9.7 mm) of the sample was in the scanner's field of view.

8.2.2 Experimental procedure

The sample was saturated with water by subsequent CO_2 sparging (3 bars overpressure, during 15 minutes) and water flushing (approximately 150 pore volumes). In order to supplement the lower signal-to-noise ratio in the fast scans during the drainage experiment, a high-quality scan of the sample was made a-priori with a voxel size of $(7.4\ \mu m)^3$ (2200 projections with an exposure time of 550 ms each, X-ray source accelerating voltage 80 kV and target power 8W). Next, a brine (10 wt % CsCl) with a high X-ray attenuation coefficient was pumped into the sample. A second high-quality scan confirmed that the sample was completely saturated with brine. Then, an oil phase (kerosene, commercially available as paraffin) was injected at a low, constant flow rate of 6 µl/min with a high-precision pump (GlobalFIA MilliGAT MG5, USA). This flow rate corresponds to a capillary number of approximately $7 \cdot 10^{-8}$ (Ca = $\mu v/\sigma$, with μ the invading fluid viscosity, v the flux of the invading fluid and σ the oil-water interfacial tension). During drainage, fast micro-CT scans with a voxel size of $(14.8\ \mu m)^3$ were performed by continuously acquiring projections throughout a 5 minute time interval. Per full 360° smooth rotation of the gantry, 600 projections were acquired (exposure time 20 ms, total acquisition time 12 s per scan). The X-ray tube was operated at an accelerating voltage of 130 kV and an target power of 16 W. The scanning parameters for both the high-quality and the fast scans were the same as for the solute transport experiment presented in Chapter 7, more details can thus be found in table 7.1. Example slices of the high-quality and fast scans can be found in figure 8.1. Within the acquisition time interval, the drainage was not halted (except close to the beginning and end of the acquisition). The dynamic data was recorded and processed with the proprietary 4D tools (XRE, Belgium) in the ACQUILA software.

Since the acquisition is continuous, it is possible to reconstruct projections acquired during any full rotation of the gantry, irrespective of the starting angle. In this experiment, a new 360° reconstruction was generated after every 120° rotation of the gantry, corresponding with consecutive reconstructions in the time series starting every 4 seconds (Figure 8.2). Note that the time frames in which consecutive reconstructions were acquired overlap. In theory, if pore filling events happen (much) faster than 4 seconds, the applied strategy allows to enhance the temporal resolution of the measurements, as a discrete event can be pin-pointed to a 4-second time interval (e.g. between the 16th and 20th second in Figure

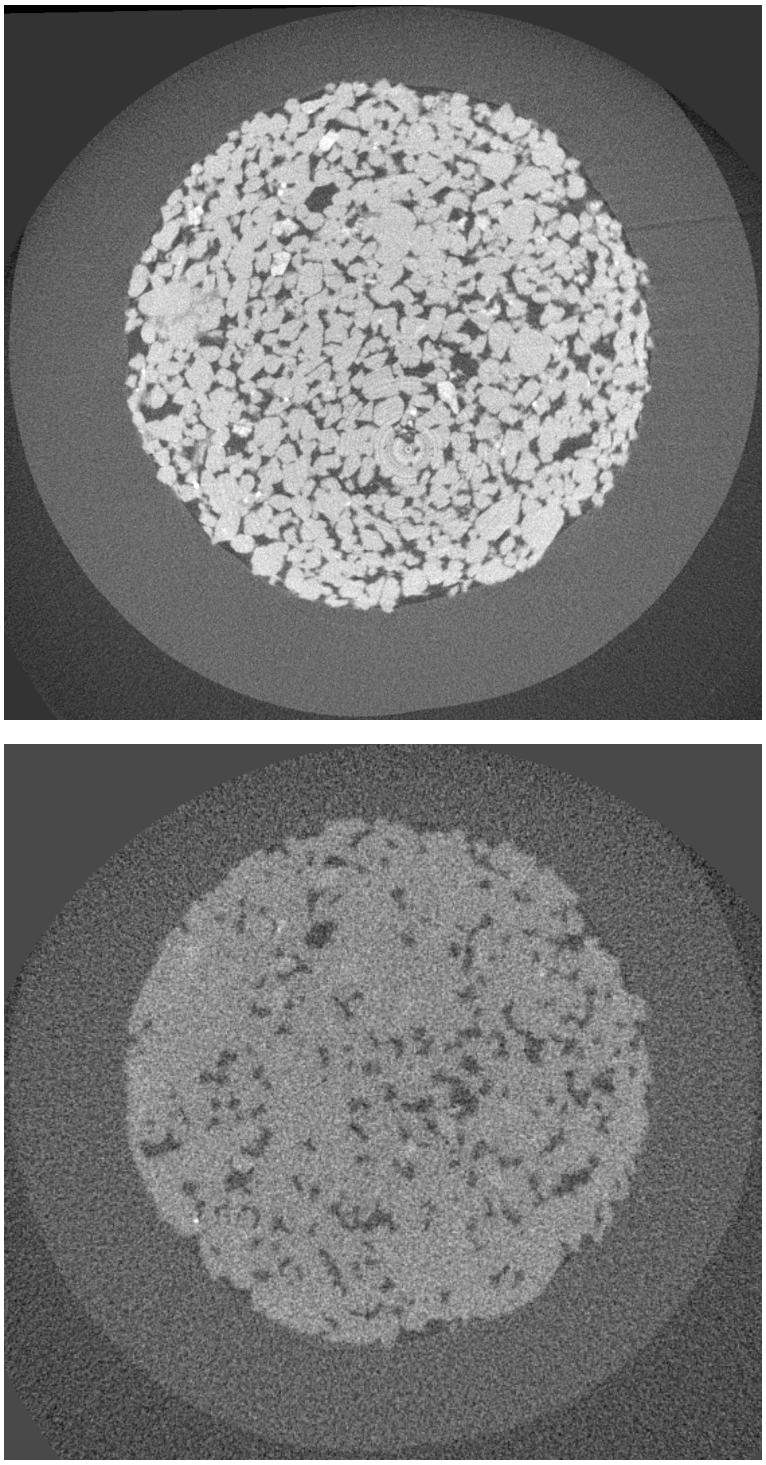

Figure 8.1: Raw slice through the high-quality scan (top), and through one of the fast scans (time step 60, bottom). The diameter of the sandstone sample is 6 mm, the high-quality scan has a voxel size of 7.4 µm, and the fast scan has a voxel size of 14.8 µm. In the fast scan, brine-filled voxels have a similar gray value as the solid, due to the high attenuation coefficient of the dissolved CsCl. Oil-filled voxels show up in darker grey values.

8.2). In reality however, it is not always possible to distinguish motion artefacts (caused by alterations in the sample during the acquisition) from noise. The resulting time series dataset consists of 72 reconstructions in the 5 minute acquisition. Due to the highly X-ray-attenuating salt, brine-filled voxels have grey values comparable to quartz-filled voxels, whereas oil-filled voxels in the reconstructed 3D images have lower grey values.

8.2.3 Image analysis: voxel-based thresholding

The image analysis work flows applied in this work are outlined in Figure 8.3. To analyse the data, the high-quality scan recorded prior to brine saturation was matched to the fast scans (which were re-binned without interpolation to fit the high-quality scan's voxel size) using an attenuation-based 3D rigid body registration algorithm (Brüker micro-CT, Belgium). The pore space was segmented from the high-quality scan by applying a manually set grey value threshold. This mask was overlaid on the fast scans to identify pore space voxels. After applying an anisotropic diffusion filter (diffusion stop threshold 24 grey values, 3 iterations) in Avizo (FEI, France) on the fast scans, these pore space voxels were segmented into oil and brine phases at each time step using grey value thresholding, followed by the application of a despeckle filter in Avizo. The despeckle filter changed the phase of an oil voxel if the percentage of brine voxels in a 3x3x3 kernel was larger than λ times the standard deviation of the phase distribution in that kernel, and vice versa. λ was set to 1.25, based on visual observation (i.e. the highest value which eliminated spurious noise in the segmentation). The resulting three-phase segmentations (which contain oil, brine and solid voxels) were used for the 3D renderings discussed further (Figure 8.8). Slices illustrating the segmentation quality can be found in Figure 8.4. Note that more sophisticated multi-phase segmentation algorithms e.g. watershed segmentation may yield more accurate results (Schlüter et al., 2014), but were not applied here due to the need for automated and computationally efficient implementations when dealing with large time series data. The voxel-based three-phase segmentations were not used for quantitative analysis in this work, but are included to show qualitatively how the distribution of fluid phases can be tracked during the experiment.

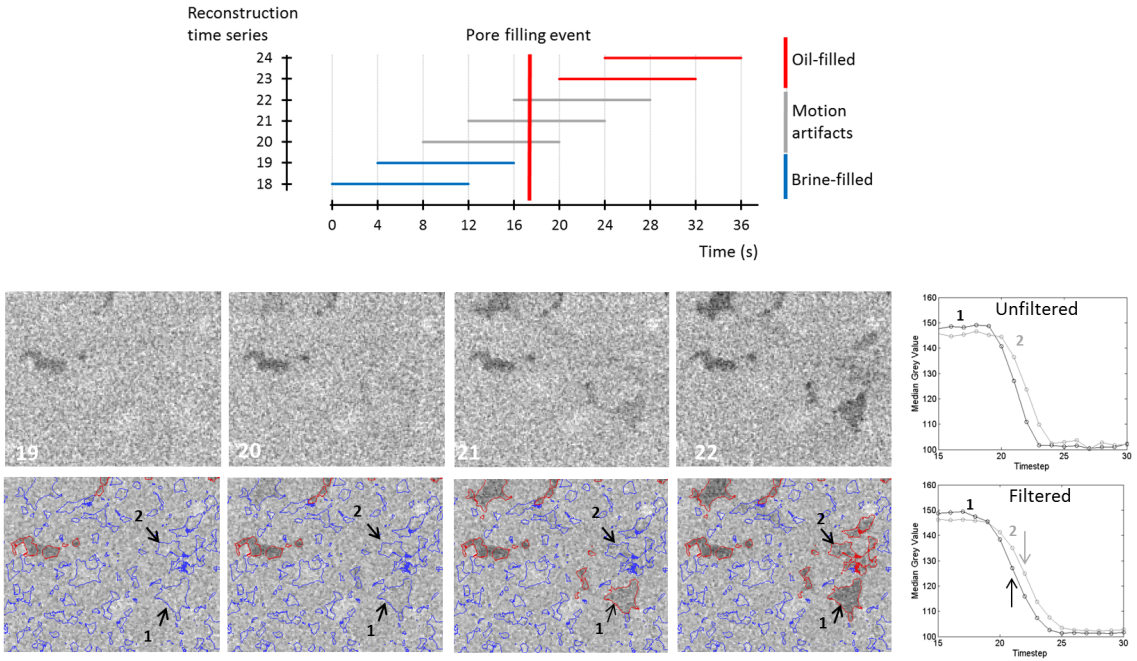

Figure 8.2: The graph (top) illustrates the acquisition time of each micro-CT reconstruction in the time series versus the saturation state of a specific pore in the sandstone during drainage. Each 360° acquisition takes 12 seconds, yet a new reconstruction is generated every 4 seconds, meaning acquisitions of subsequent reconstructions in the time series overlap. The micro-CT images (bottom) show 4 consecutive time steps (left to right) which can be compared to time steps 19-22 in the graph. The top row shows part of a slice from the unfiltered fast images, the bottom row shows contours of individual geometrical pores (blue for pores determined brine-filled and red for oil-filled) overlaid on the 4D filtered fast images. The graphs show the evolution of the median grey value in pores labelled 1 and 2 over time.

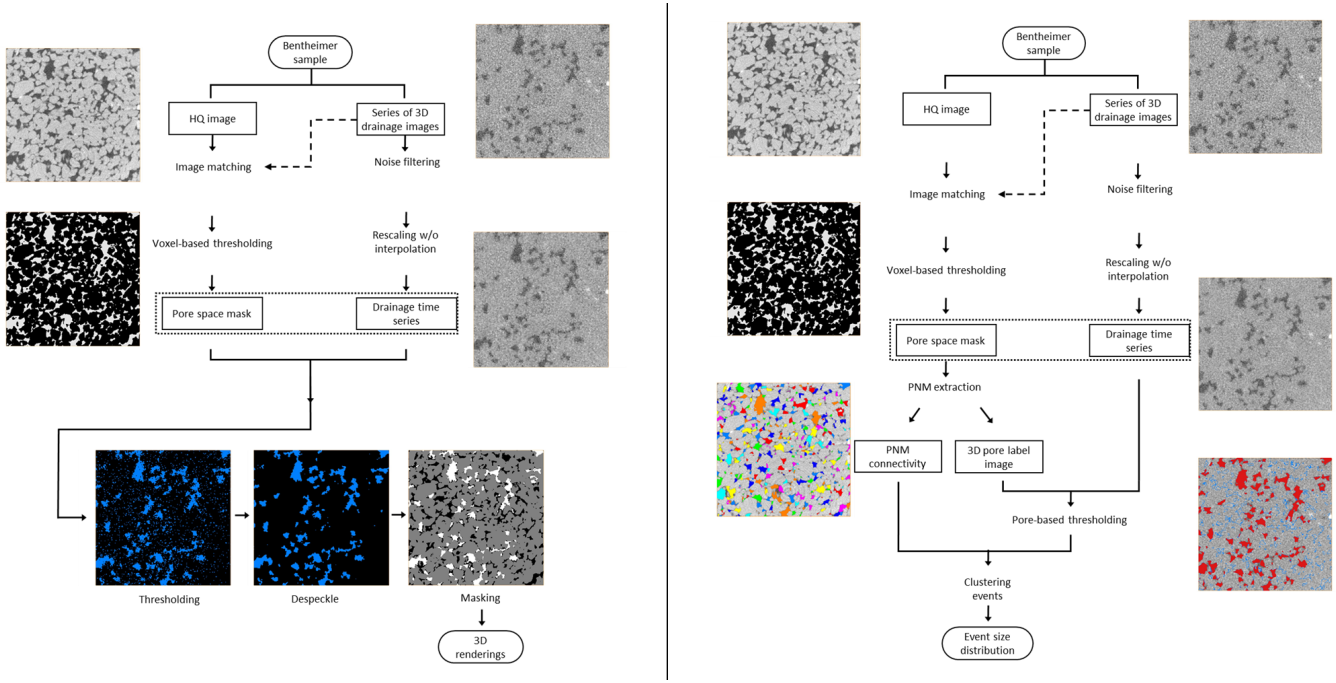

Figure 8.3: Image analysis work flow for the voxel-based segmentation (left) and the pore-based segmentation (right).

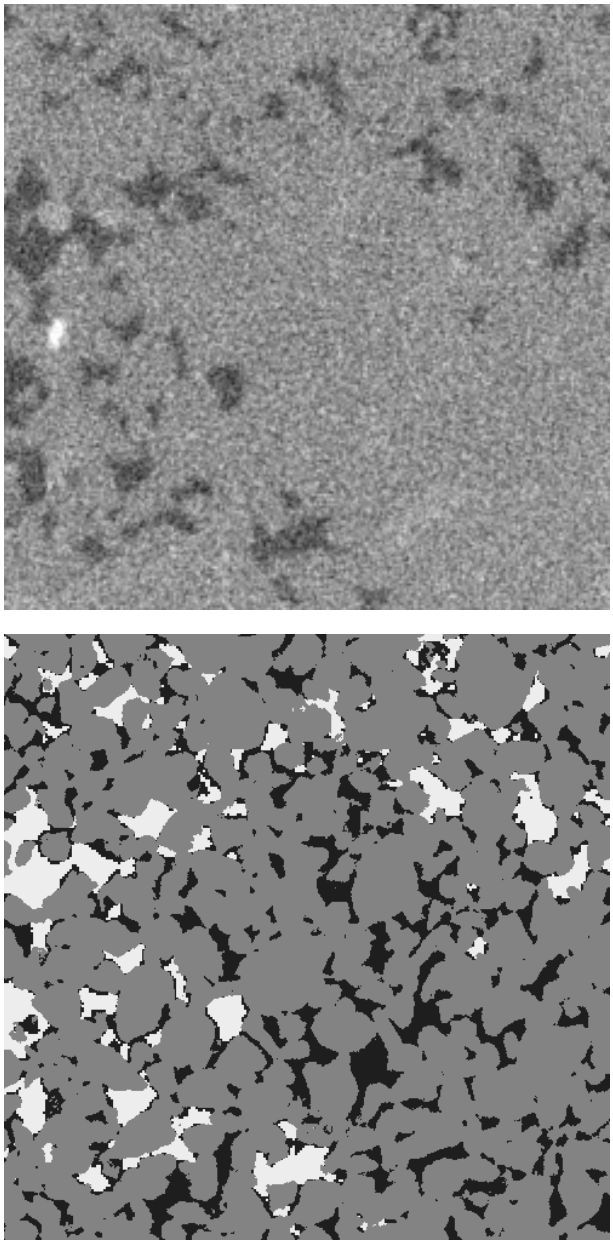

Figure 8.4: A cropped, unprocessed slice from the fast scan at time step 60 (top) and a voxel-based segmentation obtained by grey-value thresholding an anisotropic-diffusion-filtered image and subsequently applying a despeckle filter in Avizo (bottom).

8.2.4 Image analysis: pore-based thresholding

For this analysis, the fast scans were re-filtered to further reduce the image noise. A time-based median filter was first run on the fast scans by replacing the grey value in each voxel at time step t by the median of the same voxel at time steps in the interval $(t-2, t+2)$ using Matlab. Subsequently, a spatial anisotropic diffusion filter was applied in Avizo (diffusion stop threshold 24 grey values, 2 iterations). Results can be seen on the bottom row of slices in Figure 8.2, full example slices can be found in Figure 8.5.

To define the location of individual pores, a maximal ball pore network (PNM) extraction method described in Dong and Blunt (2009) was run on the pore space mask extracted from the high-quality scan. During such a network extraction, the pore space voxels are assigned to pore bodies and pore throats, the latter being local constrictions in the pore space in between pores. The extraction results in a set of files describing the graph structure of the PNM, and a 3D label image in which each voxel contains the ID number of the network element (pore body or pore throat) it was assigned to. Since the PNM was extracted from the pore space mask, which was spatially matched to the fast scans, the noise-filtered fast scans could be overlaid on the 3D label image. This way, it was possible to follow the grey values of the constituent voxels of each pore body at each time step during the drainage experiment. This procedure was performed by loading the label image and the filtered time series into Avizo, and performing a label analysis at each time step.

To get an idea on how to classify pores as oil-filled or brine-filled based on the grey values of their voxels at each time step, we first show the evolution of the grey value histogram of all the voxels in a specific pore, around the time steps where an event is observed. In Figure 8.6, the evolution of the 4D noise-filtered histograms in pore 1 and pore 2, which are marked in Figure 8.2, can be seen. In both pores, the histogram evolves from a fairly symmetric peak to an asymmetric peak with a lower mode and a long tail towards higher grey values, the latter associated with partial volume effects and remaining brine films in crevices along the pore walls. The asymmetry in the peak indicates that it is better to work with median values than with mean values. Furthermore, due to this asymmetry it makes sense to also put a threshold on the first quartile of the grey values, i.e. to demand that the core of the grey values in the pore should be

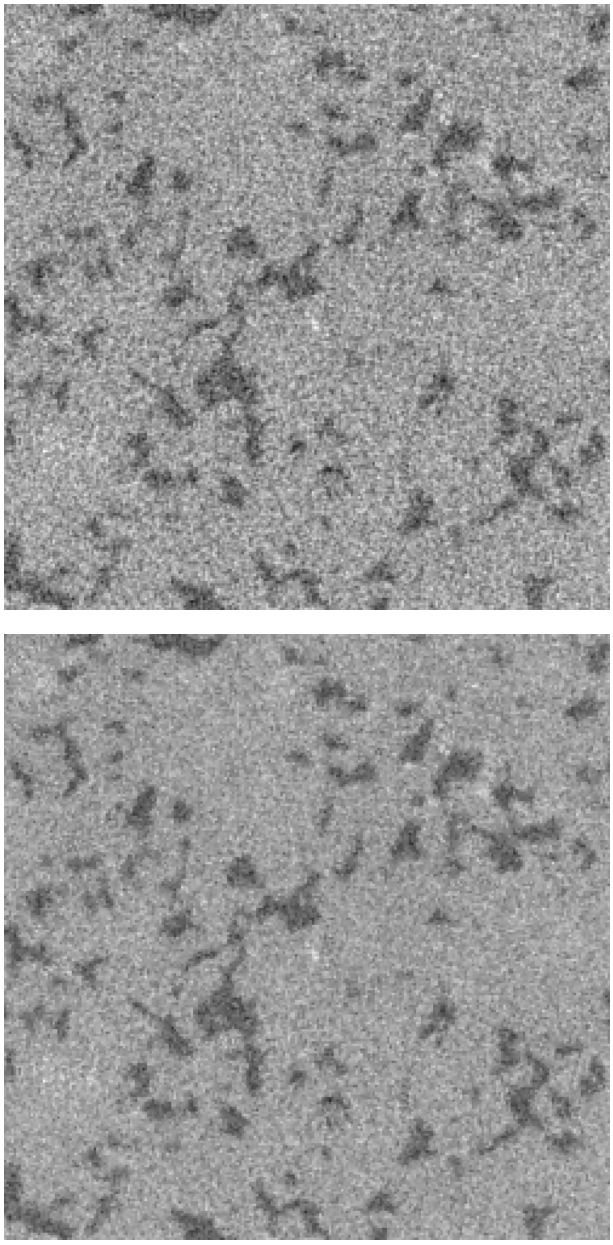

Figure 8.5: A cropped, unprocessed slice from the fast scan at time step 60 (top) and the same image noise-filtered over space and time (bottom).

dark enough. This makes it easier to distinguish between noisy pores (broad, more symmetric histogram) and pores which contain motion artefacts (asymmetric histogram), and it fixes the point in time at which a pore containing motion artefacts is segmented as oil-filled. To be selected as oil-filled, pores were thus required to have a grey value which is dark enough overall (50 % below a threshold set at a grey value of 135) , but also to contain a "core" of "very dark" voxels (25 % below a grey value threshold set at 117). Images showing results from the pore-based thresholding can be seen in Figure 8.7.

The evolution of the grey value histograms in Figure 8.6 also shows that the evolution of the histogram of pore 2 lags one time step (4 seconds) behind the evolution of pore 1, suggesting that these pores were not drained at the same time step. This illustrates how the overlapping reconstruction scheme seems to make it possible to separate events which are less than 12 seconds apart in time relative to each other, even though the technique may not allow to pinpoint the absolute time at which an event happens. Without the overlapping reconstruction, the events in both pores would much more likely have been identified at the same time step (depending on the exact timing of the pore filling relative to the start of the acquisition). This is also visible in the evolution of the median grey value of both pores, plotted in the graphs in figure 8.2. Without the use of the overlapping reconstruction, only a subset of the points in these graphs would be plotted (i.e. time steps i, i+3, i+6,...), which would make it much harder to select an appropriate threshold to separate the filling of pore 1 and pore 2 in time.

By applying the proposed pore-based thresholding, the time step at which each pore was invaded with oil (if applicable) could be identified. If two or more pores which were connected by throats in the pore network were drained during the same time step, they were clustered into one pore filling event (using a graph algorithm in Matlab). It should be noted that at this time, the filling state of the connecting throats was not taken into account, because at the achieved spatial resolution it is difficult to determine this state for narrow throats.

8.3 Results and discussion

While fast laboratory-based micro-CT can prove useful to the investigation of a host of petrophysical questions, obtaining temporal resolutions on the

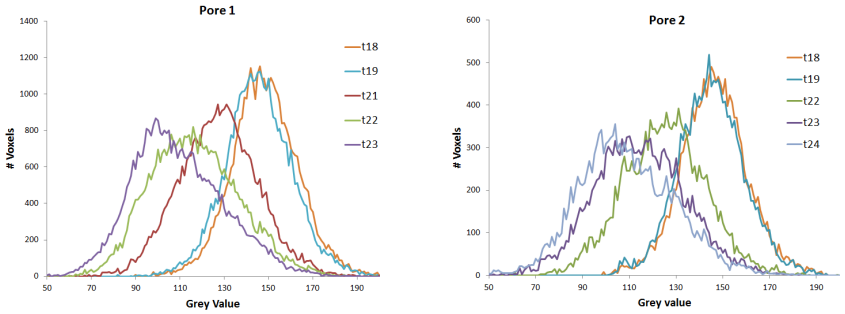

Figure 8.6: The evolution of the grey values in pore 1 (left) and pore 2 (right) marked on Figure 8.2, showing why thresholds are put on the median and first quartile rather than on the mean grey value in pores. The histogram evolution also suggest that pore 1 and pore 2 are not drained simultaneously as pore 2 lags one time step (4 seconds) behind pore 1. This shows the usefulness of the overlapping reconstruction scheme.

order of seconds is currently still very challenging. The quality of the fast scans is sufficient to identify most oil-filled pores, with the exception of the smallest pores and throats. During drainage the larger pores and throats are expected to fill with oil first, meaning most pore filling events are captured. A discussion of the technical developments which could further improve the spatial and temporal resolution of fast laboratory-based micro-CT can be found in Chapter 7.

Four selected time steps during the drainage experiment are shown in Figure 8.8A, illustrating our capability to image the fluid distribution in the sample under dynamic conditions. A pore filling event is shown in Figure 8.8B. This figure illustrates our capability of imaging pore-filling events in real-time with a lab-based micro-CT scanner. Note that the fluid distribution in these renderings is based on the 3-phase segmentation, and is therefore independent of the pore network extraction. Visual comparison of the location of the fluid-fluid interfaces at time t=136 s with the disassembly of the pore space in pores and throats also gives credibility to the quality of the pore network extraction.

To illustrate how the imaged filling sequence can be further analysed, the previously outlined pore network-based approach was used (Figure 8.2). Visual assessment suggests the network extraction succeeded well in identifying geometrical pores (i.e. locations of fluid-fluid interface typically coincide well with the locations of pore throats), however, further

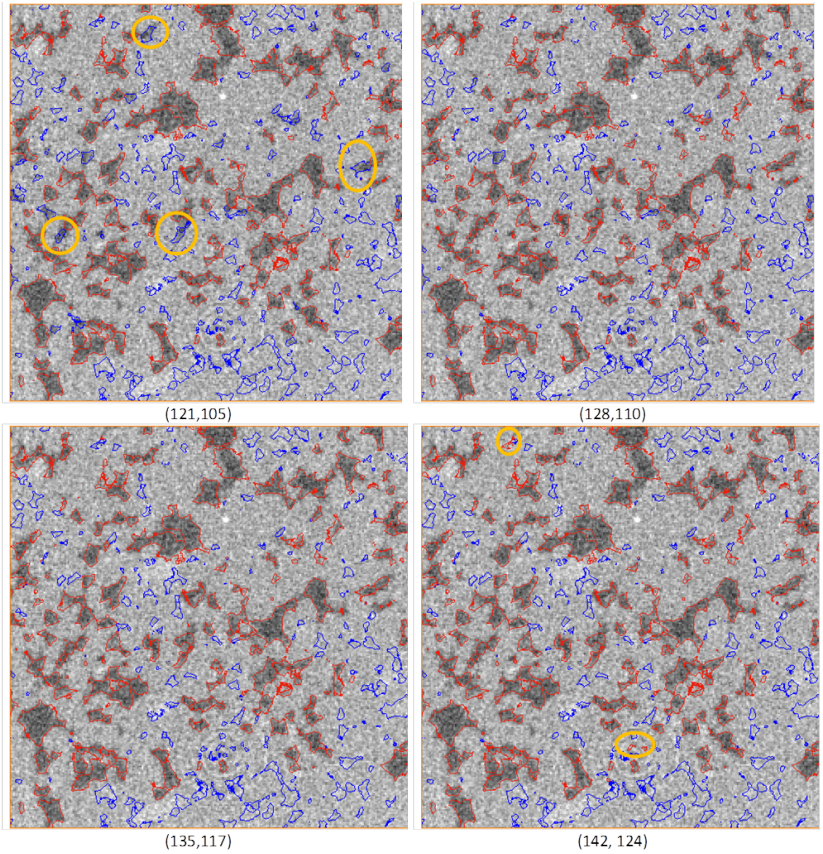

Figure 8.7: A noise-filtered slice (at time step 20) for 4 different threshold couples, including the couple (135,117) which was selected for further analysis. Outlines of pores are marked in red if they are deemed oil-filled and in blue if deemed brine-filled. In the top-left slice, under-segmented pores are marked, while over-segmented pores are marked in the bottom-right image.

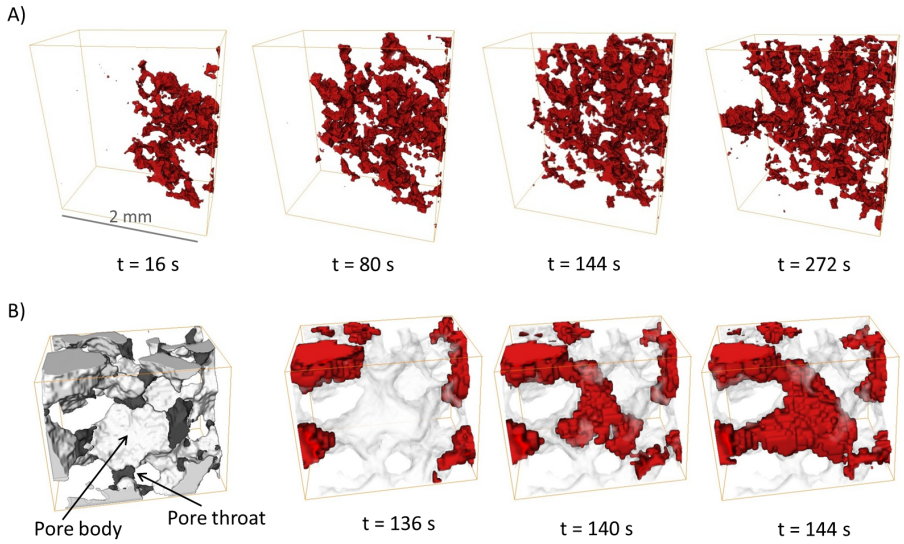

Figure 8.8: These 3D renderings illustrate our capability to image drainage under dynamic conditions. In A, the fluid distribution in a subsection of the sample is shown at four selected time steps in the experiment. Oil is rendered in red, brine and solid rock are not visualized. The left image in B shows a detail of a 3D rendering of the high-quality image after identification of pores and throats with the maximal ball network extraction (pores are rendered in white and throats in black). The 3 time series images on the right in B show that a Haines jump occurred there between time t=136 s and t=140 s. Fluid distributions were obtained by thresholding the fast micro-CT scans (acquisition time 12 s), and are independent of the pore network extraction.

work should point out how the results of this analysis are affected by the employed pore network extraction.

By measuring all the grey values in a pore volume rather than looking at single-voxel grey values, oil in smaller pores can be detected more reliably. The applied time-based median filter significantly reduces the image noise by exploiting the redundancy in the information present in the time series data, but on the other hand it can render motion artefacts worse by smoothing out the evolution of the grey value in a voxel over time. This complicates the identification of the time step in which a specific drainage event happened. Therefore, a balance has to be found by filtering the data strongly enough to limit misidentification of events in small pores without significantly smoothing out the time profile of grey values in pores too much. For example, the evolution of the grey values in pores 1 and 2 in Figure 8.2 suggests that there are at least 4 seconds in between the filling of these pores, and this is correctly captured in the pore-based segmentation. The development and implementation of more sophisticated 4D noise filtering methods, which preserve both the spatial and the temporal structure of the original 4D image, could prove important to the further development of real-time pore-scale imaging with lab-based micro-CT, (e.g. Eklund et al. (2011); Mendrik et al. (2015)). Another way to reduce motion artefacts is to select appropriate starting angles for the consecutive tomographic reconstructions (Armstrong et al., 2014a).

After clustering connected pores filled in each time step, the volume and the size of each filling event can be measured. The pore-based technique offers a unique way to compare the experimental fluid configuration to a description in terms of individual geometrical pores in a real rock sample. It should be noted that the number of single-pore events may be overestimated, as remaining image noise and motion artefacts in combination with the limited spatial resolution can result in the misidentification of filling events in small pores. Also, some of the largest events may have been broken up into smaller events in the analysis due to the fact that these events may take place over multiple seconds, and pores filled during the same large event may therefore be segmented as oil-filled in different time steps. Figure 8.9 shows the histogram of the number of geometrical pores filled in each event. In agreement with the micro-model study presented by Moebius and Or (2014a), the majority of detected events consisted of single, often small geometrical pores being filled. However, as reported in this study and in Berg et al. (2013), hundreds of

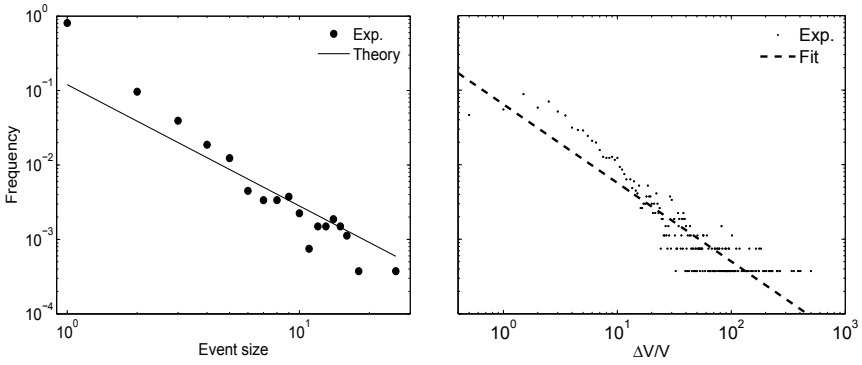

Figure 8.9: The graph on the left illustrates that most detected pore filling events consisted of the filling of single geometrical pores, and compares the event sizes to the power law behaviour predicted by percolation theory (with exponent -1.63). The distribution of filling event volumes normalized by the average pore volume (right) shows a power law behaviour with exponent -1.05 (dashed line, R^2 = 0.5 due to the smallest pores not being resolved in our experiment).

events consisting of multiple geometrical pores were detected as well.

In the literature, the statistics of the distribution of the event sizes have been analysed by modified invasion-percolation simulations and by the concept of self-organized criticality (Furuberg et al., 1996). Using percolation theory arguments, a power law behaviour is predicted. Modified invasion-percolation models predict a bending down of this power law behaviour for large events (i.e. there is an upper limit to the largest event possible), due to the finite volume of non-wetting fluid which can be drawn from the already invaded pores. The power law behaviour has been confirmed for 2D micromodels (Crandall et al., 2009). Applying the same formula from Roux and Guyon (1989) to the 3D case yields a predicted scaling exponent τ' = 1.63. Figure 8.9 shows our experimental results. As predicted by percolation theory, the measured event size histogram follows a power law distribution. However, the observed scaling exponent is larger than the theoretical prediction. This deviation from theory may be caused by non-local dynamic effects or the presence of correlated heterogeneity in the pore network and should be further examined in future work. Further investigation will also point out the possible influence of the aforementioned imaging errors (noise and motion artefacts) on this analysis.

Prior imaging experiments at synchrotron have indicated that the distribution of event volumes for real rocks follows a power law with scaling exponent τ' = 1, deviating from percolation theory predictions (Berg et al., 2013). Also, contrary to modified invasion-percolation predictions, the authors observed that large events occurred more frequently than expected from theory. Figure 8.9 shows the histogram of event volumes from our measurements, normalized by an average pore size. To allow better comparison with other measurements, the average pore size was determined from a twin sample which was scanned at higher resolution. The fit to this data yields a scaling exponent of τ' = 1.05, in accordance to Berg et al. (2013). However, it should be noted that the exact scaling exponent depends on the bin size of the histogram. Furthermore, strictly speaking percolation theory predicts the number of pores per event, rather than the volume. Therefore, we consider the new method of assessing event sizes in terms of pores per event more appropriate to judge the correspondence of invasion-percolation with experiment.

8.4 Conclusions

The drainage behaviour of porous media has often been described with quasi-static (invasion-) percolation models. However, the dynamic effects which occur during Haines jumps may influence the pore filling sequence, and the effect this has on the larger-scale flow properties is still not well understood. This raises questions to the validity of percolation models which do not take dynamics into account, spurring the investigation of the evolution of the fluid distribution in geological media. While previously, such experiments had only been performed at synchrotron facilities, we presented the visualization of Haines jumps with a laboratory-based micro-CT scanner. We showed that by tracking the filling state of individual geometrical pores during drainage, the sizes of the pore filling cascades could be compared to invasion-percolation predictions. Aside from the analysis in terms of geometrical pores, the presented 4D micro-CT work flow is directly applicable to the study of various other questions regarding two-phase flow in geological materials under dynamic conditions, e.g. hysteresis in drainage/imbibition cycles and trapped non-wetting phase remobilization.

In general, investigating the dynamics of many geophysical processes calls for real-time, pore scale 3D imaging while the process in question is taking place. The application of micro-CT in this context has mostly remained limited to synchrotron facilities. The work presented here shows that it is becoming possible to perform such studies with lab-based micro-CT scanners built with standard X-ray sources and detectors. While the subsequent image analysis is currently still challenging due to limitations in signal-to-noise ratio and motion artefacts (depending on the rate of the investigated process), we believe such experiments will become increasingly important in years to come as both hardware, tomographic reconstruction and 4D image analysis methods continue to improve.

Part IV

Conclusions

9

Conclusions and outlook

The work presented in this thesis is focused on two-phase flow, which is of key importance in numerous geological applications. Important quantities of interest for this process are the capillary pressure curve, which expresses the average pressure difference between the fluids in function of the wetting fluid saturation of the porous medium, and the relative permeability curve, which expresses the decrease of the permeability to each fluid in function of the wetting fluid saturation. The related physics are explained in Part I of this thesis. Several empirical relations to estimate these properties exist for rather simple materials, like sand packs or well-sorted, highly porous sandstones, yet often fail to describe the behaviour in more complex rocks. To understand why this is the case, models based on the pore structure obtained from micro-CT are very useful. Chapter 3 (Part II) gives an overview of these methods, and notes that pore network models (PNM) have to date been the most successful at describing two-phase flow through pore spaces extracted from micro-CT images of natural rocks. The simplifications of the fluid physics and pore geometry made in these models allow efficient simulations and facilitate interpretations of the results, yet come at the price of many tuning parameters and uncertainties (outlined in more detail further in this Chapter).

Despite the fast development of pore scale models due to increasing pore scale imaging capabilities and computational power, modeling two-phase flow in materials with pore sizes stretching over multiple orders of magnitude has remained problematic. This is important, as many geological materials of interest in e.g. reservoir applications have pore spaces of a multi-scale nature, and classical relations often fail in these materials. Previous attempts at image-based pore scale modeling of such rocks had either included individual micro-pores, often resulting in computational issues, or had only included microporosity as an added term in the saturation and/or the hydraulic conductivity of macro-pores and macro-throats, which is only useful in rocks with very well-connected resolved pore systems. In Part II, we present a new network model to settle these issues. The novelty is that a third type of network elements are added to the PNM, which have averaged microporosity properties and take part in both the flow rate calculations and the invasion-percolation scheme. As explained in Chapter 4, the model is extracted from a micro-CT scan by first identifying zones of unresolved porosity in the segmentation, clustering these regions, and adding connections ("micro-links") between any two macro-pores which touch the same region of unresolved porosity. The contact surface areas of each pore with such an area is measured on the image. In the drainage invasion-percolation sequence, the non-wetting phase can percolate through micro-links in order to invade a neighbouring macropore, if a breakthrough capillary pressure is overcome. This pressure is derived from an input value and adapted to the geometry of individual micro-links. The microporosity's saturation is calculated from an input capillary pressure curve, which should be representative for the unresolved porous medium. The micro-links are taken into account in the flow rate calculations by treating each connection as a truncated cone made of continuous porous material with an assigned permeability and relative permeability, representative of the microporosity. Additionally, Chapter 4 shows that this model manages to capture much of the drainage behaviour of network models with individual micro-pores, but at lower computational cost. The model was also tested on relatively large micro-CT data sets (1000^3 voxels) of two carbonate rocks, resulting in qualitative agreement with experimental P_c- K_r- and RI-curves. It should be noted that to quantify the relative error of the simulations compared to experiment, it is necessary to repeat both the model and the experiment on a number of different samples, in order to take into account the natural heterogeneity of the material. Unfortunately, this was not possible within

the time constraints of this PhD work, but it should be the subject of further investigation.

In Chapter 5, the extension of the new multi-scale network model to secondary imbibition (including possible wettability alteration after primary drainage) is presented. Simulating imbibition is more complex than drainage, because more pore filling mechanisms have to be taken into account (piston-like displacement, cooperative pore filling and snap-off). During the secondary invasion, which is a water flooding process in our simulations, a different set of input properties is supplied to the microporosity to take hysteresis into account. If the microporosity is water-wet, it typically fills with water at much higher pressures than macro-pores, which are then the limiting factors in the invasion sequence. In this case, microporosity breakthrough capillary pressures are of minor importance to describe piston-like invasion of a macro-pore from a neighbouring micro-link. If the microporosity is oil-wet, the breakthrough capillary pressure related to such an invasion can be described in the same way as during drainage. During a cooperative pore filling event in a pore, contact surface areas with microporous regions are regarded as rough pore walls, and micro-links are therefore not taken into account in the calculation of the pore's invasion pressure. Oil can escape from pores through micro-links, as long as the microporosity's relative permeability to oil is non-zero. Saturation and flow rate calculations proceed similarly as in the drainage simulations. Finally, Chapter 5 shows that the model produces results that fit well with those from a network model with individual micro-pores, for water-wet, oil-wet and differently distributed mixed-wet situations. Simulations on the Estaillades network show a good qualitative match to experiments.

After presenting the methodology for drainage and imbibition in Chapters 4 and 5, the multi-scale PNM is applied to qualitatively study the two-phase flow behaviour of three microporosity-rich limestones and two tight sandstones in Chapter 6. To examine how the drainage and imbibition properties of these complex rock types are influenced by the connectivity of macro-pores to each other and to zones with unresolved small-scale porosity, we varied the microporosity properties and analysed the network properties of the different samples. The network models produced results which qualitatively matched relative permeability and capillary pressure experiments, indicating that they could be applicable to tight materials as well as the previously investigated permeable

limestones. This is a significant and novel finding, because no previously published image-based multi-scale network models have shown this. This Chapter illustrates the usefulness of the PNM to analyse the cause of the observed trends, e.g. permeability jail and differences in mixed-wettability behaviour.

Despite the encouraging results in these Chapters, a number of crucial challenges remain to be solved, notably regarding reproducibility and reduction of user-defined parameters. The challenges already start with sample selection: even in the multi-scale network models, the imaged samples are typically much smaller than the core scale (cylinders of a few mm diameter compared to cylinders of a few cm diameter and several cm to m in length). Therefore, there is not only a need for multi-scale work flows which incorporate nanometre-sized porosity with pores in the micrometer range, but also for going from the micrometer scale to the the centimetre and perhaps even the meter scale. Here, core scanning in combination with region of interest scanning and automatic rock typing (e.g. Deakin et al. (2015)) may be a potential solution towards the future. After sample selection, errors resulting from imaging and (especially) image segmentation are extremely difficult to quantify, and are associated with a large operator dependence. Automatic segmentation algorithms (Iassonov et al., 2009) are part of the solution, but current implementations are not always easily available and generally applicable to all samples and images. Next, network extraction algorithms introduce simplifications in the geometry of the pore space, and may require some arbitrary decisions (e.g. regarding the length of throats). This problem can be alleviated by defining throats as surfaces, and calculating the fluid conductances of network elements by applying direct single-phase pore scale flow simulation algorithms (Raeini et al., 2015a; Sholokhova et al., 2009). For the multi-scale PNM specifically, the representation of microporous transport pathways in the form of micro-links is limited in generality, it is for example not a good approach in very tight materials with few macro-pores. Possible solutions would be to represent the microporosity as a network of generalized nodes and links in the network (e.g. as recently proposed by Ruspini et al. (2016b)), or by coupling the macroporosity network to a finite volume simulator for the microporosity. After the network extraction, the simulations also introduce simplifications. The assignment of contact angles to different parts of the pore space is a very important source of uncertainty, which could benefit from in-situ imaging studies (e.g. contact angle measurements). Further

uncertainties are caused by the parametric algorithm to calculate cooperative pore filling pressures which is used in this work, yet recently analytical solutions to calculate these invasion pressures have been developed (Ruspini et al., 2016b).

While Part II of this thesis presents a new pore network model, the validation of such models is in itself a topic in need of research. To verify whether the models correctly represent pore scale invasion processes during two-phase flow, time-resolved in-situ imaging experiments are very useful. This however requires to simultaneously achieve time resolutions on the order of tens of seconds and spatial resolutions on the order of micrometers. This has become possible at a number of synchrotron beam lines over the last few years, yet the available beam time on these instruments is very limited. For this technique to become a standard tool in the validation of pore scale models, more accessible fast imaging capabilities on lab-based micro-CT scanners are of large interest. This is treated in Part III of this work. Since fast lab-based micro-CT has received relative little attention in the literature, a current state-of-the-art of this technique is presented in Chapter 7. In general, it benefits from a strong integration of optimizing hardware, reconstruction algorithms and image analysis routines. Barring possibly disruptive technologies (e.g. liquid metal jet X-ray sources) being further developed and widely implemented, most improvements in the next few years can be expected from handling the data in a smarter way. In most fast imaging applications, a lot of information is known in advance (e.g. the pore structure is known from a pre-scan, the fluid phases are known and adhere to some well-known physics, etc.), which can then be used to supplement the lower-quality data gathered during the in-situ experiment. Most of these approaches can be thought of as decreasing the information content which needs to be extracted during the in-situ experiment, or optimally making use of the correlations between scans made at different time steps. This can either be done during reconstruction, e.g. using iterative algorithms with prior information, or during the image analysis, e.g. 4D filtering and segmentation.

After treating the state-of-the-art of fast lab-based micro-CT, we show how this technique can be applied to study the pore scale drainage behaviour of a sandstone in Chapter 8. The main goal of this work was to investigate whether dynamic effects during Haines jumps, which are neglected in quasi-static pore network models, strongly impact the

evolution of the fluid distributions. The experiment was performed using UGCT's EMCT scanner, allowing to continuously image the drainage process at 12 seconds per scan and a voxel size of 15 microns over a duration of 5 minutes. While the image quality is lower than at synchrotron, the experiment succeeded in visualizing individual Haines jumps. We show that a decomposition of the pore space in pores and throats can be used to estimate the amount of pores filled per Haines jump. This decompisition also helps to deal with the noise in the images. While improvements in the image analysis procedure should be made to improve the reliability of this analysis (e.g. by taking more than two time step images into account when identifying a jump), tentative results show a qualitative agreement to percolation theory predictions and to quasi-static simulations on pore network models. This indicates that quasi-static simulations succeed in capturing most of the relevant physics during drainage, which of course has direct implications for the averaged properties used to describe the field-scale behaviour (e.g. capillary pressure, relative permeability and resistivity index curves). This is confirmed by Berg et al. (2016), who found a good agreement between relative permeability calculations based on experimentally observed fluid distributions (from in-situ fast synchrotron tomography) and on quasi-statically simulated fluid distributions.

The work in this thesis is focussed on earth sciences, but is to a large extent also useful to the investigation and engineering of industrial porous media (e.g. paper, fuel cells and batteries, filters, superabsorbants). The current growth of initiatives like Interpore (www.interpore.org), which strive to bring scientists working on porous materials in different fields together, illustrates the wide range of applications for these methods. Some of the concepts explored in the multi-scale PNM algorithm (e.g. the notion of networks with resolved and unresolved network elements) could be valuable additions to models which describe other transport processes than two-phase flow (e.g. solute and reactive transport) in a wide range of porous materials. Fast micro-CT imaging is even more widely applicable, and can be used to investigate e.g. transport, swelling, deformation and fracturing of porous materials. The opportunity to model and visualize such micro-scale processes has the potential to revolutionize the way we understand the porous materials that surround us every day.

A

Appendix 1: microporosity properties for Chapter 5

A.1 Microporosity properties in the artificial networks

The microporosity's input properties of the artificial PNM simulations in chapter 5 can be found in table A.1 and figure A.1. These properties were calculated on the parent network of the microposity in the multi-scale network. The parent network was obtained by downscaling the original macroporosity network (without removing the "clay-clogged"pores) with a factor 5. This PNM had a domain size of 400 x 400 x 400 μm^3.

A.2 Microporosity properties in the Estaillades network

The microporosity's input properties of the Estaillades PNM simulations can be found in table A.2 and figure A.2. These properties were calculated

Microporous property	value
ϕ_{micro}	0.38
K_{micro} (mD)	538
FF_{micro}	6.5
S_{BTP} Drainage	0.16
S_{BTP} SWW	0.10
S_{BTP} IWW	0.15
S_{BTP} SOW	0.20
S_{BTP} IOW	0.15
$L_{cut-off}$ microlinks (μm)	225

Table A.1: Input properties of the microporosity in the artificial network simulation

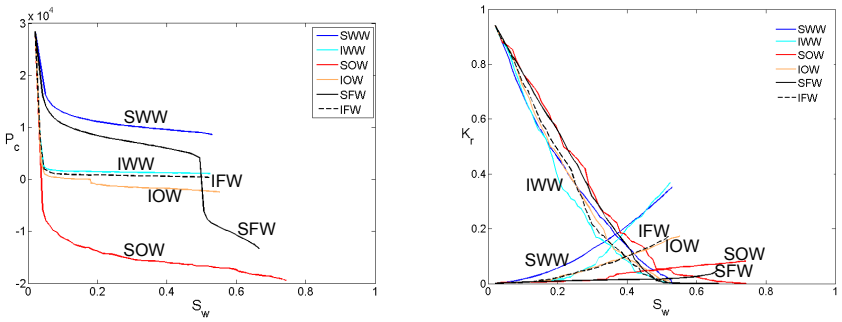

Figure A.1: P_c and K_r curves calculated on the single-scale artificial microporosity PNM and used as input to the multi-scale artificial PNM

Microporous property	value
ϕ_{micro}	0.36
K_{micro} (mD)	8
FF_{micro}	7.72
n_{micro}	2
S_{BTP} Drainage	0.3
S_{BTP} SWW	0.3
S_{BTP} IWW	0.2
S_{BTP} SOW	0.7
S_{BTP} IOW	0.7
$L_{cut-off}$ microlinks (μm)	67.5

Table A.2: Input properties of the microporosity in the Estaillades network simulation

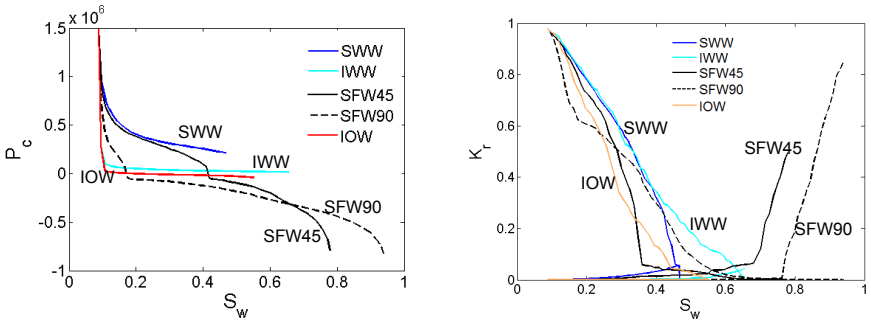

Figure A.2: P_c and K_r curves calculated on the single-scale Estaillades microporosity PNM and used as input to the multi-scale Estaillades PNM

on a single-scale PNM which was generated by assigning the pore size distribution for pores smaller than 4.4 μm diameter to a regular-cubic lattice-based PNM. This distribution was measured by a mercury intrusion experiment on a different Estaillades sample. The PNM had a domain size of 300 x 300 x 300 μm^3.

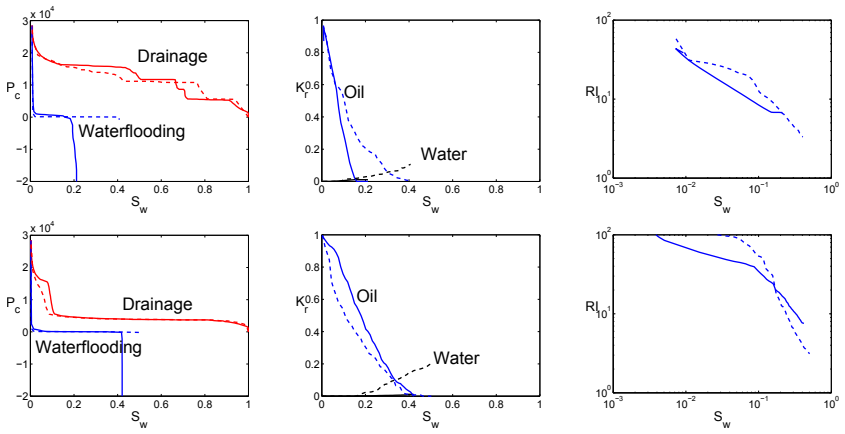

Figure A.3: Capillary pressure, relative permeability and resistivity index curves from secondary water flooding simulations where the pores are randomly assigned intermediately-oil or water-wet (IFW). These results were calculated on the artificial network where 50 % (top row) and 20 % (bottom row) of the macropores were removed and replaced by microporosity. Broken lines are the reference network, full lines represent the model presented in this paper.

A.3 Non-uniform intermediately wetted simulations on the artificial networks

Results for IFW, IMWS and IMWL simulations can be found in figures A.3 to A.5, respectively.

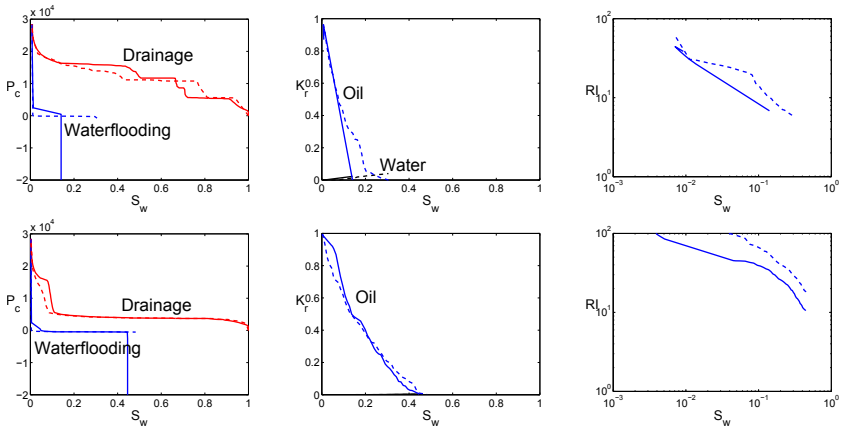

Figure A.4: Capillary pressure, relative permeability and resistivity index curves from secondary water flooding simulations where the macropores are intermediately oil-wet and the micropores intermediately water-wet (IMWL). These results were calculated on the artificial network where 50 % (top row) and 20 % (bottom row) of the macropores were removed and replaced by microporosity. Broken lines are the reference network, full lines represent the model presented in this paper.

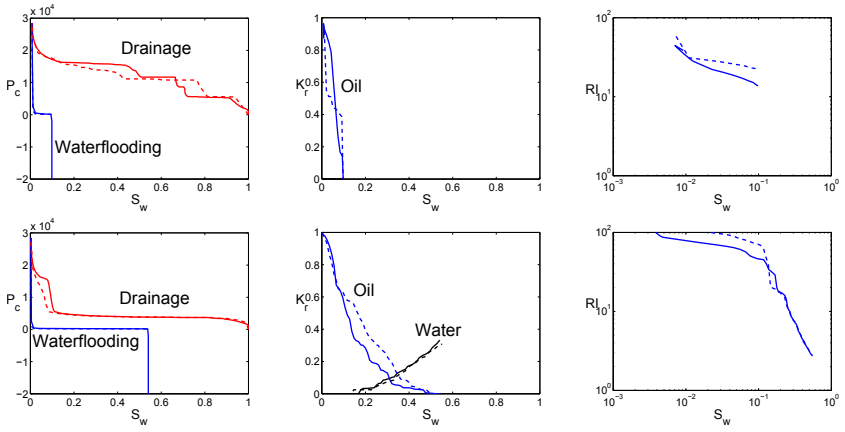

Figure A.5: Capillary pressure, relative permeability and resistivity index simulations curves from secondary water flooding simulations where the macropores are intermediately water-wet and the micropores intermediately oil-wet (IMWS). These results were calculated on the artificial network where 50 % (top row) and 20 % (bottom row) of the macropores were removed and replaced by microporosity. Broken lines are the reference network, full lines represent the model presented in this paper.

B

Appendix 2: microporosity properties for Chapter 6

Table B.1 contains the input properties for the 3 microporosity types in the multi-scale PNM simulations presented in Chapter 6. Figure B.1 contains the capillary pressure and relative permeability curves of the 3 microporosity types for primary drainage and secondary water flooding (WW, OW and FW). Figures B.2 and B.3 show water-flooding capillary pressure and relative permeability curves for the five samples treated in Chapter 6, under different wettability conditions with the M2 microporosity type. Figures B.4 and B.5 show these properties for the M3 microporosity type.

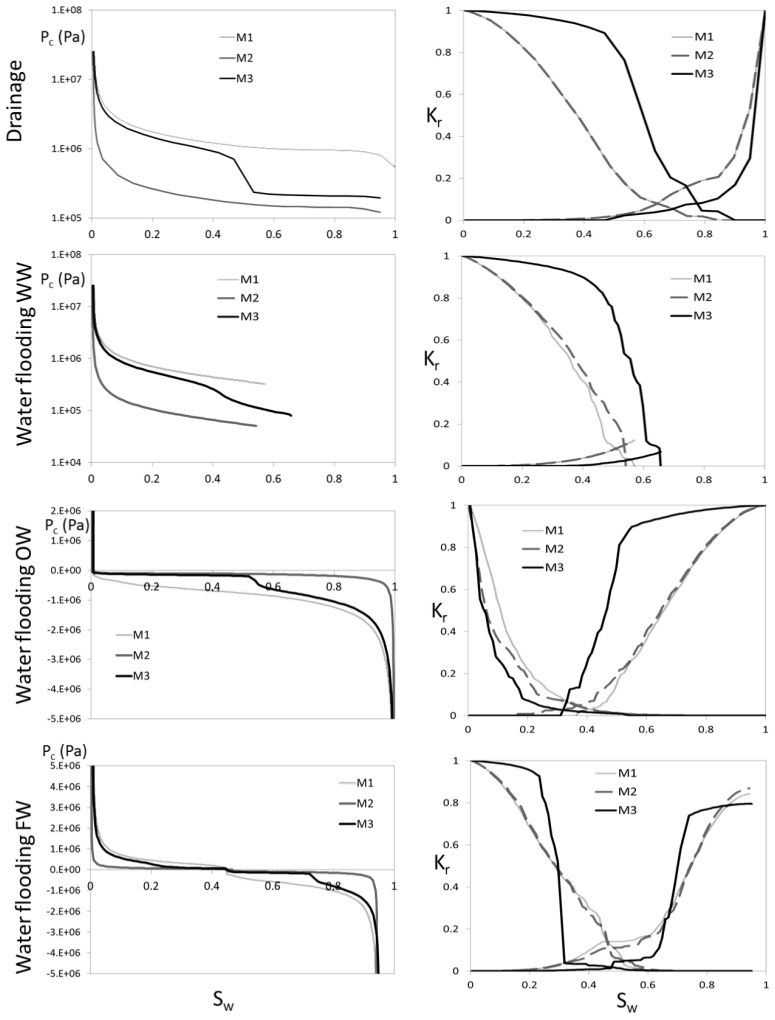

Figure B.1: P_c and K_r curves calculated on the single-scale artificial microporosity PNM and used as input to the multi-scale artificial PNM

Property	M1	M2	M3
ϕ_{micro}	0.30	0.30	0.30
K_{micro} (mD)	0.21	9.26	7.53
L_{BTP} (μm)	8.64	57.6	11.3
S_{BTP} Drainage	0.14	0.15	0.12
S_{BTP} WW	0.18	0.20	0.36
S_{BTP} OW	0.36	0.17	0.31
S_{BTP} FW	0.20	0.20	0.45

Table B.1: Input properties of the microporosity in the artificial network simulation

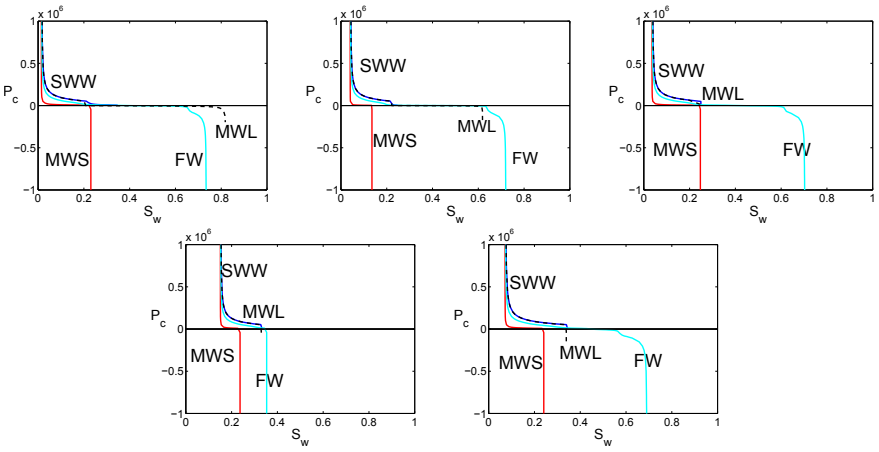

Figure B.2: Water flooding capillary pressure curves in Estaillades, Savonnieres and Massangis Jaune, Wilcox and Knorringfjellet (top to bottom, left to right) for the M2 case.

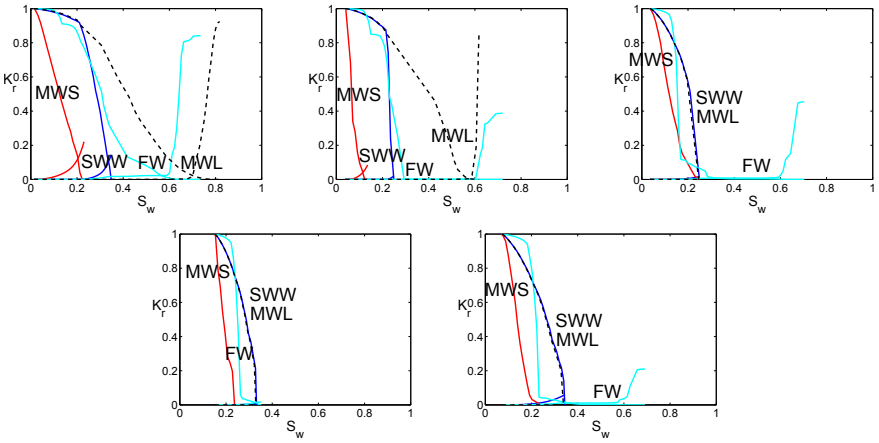

Figure B.3: Water flooding relative permeability curves in Estaillades, Savonnieres and Massangis Jaune, Wilcox and Knorringfjellet (top to bottom, left to right) for the M2 case.

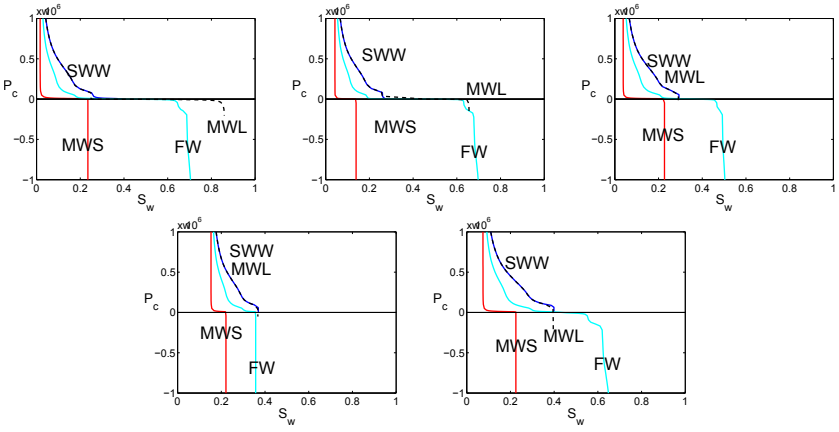

Figure B.4: Water flooding capillary pressure curves in Estaillades, Savonnieres and Massangis Jaune, Wilcox and Knorringfjellet (top to bottom, left to right) for the M3 case.

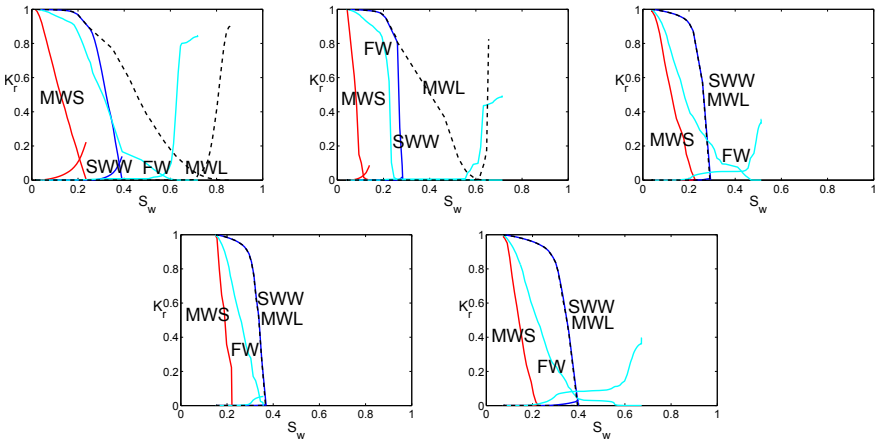

Figure B.5: Water flooding relative permeability curves in Estaillades, Savonnieres and Massangis Jaune, Wilcox and Knorringfjellet (top to bottom, left to right) for the M3 case.

C

List of Symbols

- β: Scaling exponent (percolation theory)
- μ: Linear X-ray attenuation coefficient
- ν: Scaling exponent (percolation theory)
- ρ_{micro}: Resistivity of the microporous phase
- ϕ: Porosity
- σ: Interfacial tension
- θ: Contact angle
- θ_a: Advancing contact angle
- θ_r: Receding contact angle
- τ: Scaling exponent (percolation theory)
- 2D: Two-dimensional
- 3D: Three-dimensional
- A: Cross-sectional surface area
- a: tortuosity factor
- BGK: Bhatnagar-Gross-Cook
- BIB-SEM: Broad ion beam scanning electron microscopy
- BSE: Backscattered electrons
- Ca: Capillary number

- CDI: Coherent diffractive imaging
- CFD: Computational fluid dynamics
- CN: Coordination number
- CT: Computed tomography
- C_i: input parameters in parametric cooperative pore filling model
- D: Darcy
- DOHT: Distance-ordered homotopic thinning
- DPNM: Dual pore network model
- EDS: Energy-dispersive spectroscopy
- EDX: Energy-dispersive X-ray spectroscopy
- EMCT: Environmental micro-CT scanner (at UGCT)
- ESRF: European Synchrotron Radiation Facility (France)
- eV: electron Volt
- F: Formation factor
- FBP: Filtered back-projection (reconstruction algorithm)
- FDK: Feldmann-Davis-Kress (reconstruction algorithm)
- FE-SEM: Field-emission scanning electron microscopy
- FIB: Focussed ion beam
- FIB-SEM: Focussed ion beam scanning electron microscopy
- FW: Fractionally wet (mixed wettability distribution)
- g_{ij} : Conductivity from pore i to pore j
- G: shape factor
- HECTOR: Higher-energy CT optimized for Research (scanner at UGCT)
- I_0: Incident intensity
- IFW: Intermediate fractionally wet (wettability distribution)
- IMWL: Intermediate mixed wet large (wettability distribution)
- IMWS: Intermediate mixed wet small (wettability distribution)
- IOW: Intermediately oil-wet
- IWW: Intermediately water-wet
- RI(S_w): Resistivity index at saturation Sw
- I: Intensity
- I_n: Cooperative pore filling event with n oil-filled neighbours
- K_r: Relative permeability
- $K_{r,nw}$: Relative permeability to non-wetting phase
- $K_{r,o}$: Relative permeability to oil
- $K_{r,w}$: Relative permeability to wetting phase or specifically to water

- K: Permeability
- keV: Kilo electron volt
- L_{ij}: Distance between pores i and j
- LB: Lattice-Boltzmann
- LG: Lattice-gas
- m: cementation exponent
- Micro-CT: Micro-computed tomography
- MIP: Mercury intrusion porosimetry
- MRI: Magnetic resonance imaging
- MTF: Modulation transfer function
- MSF: Minimal spanning forest
- MWL: Mixed wet large (wettability distribution)
- MWS: Mixed wet small (wettability distribution)
- n: saturation exponent
- NAPL: Non-acqueous phase liquid
- P_c: Capillary pressure
- P_i: Pressure in pore i
- PICCS: Prior image constrained compressed sensing (reconstruction algorithm)
- P: Pressure
- PEEK: Polyether ether ketone (a type of polymer)
- Pixel: Picture element
- PNM: Pore network model
- PPROGRESS: Pore scale processes in geomaterials research (team)
- PSD: Pore size distribution
- PSI: Paul Scherrer Institute (Switzerland)
- q_{ij}: Flux from pore i to pore j
- q: Fluid flux
- QEMSCAN: Quantitative Evaluation of Minerals by SCANning electron microscopy (FEI company)
- r: Radius
- R: Resistivity at full brine saturation
- Re: Reynolds number
- RI: Resistivity Index
- S_b: breakthrough saturation
- SAXS: Small-angle X-ray scattering
- SEM: Scanning electron microscopy

- SFW: Strong fractionally wet (wettability distribution)
- SMWL: Strong mixed wet large (wettability distribution)
- SMWS: Strong mixed wet small (wettability distribution)
- SOW: Strongly oil-wet
- SPH: Smoothed particle hydrodynamics
- S_w: wetting saturation
- S_or: residual oil saturation
- SWW: Strongly water-wet
- TOMCAT: The beamline for TOmographic Microscopy and Coherent rAdiology experimentTs at the Paul Scherrer Institute
- UGCT: Ghent University's Centre for X-ray Computed Tomography
- Voxel: Volume Element
- v: flow velocity
- WW: water-wet
- Z: Atomic number

Bibliography

Acharya, R. C., Van der Zee, S. E. A. T. M., and Leijnse, A. Transport modeling of nonlinearly adsorbing solutes in physically heterogeneous pore networks. *Water Resources Research*, 41(2):n/a–n/a, 2005.

Aghaei, A. and Piri, M. Direct pore-to-core up-scaling of displacement processes: Dynamic pore network modeling and experimentation. *Journal of Hydrology*, 522:488–509, 2015.

Al-Futaisi, A. and Patzek, T. W. Secondary imbibition in NAPL-invaded mixed-wet sediments. *Journal of Contaminant Hydrology*, 74(1-4):61–81, 2004.

Al-Kharusi, A. S. and Blunt, M. J. Network extraction from sandstone and carbonate pore space images. *Journal of Petroleum Science and Engineering*, 56(4):219–231, 2007.

Al-Menhali, A. S. and Krevor, S. Capillary Trapping of CO 2 in Oil Reservoirs: Observations in a Mixed-Wet Carbonate Rock. *Environmental Science & Technology*, 50(5):2727–2734, 2016.

Al-Raoush, R. and Willson, C. Extraction of physically realistic pore network properties from three-dimensional synchrotron X-ray microtomography images of unconsolidated porous media systems. *Journal of Hydrology*, 300(1-4):44–64, 2005.

Al-Raoush, R., Thompson, K., and Willson, C. S. Comparison of Network Generation Techniques for Unconsolidated Porous Media. *Soil Science Society of America Journal*, 67(6):1687, 2003.

Al-Sayari, S. S. *The Influence of Wettability and Carbon Dioxide Injection on Hydrocarbon Recovery*. PhD thesis, Imperial College, 2009.

Algive, L., Békri, S., Nader, F., Lerat, O., and Vizika, O. Impact of Diagenetic Alterations on the Petrophysical and Multiphase Flow Properties of Carbonate Rocks Using a Reactive Pore Network Modeling Approach. *Oil & Gas Science and Technology Revue d'IFP Energies nouvelles*, 67(1):147–160, 2012.

Alhashmi, Z., Blunt, M., and Bijeljic, B. Predictions of dynamic changes in reaction rates as a consequence of incomplete mixing using pore scale reactive transport modeling on images of porous media. *Journal of Contaminant Hydrology*, 179:171–181, 2015.

Andersen, A. H. and Kak, A. C. Simultaneous algebraic reconstruction technique (SART): a superior implementation of the art algorithm. *Ultrasonic imaging*, 6:81–94, 1984.

Andrä, H., Combaret, N., Dvorkin, J., Glatt, E., Han, J., Kabel, M., Keehm, Y., Krzikalla, F., et al. Digital rock physics benchmarkspart II: Computing effective properties. *Computers & Geosciences*, 50:33–43, 2013.

Andrew, M., Bijeljic, B., and Blunt, M. J. Pore-scale imaging of geological carbon dioxide storage under in situ conditions. *Geophysical Research Letters*, 40(15):3915–3918, 2013.

Andrew, M., Bijeljic, B., and Blunt, M. J. Pore-scale contact angle measurements at reservoir conditions using X-ray microtomography. *Advances in Water Resources*, 68: 24–31, 2014.

Andrew, M., Menke, H., Blunt, M. J., and Bijeljic, B. The Imaging of Dynamic Multiphase Fluid Flow Using Synchrotron-Based X-ray Microtomography at Reservoir Conditions. *Transport in Porous Media*, 110(1):1–24, 2015.

Arbogast, T. and Gomez, M. S. M. A discretization and multigrid solver for a DarcyStokes system of three dimensional vuggy porous media. *Computational Geosciences*, 13(3): 331–348, 2009.

Archie, G. The Electrical Resistivity Log as an Aid in Determining Some Reservoir Characteristics. *Transactions of the AIME*, 146(01):54–62, 1942.

Armstrong, R. T. and Berg, S. Interfacial velocities and capillary pressure gradients during Haines jumps. *Physical Review E*, 88(4):43010, 2013.

Armstrong, R. T., Evseev, N., Koroteev, D., and Berg, S. Interfacial velocities and the resulting velocity field during a Haines jump. In *Int. Symp. Soc. Core Analysts*, pages 1–12, Avignon, France, 2014a. Society of Core Analysts.

Armstrong, R. T., Georgiadis, A., Ott, H., Klemin, D., and Berg, S. Critical capillary number: Desaturation studied with fast X-ray computed microtomography. *Geophysical Research Letters*, 41(1):55–60, 2014b.

Armstrong, R. T., Ott, H., Georgiadis, A., Rucker, M., Schwing, A., and Berg, S. Subsecond pore-scale displacement processes and relaxation dynamics in multiphase flow. *Water Resour Res*, 50(12):9162–9176, 2014c.

Arns, J.-Y., Robins, V., Sheppard, A. P., Sok, R. M., Pinczewski, W. V., and Knackstedt, M. A. Effect of Network Topology on Relative Permeability. *Transport in Porous Media*, 55(1):21–46, 2004.

Arns, J. Y., Sheppard, A. P., Arns, C. H., Knackstedt, M. A., and Yelkhovsky, A. Pore level validation of representative pore networks obtained from micro-CT images. In *Int. Symp. Soc. Core Analystst*, pages 1–12, Calgary, Canada, 2007. Society of Core Analysts.

Arrufat, T., Bondino, I., Zaleski, S., LAGREE, B., and Keskes, N. Developments on Relative Permeability Computation in 3D Rock Images. In *Abu Dhabi International Petroleum Exhibition and Conference*, volume 72025-MS. Society of Petroleum Engineers, 2014.

Baker, D. R., Brun, F., O'Shaughnessy, C., Mancini, L., Fife, J. L., and Rivers, M. A four-

dimensional X-ray tomographic microscopy study of bubble growth in basaltic foam. *Nature Communications*, 3:1135, 2012.

Bakke, S. and Øren, P.-e. 3-D Pore-Scale Modelling of Sandstones and Flow Simulations in the Pore Networks. *SPE Journal*, 2(02):136–149, 1997.

Baldwin, C. A., Sederman, A. J., Mantle, M. D., Alexander, P., and Gladden, L. F. Determination and Characterization of the Structure of a Pore Space from 3D Volume Images. *Journal of Colloid and Interface Science*, 181(1):79–92, 1996.

Bale, H. a., Haboub, A., MacDowell, A. a., Nasiatka, J. R., Parkinson, D. Y., Cox, B. N., Marshall, D. B., and Ritchie, R. O. Real-time quantitative imaging of failure events in materials under load at temperatures above 1,600 C. *Nature materials*, 12:40–6, 2013.

Bandara, U., Tartakovsky, A., Oostrom, M., Palmer, B., Grate, J., and Zhang, C. Smoothed particle hydrodynamics pore-scale simulations of unstable immiscible flow in porous media. *Advances in Water Resources*, 62:356–369, 2013.

Bartels, M., Hernandez, V. H., Krenkel, M., Moser, T., and Salditt, T. Phase contrast tomography of the mouse cochlea at microfocus x-ray sources. *Applied Physics Letters*, 103, 2013.

Batenburg, K. J. and Sijbers, J. DART: A Practical Reconstruction Algorithm for Discrete Tomography. *IEEE transactions on image processing : a publication of the IEEE Signal Processing Society*, 20:2542–2553, 2011.

Bauer, D., Youssef, S., Han, M., Bekri, S., Rosenberg, E., Fleury, M., and Vizika, O. From computed microtomography images to resistivity index calculations of heterogeneous carbonates using a dual-porosity pore-network approach: Influence of percolation on the electrical transport properties. *Phys. Rev. E*, 84(1):11133, 2011.

Bauer, D., Youssef, S., Fleury, M., Bekri, S., Rosenberg, E., and Vizika, O. Improving the Estimations of Petrophysical Transport Behavior of Carbonate Rocks Using a Dual Pore Network Approach Combined with Computed Microtomography. *Transport in Porous Media*, 94(2):505–524, 2012.

Bear, J. Dynamics of Fluids in Porous Media. *Soil Science*, 120(2), 1975.

Bekri, S., Laroche, C., and Vizika, O. Pore-network models to calculate transport properties in homogeneous and heterogeneous porous media. In Hassanizadeh, Schotting, Gray, and Pinder, editors, *Computational Methods in Water Resources, Proceedings of the XIVth International Conference*, page Vol. 2 (1115), Delft, Holland, 2002. Elsevier.

Bekri, S., Laroche, C., and Vizika, O. Pore network models to calculate transport and electrical properties of single or dual-porosity rocks. In *Int. Symp. Soc. Core Analysts*, volume 35. Society of Core Analysts, 2005.

Berg, S., Ott, H., Klapp, S. A., Schwing, A., Neiteler, R., Brussee, N., Makurat, A., Leu, L., et al. Real-time 3D imaging of Haines jumps in porous media flow. *Proceedings of the National Academy of Sciences*, 110(10):3755–3759, 2013.

Berg, S., Rücker, M., Ott, H., Georgiadis, A., van der Linde, H., Enzmann, F., Kersten,

M., Armstrong, R., et al. Connected Pathway Relative Permeability from Pore-Scale Imaging of Imbibition. *Advances in Water Resources*, 2016.

Berry, R. a., Martineau, R. C., and Wood, T. R. Particle-Based Direct Numerical Simulation of Contaminant Transport and Deposition in Porous Flow. *Vadose Zone Journal*, 3(1): 164–169, 2004.

Bhat, S. and Kovscek, A. Permeability Modification of Diatomite During Hot Fluid Injection. In *SPE Western Regional Meeting*. Society of Petroleum Engineers, 2013.

Bhattad, P., Willson, C. S., and Thompson, K. E. Effect of Network Structure on Characterization and Flow Modeling Using X-ray Micro-Tomography Images of Granular and Fibrous Porous Media. *Transport in Porous Media*, 90(2):363–391, 2011.

Bijeljic, B., Mostaghimi, P., and Blunt, M. J. Insights into non-Fickian solute transport in carbonates. *Water Resources Research*, 49(April):2714–2728, 2013a.

Bijeljic, B., Raeini, A., Mostaghimi, P., and Blunt, M. Predictions of non-Fickian solute transport in different classes of porous media using direct simulation on pore-scale images. *Physical Review E*, 87(1):013011, 2013b.

Blunt, M., King, M., and Scher, H. Simulation and theory of two-phase flow in porous media. *Physical Review A*, 46(12):7680–7699, 1992.

Blunt, M. J. Physically-based network modeling of multiphase flow in intermediate-wet porous media. *Journal of Petroleum Science and Engineering*, 20(3-4):117–125, 1998.

Blunt, M. J. Flow in porous media pore-network models and multiphase flow. *Current Opinion in Colloid & Interface Science*, 6(3):197–207, 2001.

Blunt, M. J. *Multiphase Flow in Permeable Media: A Pore-Scale Perspective*. Cambridge University Press, Cambridge, UK, 2016.

Blunt, M. J., Jackson, M. D., Piri, M., and Valvatne, P. H. Detailed physics, predictive capabilities and macroscopic consequences for pore-network models of multiphase flow. *Advances in Water Resources*, 25(8-12):1069–1089, 2002.

Blunt, M. J., Bijeljic, B., Dong, H., Gharbi, O., Iglauer, S., Mostaghimi, P., Paluszny, A., and Pentland, C. Pore-scale imaging and modelling. *Advances in Water Resources*, 51: 197–216, 2013.

Boek, E. Pore scale simulations of flow in porous media using Lattice-Boltzmann computer simulations. In *SPE annual technical conference and exhibition*. Society of Petroleum Engineers, 2010.

Boek, E. S., Zacharoudiou, I., Gray, F., Shah, S. M. K., Crawshaw, J., and Yang, J. Multiphase Flow And Reactive Transport At The Pore Scale Using Lattice-Boltzmann Computer Simulations. In *SPE Annual Technical Conference and Exhibition*. Society of Petroleum Engineers, 2014.

Bondino, I., Hamon, G., Kallel, W., and Kachuma, D. Relative permeabilities from simulation in 3D rock models and equivalent pore networks: critical review and way forward. In *Int. Symp. Soc. Core Analysts*, Aberdeen, Scotland, 2012. Society for Core Analysts, Society of Core Analysts.

Boone, M., De Kock, T., Bultreys, T., De Schutter, G., Vontobel, P., Van Hoorebeke, L., and Cnudde, V. 3D mapping of water in oolithic limestone at atmospheric and vacuum saturation using X-ray micro-CT differential imaging. *Materials Characterization*, 97: 150–160, 2014.

Boone, M. N. *New imaging modalities in high resolution X-ray tomography*. Phd thesis, Ghent University, 2013.

Braathen, A., Bælum, K., Christiansen, H., Dahl, T., Flå, H., Hansen, F., Hanssen, T. H., Jochmann, M., et al. Longyearbyen CO2 lab 2007-2009 - Phase 1 final report. Technical report, Unis, 2009.

Brabant, L., Vlassenbroeck, J., De Witte, Y., Cnudde, V., Boone, M. N., Dewanckele, J., and Van Hoorebeke, L. Three-dimensional analysis of high-resolution X-ray computed tomography data with Morpho+. *Microscopy and microanalysis*, 17(2):252–63, 2011.

Brabant, L., Pauwels, E., Dierick, M., Van Loo, D., Boone, M. A., and Van Hoorebeke, L. A novel beam hardening correction method requiring no prior knowledge, incorporated in an iterative reconstruction algorithm. *NDT and E International*, 51:68–73, 2012.

Brabant, L., Dierick, M., Pauwels, E., Boone, M., and Hoorebeke, L. V. EDART, a discrete algebraic reconstructing technique for experimental data obtained with high resolution computed tomography. *Journal of X-Ray Science and Technology*, 22(1):47–61, 2014.

Brooks, R. and Corey, A. T. Hydraulic Properties of Porous Media and Their Relation to Drainage Design. *Transactions of the ASAE*, 7(1):0026–0028, 1964.

Buckley, J. S., Edwards, J., Fordham, E., Abdallah, W., Carnegie, A., Herold, B., Habashy, T., Seleznev, N., et al. Fundamentals of Wettability. *Oilfield review*, Summer:44–61, 2007.

Bultreys, T., Boone, M. A., Boone, M. N., De Schryver, T., Masschaele, B., Van Loo, D., Van Hoorebeke, L., and Cnudde, V. Real-time visualization of Haines jumps in sandstone with laboratory-based microcomputed tomography. *Water Resources Research*, 51(10): 8668–8676, 2015a.

Bultreys, T., De Boever, W., Van Hoorebeke, L., and Cnudde, V. A multi-scale, image-based pore network modeling approach to simulate two-phase flow in heterogeneous rocks. In *Int. Symp. Soc. Core Analysts*, pages 1–12, St. John's, CA, 2015b. Society of Core Analysts.

Bultreys, T., Van Hoorebeke, L., and Cnudde, V. Multi-scale, micro-computed tomography-based pore network models to simulate drainage in heterogeneous rocks. *Advances in Water Resources*, 78:36–49, 2015c.

Bultreys, T., Boone, M. A., Boone, M. N., De Schryver, T., Masschaele, B., Van Hoorebeke, L., and Cnudde, V. Fast laboratory-based micro-computed tomography for pore-scale research: Illustrative experiments and perspectives on the future. *Advances in Water Resources*, 95:341–351, 2016a.

Bultreys, T., De Boever, W., and Cnudde, V. Imaging and image-based fluid transport modeling at the pore scale in geological materials: A practical introduction to the current state-of-the-art. *Earth-Science Reviews*, 155:93–128, 2016b.

Bultreys, T., Stappen, J. V., Kock, T. D., Boever, W. D., Boone, M. A., Hoorebeke, L. V., and Cnudde, V. Investigating the relative permeability behavior of microporosity-rich carbonates and tight sandstones with multiscale pore network models. *Journal of Geophysical Research: Solid Earth*, 2016c.

Bultreys, T., Van Hoorebeke, L., and Cnudde, V. Simulating secondary waterflooding in heterogeneous rocks with variable wettability using an image-based, multiscale pore network model. *Water Resources Research*, 52(9):6833–6850, 2016d.

Cardenas, M. B. Three-dimensional vortices in single pores and their effects on transport. *Geophysical Research Letters*, 35(August):1–6, 2008.

Casteleyn, L., Robion, P., Collin, P. Y., Menéndez, B., David, C., Desaubliaux, G., Fernandes, N., Dreux, R., et al. Interrelations of the petrophysical, sedimentological and microstructural properties of the Oolithe Blanche Formation (Bathonian, saline aquifer of the Paris Basin). *Sedimentary Geology*, 230(3-4):123–138, 2010.

Caubit, C., Hamon, G., Sheppard, A. P., and Øren, P. E. Evaluation of the reliability of prediction of petrophysical data through imagery. In *Int. Symp. Soc. Core Analysts*, volume 33, 2008.

Chareyre, B., Cortis, A., Catalano, E., and Barthélemy, E. Pore-Scale Modeling of Viscous Flow and Induced Forces in Dense Sphere Packings. *Transport in Porous Media*, 94(2): 595–615, 2012.

Chen, G.-H., Tang, J., and Leng, S. Prior image constrained compressed sensing (PICCS): a method to accurately reconstruct dynamic CT images from highly undersampled projection data sets., 2008.

Chen, L., Fang, W., Kang, Q., De'Haven Hyman, J., Viswanathan, H. S., and Tao, W.-Q. Generalized lattice Boltzmann model for flow through tight porous media with Klinkenberg's effect. *Physical Review E*, 91(3):033004, 2015.

Chenouard, N., Bloch, I., and Olivo-Marin, J. C. Multiple hypothesis tracking in microscopy images. *Proceedings - 2009 IEEE International Symposium on Biomedical Imaging: From Nano to Macro, ISBI 2009*, pages 1346–1349, 2009.

Chenouard, N., Smal, I., de Chaumont, F., Maška, M., Sbalzarini, I. F., Gong, Y., Cardinale, J., Carthel, C., et al. Objective comparison of particle tracking methods. *Nature methods*, 11:281–289, 2014.

Chukwudozie, C. P., Tyagi, M., Sears, S. O., and White, C. D. Prediction of Non-Darcy Coefficients for Inertial Flows Through the Castlegate Sandstone Using Image-Based Modeling. *Transport in Porous Media*, 95(3):563–580, 2012.

Clausnitzer, V. and Hopmans, J. W. Pore-scale measurements of solute breakthrough using microfocus X-ray computed tomography, 2000.

Cluff, R. M. and Byrnes, A. P. Relative Permeability in Tight Gas Sandstone Reservoirs - the "Permeability Jail" Model. *SPWLA Annual Logging Symposium*, pages 1–16, 2010.

Cnudde, V. and Boone, M. High-resolution X-ray computed tomography in geosciences: A

review of the current technology and applications. *Earth-Science Reviews*, 123(0):1–17, 2013.

Coon, E. T., Porter, M. L., and Kang, Q. Taxila LBM: a parallel, modular lattice Boltzmann framework for simulating pore-scale flow in porous media. *Computational Geosciences*, 18(1):17–27, 2013.

Coraluppi, S. and Carthel, C. Multi-stage multiple-hypothesis tracking. *ISIF Journal of Advances in Information Fusion*, 6:57–68, 2011.

Crandall, D., Ahmadi, G., Ferer, M., and Smith, D. H. Distribution and occurrence of localized-bursts in two-phase flow through porous media. *Physica A: Statistical Mechanics and its Applications*, 388(5):574–584, 2009.

Crandall, D., Ahmadi, G., and Smith, D. H. Computational Modeling of Fluid Flow through a Fracture in Permeable Rock. *Transport in Porous Media*, 84(2):493–510, 2010.

Daccord, G., Lenormand, R., and Liétard, O. Chemical dissolution of a porous medium by a reactive fluid-I. Model for the "wormholing" phenomenon. *Chemical Engineering Science*, 48(1):169–178, 1993.

Dalla, E., Hilpert, M., and Miller, C. T. Computation of the interfacial area for two-fluid porous medium systems. *Journal of contaminant hydrology*, 56(1-2):25–48, 2002.

Dautriat, J., Gland, N., Guelard, J., Dimanov, A., and Raphanel, J. L. Axial and Radial Permeability Evolutions of Compressed Sandstones: End Effects and Shear-band Induced Permeability Anisotropy. *Pure and Applied Geophysics*, 166(5-7):1037–1061, 2009.

De Boever, W., Diaz, A., Derluyn, H., De Kock, T., Van Stappen, J., Dewanckele, J., Bultreys, T., Boone, M., et al. Characterization of composition and structure of clay minerals in sandstone with ptychographic X-ray nanotomography. *Applied Clay Science*, 118:258–264, 2015.

De Kock, T., Boone, M., Dewanckele, J., Boever, W. D., Boone, M., Schutter, G. D., and Lehmann, E. Monitoring frost susceptibility of limestone faces. In *12th International Congress on the Deterioration and Conservation of Stone*, volume 1889. 2013.

De Man, B., Nuyts, J., Dupont, P., Marchal, G., and Suetens, P. An iterative maximum-likelihood polychromatic algorithm for CT. *IEEE transactions on medical imaging*, 20: 999–1008, 2001.

De Prisco, G., Toelke, J., and Dernaika, M. R. Computation of relative permeability functions in 3D digital rocks by a fractional flow approach using the lattice Boltzmann method. In *Int. Symp. Soc. Core Analysts*, pages 1–12. Society of Core Analysts, 2012.

Deakin, L. J., Sok, R. M., Bhattad, P., and Knackstedt, M. A. Upscaling of Pore Scale Digital Rock Properties to Whole Core Scale. In *AAPG International Conference & Exhibition*, 2015.

Delerue, J., Perrier, E., Yu, Z., and Velde, B. New algorithms in 3D image analysis and their application to the measurement of a spatialized pore size distribution in soils, 1999.

Demianov, A., Dinariev, O., and Evseev, N. Density functional modelling in multiphase compositional hydrodynamics. *The Canadian Journal of Chemical Engineering*, 89(2): 206–226, 2011.

Derluyn, H. *Salt transport and crystallization in porous limestone: neutron - X-ray imaging and poromechanical modeling*. Phd thesis, ETH Zurich, 2012.

Derluyn, H., Griffa, M., Mannes, D., Jerjen, I., Dewanckele, J., Vontobel, P., Sheppard, A., Derome, D., et al. Characterizing saline uptake and salt distributions in porous limestone with neutron radiography and X-ray micro-tomography. *Journal of Building Physics*, 36 (4):353–374, 2013.

Derluyn, H., Dewanckele, J., Boone, M. N., Cnudde, V., Derome, D., and Carmeliet, J. Crystallization of hydrated and anhydrous salts in porous limestone resolved by synchrotron X-ray microtomography. *Nuclear Instruments and Methods in Physics Research Section B: Beam Interactions with Materials and Atoms*, 324:102–112, 2014.

Dierick, M., Van Loo, D., Masschaele, B., Van den Bulcke, J., Van Acker, J., Cnudde, V., and Van Hoorebeke, L. Recent micro-CT scanner developments at UGCT. *Nuclear Instruments and Methods in Physics Research Section B: Beam Interactions with Materials and Atoms*, 324:35–40, 2014.

Dinapoli, R., Bergamaschi, A., Henrich, B., Horisberger, R., Johnson, I., Kraft, P., Mozzanica, A., Schmitt, B., et al. A new family of pixel detectors for high frame rate X-ray applications. In *Nuclear Instruments and Methods in Physics Research, Section A: Accelerators, Spectrometers, Detectors and Associated Equipment*, volume 617, pages 384–386, 2010.

Dong, H. and Blunt, M. Pore-network extraction from micro-computerized-tomography images. *Physical Review E*, 80(3):036307, 2009.

Dong, H., Fjeldstad, S., Alberts, L., Roth, S., Bakke, S., and ren, P.-E. Pore network modelling on carbonate: a comparative study of different micro-CT network extraction methods. In *Int. Symp. Soc. Core Analysts*, number 31, Abu Dhabi, UAE, 2008. Society of Core Analysts, Society of Core Analysts.

Dullien, F. A. L. *Porous media - fluid transport and pore structure*. Academic Press, Inc, 1992.

Dupin, H. J., Kitanidis, P. K., and McCarty, P. L. Pore-scale modeling of biological clogging due to aggregate expansion: A material mechanics approach. *Water Resources Research*, 37(12):2965–2979, 2001.

Dupré, A. M. and Dupré, P. *Théorie mécanique de la chaleur*. Gauthier-Villars, Paris, France, 1869.

Ebrahimi, A. N., Jamshidi, S., Iglauer, S., and Boozarjomehry, R. B. Genetic algorithm-based pore network extraction from micro-computed tomography images. *Chemical Engineering Science*, 92(0):157–166, 2013.

Eggl, E., Schleede, S., Bech, M., Achterhold, K., Loewen, R., Ruth, R. D., and Pfeiffer, F. X-ray phase-contrast tomography with a compact laser-driven synchrotron source. *Proceedings of the National Academy of Sciences*, 112(18):201500938, 2015.

Eklund, A., Andersson, M., and Knutsson, H. True 4D image denoising on the GPU. *International Journal of Biomedical Imaging*, 2011, 2011.

Eller, J., Roth, J., Marone, F., Stampanoni, M., Wokaun, A., and Buchi, F. N. Towards Ultra-Fast X-ray Tomographic Microscopy of Liquid Water in PEFC. *ECS Transactions*, 41: 387–394, 2011.

Español, P. and Warren, P. Statistical Mechanics of Dissipative Particle Dynamics, 2007.

Espes, E., Andersson, T., Björnsson, F., Gratorp, C., Hansson, B. A. M., Hemberg, O., Johansson, G., Kronstedt, J., et al. Liquid-metal-jet x-ray tube technology and tomography applications. In *SPIE Optical engineering + applications*, page 92120J. International Society for Optics and Photonics, 2014.

Eymard, R., Gallouët, T., and Herbin, R. Finite Volume Methods. In Glowinski, R. and Xu, J., editors, *Handbook of numerical analysis*, chapter 7, pages 713–1018. Elsevier B.V., 2000.

Farokhpoor, R., Torsæter, O., Baghbanbashi, T., and Norwegian, N. Experimental and Numerical Simulation of CO 2 Injection Into Upper-Triassic Sandstones in Svalbard , Norway. In *SPE International Conference on CO2 Capture, Storage, and Utilization*, New Orleans, Louisiana, USA, 2010. Society of Petroleum Engineers.

Farokhpoor, R., Lindeberg, E. G. B., Torsæter, O., Mørk, M. B., and Mørk, A. Permeability and relative permeability measurements for CO2-brine system at reservoir conditions in low permeable sandstones in Svalbard. *Greenhouse Gases: Science and Technology*, 2 (6):408–418, 2013.

Fatt, I. The network model of porous media. *Petroleum Transactions, AIME*, 207:144–181, 1956.

Feldkamp, L. a., Davis, L. C., and Kress, J. W. Practical cone-beam algorithm. *Journal of the Optical Society of America A*, 1:612, 1984.

Ferrari, A. and Lunati, I. Direct numerical simulations of interface dynamics to link capillary pressure and total surface energy. *Advances in Water Resources*, 57:19–31, 2013.

Ferréol, B. and Rothman, D. H. Lattice-Boltzmann simulations of flow through Fontainebleau sandstone. *Transport in Porous Media*, 20(1-2):3–20, 1995.

Feser, M., Gelb, J., Chang, H., Cui, H., Duewer, F., Lau, S. H., Tkachuk, a., and Yun, W. Sub-micron resolution CT for failure analysis and process development. *Measurement Science and Technology*, 19(9):094001, 2008.

Fife, J. L., Rappaz, M., Pistone, M., Celcer, T., Mikuljan, G., and Stampanoni, M. Development of a laser-based heating system for in situ synchrotron-based X-ray tomographic microscopy. *Journal of Synchrotron Radiation*, 19:352–358, 2012.

Filomena, C. M., Hornung, J., and Stollhofen, H. Assessing accuracy of gas-driven permeability measurements: A comparative study of diverse Hassler-cell and probe permeameter devices. *Solid Earth*, 5(1):1–11, 2014.

Fleury, M. Resistivity in carbonates: new insights. In *Int. Symp. Soc. Core Analysts*. Society of Core Analysts, 2002.

Fourar, M. and Radilla, G. Non-Fickian description of tracer transport through heterogeneous porous media. *Transport in Porous Media*, 80:561–579, 2009.

Fredrich, J. T., DiGiovanni, A. A., and Noble, D. R. Predicting macroscopic transport properties using microscopic image data. *Journal of Geophysical Research*, 111(B3): B03201, 2006.

Freitas, D. S. and Prat, M. Pore Network Simulation of Evaporation of a Binary Liquid from a Capillary Porous Medium. *Transport in Porous Media*, 40(1):1–25, 2000.

Furuberg, L., Måløy, K., and Feder, J. Intermittent behavior in slow drainage, 1996.

Fusseis, F., Steeb, H., Xiao, X., Zhu, W.-l., Butler, I. B., Elphick, S., and Mäder, U. A low-cost X-ray-transparent experimental cell for synchrotron-based X-ray microtomography studies under geological reservoir conditions. *Journal of synchrotron radiation*, 21(Pt 1):251–3, 2014.

Gal, Y., Mehnert, a. J., Bradley, a. P., McMahon, K., Kennedy, D., and Crozier, S. Denoising of dynamic contrast-enhanced MR images using dynamic nonlocal means. *IEEE Trans Med Imaging*, 29(2):302–310, 2010.

Gao, J., Xing, H., Rudolph, V., Li, Q., and Golding, S. D. Parallel Lattice Boltzmann Computing and Applications in Core Sample Feature Evaluation. *Transport in Porous Media*, 107(1):65–77, 2015.

Geiger, S., Schmid, K. S., and Zaretskiy, Y. Mathematical analysis and numerical simulation of multi-phase multi-component flow in heterogeneous porous media. *Current Opinion in Colloid & Interface Science*, 17(3):147–155, 2012.

Gelb, J., Feser, M., Tkachuk, a., Hsu, G., Chen, S., Chang, H., Fong, T., Hunter, L., et al. Sub-micron X-ray Computed Tomography for Non-Destructive 3D Visualization and Analysis. *Microscopy and Microanalysis*, 15(S2):618–619, 2009.

Gharasoo, M., Centler, F., Regnier, P., Harms, H., and Thullner, M. A reactive transport modeling approach to simulate biogeochemical processes in pore structures with pore-scale heterogeneities. *Environmental Modelling & Software*, 30:102–114, 2012.

Gharbi, O. and Blunt, M. J. The impact of wettability and connectivity on relative permeability in carbonates: A pore network modeling analysis. *Water Resources Research*, 48(12):n/a—-n/a, 2012.

Gharbi, O., Bijeljic, B., Boek, E., and Blunt, M. J. Changes in Pore Structure and Connectivity Induced by CO2 Injection in Carbonates: A Combined Pore-Scale Approach. *Energy Procedia*, 37:5367–5378, 2013.

Ginzburg, I. Comment on An improved gray Lattice Boltzmann model for simulating fluid flow in multi-scale porous media: Intrinsic links between LBE Brinkman schemes. *Advances in Water Resources*, 2014.

Glover, P. Formation Evaluation course notes (University of Aberdeen), 2001.

Graves, W., Bessuille, J., Brown, P., Carbajo, S., Dolgashev, V., Hong, K.-H., Ihloff, E., Khaykovich, B., et al. Compact x-ray source based on burst-mode inverse Compton scattering at 100kHz. *Physical Review Special Topics - Accelerators and Beams*, 17(12), 2014.

Guizar-Sicairos, M., Johnson, I., Diaz, A., Holler, M., Karvinen, P., Stadler, H.-C., Dinapoli, R., Bunk, O., et al. High-throughput ptychography using Eiger-scanning X-ray nano-imaging of extended regions. *Optics Express*, 22(12):14859, 2014.

Gunstensen, A. K., Rothman, D. H., Zaleski, S., and Zanetti, G. Lattice Boltzmann model of immiscible fluids. *Physical Review A*, 43(8):4320–4327, 1991.

Haas, a. and Revil, a. Electrical burst signature of pore-scale displacements. *Water Resources Research*, 45(August):2–7, 2009.

Haines, W. B. Studies in the physical properties of soil. V. The hysteresis effect in capillary properties, and the modes of moisture distribution associated therewith. *The Journal of Agricultural Science*, 20:97, 1930.

Hammond, P. S. and Unsal, E. A Dynamic Pore Network Model for Oil Displacement by Wettability-Altering Surfactant Solution. *Transport in Porous Media*, 92(3):789–817, 2012.

Han, M., Fleury, M., and Levitz, P. Effect of the pore structure on resistivity index curves. In *Int. Symp. Soc. Core Analysts*, volume 34, Calgary, Canada, 2007. Society of Core Analysts.

Harting, J., Chin, J., Venturoli, M., and Coveney, P. V. Large-scale lattice Boltzmann simulations of complex fluids: advances through the advent of computational Grids. *Philosophical transactions. Series A, Mathematical, physical, and engineering sciences*, 363(1833):1895–915, 2005.

Hassanizadeh, S. M. Capillarity in porous media at micro-and macroscale, revisited. In *Henry Darcy Lecture Series*. National Ground Water Association, 2012.

Hassanizadeh, S. M. and Gray, W. G. Thermodynamic basis of capillary pressure in porous media. *Water Resources Research*, 29(10):3389–3405, 1993.

Hazlett, R., Chen, S., and Soll, W. Wettability and rate effects on immiscible displacement: Lattice Boltzmann simulation in microtomographic images of reservoir rocks. *Journal of Petroleum Science and Engineering*, 20(3-4):167–175, 1998.

Held, R. J. and Celia, M. A. Pore-scale modeling and upscaling of nonaqueous phase liquid mass transfer. *Water Resources Research*, 37(3):539–549, 2001.

Hemes, S., Desbois, G., Urai, J. L., Schröppel, B., and Schwarz, J.-O. Multi-scale characterization of porosity in Boom Clay (HADES-level, Mol, Belgium) using a combination of X-ray μ-CT, 2D BIB-SEM and FIB-SEM tomography. *Microporous and Mesoporous Materials*, 208:1–20, 2015.

Henrich, B., Bergamaschi, A., Broennimann, C., Dinapoli, R., Eikenberry, E. F., Johnson, I., Kobas, M., Kraft, P., et al. PILATUS: A single photon counting pixel detector for

X-ray applications. *Nuclear Instruments and Methods in Physics Research, Section A: Accelerators, Spectrometers, Detectors and Associated Equipment*, 607:247–249, 2009.

Herman, G. and Kuba, a. *Advances in discrete tomography and its applications*. Springer Science & Business Media, 2007.

Herman, G. T. and Lent, A. Iterative reconstruction algorithms. *Computers in biology and medicine*, 6:273–294, 1976.

Herring, A. L., Harper, E. J., Andersson, L., Sheppard, A., Bay, B. K., and Wildenschild, D. Effect of fluid topology on residual nonwetting phase trapping: Implications for geologic CO2 sequestration. *Advances in Water Resources*, 62:47–58, 2013.

Higuera, F. J., Succi, S., and Benzi, R. Lattice Gas Dynamics with Enhanced Collisions. *Europhysics Letters (EPL)*, 9(4):345–349, 1989.

Holler, M., Diaz, A., Guizar-Sicairos, M., Karvinen, P., Färm, E., Härkönen, E., Ritala, M., Menzel, a., et al. X-ray ptychographic computed tomography at 16 nm isotropic 3D resolution. *Scientific reports*, 4:3857, 2014.

Holzer, L. and Cantoni, M. Review of FIB Tomography. In Utke, I., Moshkalev, S., and Russell, P., editors, *Nanofabriaction using Focused Ion and Electron Beams*, chapter 11, pages 410–435. OUP USA, 2011.

Hoogland, F., Lehmann, P., Moebius, F., Vontobel, P., and Or, D. Liquid redistribution behind a drainage front in porous media imaged by neutron radiography. In *EGU General Assembly: Geophysical Research Abstracts*, pages EGU2013–8156, Vienna, Austria, 2013. EGU.

Huang, H., Meakin, P., and Liu, M. Computer simulation of two-phase immiscible fluid motion in unsaturated complex fractures using a volume of fluid method. *Water Resources Research*, 41(12):n/a–n/a, 2005.

Huber, C., Shafei, B., and Parmigiani, A. A new pore-scale model for linear and non-linear heterogeneous dissolution and precipitation. *Geochimica et Cosmochimica Acta*, 124: 109–130, 2014.

Huber, F., Enzmann, F., Wenka, A., Bouby, M., Dentz, M., and Schäfer, T. Natural micro-scale heterogeneity induced solute and nanoparticle retardation in fractured crystalline rock. *Journal of Contaminant Hydrology*, 133:40–52, 2012.

Hunt, A., Ewing, R., and Ghanbarian, B. *Percolation theory for flow in porous media*. Springer, 3 edition, 2014.

Huysmans, M., Peeters, L., Moermans, G., and Dassargues, A. Relating small-scale sedimentary structures and permeability in a cross-bedded aquifer. *Journal of Hydrology*, 361(1-2):41–51, 2008.

Hyman, J. D., Smolarkiewicz, P. K., and Winter, C. L. Heterogeneities of flow in stochastically generated porous media. *Physical Review E*, 86(5):056701, 2012.

Iassonov, P., Gebrenegus, T., and Tuller, M. Segmentation of X-ray computed tomography images of porous materials: a crucial step for characterization and quantitative analysis of pore structures. *Water resources research*, 45(W09415):n/a–n/a, 2009.

Icardi, M., Boccardo, G., Marchisio, D. L., Tosco, T., and Sethi, R. Pore-scale simulation of fluid flow and solute dispersion in three-dimensional porous media. *Physical Review E*, 90(1):013032, 2014.

Idowu, N., Nardi, C., Long, H., and Øren, P.-e. Pore-scale modeling: effects of network properties on predictive capabilities. In *Int. Symp. Soc. Core Analysts*, pages 1–12, Aberdeen, Scotland, 2012. Society of Core Analysts.

Idowu, N., Nardi, C., Long, H., and Bondino, I. Improving digital rock physics predictive potential for relative permeabilities from equivalent pore networks. In *Int. Symp. Soc. Core Analysts*, pages 1–12, Napa Valley, USA, 2013. Society of Core Analysts.

Idowu, N. a. and Blunt, M. J. Pore-Scale Modelling of Rate Effects in Waterflooding. *Transport in Porous Media*, 83(1):151–169, 2010.

Idowu, N. A., Nardi, C., Long, H., Varslot, T., and Øren, P.-E. Effects of Segmentation and Skeletonization Algorithms on Pore Networks and Predicted Multiphase-Transport Properties of Reservoir-Rock Samples. *SPE Reservoir Evaluation & Engineering*, pages 1–13, 2014.

Iglauer, S., Paluszny, A., Pentland, C. H., and Blunt, M. J. Residual CO2 imaged with X-ray micro-tomography. *Geophysical Research Letters*, 38(21):n/a–n/a, 2011.

Iglauer, S., Fernø, M. a., Shearing, P., and Blunt, M. J. Comparison of residual oil cluster size distribution, morphology and saturation in oil-wet and water-wet sandstone. *Journal of colloid and interface science*, 375(1):187–92, 2012.

Jerauld, G. R. and Salter, S. J. The effect of pore-structure on hysteresis in relative permeability and capillary pressure: Pore-level modeling. *Transport in Porous Media*, 5 (2):103–151, 1990.

Jiang, F. and Tsuji, T. Impact of interfacial tension on residual CO 2 clusters in porous sandstone. *Water Resources Research*, 51(3):1710–1722, 2015.

Jiang, F., Tsuji, T., and Hu, C. Elucidating the Role of Interfacial Tension for Hydrological Properties of Two-Phase Flow in Natural Sandstone by an Improved Lattice Boltzmann Method. *Transport in Porous Media*, 2014.

Jiang, Z., Wu, K., Couples, G., van Dijke, M. I. J., Sorbie, K. S., and Ma, J. Efficient extraction of networks from three-dimensional porous media. *Water Resources Research*, 43(12):n/a—-n/a, 2007.

Jiang, Z., van Dijke, M. I. J., Wu, K., Couples, G. D., Sorbie, K. S., and Ma, J. Stochastic Pore Network Generation from 3D Rock Images. *Transport in Porous Media*, 94(2): 571–593, 2011.

Jiang, Z., van Dijke, M. I. J., Sorbie, K. S., and Couples, G. D. Representation of multiscale heterogeneity via multiscale pore networks. *Water Resources Research*, 49(9):5437–5449, 2013.

Jiménez-Hornero, F. J., Giráldez, J. V., and Laguna, A. Simulation of Tracer Dispersion in Porous Media Using Lattice Boltzmann and Random Walk Models. *Vadose Zone Journal*, 4(2):310, 2005.

Jin, G., Patzek, T. W., and Silin, D. B. Direct Prediction of the Absolute Permeability of Unconsolidated and Consolidated Reservoir Rock. In *SPE Annual Technical Conference and Exhibition*. Society of Petroleum Engineers, 2004.

Joekar-Niasar, V. and Hassanizadeh, S. M. Analysis of Fundamentals of Two-Phase Flow in Porous Media Using Dynamic Pore-Network Models: A Review. *Critical Reviews in Environmental Science and Technology*, 42(18):1895–1976, 2012.

Joekar-Niasar, V., Hassanizadeh, S. M., and Dahle, H. K. Non-equilibrium effects in capillarity and interfacial area in two-phase flow: dynamic pore-network modelling. *Journal of Fluid Mechanics*, 655:38–71, 2010a.

Joekar-Niasar, V., Prodanović, M., Wildenschild, D., and Hassanizadeh, S. M. Network model investigation of interfacial area, capillary pressure and saturation relationships in granular porous media. *Water Resources Research*, 46(6):n/a—-n/a, 2010b.

Joekar-Niasar, V., Doster, F., Armstrong, R. T., Wildenschild, D., and Celia, M. A. Trapping and hysteresis in two-phase flow in porous media: A pore-network study. *Water Resources Research*, 49(7):4244–4256, 2013.

Johnson, I., Bergamaschi, A., Billich, H., Cartier, S., Dinapoli, R., Greiffenberg, D., Guizar-Sicairos, M., Henrich, B., et al. Eiger: a single-photon counting x-ray detector. *Journal of Instrumentation*, 9(05), 2014.

Kaestner, a., Lehmann, E., and Stampanoni, M. Imaging and image processing in porous media research. *Advances in Water Resources*, 31:1174–1187, 2008.

Kak, A. C. and Slaney, M. *Principles of Computerized Tomographic Imaging*. IEEE Press, 1988.

Kallel, W., van Dijke, M., Sorbie, K., Wood, R., Jiang, Z., and Harland, S. Modelling the effect of wettability distributions on oil recovery from microporous carbonate reservoirs. *Advances in Water Resources*, 000:1–12, 2015.

Kaminski, R., Nottingham, G., and Coppens, P. An optical chopper for generation of short X-ray pulses to allow in-house time-resolved photocrystallography. *Journal of Applied Crystallography*, 47:1765–1768, 2014.

Kang, Q., Zhang, D., and Chen, S. Unified lattice Boltzmann method for flow in multiscale porous media. *Physical Review E*, 66(5):056307, 2002.

Kang, Q., Lichtner, P. C., Viswanathan, H. S., and Abdel-Fattah, A. I. Pore Scale Modeling of Reactive Transport Involved in Geologic CO2 Sequestration. *Transport in Porous Media*, 82(1):197–213, 2009.

Kang, Q., Wang, M., Mukherjee, P. P., and Lichtner, P. C. Mesoscopic Modeling of Multiphysicochemical Transport Phenomena in Porous Media. *Advances in Mechanical Engineering*, 2, 2010.

Kathel, P. and Mohanty, K. K. Wettability alteration in a tight oil reservoir. *Energy and Fuels*, 27(11):6460–6468, 2013.

Keehm, Y. Permeability prediction from thin sections: 3D reconstruction and Lattice-Boltzmann flow simulation. *Geophysical Research Letters*, 31(4):L04606, 2004.

Keller, L. M., Holzer, L., Schuetz, P., and Gasser, P. Pore space relevant for gas permeability in Opalinus clay: Statistical analysis of homogeneity, percolation, and representative volume element. *Journal of Geophysical Research: Solid Earth*, 118(6):2799–2812, 2013.

Kelly, S., El-Sobky, H., Torres-Verdín, C., and Balhoff, M. T. Assessing the utility of FIB-SEM images for shale digital rock physics. *Advances in Water Resources*, 2015.

Khan, F., Enzmann, F., Kersten, M., Wiegmann, A., and Steiner, K. 3D simulation of the permeability tensor in a soil aggregate on basis of nanotomographic imaging and LBE solver. *Journal of Soils and Sediments*, 12(1):86–96, 2012.

Kim, D., Peters, C. A., and Lindquist, W. B. Upscaling geochemical reaction rates accompanying acidic CO 2 -saturated brine flow in sandstone aquifers. *Water Resources Research*, 47(1):n/a–n/a, 2011.

Kim, D.-S. and Fogler, H. S. Biomass evolution in porous media and its effects on permeability under starvation conditions. *Biotechnology and Bioengineering*, 69(1):47–56, 2000.

King, A., Reischig, P., Adrien, J., and Ludwig, W. First laboratory X-ray diffraction contrast tomography for grain mapping of polycrystals. *Journal of Applied Crystallography*, 46: 1734–1740, 2013.

Kišon, P., Malengier, B., Di Emidio, G., Peiffer, H., and Van Keer, R. Inverse determination of saturated and relative permeability with a bench-scale centrifuge. *Inverse Problems in Science and Engineering*, 23(1):16–37, 2015.

Knackstedt, M., Arns, C., Ghous, A., Sakellariou, A., Senden, T., Sheppard, A., Sok, R., Averdunk, H., et al. 3D Imaging and Flow Characterization of the Pore Space of Carbonate Core Samples. In *Int. Symp. Soc. Core Analysts*. Society of Core Analysts, Society of Core Analysts, 2006.

Koenig, T., Schulze, J., Zuber, M., Rink, K., Butzer, J., Hamann, E., Cecilia, A., Zwerger, A., et al. Imaging properties of small-pixel spectroscopic x-ray detectors based on cadmium telluride sensors, 2012.

Koestel, J. and Larsbo, M. Imaging and quantification of preferential solute transport in soil macropores. *Water Resources Research*, 50:4357–4378, 2014.

Köhne, J. M., Schlüter, S., and Vogel, H.-J. Predicting Solute Transport in Structured Soil Using Pore Network Models. *Vadose Zone Journal*, 10(3):1082, 2011.

Koroteev, D., Dinariev, O., Evseev, N., Klemin, D., Safonov, S., Berg, S., Kruijsdijk, C. V., Armstrong, R., et al. Direct hydrodynamic simulation of multiphase flow in porous rock. In *Int. Symp. Soc. Core Analysts*, Napa Valley, USA, 2013. Society of Core Analysts.

Kosior, J. C., Kosior, R. K., and Frayne, R. Robust dynamic susceptibility contrast MR perfusion using 4D nonlinear noise filters. *Journal of Magnetic Resonance Imaging*, 26: 1514–1522, 2007.

Kovscek, A. R., Wong, H., and Radke, C. J. A pore-level scenario for the development of mixed wettability in oil reservoirs. *AIChE Journal*, 39(6):1072–1085, 1993.

Krevor, S., Blunt, M. J., Benson, S. M., Pentland, C. H., Reynolds, C., Al-Menhali, A., and Niu, B. Capillary trapping for geologic carbon dioxide storage From pore scale physics to field scale implications. *International Journal of Greenhouse Gas Control*, 40:221–237, 2015.

Krotkiewski, M., Ligaarden, I. S., Lie, K.-A., and Schmid, D. W. On the Importance of the Stokes-Brinkman Equations for Computing Effective Permeability in Karst Reservoirs. *Communications in Computational Physics*, 2011.

Kruskal, J. B. On the shortest spanning subtree of a graph and the traveling salesman problem. *Proceedings of the American Mathematical Society*, 7(1):48–48, 1956.

Krymski, A. I., Bock, N. E., Tu, N., Van Blerkom, D., and Fossum, E. R. A high-speed, 240-frames/s, 4.1-Mpixel CMOS sensor. *IEEE Transactions on Electron Devices*, 50: 130–135, 2003.

Kuzmin, A. and Mohamad, A. Multirange multi-relaxation time ShanChen model with extended equilibrium. *Computers & Mathematics with Applications*, 59(7):2260–2270, 2010.

Landrot, G., Ajo-Franklin, J. B., Yang, L., Cabrini, S., and Steefel, C. I. Measurement of accessible reactive surface area in a sandstone, with application to CO 2 mineralization. *Chemical Geology*, 318-319:113–125, 2012.

Landry, C. J., Karpyn, Z. T., and Ayala, O. Pore-Scale Lattice Boltzmann Modeling and 4D X-ray Computed Microtomography Imaging of Fracture-Matrix Fluid Transfer. *Transport in Porous Media*, 103(3):449–468, 2014a.

Landry, C. J., Karpyn, Z. T., and Ayala, O. Relative permeability of homogenous-wet and mixed-wet porous media as determined by pore-scale lattice Boltzmann modeling. *Water Resources Research*, 50(5):3672–3689, 2014b.

Lang, C., Ohser, J., and Hilfer, R. On the analysis of spatial binary images. *Journal of microscopy*, 203(September):303–313, 2001.

Larsson, D. H., Takman, P. A. C., Lundström, U., Burvall, A., and Hertz, H. M. A 24 keV liquid-metal-jet x-ray source for biomedical applications. *Review of Scientific Instruments*, 82, 2011.

Larsson, D. H., Lundström, U., Westermark, U. K., Arsenian Henriksson, M., Burvall, A., and Hertz, H. M. First application of liquid-metal-jet sources for small-animal imaging: high-resolution CT and phase-contrast tumor demarcation. *Medical physics*, 40:021909, 2013.

Latham, S., Varslot, T., and Sheppard, A. Image Registration : Enhancing and Calibrating X-Ray Micro-Ct Imaging. In *Int. Symp. Soc. Core Analysts*, pages 1–12, Abu Dhabi, UAE, 2008. Society of Core Analysts.

Le Guen, Y., Renard, F., Hellmann, R., Brosse, E., Collombet, M., Tisserand, D., and Gratier, J.-P. Enhanced deformation of limestone and sandstone in the presence of high P co 2 fluids. *Journal of Geophysical Research*, 112(B5):B05421, 2007.

Lee, J., Stayman, J. W., Otake, Y., Schafer, S., Zbijewski, W., Khanna, A. J., Prince, J. L., and Siewerdsen, J. H. Volume-of-change cone-beam CT for image-guided surgery. *Physics in Medicine and Biology*, 57:4969–4989, 2012.

Lenormand, R. and Zarcone, C. Role of roughness and edges during imbibition in square capillaries. *SPE Journal*, 13264, 1984.

Lenormand, R., Zarcone, C., and Sarr, A. Mechanisms of the displacement of one fluid by another in a network of capillary ducts. *Journal of Fluid Mechanics*, 135:337, 1983.

Li, L., Peters, C. A., and Celia, M. A. Upscaling geochemical reaction rates using pore-scale network modeling. *Advances in Water Resources*, 29(9):1351–1370, 2006.

Li, R., Yang, Y. S., Pan, J., Pereira, G. G., Taylor, J. a., Clennell, B., and Zou, C. Lattice Boltzmann modeling of permeability in porous materials with partially percolating voxels. *Physical Review E*, 90(3):033301, 2014.

Liang, Z., Ioannidis, M., and Chatzis, I. Geometric and Topological Analysis of Three-Dimensional Porous Media: Pore Space Partitioning Based on Morphological Skeletonization. *Journal of colloid and interface science*, 221(1):13–24, 2000.

Ligaarden, I., Krotkiewski, M., Lie, K., Pal, M., and Schmid, D. On the Stokes-Brinkman Equations for Modeling Flow in Carbonate Reservoirs. In *Proceedings of the12th European Conference on the Mathematics of Oil Recovery*, 2010.

Lindblad, J. Surface area estimation of digitized 3D objects using weighted local configurations. *Image and Vision Computing*, 23(2):111–122, 2005.

Lindquist, W. and Venkatarangan, A. Investigating 3D geometry of porous media from high resolution images. *Physics and Chemistry of the Earth, Part A: Solid Earth and Geodesy*, 24(7):593–599, 1999.

Lindquist, W. B. Quantitative analysis of three-dimensional x-ray tomographic images. In Bonse, U., editor, *Developments in X-ray Tomography III, Proceedings of SPIE 4503*, pages 103–115. SPIE, 2002.

Lindquist, W. B., Lee, S.-m., Coker, D. A., Jones, K. W., and Spanne, P. Medial axis analysis of void structure in three-dimensional tomographic images of porous media. *Journal of Geophysical Research*, 101(B4):8297, 1996.

Liu, H., Valocchi, A. J., Kang, Q., and Werth, C. Pore-Scale Simulations of Gas Displacing Liquid in a Homogeneous Pore Network Using the Lattice Boltzmann Method. *Transport in Porous Media*, 99(3):555–580, 2013.

Liu, H., Kang, Q., Leonardi, C. R., Schmieschek, S., Narváez, A., Jones, B. D., Williams, J. R., Valocchi, A. J., et al. Multiphase lattice Boltzmann simulations for porous media applications – a review. 2014.

Llewellin, E. LBflow: An extensible lattice Boltzmann framework for the simulation of geophysical flows. Part I: theory and implementation. *Computers & Geosciences*, 36(2): 115–122, 2010.

Long, H., Nardi, C., Idowu, N., Carnerup, A., Øren, P. E., Knackstedt, M. A., Varslot, T., and Sok, R. M. Multi-scale imaging and modeling workflow to capture and characterize

microporosity in sandstone. In *Int. Symp. Soc. Core Analysts*, volume 13, pages 1–13. Society of Core Analysts, 2013.

Lundström, U., Larsson, D. H., Burvall, A., Scott, L., Westermark, U. K., Wilhelm, M., Arsenian Henriksson, M., and Hertz, H. M. angiography for sub-10 μm vessel imaging, 2012.

Ma, J., Wu, K., Jiang, Z., and Couples, G. D. SHIFT: An implementation for lattice Boltzmann simulation in low-porosity porous media. *Physical Review E*, 81(5):056702, 2010.

Ma, S., Mason, G., and Morrow, N. R. Effect of contact angle on drainage and imbibition in regular polygonal tubes. *Colloids and Surfaces A: Physicochemical and Engineering Aspects*, 117(3):273–291, 1996.

Mahmud, W. M., Arns, J. Y., Sheppard, A., Knackstedt, M. a., and Pinczewski, W. V. Effect of network topology on two-phase imbibition relative permeability. *Transport in Porous Media*, 66(3):481–493, 2007.

Maire, E. and Withers, P. J. Quantitative X-ray tomography. *International Materials Reviews*, 59(1):1–43, 2014.

Makhloufi, Y., Collin, P. Y., Bergerat, F., Casteleyn, L., Claes, S., David, C., Menendez, B., Monna, F., et al. Impact of sedimentology and diagenesis on the petrophysical properties of a tight oolitic carbonate reservoir. The case of the Oolithe Blanche Formation (Bathonian, Paris Basin, France). *Marine and Petroleum Geology*, 48:323–340, 2013.

Måloy, K. J., Furuberg, L., Feder, J., and Jossang, T. Dynamics of slow drainage in porous media. *Physical Review Letters*, 68(14):2161–2164, 1992.

Manwart, C., Aaltosalmi, U., Koponen, A., Hilfer, R., and Timonen, J. Lattice-Boltzmann and finite-difference simulations for the permeability for three-dimensional porous media. *Physical Review E*, 66(1):016702, 2002.

marquis de Laplace, P. S. *Traité de Mécanique Céleste*. Courcier, Paris, France, 1805.

Marrink, S. and Knackstedt, M. Finite size scaling for percolation on elongated lattices in two and three dimensions. *Physical Review E*, 62(3):3205–3214, 2000.

Marrink, S. J. and Knackstedt, M. A. Percolation thresholds on elongated lattices, 1999.

Maška, M., Ulman, V., Svoboda, D., Matula, P., Matula, P., Ederra, C., Urbiola, A., España, T., et al. A benchmark for comparison of cell tracking algorithms. *Bioinformatics (Oxford, England)*, 30:1609–17, 2014.

Mason, G. and Morrow, N. R. Capillary behavior of a perfectly wetting liquid in irregular triangular tubes. *Journal of Colloid and Interface Science*, 141(1):262–274, 1991.

Masschaele, B., Cnudde, V., Dierick, M., Jacobs, P., Van Hoorebeke, L., and Vlassenbroeck, J. UGCT: New X-ray radiography and tomography facility. *Nuclear Instruments and Methods in Physics Research Section A: Accelerators, Spectrometers, Detectors and Associated Equipment*, 580(1):266–269, 2007.

Masschaele, B., Dierick, M., Loo, D. V., Boone, M. N., Brabant, L., Pauwels, E., Cnudde, V., and Hoorebeke, L. V. HECTOR: A 240kV micro-CT setup optimized for research. *Journal of Physics: Conference Series*, 463:012012, 2013.

McClure, J., Prins, J., and Miller, C. A novel heterogeneous algorithm to simulate multiphase flow in porous media on multicore CPUGPU systems. *Computer Physics Communications*, 185(7):1865–1874, 2014.

Meakin, P. and Tartakovsky, A. M. Modeling and simulation of pore-scale multiphase fluid flow and reactive transport in fractured and porous media. *Reviews of Geophysics*, 47 (3):RG3002, 2009.

Mehmani, A. and Prodanović, M. The effect of microporosity on transport properties in porous media. *Advances in Water Resources*, 63:104–119, 2014.

Mehmani, A., Milliken, K., and Prodanovic, M. A Quantitative Pore-Scale Investigation on the Paragenesis of Wilcox Tight Gas Sandstone. In *Proceedings of the 3rd Unconventional Resources Technology Conference*, number 2147717, Tulsa, OK, USA, 2015a. American Association of Petroleum Geologists.

Mehmani, A., Prodanovic, M., and Milliken, K. L. Wilcox Tight Gas Sandstone, 2015b.

Mendrik, A., Vonken, E. P. A., Dankbaar, J. W., Prokop, M., and van Ginneken, B. Noise filtering in thin-slice 4D cerebral CT perfusion scans. In Benoit M. Dawant; David R. Haynor, editor, *SPIE Medical Imaging: Image Processing*, volume 7623, pages 76230N1–76230N8, San Diego, 2010.

Mendrik, A., Vonken, E.-j., Witkamp, T., Prokop, M., van Ginneken, B., and Viergever, M. *Using the Fourth Dimension to Distinguish Between Structures for Anisotropic Diffusion Filtering in 4D CT Perfusion Scans*. Springer International Publishing, Boston, MA, USA, 2015.

Menke, H., Bijeljic, B., Andrew, M., and Blunt, M. J. Dynamic Pore-scale Imaging of Reactive Transport in Heterogeneous Carbonates at Reservoir Conditions. *Energy Procedia*, 63:5503–5511, 2014.

Menke, H. P., Bijeljic, B., Andrew, M. G., and Blunt, M. J. Dynamic three-dimensional pore-scale imaging of reaction in a carbonate at reservoir conditions. *Environmental science & technology*, 49(7):4407–14, 2015.

Möbus, G. and Inkson, B. J. Nanoscale tomography in materials science. *Materials Today*, 10(12):18–25, 2007.

Moctezuma, A., Bękri, S., Laroche, C., and Vizika, O. A Dual network model for relative permeability of bimodal rocks application in a vuggy carbonate. In *Int. Symp. Soc. Core Analysts*. Society of core analysts, Society of Core Analysts, 2003.

Moctezuma-Berthier, P., Vizika, O., and Adler, P. Water-oil relative permeability in vugular porous media: experiments and simulations. In *Int. Symp. Soc. Core Analysts*, page 02, Monterey, CA, 2002. Society of Core Analysts.

Moebius, F. and Or, D. Pore scale dynamics underlying the motion of drainage fronts in porous media. *Water Resources Research*, 50:8441–8457, 2014a.

Moebius, F. and Or, D. Inertial forces affect fluid front displacement dynamics in a pore-throat network model. *Physical Review E*, 90(August):023019, 2014b.

Moebius, F., Canone, D., and Or, D. Characteristics of acoustic emissions induced by fluid front displacement in porous media. *Water Resources Research*, 48(November):1–12, 2012.

Mohanty, K., Davis, H., and Scriven, L. Physics of Oil Entrapment in Water-Wet Rock. *SPE Reservoir Engineering*, 2(01):113–128, 1987.

Mohnke, O., Stiebler, M., and Klitzsch, N. Joint numerical microscale simulations of multiphase flow and NMR relaxation behavior in porous media using Lattice Boltzmann methods. *Water Resources Research*, 50(9):7378–7393, 2014.

Mokso, R., Marone, F., Haberthür, D., Schittny, J. C., Mikuljan, G., Isenegger, a., and Stampanoni, M. Following dynamic processes by X-ray tomographic microscopy with sub-second temporal resolution. In *AIP Conference Proceedings*, volume 1365, pages 38–41, 2010.

Molins, S., Trebotich, D., Yang, L., Ajo-Franklin, J. B., Ligocki, T. J., Shen, C., and Steefel, C. I. Pore-Scale Controls on Calcite Dissolution Rates from Flow-through Laboratory and Numerical Experiments. *Environmental Science & Technology*, 48(13):7453–7460, 2014.

Monetti, R. a. and Albano, E. V. Critical behavior of the site percolation model on the square lattice in a LxM geometry. *Zeitschrift für Physik B Condensed Matter*, 82(1): 129–134, 1991.

Monga, O., Ndeye Ngom, F., and François Delerue, J. Representing geometric structures in 3D tomography soil images: Application to pore-space modeling. *Computers & Geosciences*, 33(9):1140–1161, 2007.

Mooser, R., Forsberg, F., Hack, E., Székely, G., and Sennhauser, U. Estimation of affine transformations directly from tomographic projections in two and three dimensions. *Machine Vision and Applications*, 24:419–434, 2013.

Morrow, N. R. The Effects of Surface Roughness On Contact: Angle With Special Reference to Petroleum Recovery. *Journal of Canadian Petroleum Technology*, 14(04): 42–53, 1975.

Mostaghimi, P., Bijeljic, B., and Blunt, M. Simulation of Flow and Dispersion on Pore-Space Images. *SPE Journal*, 17(04):1131–1141, 2012.

Mostaghimi, P., Blunt, M. J., and Bijeljic, B. Computations of Absolute Permeability on Micro-CT Images. *Mathematical Geosciences*, 45(1):103–125, 2013.

Muljadi, B. P., Blunt, M. J., Raeini, A. Q., and Bijeljic, B. The impact of porous media heterogeneity on non-Darcy flow behaviour from pore-scale simulation. *Advances in Water Resources*, 2015.

Myers, G. R., Kingston, A. M., Varslot, T. K., Turner, M. L., and Sheppard, A. P. Dynamic X-ray micro-tomography for real time imaging of drainage and imbibition processes at the pore scale. In *Int. Symp. Soc. Core Analysts*. Society of Core Analysts, 2011a.

Myers, G. R., Kingston, A. M., Varslot, T. K., Turner, M. L., and Sheppard, A. P. Dynamic tomography with a priori information. *Applied optics*, 50(20):3685–90, 2011b.

Myers, G. R., Varslot, T., Kingston, A., Herring, A., and Sheppard, A. P. Ground-truth verification of dynamic x-ray micro-tomography images of fluid displacement. In *Proc. SPIE: Developments in X-Ray Tomography VIII*, volume 8506, page 85060P, 2012.

Naik, S., You, Z., and Bedrikovetsky, P. Rate enhancement in unconventional gas reservoirs by wettability alteration. *Journal of Natural Gas Science and Engineering*, 26:1–12, 2015.

Ngom, N. F., Garnier, P., Monga, O., and Peth, S. Extraction of three-dimensional soil pore space from microtomography images using a geometrical approach. *Geoderma*, 163(1-2):127–134, 2011.

Nguyen, V. H., Sheppard, A. P., Knackstedt, M. A., and Val Pinczewski, W. The effect of displacement rate on imbibition relative permeability and residual saturation. *Journal of Petroleum Science and Engineering*, 52(1-4):54–70, 2006.

Ochi, J. and Vernoux, J.-F. A Two-Dimensional Network Model to Simulate Permeability Decrease Under Hydrodynamic Effect of Particle Release and Capture. *Transport in Porous Media*, 37(3):303–325, 1999.

Ohser, J. and Mücklich, F. *Statistical analysis of microstructures in materials science*. John Wiley & Sons, Ltd, 2000.

Okabe, H. and Blunt, M. J. Pore space reconstruction using multiple-point statistics. *Journal of Petroleum Science and Engineering*, 46(1-2):121–137, 2005.

Øren, P.-e. and Bakke, S. Process Based Reconstruction of Sandstones and Prediction of Transport Properties. *Transport in Porous Media*, 46(2):311–343, 2002.

Øren, P.-e. and Bakke, S. Reconstruction of Berea sandstone and pore-scale modelling of wettability effects. *Journal of Petroleum Science and Engineering*, 39(3-4):177–199, 2003.

Øren, P.-E., Bakke, S., and Arntzen, O. Extending Predictive Capabilities to Network Models. In *SPE Journal*, volume 3, pages 324–336. Society of petroleum engineers, 1998.

Ott, H., de Kloe, K., van Bakel, M., Vos, F., van Pelt, A., Legerstee, P., Bauer, A., Eide, K., et al. Core-flood experiment for transport of reactive fluids in rocks. *The Review of scientific instruments*, 83(8):084501, 2012.

Ott, H., Oedai, S., Pentland, C. H., and Linden, a. J. V. D. CO2 Reactive Transport in Limestone : Flow Regimes , Fluid Flow and Mechanical Rock Properties. In *Int. Symp. Soc. Core Analysts*, pages 1–12, Napa Valley, USA, 2013. Society of Core Analysts.

Ott, H., Pentland, C., and Oedai, S. CO2brine displacement in heterogeneous carbonates. *International Journal of Greenhouse Gas Control*, 33:135–144, 2015.

Ovaysi, S. and Piri, M. Pore-scale modeling of dispersion in disordered porous media. *Journal of Contaminant Hydrology*, 124(1-4):68–81, 2011.

Ovaysi, S., Wheeler, M. F., and Balhoff, M. Quantifying the Representative Size in Porous Media. *Transport in Porous Media*, 104(2):349–362, 2014.

Pak, T., Butler, I., van Dijke, M. I. J., Geiger, S., and Jiang, Z. Visualisation of Two-Phase Fluid Displacement Processes at Pore Scale in Carbonate Rocks using Computed Tomography Technique. In *ICTMS2013*, pages 5–8, 2013.

Pan, C., Hilpert, M., and Miller, C. T. Lattice-Boltzmann simulation of two-phase flow in porous media. *Water Resources Research*, 40(1):n/a–n/a, 2004.

Pan, W. and Tartakovsky, A. Dissipative particle dynamics model for colloid transport in porous media. *Advances in Water Resources*, 58:41–48, 2013.

Parmigiani, A., Huber, C., Bachmann, O., and Chopard, B. Pore-scale mass and reactant transport in multiphase porous media flows. *Journal of Fluid Mechanics*, 686(686): 40–76, 2011.

Patel, R. a., Perko, J., Jacques, D., De Schutter, G., Van Breugel, K., and Ye, G. A versatile pore-scale multicomponent reactive transport approach based on lattice Boltzmann method: Application to portlandite dissolution. *Physics and Chemistry of the Earth, Parts A/B/C*, 70-71:127–137, 2014a.

Patel, R. a., Perko, J., Jacques, D., De Schutter, G., Ye, G., and van Breugel, K. Application of a pore-scale reactive transport model to study the influence of pore network characteristics on calcium leaching in cementitious systems. In *CONMOD*, Beijing, China, 2014b. RILEM Publications.

Patzek, T. W. Verification of a Complete Pore Network Simulator of Drainage and Imbibition. *SPE Journal*, 6(2):144–156, 2001.

Peng, S., Marone, F., and Dultz, S. Resolution effect in X-ray microcomputed tomography imaging and small pore's contribution to permeability for a Berea sandstone. *Journal of Hydrology*, 510:403–411, 2014.

Pereira Nunes, J. P., Bijeljic, B., and Blunt, M. J. Time-of-Flight Distributions and Breakthrough Curves in Heterogeneous Porous Media Using a Pore-Scale Streamline Tracing Algorithm. *Transport in Porous Media*, 109(2):317–336, 2015.

Peters, C. a. Accessibilities of reactive minerals in consolidated sedimentary rock: An imaging study of three sandstones. *Chemical Geology*, 265(1-2):198–208, 2009.

Piller, M., Casagrande, D., Schena, G., and Santini, M. Pore-scale simulation of laminar flow through porous media. *Journal of Physics: Conference Series*, 501:012010, 2014.

Piri, M. and Blunt, M. Three-dimensional mixed-wet random pore-scale network modeling of two- and three-phase flow in porous media. II. Results. *Physical Review E*, 71(2): 026302, 2005.

Plougonven, E. and Bernard, D. Optimal removal of topological artefacts in microtomographic images of porous materials. *Advances in Water Resources*, 34(6): 731–736, 2011.

Popov, P., Efendiev, Y., and Qin, G. Multiscale Modeling and Simulations of Flows in Naturally Fractured Karst Reservoirs. *Communications in Computational Physics*, 6(1): 162–184, 2009.

Porter, M. L., Schaap, M. G., and Wildenschild, D. Lattice-Boltzmann simulations of the capillary pressuresaturationinterfacial area relationship for porous media. *Advances in Water Resources*, 32(11):1632–1640, 2009.

Porter, M. L., Wildenschild, D., Grant, G., and Gerhard, J. I. Measurement and prediction of the relationship between capillary pressure, saturation, and interfacial area in a NAPL-water-glass bead system. *Water Resources Research*, 46(8):n/a—-n/a, 2010.

Powers, S. E., Anckner, W. H., and Seacord, T. F. Wettability of NAPL-Contaminated Sands. *Journal of Environmental Engineering*, 122(10):889–896, 1996.

Prodanović, M. A level set method for fluid displacement in realistic porous media, 2008.

Prodanović, M. and Bryant, S. L. A level set method for determining critical curvatures for drainage and imbibition. *Journal of colloid and interface science*, 304(2):442–58, 2006.

Prodanović, M., Lindquist, W., and Seright, R. 3D image-based characterization of fluid displacement in a Berea core. *Advances in Water Resources*, 30(2):214–226, 2007.

Prodanović, M., Mehmani, A., and Sheppard, A. P. Imaged-based multiscale network modelling of microporosity in carbonates. *Geological Society, London, Special Publications*, 406:SP406–9, 2014.

Prodanovic, M., Esteva, M., Hanlon, M., Nanda, G., and Agarwal, P. Digital Rocks Portal: a repository for porous media images, 2015.

Pudney, C. Distance-ordered homotopic thinning: a skeletonization algorithm for 3D digital images. *Comput. Vis. Image Underst.*, 72(3):404–413, 1998.

Rabbani, A., Jamshidi, S., and Salehi, S. An automated simple algorithm for realistic pore network extraction from micro-tomography images. *Journal of Petroleum Science and Engineering*, 123:164–171, 2014.

Rack, A., Garcia-Moreno, F., Schmitt, C., Betz, O., Cecilia, A., Ershov, A., Rack, T., Banhart, J., et al. On the possibilities of hard X-ray imaging with high spatio-temporal resolution using polychromatic synchrotron radiation. *Journal of X-Ray Science and Technology*, 18:429–441, 2010.

Raeini, A. Q. *Modelling multiphase flow through micro-CT images of the pore space*. PhD thesis, Imperial College, 2013.

Raeini, A. Q., Blunt, M. J., and Bijeljic, B. Direct simulations of two-phase flow on micro-CT images of porous media and upscaling of pore-scale forces. *Advances in Water Resources*, 74:116–126, 2014.

Raeini, A. Q., Bijeljic, B., and Blunt, M. Generalized pore-network modelling. In *7th International Conference on Porous Media & Annual Meeting*. Interpore, 2015a.

Raeini, A. Q., Bijeljic, B., and Blunt, M. J. Modelling capillary trapping using finite-volume simulation of two-phase flow directly on micro-CT images. *Advances in Water Resources*, 83:102–110, 2015b.

Ramandi, H. L., Mostaghimi, P., Armstrong, R. T., Saadatfar, M., and Val Pinczewski, W. Porosity and permeability characterization of coal a micro-computed tomography study. *International Journal of Coal Geology*, 2015.

Ramstad, T., Øren, P.-E., and Bakke, S. Simulation of Two-Phase Flow in Reservoir Rocks Using a Lattice Boltzmann Method. Technical Report 04, Numerical Rocks A.S., 2010.

Ramstad, T., Idowu, N., Nardi, C., and Øren, P. E. Relative Permeability Calculations from Two-Phase Flow Simulations Directly on Digital Images of Porous Rocks. *Transport in Porous Media*, 94(2):487–504, 2012.

Raoof, a. and Hassanizadeh, S. M. Saturation-dependent solute dispersivity in porous media: Pore-scale processes. *Water Resources Research*, 49(4):1943–1951, 2013.

Raoof, A., Hassanizadeh, S. M., and Leijnse, A. Upscaling Transport of Adsorbing Solutes in Porous Media: Pore-Network Modeling. *Vadose Zone Journal*, 9(3):624, 2010.

Raoof, A., Nick, H., Wolterbeek, T., and Spiers, C. Pore-scale modeling of reactive transport in wellbore cement under CO2 storage conditions. *International Journal of Greenhouse Gas Control*, 11:S67–S77, 2012.

Ravlo, V. and Arland, K. Calibration of digital pore scale models. In *Int. Symp. Soc. Core Analysts*, Avignon, France, 2014. Society of Core Analysts.

Renardy, Y. and Renardy, M. PROST: A Parabolic Reconstruction of Surface Tension for the Volume-of-Fluid Method. *Journal of Computational Physics*, 183(2):400–421, 2002.

Roels, S., Elsen, J., Carmeliet, J., and Hens, H. Characterisation of pore structure by combining mercury porosimetry and micrography. *Materials and Structures*, 34(2):76–82, 2001.

Rolle, M., Hochstetler, D., Chiogna, G., Kitanidis, P. K., and Grathwohl, P. Experimental Investigation and Pore-Scale Modeling Interpretation of Compound-Specific Transverse Dispersion in Porous Media. *Transport in Porous Media*, 93:347–362, 2012.

Rosenzweig, R., Furman, A., and Shavit, U. A Channel Network Model as a Framework for Characterizing Variably Saturated Flow in Biofilm-Affected Soils. *Vadose Zone Journal*, 12(2), 2013.

Roth, S., Li, D., Dong, H., and Blunt, M. J. Numerical pore-network fusion to predict capillary pressure and relative permeability in carbonates. In *Int. Symp. Soc. Core Analysts*, volume 02. Society for Core Analysts, 2012.

Rothman, D. H. and Zaleski, S. Lattice-gas models of phase separation: Interfaces, phase transitions, and multiphase flow. *Reviews of Modern Physics*, 66(4):1417–1479, 1994.

Roux, S. and Guyon, E. Temporal development of invasion percolation, 1989.

Rücker, M., Berg, S., Armstrong, R. T., Georgiadis, A., Ott, H., Schwing, A., Neiteler, R., Brussee, N., et al. From connected pathway flow to ganglion dynamics. *Geophysical Research Letters*, 42(10):3888–3894, 2015.

Ruspini, L., Farokhpoor, R., Varslot, T., and Øren, P. E. Pore-scale modeling of two-phase imbibition. In *Book of abstracts of International Conference on Porous Media (InterPore)*, page 147, Cincinnati, 2016a. Interpore.

Ruspini, L. C., Lindkvist, G., Bakke, S., Alberts, L., Carnerup, A. M., and Øren, P. E. A Multi-Scale Imaging and Modeling Workflow for Tight Rocks. In *SPE Low Perm Symposium*, number May, pages 5–6. Society of Petroleum Engineers, 2016b.

Russ, J. C. *The image processing handbook*. CRC Press, Boca Raton, FL, 4 edition, 1999.

Ryazanov, A. V., van Dijke, M. I. J., and Sorbie, K. S. Two-Phase Pore-Network Modelling: Existence of Oil Layers During Water Invasion. *Transport in Porous Media*, 80(1):79–99, 2009.

Saha, P. K., Borgefors, G., and Sanniti di Baja, G. A Survey on skeletonization algorithms and their applications. *Pattern Recognition Letters*, 000:1–10, 2015.

Sahimi, M. *Flow and Transport in Porous Media and Fractured Rock*. Wiley-VCH, 2011.

Sahimi, M., Mehrabi, A. R., Mirzaee, N., and Rassamdana, H. The Effect of Asphalt Precipitation on Flow Behavior and Production of a Fractured Carbonate Oil Reservoir During Gas Injection. *Transport in Porous Media*, 41(3):325–347, 2000.

Schaap, M. G., Porter, M. L., Christensen, B. S. B., and Wildenschild, D. Comparison of pressure-saturation characteristics derived from computed tomography and lattice Boltzmann simulations. *Water Resources Research*, 43(12):n/a–n/a, 2007.

Scheibe, T. D., Perkins, W. A., Richmond, M. C., McKinley, M. I., Romero-Gomez, P. D. J., Oostrom, M., Wietsma, T. W., Serkowski, J. A., et al. Pore-scale and multiscale numerical simulation of flow and transport in a laboratory-scale column. *Water Resources Research*, 51(2):1023–1035, 2015.

Schlüter, S., Sheppard, A., Brown, K., and Wildenschild, D. Image processing of multiphase images obtained via X-ray microtomography: A review. *Water Resources Research*, 50(4):3615–3639, 2014.

Sedighi Gilani, M., Fife, J. L., Boone, M. N., and Ghazi Wakili, K. Dynamics of microcrack propagation in hardwood during heat treatment investigated by synchrotron-based X-ray tomographic microscopy. *Wood Science and Technology*, 47:889–896, 2013.

Shah, S., Gray, F., Crawshaw, J., and Boek, E. Micro-computed tomography pore-scale study of flow in porous media: Effect of voxel resolution. *Advances in Water Resources*, 000:1–12, 2015.

Shan, X. and Chen, H. Lattice Boltzmann model for simulating flows with multiple phases and components. *Physical Review E*, 47(3):1815–1819, 1993.

Shanley, K. W., Cluff, R. M., and Robinson, J. W. Factors controlling prolific gas production from low-permeability sandstone reservoirs: Implications for resource assessment, prospect development, and risk analysis. *AAPG Bulletin*, 88(8):1083–1121, 2004.

Sheppard, A., Latham, S., Middleton, J., Kingston, A., Myers, G., Varslot, T., Fogden, A., Sawkins, T., et al. Techniques in helical scanning, dynamic imaging and image segmentation for improved quantitative analysis with X-ray micro-CT. *Nuclear Instruments and Methods in Physics Research Section B: Beam Interactions with Materials and Atoms*, 324:49–56, 2014.

Sheppard, A. P., Sok, R. M., and Averdunk, H. Improved pore network extraction methods. In *Int. Symp. Soc. Core Analysts*, number 20. Society of Core Analysts, Society of Core Analysts, 2005.

Sheppard, A. P., Sok, R. M., Averdunk, H., Robins, V. B., and Ghous, A. Analysis of rock microsctructure using high-resolution X-ray tomography. In *Int. Symp. Soc. Core Analysts*, pages 1–12. Society of Core Analysts, 2006.

Sholokhova, Y., Kim, D., and Brent Lindquist, W. Network flow modeling via lattice-Boltzmann based channel conductance. *Advances in Water Resources*, 32(2):205–212, 2009.

Siena, M., Riva, M., Hyman, J. D., Winter, C. L., and Guadagnini, A. Relationship between pore size and velocity probability distributions in stochastically generated porous media. *Physical Review E*, 89(1):013018, 2014.

Siena, M., Hyman, J. D., Riva, M., Guadagnini, A., Winter, C. L., Smolarkiewicz, P. K., Gouze, P., Sadhukhan, S., et al. Direct numerical simulation of fully saturated flow in natural porous media at the pore scale: a comparison of three computational systems. *Computational Geosciences*, 19(2):423–437, 2015.

Silin, D. and Patzek, T. Pore space morphology analysis using maximal inscribed spheres. *Physica A: Statistical Mechanics and its Applications*, 371(2):336–360, 2006.

Silin, D. B., Jin, G., and Patzek, T. W. Robust Determination of the Pore Space Morphology in Sedimentary Rocks. In *SPE Annual Technical Conference and Exhibition*, Denver, 2003.

Singh, B., Miller, S. R., Bhandari, H. B., Graceffa, R., Irving, T. C., and Nagarkar, V. V. High-speed detector for time-resolved diffraction studies. *Journal of physics. Conference series*, 425, 2013.

Sivanesapillai, R., Falkner, N., Hartmaier, A., and Steeb, H. A CSF-SPH method for simulating drainage and imbibition at pore-scale resolution while tracking interfacial areas. *Advances in Water Resources*, 2015.

Skauge, A., Spildo, K., Høiland, L., and Vik, B. Theoretical and experimental evidence of different wettability classes. *Journal of Petroleum Science and Engineering*, 57(3-4): 321–333, 2007.

Soete, J. *Pore network characterization in complex carbonate systems - A multidisciplinary approach*. Phd thesis, KU Leuven, 2016.

Sok, R. M., Knackstedt, M. A., Sheppard, A. P., Pinczewski, W., Lindquist, W., Venkatarangan, A., and Paterson, L. Direct and Stochastic Generation of Network Models from Tomographic Images; Effect of Topology on Residual Saturations. *Transport in Porous Media*, 46(2/3):345–371, 2002.

Sorbie, K. S. and Skauge, A. Can network modelling predict two-phase flow functions? In *Int. Symp. Soc. Core Analysts*, number 1956, Austin, USA, 2011. Society of Core Analysts.

Stockman, H. W. Lattice Boltzmann Method for Calculating Fluid Flow and Dispersion in Porous and Fractured Media. In *Gas Transport in Porous Media*, volume 38, pages 221–242. Springer Netherlands, 2006.

Suchomel, B. J., Chen, B. M., and Allen III, M. B. No Title. *Transport in Porous Media*, 30(1):1–23, 1998.

Sukop, M. C. and Thorne, D. T. *Lattice Boltzmann Modeling: an introduction for geoscientists and engineers*. Springer Berlin Heidelberg, Berlin, Heidelberg, 2006.

Sukop, M. C., Huang, H., Lin, C. L., Deo, M. D., Oh, K., and Miller, J. D. Distribution of multiphase fluids in porous media: Comparison between lattice Boltzmann modeling and micro-x-ray tomography. *Physical Review E*, 77(2):026710, 2008.

Sullivan, S., Sani, F., Johns, M., and Gladden, L. Simulation of packed bed reactors using lattice Boltzmann methods. *Chemical Engineering Science*, 60(12):3405–3418, 2005.

Swift, M. R., Orlandini, E., Osborn, W. R., and Yeomans, J. M. Lattice Boltzmann simulations of liquid-gas and binary fluid systems. *Physical Review E*, 54(5):5041–5052, 1996.

Szczygiel, R., Grybos, P., and Maj, P. High frame rate measurements of semiconductor pixel detector readout IC. *Nuclear Instruments and Methods in Physics Research, Section A: Accelerators, Spectrometers, Detectors and Associated Equipment*, 680:56–60, 2012.

Talon, L., Bauer, D., Gland, N., Youssef, S., Auradou, H., and Ginzburg, I. Assessment of the two relaxation time Lattice-Boltzmann scheme to simulate Stokes flow in porous media. *Water Resources Research*, 48(4):n/a–n/a, 2012.

Tanino, Y. and Blunt, M. J. Capillary trapping in sandstones and carbonates: Dependence on pore structure. *Water Resources Research*, 48(8):n/a—-n/a, 2012.

Tartakovsky, A. M. and Meakin, P. Pore scale modeling of immiscible and miscible fluid flows using smoothed particle hydrodynamics. *Advances in Water Resources*, 29(10): 1464–1478, 2006.

Tartakovsky, A. M. and Panchenko, A. Pairwise Force Smoothed Particle Hydrodynamics model for multiphase flow: Surface tension and contact line dynamics. *Journal of Computational Physics*, 2015.

Tartakovsky, A. M., Ferris, K. F., and Meakin, P. Lagrangian particle model for multiphase flows. *Computer Physics Communications*, 180(10):1874–1881, 2009.

Thijssen, J. *Computational physics*. Cambridge University Press, Cambridge, 2007.

Thompson, K. E., Willson, C. S., White, C. D., Nyman, S., Bhattacharya, J., and Reed, A. H. Application of a New Grain-Based Reconstruction Algorithm to Microtomography Images for Quantitative Characterization and Flow Modeling. *SPE Annual Technical Conference and Exhibition*, 2005.

Trebotich, D., Adams, M. F., Molins, S., Steefel, C. I., and Shen, C. High-Resolution Simulation of Pore-Scale Reactive Transport Processes Associated with Carbon Sequestration. *Computing in Science & Engineering*, 16(6):22–31, 2014.

Valvatne, P. H. and Blunt, M. J. Predictive pore-scale modeling of two-phase flow in mixed wet media. *Water Resources Research*, 40(7):n/a–n/a, 2004.

Van Eyndhoven, G., Batenburg, K. J., and Sijbers, J. Region-based iterative reconstruction of structurally changing objects in CT. *IEEE Transactions on Image Processing*, 23: 909–919, 2014.

Van Genuchten, M. Closed-Form Equation for Predicting the Hydraulic Conductivity of Unsaturated Soils. *Soil Science Society of America Journal*, 44(5):892–898, 1980.

Van Stappen, J., De Kock, T., Boone, M. A., Olaussen, S., and Cnudde, V. Pore-scale characterisation and modelling of CO2 flow in tight sandstones using X-ray micro-CT; knorringfjellet formation of the longyearbyen CO2 lab, Svalbard. *Norsk Geologisk Tidsskrift*, 94(2-3):201–215, 2014.

Varloteaux, C., Békri, S., and Adler, P. M. Pore network modelling to determine the transport properties in presence of a reactive fluid: From pore to reservoir scale. *Advances in Water Resources*, 53:87–100, 2013.

Vasilyev, L., Raoof, A., and Nordbotten, J. M. Effect of Mean Network Coordination Number on Dispersivity Characteristics. *Transport in Porous Media*, 95(2):447–463, 2012.

Veselý, M., Bultreys, T., Peksa, M., Lang, J., Cnudde, V., Van Hoorebeke, L., Kočiík, M., Hejtmánek, V., et al. Prediction and Evaluation of Time-Dependent Effective Self-diffusivity of Water and Other Effective Transport Properties Associated with Reconstructed Porous Solids. *Transport in Porous Media*, 110(1):81–111, 2015.

Vincent, L. and Soille, P. Watersheds in digital spaces: an efficient algorithm based on immersion simulations. *IEEE Transactions on Pattern Analysis and Machine Intelligence*, 13(6):583–598, 1991.

Vogel, H.-J. and Roth, K. Quantitative morphology and network representation of soil pore structure. *Advances in Water Resources*, 24(3-4):233–242, 2001.

Welch, N. J., Crawshaw, J. P., and Boek, E. S. Computerized X-Ray Microtomography Observations and Fluid Flow Measurements of the Effect of Effective Stress on Fractured Low Permeability Porous Media. In *Int. Symp. Soc. Core Analysts*, pages 1–12, St. John's, CA, 2015. Society of Core Analysts.

Whitaker, S. Flow in porous media II: The governing equations for immiscible, two-phase flow. *Transport in Porous Media*, 1(2):105–125, 1986.

Wildenschild, D. and Sheppard, A. P. X-ray imaging and analysis techniques for quantifying pore-scale structure and processes in subsurface porous medium systems. *Advances in Water Resources*, 51(0):217–246, 2013.

Wildenschild, D., Hopmans, J., and Simunek, J. Flow Rate Dependence of Soil Hydraulic Characteristics. *Soil Science Society of America Journal*, 65(1):35, 2001.

Wilkinson, D. and Willemsen, J. F. Invasion percolation: a new form of percolation theory. *Journal of Physics A: Mathematical and General*, 16(14):3365–3376, 1983.

Wu, K., Dijke, M. I. J., Couples, G. D., Jiang, Z., Ma, J., Sorbie, K. S., Crawford, J., Young, I., et al. 3D Stochastic Modelling of Heterogeneous Porous Media Applications to Reservoir Rocks. *Transport in Porous Media*, 65(3):443–467, 2006.

Yang, J. and Boek, E. S. A comparison study of multi-component Lattice Boltzmann models for flow in porous media applications. *Computers & Mathematics with Applications*, 65 (6):882–890, 2013.

Yang, J., Crawshaw, J., and Boek, E. S. Quantitative determination of molecular propagator distributions for solute transport in homogeneous and heterogeneous porous media using lattice Boltzmann simulations. *Water Resources Research*, 49(12):8531–8538, 2013a.

Yang, X., Liu, C., Shang, J., Fang, Y., and Bailey, V. L. A Unified Multiscale Model for Pore-Scale Flow Simulations in Soils. *Soil Science Society of America Journal*, 78(1): 108, 2014.

Yang, X., Mehmani, Y., Perkins, W. a., Pasquali, A., Schönherr, M., Kim, K., Perego, M., Parks, M. L., et al. Intercomparison of 3D pore-scale flow and solute transport simulation methods. *Advances in Water Resources*, 000:1–14, 2015.

Yang, Z., Niemi, A., Fagerlund, F., and Illangasekare, T. Two-phase flow in rough-walled fractures: Comparison of continuum and invasion-percolation models. *Water Resources Research*, 49(2):993–1002, 2013b.

Yehya, a., Naji, H., and Sukop, M. Simulating flows in multi-layered and spatially-variable permeability media via a new Gray Lattice Boltzmann model. *Computers and Geotechnics*, 70:150–158, 2015.

Yiotis, A. G., Tsimpanogiannis, I. N., Stubos, A. K., and Yortsos, Y. C. Pore-network study of the characteristic periods in the drying of porous materials. *Journal of colloid and interface science*, 297(2):738–48, 2006.

Yoon, H. and Dewers, T. A. Nanopore structures, statistically representative elementary volumes, and transport properties of chalk. *Geophysical Research Letters*, 40(16):4294–4298, 2013.

Yoon, H., Kang, Q., and Valocchi, A. J. Lattice Boltzmann-Based Approaches for Pore-Scale Reactive Transport. *Reviews in Mineralogy and Geochemistry*, 80(1):393–431, 2015.

Young, T. An Essay on the Cohesion of Fluids. *Philosophical Transactions of the Royal Society of London*, 95(0):65–87, 1805.

Youssef, S., Rosenberg, E., Gland, N., Bekri, S., and Vizika, O. Quantitative 3D characterisation of the pore space of real rocks: improved CT resolution and pore extraction methodology. In *Int. Symp. Soc. Core Analysts*. Society of Core Analysts, 2007.

Youssef, S., Han, M., Bauer, D., Rosenberg, E., Bekri, S., Fleury, M., and Vizika, O. High resolution -CT combined to numerical models to assess electrical properties of bimodal

carbonates. In *Int. Symp. Soc. Core Analysts*, volume 2, pages 1–12, Abu Dhabi, UAE, 2008. Society of Core Analysts.

Youssef, S., Deschamps, H., Dautriat, J., Rosenberg, E., Oughanem, R., Maire, E., and Mokso, R. 4D Imaging of fluid flow dynamics in natural porous media with ultra-fast X-ray microtomography. In *Int. Symp. Soc. Core Analysts*, Napa Valley, USA, 2013. Society of Core Analysts.

Zaretskiy, Y., Geiger, S., Sorbie, K., and Förster, M. Efficient flow and transport simulations in reconstructed 3D pore geometries. *Advances in Water Resources*, 33(12):1508–1516, 2010.

Zhang, S., Klimentidis, R. E., and Barthelemy, P. Micron to millimeter upscaling of shale rock properties based on 3D imaging and modeling. In *Int. Symp. Soc. Core Analysts*. Society of Core Analysts, Society of Core Analysts, 2012.

Zhou, D., Dillard, L. A., and Blunt, M. J. A Physically Based Model of Dissolution of Nonaqueous Phase Liquids in the Saturated Zone. *Transport in Porous Media*, 39(2): 227–255, 2000.

Zhou, T., Lundström, U., and Thüring, T. Comparison of two x-ray phase-contrast imaging methods with a microfocus source. *Optics Express*, 21(25):1141–1148, 2013.

Zhu, J. and Ma, J. An improved gray lattice Boltzmann model for simulating fluid flow in multi-scale porous media. *Advances in Water Resources*, 56:61–76, 2013.

Zitová, B. and Flusser, J. Image registration methods: a survey. *Image and Vision Computing*, 21(11):977–1000, 2003.